UNIVERSIDADE FEDERAL DO RIO GRANDE DO SUL
PROGRAMA DE PÓS-GRADUAÇÃO EM FÍSICA

Tese de Doutorado

Estudo da Alimentação e Retro-alimentação de núcleos ativos de galáxias a partir de observações no infravermelho próximo

Astor João Schönell Júnior

Tese desenvolvida sob a orientação da Professora Dra. Thaisa Storchi-Bergmann, apresentado ao Programa de Pós Graduação em Física do Instituto de Física da UFRGS, em preenchimento parcial dos requisitos para a obtenção do título de Doutor em Física.

Porto Alegre, 6 de Novembro de 2017

Aos meus pais...

Agradecimentos

Primeiramente gostaria de agradecer à minha orientadora prof^{a}. dr^{a}. Thaisa Storchi-Bergmann pela incansável busca ao conhecimento e à ciência. Além de ser uma cientista extraordinária foi uma pessoa incrível nos momentos em que mais encontrei dificuldade na minha vida acadêmica e pessoal. Agradeço, então, por todos os gestos, paciência, conhecimentos compartilhados e ensinamentos!

Deixo registrado a importância do Programa de Pós Graduação em Física da UFRGS, que me acolheu e deu chances para que meu trabalho se desenolvesse.

Ao órgão financiador durante o período de 4 anos do doutorado, o Conselho Nacional de Desenvolvimento Científico e Tecnológico (CNPq).

Aos colegas de laboratório e do departamento de astronomia, mas principalmente aos amigos Guilherme Couto e a Natacha Zanon pela parceria e inúmeras ajudas ao longo desses anos.

Aos irmãos, Rogério e Rogemar Riffel, que são os responsáveis por toda a minha caminhada dentro da astrofísica, como incentivadores, professores, orientadores e amigos nas horas difíceis.

Aos meus pais e meu irmão, por serem tudo que eu precisava todos os dias da minha vida. Tenho a certeza de que seria impossível chegar até aqui sem o apoio incondicional dos maiores exemplos da minha vida.

À minha namorada, que me acalmou nos momentos mais conturbados, me incentivou quando mais precisei e vibrou ao meu lado a cada conquista.

A TODOS meus amigos, pelas palavras incentivadoras e gestos de apoio a cada degrau dessa caminhada.

A cada conhecido e familiar que sempre que podia me perguntava sobre o trabalho e me incentivava a continuar.

A todos vocês, o meu mais profundo obrigado!

Resumo

Neste trabalho discutimos a excitação, cinemática e distribuição do gás e das estrelas, bem como um estudo das populações estelares nos kpc centrais de 20 galáxias ativas, que fazem parte de uma amostra estatisticamente completa de 29 galáxias ativas, 16 das quais estão sendo observada através de um *Large and Long Program* (LLP) do telescópio Gemini: "*NIFS survey of feeding and feedback processes in nearby Active Galaxies*", onde foi usado o instrumento NIFS nas bandas J e K_l com resolução espectral de R$\approx$ 5000 e angular de $\approx$ 0,15". A finalidade do projeto é mapear os processos de *feeding* e *feedback* em galáxias ativas próximas para investigar o efeito destes processos na evolução de galáxias. Encontramos feedbacks potentes o suficiente para influenciar significativamente na galáxia hospodeira em $\approx$ 20% dos casos.

O gás apresenta emissão estendida tanto para a fase molecular quanto para a fase ionizada. Porém, o gás molecular é muitas vezes mais uniformemente distribuído no plano da galáxia, enquanto que o gás ionizado é mais concentrado ou colimado ao longo do eixo de ionização do AGN. Na cinemática, também observa-se distinções: enquanto o gás molecular está normalmente em rotação no plano da galáxia com baixa dispersão de velocidades, o gás ionizado apresenta outras componentes associadas a altas dispersões de velocidades. Verifica-se uma anticorrelação entre o momento de Gauss-Hermite h_3 e os campos de velocidade, em que valores positivos de h_3 são associados a $blueshifts$ e valores negativos de h_3 à $redshifts$, o que atribuímos ao efeito conhecido como "$asymmetric\ drift$".

A massa integrada de hidrogênio ionizado varia de $2{,}2\times10^4$ a $3{,}2\times10^7$ $M_\odot$, enquanto a massa de hidrogênio molecular quente ($\approx$ 2000K) varia de 29 a 3300 $M_\odot$. A massa de hidrogênio molecular frio é estimada entre 2×10^7 e $2{,}4\times10^9$ $M_\odot$. A densidade superficial média de massa de gás molecular quente varia de $7{,}6\times10^{-4}$ a $1{,}8\times10^{-2}$ $M_\odot/pc^2$, enquanto para o gás molecular frio varia de 526 a 20682 $M_\odot/pc^2$. A densidade superficial média de massa para o gás ionizado varia de 4,8 a 244 $M_\odot/pc^2$. A excitação mostra 3 comportamentos principais: i) núcleo com excitação tipo Seyfert circundado por excitação LINER; ii) núcleo com valores de excitação típica de Starbursts circundado por valores Seyfert e/ou LINER; iii) somente valores de Seyfert/somente valores de LINER. Constatou-se evidências de inflow em gás quente para 4 galáxias, com as taxas variando de 4×10^{-5} a 4×10^{-3} $M_\odot$ por ano. A maioria dos outflows encontrados foram em gás ionizado com valores para as taxas de outflow variando entre 6×10^{-2} a 10,7 $M_\odot$ por ano e a potência desses outflows foi estimada entre $9{,}5\times10^{37}$ ergs/s e $5{,}7\times10^{41}$ ergs/s. Somente em 3 galáxias encontramos potências da ordem de 0,5% L_{bol}, para as quais o feedback pode influenciar de forma significativa a evolução do bojo da galáxia.

A cinemática estelar pode ser bem descrita através de modelos de discos em rotação e mais uma vez encontramos o efeito do "$asymmetric\ drift$", como encontrado para o gás. Em 4 galáxias da amostra em que estudamos a população estelar, encontramos estrelas jovens ($t < 50\times10^6$ anos) a distâncias do núcleo entre 200 e 300 pc, estrelas de idade intermediária ($50\times10^6 \leq t < 2\times10^9$ anos) mais afastadas e populações mais velhas dominando nos 250 pc centrais das galáxias.

Abstract

In this work we discuss the excitation, gas and stellar kinematics, as well as the study of the stellar populations in the inner kpc of 20 active galaxies, which are part of a complete sample of 29 active galaxies, 16 of which comprise a "Large and Long Program" (LLP) of the Brazilian participation in the Gemini Telescope: "NIFS survey of feeding and feedback processes in nearby Active Galaxies", where the NIFS instrument was used, with observations in the J and K_l spectral bands, with spectral resolution of R$\approx$ 5000 and angular of $\approx$ 0.15". The project goal is to map the feeding and feedback processes in nearby active galaxies to investigate the effect of these processes in the evolution of the galaxies. We found feedbacks powerful enough to have significant influence in the evolution of the host galaxy in $\approx$ 20% of the cases.

The gas shows extended emission in both the molecular and ionized phases. However, the molecular gas is usually more evenly distributed in the galaxy plane, while the ionized gas is more concentrated or colimated along the ionization axis of the AGN. In the kinematics, there are also distinctions: while the molecular gas is usually in rotation in the galaxy plane with low velocity dispersions, the ionized gas shows other componentes associated with high velocity dispersions. It is verified an anticorrelation between the Gauss-Hermite moment h_3 and the velocity field, where positive values of h_3 are associated to blueshifts and negative values of h_3 to redshits, what we attribute to the effect known as "asymmetric drift".

The integrated mass of ionized hydrogen ranges from 2.2×10^4 to 3.2×10^7 $M_\odot$, while the mass of warm ($\approx$ 2000K) molecular hydrogen ranges from 29 to 3300 $M_\odot$. The mass of cold molecular hydrogen is estimated between 2×10^7 to 2.4×10^9 $M_\odot$. The average surface mass density of the molecular gas ranges from 7.6×10^{-4} to 1.8×10^{-2} $M_\odot/pc^2$, while for the cold molecular it ranges from 526 to 20682 $M_\odot/pc^2$. The average surface mass density for the ionized gas ranges from 4.8 to 244 $M_\odot/pc^2$. The excitation shows 3 main behaviors: i) nucleus with Seyfert excitation surrounded by LINER excitation; ii) nucleus with Starburst excitation surrounded by Seyfert and/or LINER excitation; iii) only LINER excitation. It was found evidence of inflow in warm molecular gas for 4 galaxies, with rates ranging from 4×10^{-5} to 4×10^{-3} $M_\odot$ per year. Most outflows were found in ionized gas with values ranging from 6×10^{-2} to 10.7 $M_\odot$ per year, and the power of the outflows was estimated between 9.5×10^{37} ergs/s and 5.7×10^{41} ergs/s. Only in three galaxies we found the power of the outflow in the order of 0.5% L_{Bol}, for which the feedback can have a significant influence in the evolution of the galaxy.

The stellar kinematics can be well descibed by models of rotating disks, and once more we find the "asymmetric drift" effect, like the one found for the gas. In 4 galaxies of the sample for which we studied the stellar population, we found young stars ($t < 50$ Myr) at distances ranging from 200 to 300 pc from the nucleus, while intermediate age stars (50 Myr $\leq t < 2$ Gyr) are found farther away, while old stars dominate in the inner $\approx$ 250 pc.

Sumário

1 Introdução p. 12

1.1 Núcleos ativos de galáxias . . . . . p. 12

1.1.1 AGNs do tipo Seyfert . . . . . p. 14

1.2 Evolução da galáxia e o seu AGN . . . . . p. 16

1.2.1 O "Green Valley" . . . . . p. 17

1.2.2 A relação $M_{SMBH} - \sigma_*$ . . . . . p. 18

1.2.3 A função de luminosidade . . . . . p. 19

1.3 Motivação: Feeding e Feedback . . . . . p. 21

1.4 Objetivos . . . . . p. 22

2 Amostra p. 24

3 Obtenção e redução dos dados p. 25

3.1 O instrumento NIFS . . . . . p. 25

3.2 Observações . . . . . p. 26

3.3 Redução de Dados . . . . . p. 27

3.3.1 Remoção da corrente de escuro . . . . . p. 28

3.3.2 Divisão por flat-field . . . . . p. 28

3.3.3 Correção por distorção espacial . . . . . p. 28

3.3.4 Calibração em comprimento de onda . . . . . p. 28

3.3.5 Subtração do Céu . . . . . p. 29

3.3.6 Remoção de absorções telúricas . . . . . p. 29

3.3.7 Calibração em Fluxo . . . . . p. 30

3.3.8 Construção dos Cubos de Dados . . . . . p. 30

4 Metodologia p. 32

4.1 Diferenciando séries de Gauss-Hermite de Gaussianas . . . . . p. 32

4.2 Construção dos mapas bidimensionais . . . . . p. 34

4.3 Construção dos *Channel Maps* . . . . . p. 34

4.4 Construção dos mapas de razões de fluxo . . . . . p. 35

4.5 O modelo de rotação . . . . . p. 35

4.6 Cálculos de Massas, distribuição de densidades superficiais e gradientes . . . p. 37

4.7 O código Starlight . . . . . p. 38

5 Resultados p. 40

5.1 Feeding versus feedback in AGN from near-infrared IFU observations: the case of Mrk 766 . . . . . p. 40

5.2 Feeding versus feedback in active galactic nuclei from near-infrared integral field spectroscopy - XII. NGC 5548 . . . . . p. 40

5.3 Gemini NIFS survey of feeding and feedback processes in nearby Active Galaxies: III - Gas distribution and excitation . . . . . p. 40

6 Discussão geral p. 41

6.1 Massas totais de gás e densidades superficiais médias de massa . . . . . p. 41

6.1.1 Gás molecular . . . . . p. 41

6.1.2 Gás ionizado . . . . . p. 42

6.1.3 Distribuições de densidade superficial de massa . . . . . p. 45

6.2 Excitação . . . . . p. 45

6.3 Cinemática do gás . . . . . p. 46

6.3.1 Momentos h_3 e h_4 . . . . . p. 47

6.4 Cinemática Estelar . . . . . p. 47

6.5 Feeding e Feedback . . . . . p. 48
6.5.1 Inflows . . . . . p. 48
6.5.2 Outflows . . . . . p. 48
6.5.3 Populações estelares . . . . . p. 51

7 Conclusões p. 52

Lista de Figuras

1.1 Ilustração o modelo unificado para AGN. . . . . p. 13

1.2 Espectro Infravermelho de um AGN Seyfert 1. . . . . p. 15

1.3 Espectro infravermelho de um AGN Seyfert 2. . . . . p. 15

1.4 Figura da distribuição bi-modal das galáxias. . . . . p. 16

1.5 Figura da relação da M. . . . . p. 19

1.6 Plot esquemático da função de Schechter. . . . . p. 20

1.7 Figura do papel do AGN. . . . . p. 20

3.1 Ilustração do princípio do AIS equipado com três slices. . . . . p. 26

3.2 Imagem flat-field obtida com o NIFS. . . . . p. 29

3.3 Imagem da máscara de Ronchi obtida com o NIFS. . . . . p. 30

3.4 Imagem da lâmpada padrão - ArXe. . . . . p. 31

4.1 Gaussianas e séries de Gauss hermite. . . . . p. 33

4.2 Exemplo ilustrado da construção dos channel maps. . . . . p. 35

4.3 Figura da distribuição de pontos de velocidade. . . . . p. 37

6.1 Histogramas densidades superficiais médias de massa. . . . . p. 43

6.2 Mapa de razões de Maksym et al. 2017. . . . . p. 46

Lista de Tabelas

3.1 Observações. (1) Galaxia; (2) Identificação do Projeto; Resolução angular na banda (3) J e (4) K; Resolução espectral na banda (5) J e (6) K; Referência. . p. 27

6.1 Área total, massa total e densidade superficial média de massa para o gás ionizado, molecular quente e molecular frio para 16 galáxias observadas da amostra. . . . . p. 44

6.2 Distância, área observada, taxa de outflow, potência do outflow, razão percentual entre a potência do outflow e a luminosidade bolométrica do AGN e taxa de inflow para as galáxias correspondentes. . . . . p. 50

1 Introdução

1.1 Núcleos ativos de galáxias

Os Núcleos Ativos de Galáxias (AGNs, do inglês Active Galactic Nuclei) são regiões nucleares de galáxias que emitem radiação e energia cuja natureza não pode ser explicada como sendo unicamente proveniente de estrelas. Essa energia é, na verdade, gerada a partir da captura de matéria proveniente de um disco de acreção que se forma no entorno de um buraco negro supermassivo. Quando a matéria é capturada pelo buraco negro supermassivo sua energia potencial gravitacional se transforma na energia irradiada pelo AGN. Além da energia sob a forma de radiação a partir do disco de acreção e sua atmosfera, muitas vezes jatos de partículas surgem na borda interna do disco de acreção, bem como ventos emitidos de raios intermediários do disco.

Os AGN são classificados em categorias distintas de acordo com suas características espectrais e de luminosidade: Quasares (QSOs), Seyferts, Rádio-Galáxias, LINERS (*Low Ionization Nuclear Emission Regions*) e Blazares, onde os Quasares são a classe mais luminosa e os LINERS a menos luminosa. A Fig. 1.1, extraída de Beckmann e Shrader (2012) e inspirada no "Modelo unificado" (Antonucci, 1993) mostra as principais estruturas presentes num AGN e como diferentes características e luminosidade, bem como diferentes linhas de visada podem levar a diferentes classificações. Estas estruturas são:

- Buraco negro supermassivo (daqui para frente SMBH, do inglês Supermassive Black Hole): Um buraco negro é uma região no espaço na qual um corpo curvou tanto o espaço-tempo que nenhum tipo de radiação eletromagnética é capaz de escapar (Robson, 1996). Os SMBH possuem uma massa da ordem de milhões a bilhões de massas solares confinadas dentro do seu raio de Schwarzschild $R_{Sch} = \frac{2GM}{c^2}$ e acredita-se existir um, pelo menos, no centro de cada galáxia que possui bojo.

- Disco de acreção: Disco formado gás capturado pelo campo gravitacional do SMBH. As nuvens de gás que orbitam no disco, através da viscosidade da fricção com as demais

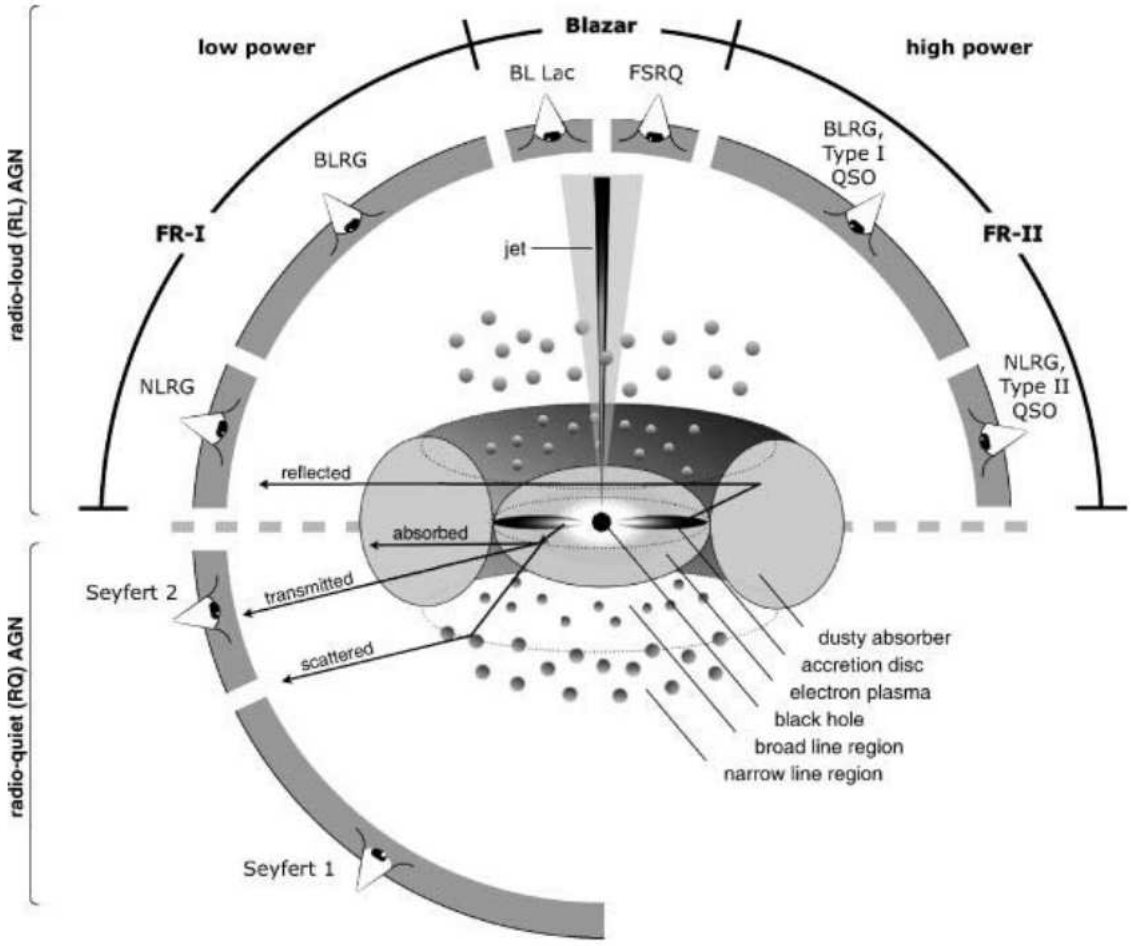

Figura 1.1: Representação esquemática baseada no modelo unificado. A categoria de objeto depende do ângulo de visada, se o AGN produz jatos rádio e de quão poderoso é o "motor central". Figura extraída de Beckmann e Shrader (2012).

nuvens aquecendo-o, o gás fica iozinado e se transforma num plasma. Nesse processo o gás perderá energia cinética que será transformada em radiação emitida pelo disco e assim a matéria vai perdendo momento angular até ser capturada pelo SMBH. Este disco de plasma quente é chamado de disco de acreção.

- Região de linhas largas (BLR, do inglês "Broad Line Region"): Região compacta ($<$1 pc) com nuvens de gás próximas ao disco de acreção, com alta dispersão de velocidades ($\approx$ 5000 km s^{-1} - largura a meia altura da linha). A densidade eletrônica média da região é de 10^9 elétrons cm^{-3} e sua temperatura efetiva da ordem de 10^4 K (Osterbrock; Ferland, 2006).

- Toro de poeira externo ao disco de acreção e BLR: Tem um raio interno (definido pela região que emite à temperatura de sublimação da poeira, da ordem de $\approx$ 1200 K) que pode ser menor do que 1 parsec, mas cujo raio externo depende da temperatura. Em

AGNs do tipo 2 obscurece a radiação do disco de acreção e da BLR. É, em muitos casos, detectado espectroscopicamente e por interferometria no infravermelho (Jaffe et al., 2004; Rodríguez-Ardila; Mazzalay, 2006; Burtscher et al., 2009; Riffel et al., 2009b).

- Região de formação de linhas estreitas (NLR, do inglês "Narrow Line Region"): Região extensa (10-100 pc) com nuvens de gás ionizadas pelo AGN, com dispersão de velocidades entre 200 e 900 km s^{-1} (largura a meia altura da linha). É a única estrutura resolvida espacialmente no óptico.

- Jato Rádio: Estrutura colimada que pode ser observada em grande escala em muitos AGNs (pode alcançar milhares de parsecs) formada por partículas relativísticas aceleradas ao longo de linhas de campos magnéticos originados na borda interna do disco de acreção e que emitem radiação sincrotrônica observada em rádio frequência.

1.1.1 AGNs do tipo Seyfert

Foram escolhidas para o presente estudo AGNs do tipo Seyfert, que são AGNs de luminosidade intermediária, com $M_B > -21.5 + \log h$, onde $h = 0.7$ é a constante de Hubble (Schmidt; Green, 1983).

As galáxias Seyferts apresentam núcleos brilhantes, porém, não ofuscam a galáxia hospedeira, se tornando adequadas ao nosso estudo, em que objetivamos mapear os fenômenos de feeding e feedback do AGN através da interação do mesmo com a galáxia. Morfologicamente, os membros dessa categoria possuem a aparência de galáxias espirais comuns, com um núcleo brilhante, que apresenta fortes linhas de emissão de alta ionização. Estudos como o de Heckman (1978) mostraram que a maior parte das galáxias Seyfert são espirais. As galáxias Seyfert se subdividem em dois grandes grupos, de acordo com uma divisão primeiramente estabelecida por Khachikian e Weedman (1974): as Seyfert de tipo 1 e as Seyfert de tipo 2.

Os objetos de tipo 1 (ver Fig. 1.2) apresentam linhas de emissão permitidas bastante alargadas, com valores típicos de FWHM da ordem de 5000 km s^{-1}, e linhas proibidas mais estreitas, com valores de FWHM na faixa de 200 km s^{-1} < FWHM < 900 km s^{-1}, sendo que, na maioria dos casos, FWHM$= 350 - 400$ km s^{-1} (Peterson, 1997). Os objetos de tipo 2 (ver Fig. 1.3), por outro lado, apresentam, apenas, linhas estreitas com valores de FWHM comparáveis aos das linhas estreitas dos objetos de tipo 1. Dessa forma, pode-se dizer que, embora as linhas estreitas dessa categoria de AGNs apresentem valores consideravelmente menores do que as linhas mais alargadas, elas ainda são mais largas do que as vistas em vários outros tipos de objetos, como galáxias *Starburst* ou regiões HII (Peterson, 1997).

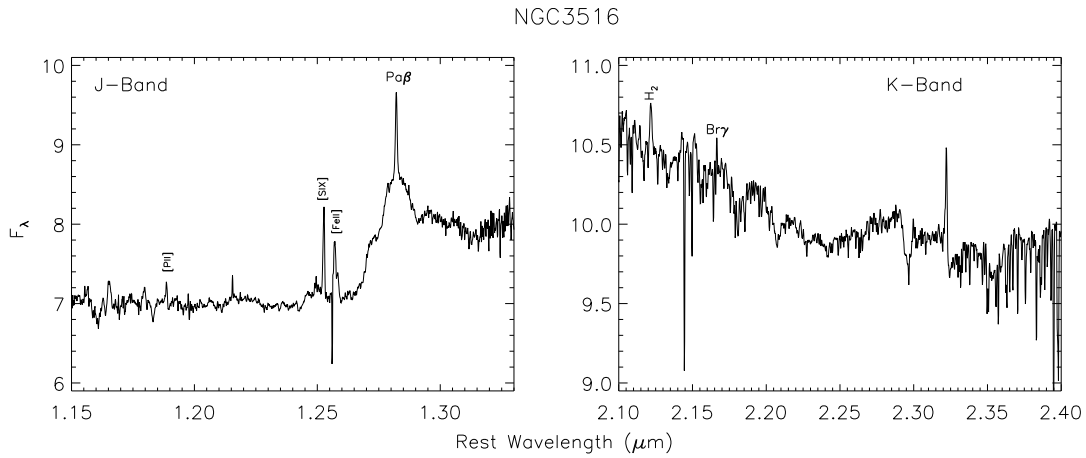

Figura 1.2: Espectro infravermelho da galáxia Seyfert 1 NGC 3516. O espectro mostra o alargamento na linha de Paβ e linhas proibidas estreitas como as do [Fe II], [S IX] e [P II].

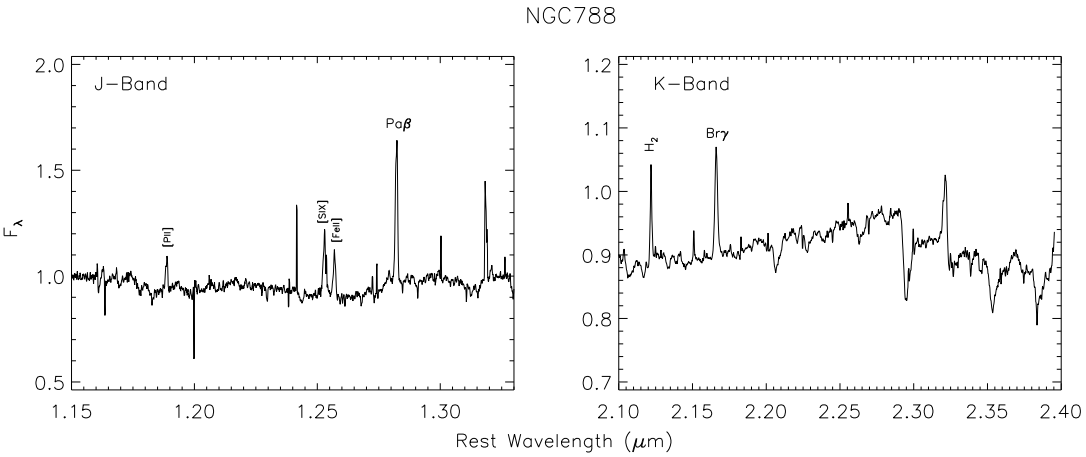

Figura 1.3: Espectro infravermelho da galáxia NGC 788. Podemos notar a ausência de linhas de emissão largas nesta Seyfert 2.

Baseando-se na aparência dos espectros ópticos, Osterbrock (1981) introduziu as subcategorias Seyfert 1.5, 1.8 e 1.9 para esse tipo de AGNs. As galáxias Seyfert 1.9 apresentam uma fraca componente alargada, apenas, na linha Hα. Nas galáxias Seyfert 1.8, as componentes largas também são bastante fracas, mas detectadas tanto em Hα quanto em Hβ. Por fim, as galáxias Seyfert 1.5 apresentam componentes largas e estreitas das linhas de emissão com intensidades comparáveis.

Estas características que diferenciam as Seyferts de diferentes tipos citados acima, são explicadas dentro do Modelo Unificado (Ver Fig.1.1) como sendo devido ao obscurecimento total (no caso das Seyfert 2) ou parcial da BLR (no caso das Seyfert 1.5, 1.8 e 1.9).

1.2 Evolução da galáxia e o seu AGN

Estudos fotométricos recentes das galáxias do universo local (Faber et al., 2007; Rodríguez-Puebla et al., 2017; Krywult et al., 2017) mostram que elas ocupam duas regiões distintas num diagrama cor versus massa (ver Fig. 1.4): uma "nuvem azul" e uma "sequência vermelha", onde as primeiras são compostas por galáxias espirais, com formação estelar, enquanto as últimas são compostas por galáxias elípticas e lenticulares (Early Type Galaxies - ETGs) onde a taxa de formação estelar já é insignificante. Para suprimir a formação estelar deve haver algum fenômeno de expulsão de gás fazendo com que as galáxias migrem rapidamente da "nuvem azul" para a "sequência vermelha" (Faber et al., 2007), já que há poucas galáxias na região entre a nuvem azul e a sequência vermelha ("*Green Valley*").

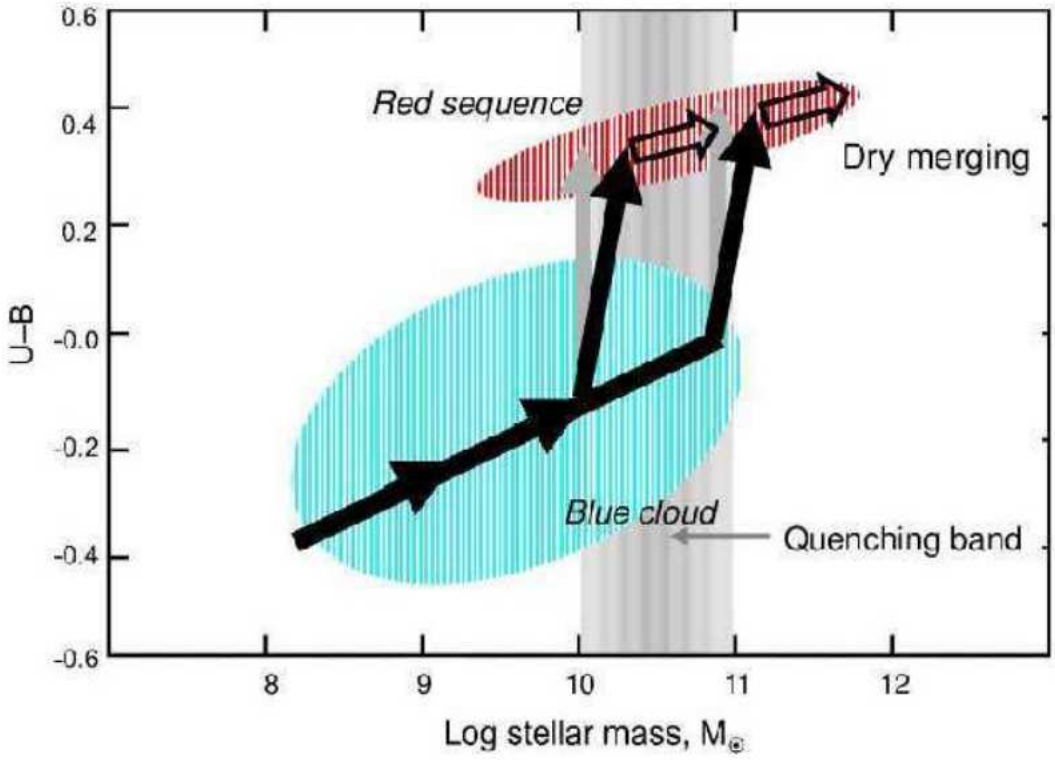

Figura 1.4: Diagrama cor-massa com a distribuição das galáxias em sua evolução. As flechas pretas e verticais situam fusões que serão ricas em gás (wet - molhadas) e dissipativas, uma vez que as duas galáxias em fusão são azuis, formam estrelas e contém gás. As flechas pretas vazadas mostram as galáxias na sequência vermelha, onde se deslocam mais lentamente por uma sequência de fusões não-dissipativas e sem gás (dry - secas). As flechas verticais cinzentas representam a trajetória de galáxias em que o suprimento de gás dos discos é expulso por choques, sem ocorrer fusão - por exemplo, em interações sofridas dentro de aglomerados de galáxias, onde o gás de galáxias espirais é redistribuído transformando-as em S0. Figura de (Faber et al., 2007).

Sugere-se que as galáxias da sequência vermelha sejam provenientes da fusão dissipativa

("wet mergers") de galáxias azuis. Acredita-se que a formação estelar nestas galáxias é rapidamente extinta devido à ejeção de gás, que é causada pela retro-alimentação (feedback) do buraco negro supermassivo, ventos de supernovas e aquecimento por choques nos halos mais massivos (Granato et al., 2004; Kereš et al., 2005; Dekel; Birnboim, 2006).

Porém, a fusão de galáxias azuis não é o bastante para que se formem as galáxias da sequência vermelha. Para tal, é indispensável que fusões não-dissipativas, ("dry mergers"), também ocorram para formar as galáxias vermelhas mais massivas (ou seja, uma evolução dentro da sequência vermelha) (Hopkins et al., 2009; Khochfar; Silk, 2009; Oser et al., 2010).

As galáxias da sequência vermelha têm, tipicamente, os chamados "bojos clássicos", produto da fusão de galáxias, enquanto as galáxias azuis possuem "pseudo-bojos", estruturas que evoluem secularmente (Kormendy; Kennicutt JR., 2004). Quando incluímos o "feedback" nos modelos de fusão, as duas formas, não-dissipativa e dissipativa (sem e com gás) produzem galáxias vermelhas. Porém, a estrutura cinemática pode ser muito diferente. Em fusões entre galáxias de massas semelhantes, ricas em gás, este gás forma um disco; após a ejeção do gás, seu aquecimento ou sua transformação em estrelas, obtemos um sistema estelar vermelho dominado por rotação (Cox et al., 2006; Jesseit et al., 2009); já uma fusão igualitária não-dissipativa resulta em uma galáxia vermelha com pouca ou nenhuma rotação (Naab; Burkert, 2003; Cox et al., 2006).

Quando as fusões são entre galáxias de massas diferentes vemos um cenário bem diferente, já que a galáxia mais massiva conserva aproximadamente a sua estrutura, na medida em que depende da quantidade de massa e gás acrescidas, de forma que a galáxia resultante, na maior parte dos casos, mantém uma rotação significativa (Cox et al., 2006; Jesseit et al., 2009).

Nesse contexto vê-se a importância dos mecanismos de feedback para a evolução das galáxias. Mais adiante discutiremos também sua importância para moldar a função de luminosidade de galáxias.

1.2.1 O "Green Valley"

Vários estudos (Schawinski et al., 2007; Nandra et al., 2007; Silverman et al., 2008; Powell et al., 2017; Martin et al., 2017) de galáxias hospedeiras de AGNs tanto no universo local como para redshifts de z$\approx$1, mostram que as galáxias hospedeira têm, no óptico, um pico em cores intermediárias, entre a nuvem azul e a sequência vermelha, ou seja, no *Green Valley*. Segundo Schawinski et al. (2009) se considerarmos as cores *u-r* do óptico como um proxy para a idade estelar, chegamos a uma sequência evolutiva para galáxias early-type de baixa massa: começamos

com formação estelar na núvem azul seguida pelo começo de acreção de matéria pelo buraco negro supermassivo central acompanhada pelo declínio na taxa de formação estelar, resultando numa galáxia hospedeira opticamente verde. Enquanto as populações estelares restantes envelhecem, a galáxia segue para o ramo de baixa massa da sequência vermelha, exibindo uma fase LINER, provavelmente dirigida por estrelas pós-AGB (Stasińska et al., 2008; Sarzi et al., 2010) por um pequeno tempo antes de se acomodar em uma evolução passiva na sequência vermelha. Segundo Powell et al. (2017) há uma fração de galáxias hospedeiras de AGNs na núvem azul e *Green Valley* em que seu AGN promove o cessamento da formação estelar, indo ao encontro de estudos [e.g.](Cheung et al., 2012; Mancini et al., 2015) que sugerem que o cessamento da formação estelar pode estar relacionado com a atividade nuclear do AGN e crescimento do bojo da galáxia.

1.2.2 A relação $M_{SMBH} - \sigma_*$

Observações da cinemática estelar da região central de galáxias vizinhas com o telescópio espacial Hubble revelaram a existência de um SMBH em todas as galáxias em que foi possível resolver o raio de influência do mesmo (Magorrian et al., 1998):

$$r_{inf} = GM\sigma^{-2}, \tag{1.1}$$

onde G é a constante gravitacional, M é a massa contida nessa zona e σ é a dispersão de velocidades na região central. Isto levou à conclusão que todas as galáxias que possuam bojo possuam também um SMBH no seu centro. Quando o SMBH começa a acretar matéria do seu entorno, inicia uma fase de atividade nuclear (AGN). Indícios muito fortes da co-evolução do buracos negro supermassivo e sua galáxia (Granato et al., 2004) surgiram depois da descoberta da relação entre a dispersão de velocidades estelar e a massa do SMBH, a relação $M - \sigma$ (Ferrarese; Merritt, 2000):

$$log(M_{SMBH}/M_{\odot}) = 8.12 + 4.24\,log(\sigma/200kms^{-1}). \tag{1.2}$$

Esta relação sugere que a medida que o bojo crece - a massa do bojo sendo proporcional a σ - a massa do SMBH também cresce, ou seja, há uma co-evolução (ver Fig. 1.5).

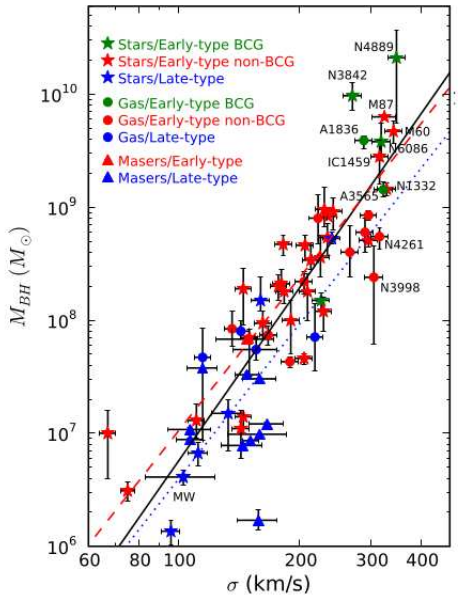

Figura 1.5: Massa do buraco negro supermassivo versus a dispersão de velocidades do bojo da galáxia hospedeira. Figura de McConnell et al. (2011).

1.2.3 A função de luminosidade

A função de luminosidade especifica a distribuição de uma classe de objetos em função de sua luminosidade (Schneider, 2015). Esta distribuição para galáxias é bem reproduzida pela função de Schechter:

$$\Phi(L) = \left(\frac{\Phi^*}{L^*}\right)\left(\frac{L}{L^*}\right)^{\alpha} exp\left(-L/L^*\right), \tag{1.3}$$

onde Φ é a densidade de galáxias, L^* é a luminosidade a partir da qual a distribuição cai exponencialmente, α é a inclinação da função luminosidade para L pequeno e Φ^* especifica a normalização da distribuição. Um gráfico esquemático desta função pode ser visto na Fig. 1.6.

Entretanto, modelos motivados pela teoria ΛCDM (Lambda Cold Dark Matter) preveem uma função luminosidade diferente da observada (ver Fig. 1.7), com um excesso tanto no número de galáxias pouco luminosas como no número de galáxias de maior luminosidade. Para reconciliar as observações com a teoria é necessário considerar o efeito de feedback (Silk; Mamon, 2012).

No caso de galáxias menos luminosas, tem se invocado o efeito de feedback das supernovas associadas à formação estelar. Entretanto, explosões de supernova têm pouco impacto no caso da formação de galáxias massivas. O feedback de SNe não consegue evitar o fluxo de matéria

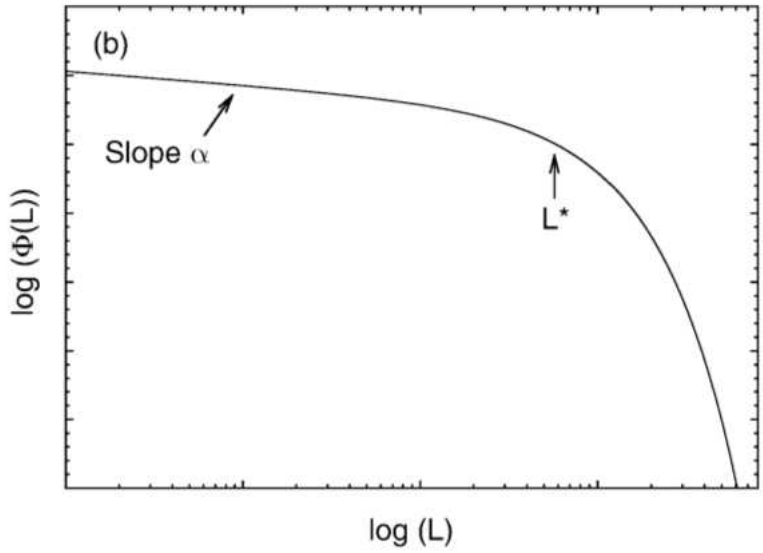

Figura 1.6: Gráfico esquemático da função de Schechter. Figura extraída de Schneider (2015).

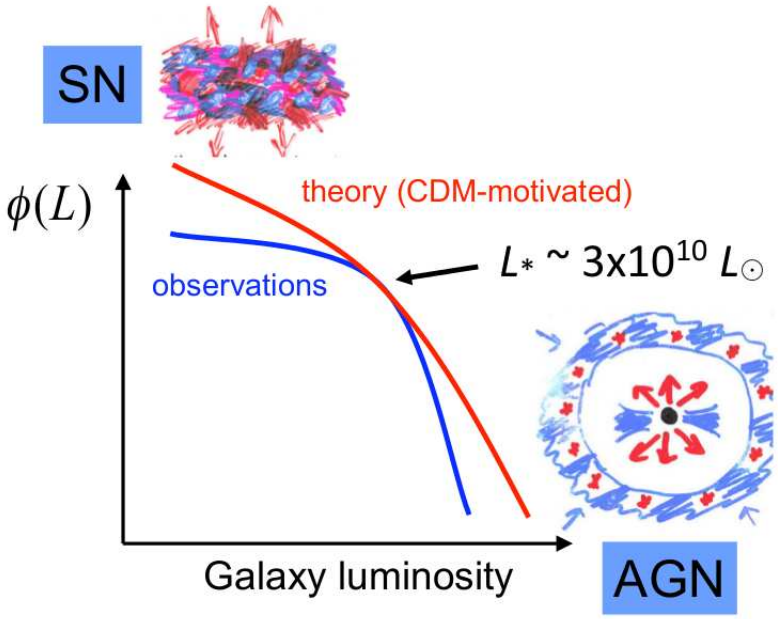

Figura 1.7: O papel do AGN na modificação da função de luminosidade da galáxia. Figura de Silk e Mamon (2012).

fria em direção ao centro da galáxia (Powell et al., 2011). Um fenômeno mais eficiente é o feedback produzido pelas ejeções de massa e a emissão de radiação do AGN, o que também contribuiria para explicar a relação entre a evolução da galáxia e do AGN sugerida pela relação $M - \sigma$.

Isso requer uma conexão entre o crescimento do buraco negro supermassivo e o conteúdo inicial de gás da galáxia. Convencionalmente os outflows do AGN perdem momento para o gás intergaláctico. Quando o buraco negro supermassivo está suficientemente grande, a luminosidade de Eddington é alta o suficiente para ejetar o gás no meio galático. Para fazer uma estimativa do momento disponível podemos calcular o momento de Eddington em conchas de gás no meio galático, $L_{Edd}/c = 4\pi GM/\kappa = GMM_{gas}/r^2$, onde κ é a opacidade. A formação estelar termina quando a relação $M-\sigma$ satura. Isso ocorre para $M_{SMBH} \propto \sigma^4$, perto do declive observado de ≈ 5 (Graham et al., 2011), e dá a normalização correta da relação, pelo menos em uma ordem de magnitude. Esse é o "modo quasar" de feedback, um feedback inicial (Silk; Mamon, 2012).

Ainda há um papel do feedback do AGN para períodos mais tardios, quando o jato rádio do AGN aquece o gás no halo, inibe o esfriamento, resolve o problema da função de luminosidade final da galáxia e favorece o aparecimento das galáxias vermelhas massivas early-type.

1.3 Motivação: Feeding e Feedback

AGNs caracterizam uma fase crítica na evolução de galáxias, em que o seu SMBH é alimentado através da acreção de gás da região nuclear. Uma vez que o disco de acreção no entorno do SMBH é formado, processos de feedback começam a acontecer, que abranjem jatos de partículas relativísticas emitidas da porção mais interna no disco de acreção, ventos emanados de partes mais externas do disco e radiação emitida pelo gás quente no disco ou pela sua zona coronal (Frank et al., 2002; Elvis, 2000; Ciotti et al., 2010). Os processos de feeding e feedback do AGN estão ligados ao crescimento dos SMBHs e suas galáxias hospedeiras, e possivelmente são os responsáveis pela correlação entre a massa do SMBH e a massa do bojo da galáxia (Ferrarese; Ford, 2005; Somerville et al., 2008; Kormendy; Ho, 2013). Os processos de feeding são uma condição necessária para dar inicio à atividade nuclear, enquanto os precessos de feedback são um ingrediente fundamental nos modelos de evolução de galáxias, como visto na seção anterior.

Em galáxias hopedeiras de AGNs, a emissão do gás molecular (H_2) e do gás ionizado apresentam distribuições de fluxo e cinemática diferentes. A emissão do H_2 é mais uniformemente distribuída, sendo mais restrita ao plano da galáxia, apresenta baixa dispersão de velocidades ($<$ 100 km/s) e é dominada por rotação. Em vários casos podemos observar também o movimento do gás em direção ao núcleo via braços espirais, onde as taxas de inflow para o gás molecular, incluindo uma estimativa da contribuição do gás frio varia de alguns décimos a algumas massas

solares por ano (Riffel et al., 2008, 2009a; Davies et al., 2009; Sanchez et al., 2009; Riffel et al., 2013).

O gás ionizado mostra emissão mais colimada e dipersão de velocidades maior ($>$ 100 km/s) do que o gás molecular na galáxia hospedeira. Muitas vezes ele se estende até altas latitudes e sua cinemática apresenta tanto indícios de rotação quanto de outflows (Riffel et al., 2013, 2006; Riffel; Storchi-Bergmann, 2011c; Müller-Sánchez et al., 2011; Riffel; Storchi-Bergmann, 2011a). Um diagnóstico importante desses outflows é a cinemática medida para as linhas de emissão do [Fe II]1.257μm e 1.644μm. Em Storchi-Bergmann (2012) é visto que essas linhas parecem ser melhores traçadoras dos outflows do AGN do que a linha do [OIII]5007Å usada previamente. Isso se deve ao fato de que a emissão do [Fe II] é mais estendida do que a do [OIII], chegando à região parcialmente ionizada (depois da região totalmente ionizada). No infravermelho próximo, usando a cinemática do [Fe II] pode-se estimar massas de outflow acima de algumas massas solares por ano (Riffel; Storchi-Bergmann, 2011c; Storchi-Bergmann et al., 2010; Riffel et al., 2013; Schönell et al., 2014). Em estudos mais recentes, tem-se visto também outflows em gás molecular (García-Burillo et al., 2014; Combes, 2015), com velocidades de 200 a 1200 km/s e taxas de dezenas de massas solares por ano.

A co-evolução do AGN com as galáxias é agora um paradigma aceito que permeia *reviews* recentes (Kormendy; Ho, 2013; Heckman; Best, 2014). Mas as conclusões alcançadas nesses reviews são na sua maioria baseadas em *surveys* de propriedades de galáxias, e os processos de feeding e feedback que levam à co-evolução foram implementados por modelos de uma forma muito simplista (Somerville et al., 2008; Springel et al., 2005; Croton et al., 2006). Isso se dá pela falta de estudos observacionais dos quiloparsecs centrais do AGN sendo espacialmente resolvidos, o que só pode ser observado em galáxias locais. As grandes quantidades de poeira nos quiloparsecs centrais do AGN, estimada entre 10^5 e 10^7 $M_\odot$ (Simões Lopes et al., 2007; Martini et al., 2013) e o grande volume de gás molecular (10^7 a 10^9 $M_\odot$) mostram a importância de se procurar sinais de feeding no gás molecular nos quiloparsecs centrais do AGN. Recentemente, registrou-se também feedback na forma de outflows bem massivos dominados pelo gás molecular (Sakamoto et al., 2010; Aalto et al., 2012; Veilleux et al., 2013), pelo menos em LIRGS e ULIRGS (Ultra Luminous Infrared Galaxies).

1.4 Objetivos

O principal objetivo deste trabalho é investigar a relação entre o SMBH e sua galáxia hopedeira através da observação da fase ativa das galáxias, mapeando e quantificando os mecanismos

de alimentação ($feeding$) do SMBH bem como os de $feedback$ na região central das galáxias (kpc central). Este mapeamento será feito através da espectroscopia de campo integral no infravermelho próximo de uma amostra de galáxias Seyferts próximas (descrita na próxima seção). Observações nesta faixa espectral são menos afetadas por extinção interestelar devido a poeira e os instrumentos utilizados possuem muitas vezes ótica adaptativa, resultando em melhores resoluções espaciais nas galáxias. Para atingir o nosso objetivo vamos:

- Mapear a distribuição de fluxo do gás emissor nas diferentes linhas espectrais; desta forma estudaremos a distribuição de massa e excitação do gás, o que permite separar gás ionizado/excitado pelo AGN de gás ionizado por regiões de formação estelar;
- Mapear a cinemática dos gás emissor para procurar e separar movimentos orbitais do gás no plano da galáxias de movimentos radiais ($inflows$ e $outflows$), quantificando os fluxos de gás e a potência dos outflows para verificar qual o seu efeito na galáxia hospedeira;
- Mapear a cinemática da população estelar e compará-la com a do gás para facilitar a identificação de inflows e outflows no gás.
- Investigar a história formação estelar na vizinhança do núcleo, procurando em particular por estrelas jovens e verificar se há alguma relação entre a atividade nuclear e a formação de novas estrelas como sugerido em trabalhos anteriores.
- Investigar possíveis correlações entre as propriedades medidas e entre essas propriedades e a luminosidade do AGN (incluindo raios-X).

2 *Amostra*

A amostra da Tese é composta pelas galáxias já observadas pelo grupo AGNIFS com o instrumento NIFS (*Near-Infrared Integral Field Spectrograph*), e em particular àquelas da *Large Proposal* (LLP) do observatório Gemini: NIFS survey of feeding and feedback processes in nearby Active Galaxies, cuja PI é a Dra. Thaisa Storchi-Bergmann. A amostra completa foi extraída do catálogo Swift-BAT, que é um catálogo de fontes de raios-X detectados pelo instrumento BAT do satélite Swift. As galáxias selecionadas tem luminosidades $L_X \geq 10^{41.5}$ erg/s, redshift z$\leq$0.015 e são acessíveis ao NIFS (-30° $< \delta <$ 73°). A banda de 14-195 keV do Swift-BAT, que foi a banda de luminosidades utilizada como critério para essa amostra, detecta a emissão direta do AGN, ao invés da emissão espalhada ou reemitida, além de ser bem menos sensível a possível obscurecimento na linha de visada do que raios-X moles ou em comprimentos de onda visíveis, permitindo que sejam selecionadas galáxias com base apenas nas propriedades do seu AGN. Além disso, para termos maior certeza de que haveria emissão do gás suficiente para permitir mapearmos os processos de feeding e feedback, selecionamos galáxias que já haviam sido observadas como tendo emissão estendida, e em particular na linha do [OIII]5007Å, pois percebemos por experiências passadas que encontraríamos a emissão nas linhas do [Fe II].

As 11 galáxias já observadas dentro da LLP serão chamadas de "amostra principal". Como já temos também outras 9 galáxias observadas com o NIFS resolvemos incluí-las como uma amostra complementar com o objetivo de aumentar o número de objetos estudados e a significância dos resultados procurando por propriedades globais de galáxias ativas no infravermelho próximo. As galáxias da amostra estão listadas na tabela 3.1, e sua caracterização é feita no paper a seguir, que foi um trabalho liderado por Rogemar A. Riffel e com grande contribuição minha.

MNRAS **000**, 1–17 (2017) Preprint 26 June 2017 Compiled using MNRAS LATEX style file v3.0

Gemini NIFS survey of feeding and feedback processes in nearby Active Galaxies: II -The sample and surface mass density profiles

R. A. Riffel[1]⋆, T. Storchi-Bergamann[2], R. Riffel[2], R. Davies[3], M. Bianchin[1], A. J. Schönell[2,7], M. R. Diniz[1], L. Burtscher[3], M. Crenshaw[4], T. C. Fischer[5], L. G. Dahmer-Hahn[2], N. Z. Dametto[2], D. Rosario[6]

[1] *Departamento de Física, CCNE, Universidade Federal de Santa Maria, 97105-900, Santa Maria, RS, Brazil*
[2] *Departamento de Astronomia, IF, Universidade Federal do Rio Grande do Sul, CP 15051, 91501-970, Porto Alegre, RS, Brazil*
[3] *Max-Planck-Institut für extraterrestrische Physik, Postfach 1312, D-85741, Garching, Germany*
[4] *Department of Physics and Astronomy, Georgia State University, Astronomy Offices, 25 Park Place, Suite 605, Atlanta, GA 30303, USA*
[5] *Astrophysics Science Division, Goddard Space Flight Center, Code 665, Greenbelt, MD 20771, USA.*
[6] *Department of Physics, Durham University, South Road, Durham DH1 3LE, UK*
[7] *Instituto Federal de Educação, Ciência e Tecnologia Farroupilha, BR287, km 360, Estrada do Chapadão, 97760-000, Jaguari - RS, Brazil.*

Accepted XXX. Received YYY; in original form ZZZ

ABSTRACT

We present and characterize a sample of nearby Seyfert galaxies selected from hard X-ray luminosities aimed to study Active Galactic Nuclei (AGN) feeding and feedback processes using the Gemini Near-Infrared Integral Field Spectrograph (NIFS). The main selection criteria are 14–195 keV luminosities $L_X \geq 10^{41.5}$ ergs s^{-1} and redshift $z \leq 0.015$. In addition the galaxy must be accessible for Gemini NIFS ($-30° < \delta < 73°$) and show extended [O III]λ5007 emission, in order to ensure the presence of extended emission in order to spatially resolve its kinematics. The resulting sample contains 20 galaxies and plus another 9 from previous runs comprising a complementary sample. We show that the inclusion of these additional criteria (besides L_X and z) do not inlcude any bias in the distributions of the host galaxy properties (M_B, M_H, central stellar velocity dispersion σ and axial ratio b/a). For the 20 galaxies already observed, we present surface mass density profiles for the hot molecular (Σ_{H2}) and ionized Σ_{HII} gas in the inner ~ 500 pc of the galaxies and found that both decrease with the distance from the nucleus, with the ionized gas showing a steeper gradient for most galaxies. NGC 1068 is an exception and shown an increase in Σ_{H2} at 25–75 pc from the nucleus due to the presence of a molecular gas ring. The mean surface mass density for the ionized and hot molecular gas are in the ranges (0.2–35.9) M$_\odot$ pc^{-2} and (0.2–13.9)$\times 10^{-3}$ M$_\odot$ pc^{-2}, while the ratio between the mass of ionized and hot molecularranges between ∼200 for Mrk 607 to ∼8000 for NGC 5506.

Key words: galaxies: active – galaxies: nuclei – infrared: galaxies

1 INTRODUCTION

The co-evolution of Active Galactic Nuclei (AGN) and galaxies is now an accepted paradigm that permeates recent reviews (Kormendy & Ho 2013; Heckman & Best 2014). But the conclusions put forth in these reviews are mostly based on surveys of integrated galaxy properties, and the feeding and feedback processes that lead to the co-evolution have been implemented in models in a simplistic way Somerville et al. (2008); Springel et al. (2005); Croton et al. (2006). This is due to the lack of observational constraints from spatially resolved studies. Physical motivated models Hopkins & Quataert (2010) show that the relevant feeding processes occur within the inner kiloparsec, that can only be resolved in nearby galaxies. The large quantities of dust in the inner kiloparsec of AGN, estimated to range from 10^5 to 10^7 M$_\odot$ (Simões Lopes et al. 2007; Martini, Dicken & Storchi-Bergmann 2013; Audibert et al. 2017) and the associated large content of molecular gas (10^7 to 10^9 M$_\odot$) points to the importance of looking for signatures

⋆ E-mail: rogemar@ufsm.br

of the feeding in the molecular gas within the inner kiloparsec. Recently it has also been argued that the feedback in the form of massive outflows is also dominated by molecular gas (Sakamoto et al. 2010; Aalto et al. 2012; Veilleux et al. 2013), at least in LIRGS or ULIRGS (Ultra Luminous Infrared Galaxies).

The co-evolution scenario, and the feeding of gas to the inner kiloparsec of galaxies when they are in the active phase implies that the galaxy bulge grows in consonance with the SMBH. Since the early studies of Terlevich and collaborators (e.g. Terlevich et al. 1990), it has been argued that the excess blue light and dilution of the absorption features of the nuclear spectra of active galaxies was due to young stars. Subsequent long-slit studies Storchi-Bergmann et al. (2000); Cid Fernandes et al. (2004); Davies et al. (2007); Kauffmann & Heckman (2009) have found an excess contribution of young to to intermediate age stars to the stellar population in the inner kiloparsec of active galaxies when compared to non-active ones. This result has led to the proposition of an evolutionary scenario (Storchi-Bergmann et al. 2001; Davies et al. 2007; Hopkins 2012), in which the gas inflow to the nuclear region first triggers star formation in the circumnuclear region, and is then followed by the ignition of the nuclear activity.

Observational constraints for the feeding and feedback processes can be obtained via spatially resolved studies of nearby active galaxies using integral field spectroscopy (IFS). The radiation from the AGN heats and ionizes the surrounding gas in the galaxy up to hundreds of pc (and even kpc) scales. The heating excites rotational and vibrational states of the H_2 molecule that then emits in the near-IR, and the AGN radiation ionizes the gas that, in turn, emits permitted and forbidden lines that can be used to probe the ionized gas kinematics and excitation. Emission from both the molecular and ionized gas phases can be observed in the near-IR domain, where the effects of dust extinction can also be minimized. In the near-infrared, IFS at 10 meter class telescopes has been using to probe the feeding in feedback processes in nearby active galaxies, by mapping and modeling the molecular and ionized gas kinematics in the inner kiloparsec of active galaxies – on 10–100 pc scales – leading to insights on both the feeding and feedback mechanisms. For high signal-to-noise ratio in the continuum, the stellar kinematics as well as the age distribution of the stellar population have also been mapped. So far, these studies show that (i) Emission from molecular (H_2) and ionized gases present distinct flux distributions and kinematics. The H_2 emission is distributed all around the nucleus, seems to be located in the plane of the galaxy, shows low velocity dispersion ($<100\,km\,s^{-1}$) and is dominated by rotational motion. In a few cases a very steep rotation curve is observed suggesting the presence of compact molecular disks Riffel & Storchi-Bergmann (2011a); Schönel et al. (2014); Hicks et al. (2013); Mazzalay et al. (2014). In a number of cases, streaming motions towards the central regions were mapped along nuclear spiral arms with estimated inflow rates in total molecular gas range from a few tenths to a few solar masses per year (Riffel et al. 2008; Riffel, Storchi-Bergmann & Winge 2013; Davies et al. 2009; Müller-Sánchez et al. 2009; Diniz et al. 2015). (ii) The ionized gas emission is more collimated and shows higher velocity dispersion ($>100\,km\,s^{-1}$) than the molecular gas, seems to extend to high latitudes and its kinematics comprises both rotation and outflow (e.g. Riffel et al. 2006; Riffel, Storchi-Bergmann & Nagar 2010; Müller Sánchez et al. 2011; Riffel, Storchi-Bergmann & Winge 2013; Barbosa et al. 2014; Storchi-Bergmann et al. 2010). (iii) Only for a few cases, the study of stellar population was done using near-IR IFS. These works show the presence of young to intermediate age ($\sim10^8$ yr) stars, usually in ~100 pc rings (e.g. Riffel et al. 2010, 2011c; Storchi-Bergmann et al. 2012), that correlate with rings of low velocity dispersion. This correlation has been interpreted as being a signature of the co-evolution of the bulge and SMBH: as the estimated mass inflow rates are ~3 orders of magnitude larger than the accretion rate to the AGN, most of the molecular gas that is accumulated in the nuclear regions of AGNs is forming new stars in the inner few hundred parsecs of the galaxy, leading to the growth of the bulge.

Most of the results summarized above were obtained by studying individual galaxies, selected using distinct criteria, and a study of a large, well-defined sample is of fundamental importance to understand the relation among AGN feeding, feedback and galaxy evolution (e.g. Davies et al. 2017). In this work, we describe a sample of nearby active galaxies that are being observed with the Gemini Near-Infrared Integral Field Spectrograph (NIFS), aimed to study the details of inner few hundreds of parsecs of AGNs and better constrain the feeding and feedback processes. This paper is organized as follows. Section 2 describes the selection criteria of the sample, the instrument configuration, observations, data reduction and compare nuclear and large scale properties of the galaxies. In section 3 we present and discuss measurements with of the molecular and ionized gas masses and surface densities for the galaxies already observed and Section 4 discusses the implications of the derived amount of gas to the AGN feeding process and star formation. Finally, section 5 presents the conclusions of this work.

2 DEFINITION OF A SAMPLE AND OBSERVATIONS

2.1 The sample

In order to select out AGN sample, we used the Swift-BAT 60-month catalogue (Ajello et al. 2012), and selected nearby galaxies with 14–195 keV luminosities $L_X \geq 10^{41.5}$ ergs s^{-1} and redshift $z \leq 0.015$. The hard (14–195 keV) band of the Swift-BAT survey measures direct emission from the AGN rather than scattered or re-processed emission, and is much less sensitive to obscuration in the line-of-sight than soft X-ray or optical wavelengths, allowing a selection based only on the AGN properties. Davies et al. (2015) describe a southern hemisphere sample selected is a similar way and discuss its rationale for studying AGN feeding and feedback processes (see also, Davies et al. 2017). As additional criteria, the object must be accessible for Gemini NIFS ($-30^\circ < \delta < 73^\circ$) and its nucleus being bright/pointy enough to guide the observations or with natural guide stars available in the field. Finally, we only include in the sample galaxies already previously observed in the optical and with extended [O III]λ5007 emission. We have used this constraint in order to ensure

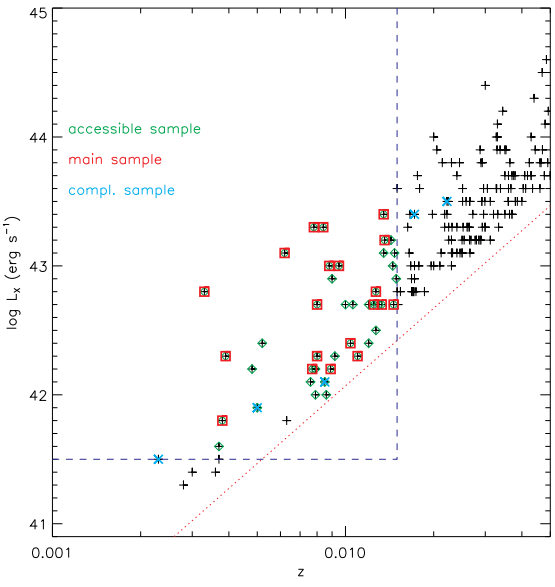

Figure 1. Plot of L_X vs. z for the galaxies of our sample.

that we will have extended gas emission in order to be able to spatially resolve its kinematics in order to look for possible inflows and outflows. From our previous experience, a galaxy that shows extended [O III] emission will also have a similarly extended [Fe II] or Paβ emission. Table 1 presents the resulting sample, which is composed by 20 galaxies. In addition, we include 9 galaxies observed with NIFS by our group in previous works, shown below the horizontal line in Table 1. These aditional galaxies may be used as a complementary sample in forthcoming works.

Figure 1 shows a plot of L_X vs. z for all Swift BAT AGN with $z \leq 0.05$ and accessible to Gemini North ($-30^0 < \delta < 73^0$).Green diamonds show the galaxies accessible to Gemini North that satisfy the following criteria: $L_X \geq 10^{41.5}$ ergs s^{-1} and $z \leq$0.015, while the red squares show our main sample (defined as having [O III] extended emission). The cyan $\times$ symbols show the objects of the complementary sample detected in the Swift-BAT 60-month catalogue. The red dotted line shows the detection limit of the Swift 60-month catalogue and the vertical and horizontal lines show the L_X and z cuts used to define our sample, respectively.

2.2 Characterization of the sample

It is known that hard X-ray emission is a good tracer of nuclear activity in galaxies and thus a X-ray selected sample is representative of the population of AGN within the limited volume. However, besides the limits in X-ray luminosity and redshift, we included a constraint based on the detection of [O III]λ5007 emission line in order to increase the rate of detection of extended emission in near-IR lines, necessary to map the gas kinematics and flux distributions. In order to test if this additional criteria produces any bias on our sample, as compared to objects selected only on the basis of their X-ray emission, we compare the distribution of physical properties of the nucleus and host galaxies of the whole BAT sample (composed by galaxies with $L_X \geq 10^{41.5}$ ergs s^{-1} and redshift $z \leq$0.015) with the distributions of our main and complementary samples.

The total number of galaxies in the 60 month BAT catalogue that follows the constraints above is 69 galaxies (hereafter we will call this sample as the "restricted BAT sample"), while our main sample is composed by 20 objects, as shown in Table 1. In the left panel of Figure 2 we present a histogram for the distribution of L_X of our main sample in bins of $\log L_X = 0.3$ crosshatched histogram, overlaid on the histogram for the restricted BAT sample, which is shown in gray. As can be observed in this plot, both samples show a very similar distribution whit mean luminosities of $< logL_X >= 42.6 \pm 0.1$ erg s^{-1} and $< logL_X >= 42.7 \pm 0.1$ erg s^{-1} for the BAT and our main sample, respectively. The inclusion of the additional selection criteria of having extended [O III] emission already published and being observable with NIFS does not change significantly the distribution of the sample in terms of X-ray luminosities. Thus, the main sample can be considered a representative sample of nearby AGNs within adopted constrains in X-ray luminosity and redshift. Five galaxies of the complementary sample have X-ray luminosities available in the 60 month BAT catalogue. Including these sources, the distribution of galaxies shows an extension to lower X-ray luminosities as seen in the central panel of Fig. 2. However, the averaged luminosity does not change significantly, being $< logL_X >= 42.4 \pm 0.1$ erg s^{-1} for the main plus complementary sample.

Besides the 20 galaxies of our main sample, [O III]5007 luminosities are available for two galaxies of the complementary sample. Our sample shows [O III]5007 luminosities in the range $L_{[OIII]} = (0.2 - 155) \times 10^{40}$ erg s^{-1}, with a mean value of $< logL_{[OIII]} >= 41.0 \pm 0.2$ erg s^{-1}.

We compiled physical properties of the host galaxies from the Hyperleda database [1] (Makarov et al. 2014) and NED[2]. In figures 3 and 4 we present histograms for the absolute B (top panels of Fig. 3) and H magnitudes (bottom panels of Fig. 3), the nuclear stellar velocity dispersion (top panels of Fig. 4) and axial ratio (bottom panels of Fig. 4). The left panels of these figures show the distribution of these properties for the main sample, while the the right panels show the same properties for the main plus complementary sample. As in Fig. 2 the restricted BAT sample is shown as the gray histogram.

The B absolute magnitude M_B was obtained from the Hyperleda database, and is available for 58 objects from the restricted BAT sample and for 28 galaxies of our sample, the only exception being NGC 3035. The mean value of M_B for our main sample ($M_B = -20.75 \pm 0.16$ mag) is similar to that of the BAT sample ($M_B = -20.52 \pm 0.12$ mag), but the distributions are somewhat distinct as the BAT sample includes more low luminosity galaxies with $M_B > -20$ mag.

The total H absolute magnitude was obtained from the apparent H magnitudes from the The Two Micron All Sky Survey catalogue (2MASS, Skrutskie et al. 2006). The H band is dominated by emission from the galaxy bulges and the H-band luminosity can be used as a proxy for stellar

[1] The Hyperleda database is available at *http://leda.univ-lyon1.fr/*

[2] NASA/IPAC Extragalactic Database available at *http://ned.ipac.caltech.edu/*

Table 1. The sample. (1) Galaxy name; (2) Redshift; (3) Morphological classification; (4) Nuclear Activity, (5) Swift 14-195 keV luminosity, (6) [O III]λ5007 luminosity in units of ergs s^{-1}, (7) reference for the [O III] luminosity. Table 2 list the galaxies already observed.

(1) Galaxy	(2) z	(3) Hubble Type	(4) Nuc. Act.	(5) log(L_X)	(6) log(L_{OIII})	(7) Ref.
		Main sample				
NGC788	0.014	SA0/a?(s)	Sy2	43.20	41.06	a
NGC1068	0.004	(R)SA(rs)b	Sy2	41.80	41.53	b
NGC1125	0.011	(R')SB0/a?(r)	Sy2	42.30	39.69	c
NGC1194	0.013	SA0$^+$?	Sy1	42.70	39.60	b
NGC2110	0.008	SAB0$^-$	Sy2	43.30	40.64	a
Mrk3	0.014	S0?	Sy2	43.40	41.83	b
NGC2992	0.008	Sa pec	Sy2	42.20	41.42	a
NGC3035	0.015	SB(rs)bc	Sy1	42.70	39.83	c
NGC3081	0.008	(R)SAB0/a(r)	Sy2	42.70	41.58	a
NGC3227	0.004	SAB(s)a pec	Sy1.5	42.30	40.84	a
NGC3393	0.013	(R')SB(rs)a?	Sy2	42.70	41.58	b
NGC3516	0.009	(R)SB0^0?(s)	Sy1.5	43.00	41.02	b
NGC3786	0.009	SAB(rs)a pec	Sy1.8	42.20	40.59	a
NGC4151	0.003	(R')SAB(rs)ab?	Sy1.5	42.80	42.19	a
NGC4235	0.008	SA(s)a edge-on	Sy1	42.30	39.31	a
Mrk766	0.013	(R')SB(s)a?	Sy1.5	42.80	41.10	b
NGC4388	0.008	SA(s)b? edge-on	Sy2	43.30	41.26	b
NGC4939	0.010	SA(s)bc	Sy1	42.40	40.64	c
NGC5506	0.006	Sa pec edge-on	Sy1.9	43.10	40.97	a
NGC5728	0.009	SAB(r)a?	Sy2	43.00	41.47	a
		Complementary Sample				
NGC1052	0.005	E4	Sy2	41.90	–	–
NGC4051	0.002	SAB(rs)bc	Sy1	41.50	–	–
NGC5548	0.017	(R')SA0/a(s)	Sy1	43.40	41.37	b
NGC5899	0.009	SAB(rs)c	Sy2	42.10	–	–
NGC5929	0.008	Sab? pec	Sy2	–	–	–
Mrk79	0.022	SBb	Sy1	43.50	41.58	b
Mrk607	0.009	Sa? edge-on	Sy2	–	–	–
Mrk1066	0.012	(R)SB0$^+$(s)	Sy2	–	–	–
Mrk1157	0.015	(R')SB0/a	Sy2	–	–	–

References: a: Wittle (1992), b: Schmitt et al. (2003), c: Gu et al. (2006); d: Noguchi et al. (2010); e: Zhu et al. (2011).

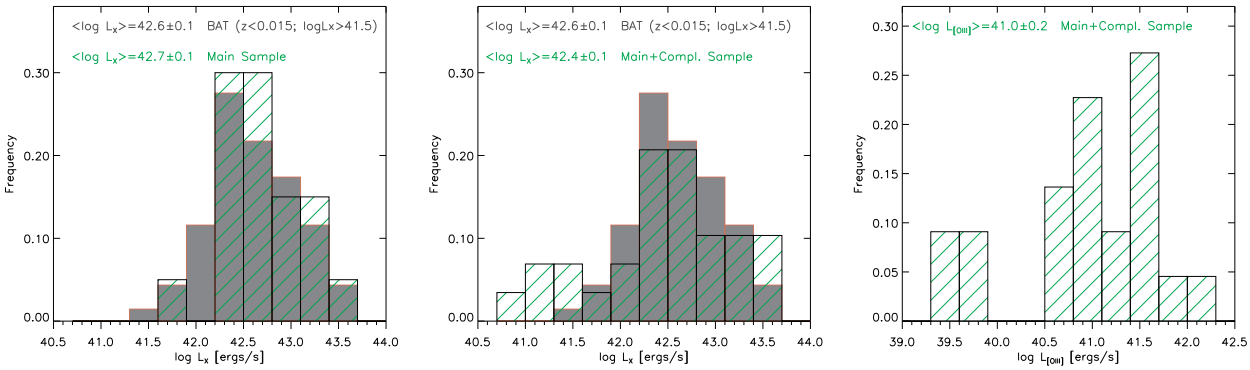

Figure 2. Histograms for the distribution of X-ray and [O III]5007 luminosities of the galaxies of our sample. The left panel shows the distribution of $logL_X$ of all galaxies with $L_X \geq 10^{41.5}$ ergs s^{-1} and $z \leq 0.015$ from the 60 month BAT catalogue in gray, with the distribution of our main sample overploted and crosshatch green histogram. In the central panel, the complementary sample is included and the right panel shows the distribution of the [O III]5007 luminosities for our sample, including the two objects from the complementary sample with [O III] luminosities available. All histograms were constructed using a bin of $logL_X = 0.3$ erg s^{-1} and the mean values for each distribution are shown at the top of each panel.

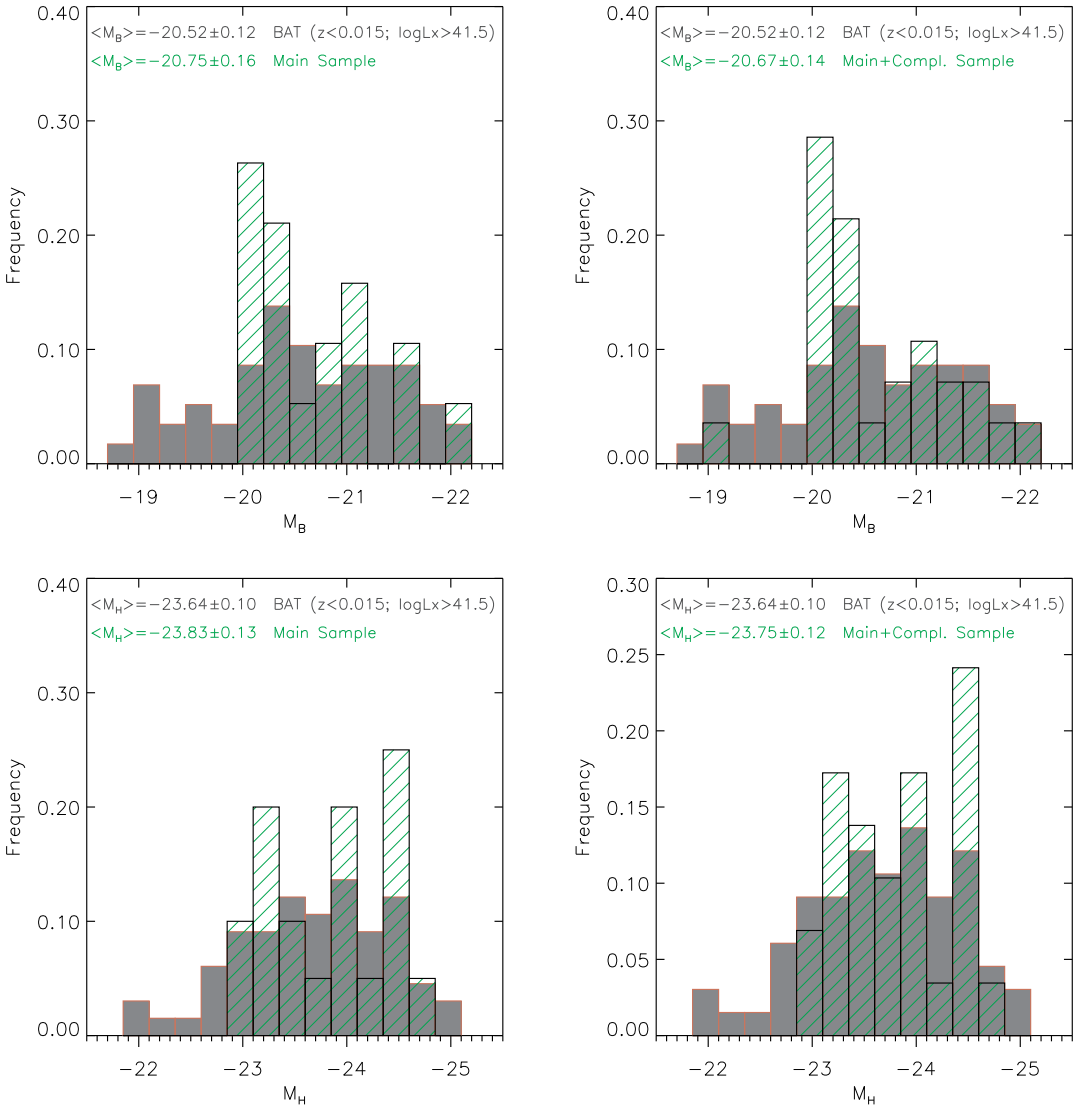

Figure 3. Distribution of B (top) and H (bottom) band absolute magnitudes for the galaxies of the main sample (left) and main+complementary sample (right) in bins of 0.25 mag. The distribution of the restricted BAT sample is shown as the gray histogram.

mass of the galaxy (Davies et al. 2015, 2017). As for M_B, the distribution of the galaxies of our main sample is similar to that of the main plus complementary sample and the mean value of M_H for both samples are very similar to that observed for the BAT sample.

In Figure 4 we show histograms for the distribution of the nuclear stellar velocity dispersion (σ – top panels) and axial ratio (b/a – bottom panels). The σ values were obtained from the Hyperleda database and are standardized to an aperture of 0.595 h^{-1} kpc. Measurements of σ are available at Hyperleda database for 30 galaxies of the restricted BAT sample, 14 galaxies of the main sample and 8 objects of the complementary sample. The histograms for σ were constructed using bins of 20 km s^{-1}. As seen in Fig. 4 the distribution of σ values for the main and restricted BAT samples are similar, with mean σ values of $<\sigma>=165\pm13$ km s^{-1} and $<\sigma>=157\pm8$ km s^{-1}, respectively. By including the complementary sample, the fraction of objects with $\sigma\leq120$ km s^{-1} increases, while the mean σ values are still consistent with that of the restricted BAT sample, as observed at the top-right panel of Fig. 4.

Considering that the central σ values are representative of the bulge of the galaxies, we can use the $M_\bullet-\sigma$ relationship (e.g. Ferrarese & Merritt 2000; Gebhardt et al. 2000; Tremaine et al. 2002; Ferrarese & Ford 2005; Graham et al. 2011) to determine the mass of the central supermassive black hole ($M_\bullet$). Using equation 3 from Kormendy & Ho (2013) and the σ values from Fig. 4, we obtain $(0.15\lesssim M_\bullet\lesssim 13.5)\times10^8$ M$_\odot$ and mean values of $<M_\bullet>\approx1.3\times10^8$ M$_\odot$ for the main sample and $<M_\bullet>\approx9.8\times10^7$ M$_\odot$ including the complementary sample.

The main goals of our project are to map and quantify AGN feeding and feedback process via gas inflows and outflows. While inflows are usually restricted to the plane of de galaxy disk (e.g. Riffel et al. 2008; Riffel, Storchi-Bergmann & Winge 2013), outflows do not

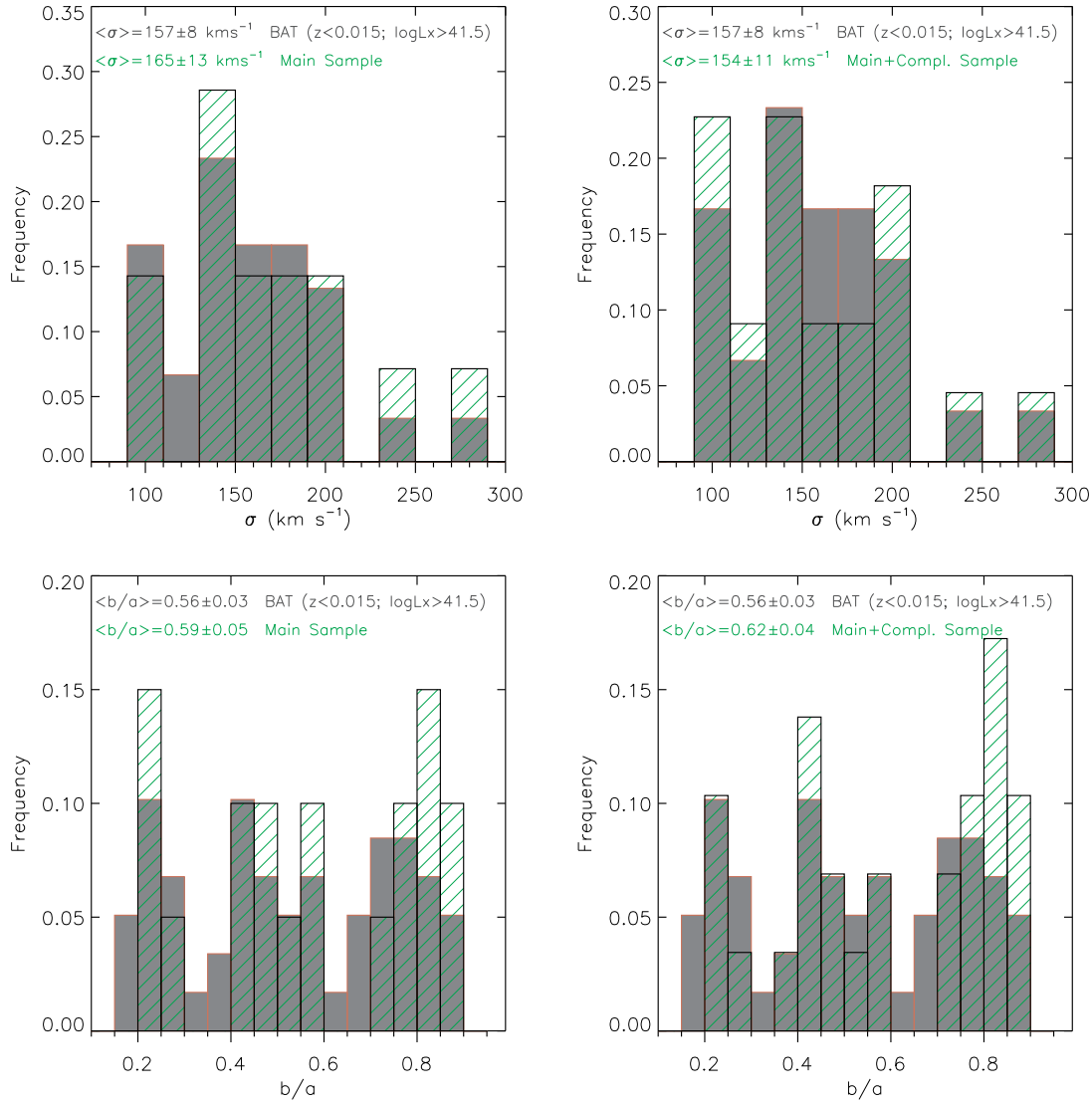

Figure 4. Distribution of central stellar velocity dispersion (top) and axial ratio (bottom) for the galaxies of the main sample (left) and main+complementary sample (right). The distribution of the restricted BAT sample is shown in gray scale on the background. Bins of 20 km s^{1} are used in the histograms for the velocity dispersion and of 0.05 for the axial ratio.

show any preferential orientation (Schmitt et al. 2001; Barbosa et al. 2014; Schönel et al. 2017). Thus, in order to optimize the search for inflows and outflows, it is desirable that the sample of galaxies show a wide range of disk orientations. The bottom panels of Figure 4 show histograms for the axial ratio b/a for our sample and restricted BAT sample (where a and b are the semi-major and semi-minor axes of the galaxy obtained from the Hyperleda database, measured from at the isophote 25 mag/arcsec^2 in the B-band surface brightness distribution). Measurements of the axial ratio are available for all galaxies of our sample and for 59 objects of the restricted BAT sample. The bottom panels of Fig. 4 show histograms for the axial ratio in bins of 0.05. The mean values of b/a of our main samples are similar to that of the restricted BAT sample and including the complementary sample. Our sample shows a wide range of axial ratio, from nearly edge-on galaxies ($b/a \sim 0.2$, corresponding to a disk inclination $i \sim 80°$) to nearly face-on galaxies ($b/a \sim 0.9$, $i \sim 25°$).

2.3 Observations

The Integral Field Spectroscopic observations of the galaxies of our sample have been obtained with the Gemini Near-Infrared Integral Field Spectrograph (NIFS, McGregor et al. 2003) operating with the Gemini North adaptive optics module ALTAIR. NIFS has a square field of view of $\approx 3\farcs0 \times 3\farcs0$, divided into 29 slices with an angular sampling of $0\farcs1 \times 0\farcs04$. The observations of our sample are part of a Large and Long Program (LLP) approved by Brazilian National Time Allocation Committee (NTAC) and have started in semester 2015A and are planned to be concluded in 2017B. Some galaxies shown in Table 1 were observed as part of previous proposals by our group. The data comprise J and K(K$_l$)-

band observations at angular resolutions in the range 0.″12–0.″20, depending on the performance of the adaptive optics module and velocity resolution of about 40 km s^{-1} at both bands.

Emission lines from high, low-ionization and molecular gas, as well as strong CO absorptions, are usually observed at these spectral bands in spectra of active galaxies (e.g. Riffel, Rodríguez-Ardila, & Pastoriza 2006), allowing the mapping of the gas kinematics, distribution, excitation and extinction and the stellar kinematics. The relatively high spatial and spectral resolutions, together with the spatial coverage, make this an unprecedented data set to map the AGN feeding and feedback processes in nearby galaxies. The on-source exposure time for each galaxy is in the range 0.7–1.7 hours at each band, expected to result in a signal-to-noise ratio $snr > 10$, which allows the fitting of the emission and absorption lines. The observations have been following the standard object-sky-object dithering sequence and the data reduction have been done following the standard procedures of spectroscopic data treatment.

2.4 Data reduction

The data reduction for the J and K band are being performed following the same procedure used in previous works (e.g. Riffel et al. 2008; Diniz et al. 2015; Riffel et al. 2017), including the trimming of the images, flat-fielding, sky subtraction, wavelength and s-distortion calibrations and correction of the telluric absorptions. The spectra are then flux calibrated by interpolating a black body function to the spectrum of the telluric standard star. Finally, datacubes for each individual exposure are created with at an angular sampling of 0.″05×0.″05. These cubes are than mosaicked using the continuum peak as reference and median combined to produce a single final datacube for each band.

Table 2 presents a summary of the galaxies already observed. The angular resolution at J (PSF$_J$) and K (PSF$_J$) was estimated by measuring the full width at half maximum (FWHM) of the telluric standard star flux distributions. The uncertainties in the measurements are about 0.″03 for all galaxies at both bands. The spectral resolution at the J and K band was estimated from the FWHM of emission lines of the Ar and ArXe lamps used to wavelength calibration, respectively. For the J band we fitted the profiles of typical lines observed near 1.25 μm, while for the K band the spectral resolution was estimated from lines seen around 2.2 μm. The spectral resolution ranges from 1.7 to 2.0 Åat the J band, corresponding to an instrumental broadening ($\sigma_{inst} = \frac{FWHM}{2.355}\frac{c}{\lambda_c}$) of 17–20 km s^{-1}. At the K band the spectral resolutions ranges from 3 a 3.7 Å, translating into $\sigma_{inst} \approx 17-21$ km s^{-1}.

Reduced datacubes will be made available for the community after publication of the results by the group.

3 MOLECULAR AND IONIZED GAS SURFACE MASS DENSITY

We can use the fluxes of the H$_2\lambda$2.12 μm and Brγ emission lines to estimated the mass of hot molecular and ionized gas, respectively. Following Osterbrock & Ferland (2006) and Storchi-Bergmann et al. (2009), the mass of ionized ($M_{\rm HII}$) gas can be obtained by

$$\left(\frac{M_{\rm HII}}{M_\odot}\right) = 3\times10^{19}\left(\frac{F_{\rm Br\gamma}}{\rm erg\,cm^{-2}\,s^{-1}}\right)\left(\frac{D}{\rm Mpc}\right)^2\left(\frac{N_e}{\rm cm^{-3}}\right)^{-1}, \quad (1)$$

where D is the distance to the galaxy, $F_{\rm Br\gamma}$ is the Brγ flux and N_e is the electron density, and assuming an electron temperature of 10^4K.

The mass of hot molecular ($M_{\rm H2}$) gas can be obtained from (e.g. Scoville et al. 1982; Riffel et al. 2014), under the assumptions of local thermal equilibrium and excitation temperature of 2000 K:

$$\left(\frac{M_{H_2}}{M_\odot}\right) = 5.0776\times10^{13}\left(\frac{F_{H_2\lambda2.1218}}{\rm erg\,s^{-1}\,cm^{-2}}\right)\left(\frac{D}{\rm Mpc}\right)^2, \quad (2)$$

where $F_{H_2\lambda2.1218}$ is the H$_2$ (2.1218μm) emission-line flux.

We used the equations 1 and 2 to calculate the molecular and ionized gas mass density spaxel-by-spaxel by $\Sigma_{H2} = \frac{M_{H_2}}{A_s}$ and $\Sigma_{HII} = \frac{M_{\rm HII}}{A_s}$, respectively, where A_s is the area of each spaxel. Using the calculated values of Σ_{H2} and Σ_{HII} we constructed the surface mass density profiles shown in Figures 5–9. Following Barbosa et al. (2006), we calculate the position (r) of each spaxel in the plane of the disk by $r = \alpha R$, where

$$R = \sqrt{(x-x_0)^2 + (y-y_0)^2}$$

is the position projected in the plane of the sky (observed position) and

$$\alpha = \sqrt{\cos^2(\Psi-\Psi_0) + \sin^2(\Psi-\Psi_0)/\cos^2(\rm i)},$$

where Ψ_0 is the orientation of the line of nodes, i is the disk inclination and $\Psi = \tan^{-1}\left(\frac{y-y_0}{x-x_0}\right)$ with (x,y) being the spaxel coordinates and (x_0,y_0) the location of the kinematical center. Then, the surface mass density profiles were constructed by averaging the surface masses within concentric rings in the plane with width of dr =25 pc. For all galaxies we fixed the (x_0,y_0) as the position of the continuum peak and included only spaxels with flux measurements for the corresponding emission lines. For most galaxies, the H$_2\lambda$2.12 μm and Brγ flux maps have already been published by our group. Although the Brγ line is weaker than Paβ, is use is justified due to the fact that using Brγ and H$_2\lambda$2.12 lines, both ionized and molecular masses are derived from the same spectral band and thus the ratio between them is less sensitive to uncertainties in the flux calibrations. For two galaxies (NGC 1052 and NGC 5548) the Brγ line was not detected in our spectra and thus we use the Paβ emission line to estimate $M_{\rm HII}$ by assuming the theoretical ratio between the fluxes of Paβ and Brγ of 5.85 for the Case B of recombination (Osterbrock & Ferland 2006). The references for the corresponding measurements are included in the last column of Table 3, as well as the discussion about the fitting procedure. This table present also the Ψ_0 and i of the disk used in the decomposition, most of them from Riffel et al. (2017). For Mrk 3 and Mrk 79 we used the disk geometric parameters from Hyperleda database (Makarov et al. 2014), for NGC 1068 from Davies et al. (2007) and for NGC 4151 those presented in Onken et al. (2014).

Table 2. Observations. (1) Galaxy name; (2) Gemini project identification; (3) J and (4) K-band on-source exposure time; (5) J and (6) K-band angular resolution estimated from the FWHM of the flux distribution of the telluric standard star; (7) J and (8) K-band spectral resolution estimated from the FWHM of the Arc Lamp lines used to wavelength calibrate the datacubes; (9) References to published studies using this dataset.

(1) Galaxy	(2) Programme	(3) J Exp. T. (seconds)	(4) K Exp. T. (seconds)	(5) PSF_J (arcsec)	(6) PSF_K (arcsec)	(7) $FWHM_J$ (Å)	(8) $FWHM_K$ (Å)	(9) Refs.
			Main sample					
NGC788	GN-2015B-Q-29	7×400	11×400	0.13	0.13	1.9	3.5	a
NGC1068	GN-2006B-C-9*	27×90	27×90	0.14	0.11	1.7	3.0	b, c, d
NGC2110	GN-2015B-Q-29	6×400	–	0.13	–	1.9	–	a, e
–	GN-2010B-Q-25	-	6×600	0.15	–	–	3.4	–
Mrk3	GN-2010A-Q-5*	6×600	6×600	?	?	2.0	3.2	–
NGC3227	GN-2016A-Q-6	6×400	6×400	0.13	0.12	1.8	3.5	a
NGC3516	GN-2015A-Q-3	10×450	10×450	0.17	0.15	1.8	3.5	a
NGC4151	GN-2006B-C-9*	8×90	8×90	0.16	0.12	1.6	3.3	f, g, h
NGC4235	GN-2016A-Q-6	9×400	10×400	0.12	0.13	1.8	3.5	a
Mrk766	GN-2010A-Q-42	6×550	6×550	0.21	0.19	1.7	3.5	a, j
NGC4388	GN-2015A-Q-3	–	2×400	–	0.19	–	3.7	a
NGC5506	GN-2015A-Q-3	10×400	10×400	0.15	0.18	1.9	3.6	a
			Complementary Sample					
NGC1052	GN-2010B-Q-25	6×610	4×600		0.15	1.7		a
NGC4051	GN-2006A-SV-123	–	6×750	–	0.18	–	3.2	a, k
NGC5548	GN-2012A-Q-57	12×450	12×450	0.28	0.20	1.7	3.5	a, l
NGC5899	GN-2013A-Q-48	10×460	10×460	0.13	0.13	1.8	3.4	a
NGC5929	GN-2011A-Q-43	10×600	10×600	0.12	0.12	1.7	3.2	a, m, n
Mrk79	GN-2010A-Q-42	6×520	6×550	0.25	0.25	1.8	3.5	o
Mrk607	GN-2012B-Q-45	10×500	12×500	0.14	0.14	2.0	2.2	a
Mrk1066	GN-2008B-Q-30	8×600	8×600	0.13	0.15	1.7	3.3	a, p, q, r, s
Mrk1157	GN-2009B-Q-27	8×550	8×550	0.11	0.12	1.8	3.5	a, t, u

* From Gemini Science Archive
References: a: Riffel et al. (2017); b: Storchi-Bergmann et al. (2012); c: Riffel et al. (2014); d: Barbosa et al. (2014); e: Diniz et al. (2015); f: Storchi-Bergmann et al. (2009), g: Storchi-Bergmann et al. (2010); h: Riffel, Storchi-Bergmann & McGregor (2009); i: Schönel et al. (2014); k: Riffel et al. (2008); l: Schönel et al. (2017); m: Riffel, Storchi-Bergmann & Riffel (2014); n: Riffel, Storchi-Bergmann & Riffel (2015); o: Riffel, Storchi-Bergmann & Winge (2013); p: Riffel et al. (2010); q: Riffel, Storchi-Bergmann & Nagar (2010); r: Riffel & Storchi-Bergmann (2011a); s: Ramos Almeida et al. (2014); t: Riffel et al. (2011c); u: Riffel & Storchi-Bergmann (2011b).

The top panels of figures 5–9 present for each galaxy the profiles for Σ_{H2} in black, in units of $10^{-3}\,M_\odot\,pc^{-2}$, and Σ_{HII} in red in units of $M_\odot\,pc^{-2}$. The bottom panel shows the ratio between Σ_{HII} and Σ_{H2} or equivalently $\frac{M_{HII}}{M_{H_2}}$, calculated considering only spaxels in which both Brγ and $H_2\lambda2.12$ flux measurements are available. The dotted horizontal line shows the mean value of $\frac{M_{HII}}{M_{H_2}}$, indicated at the top-right corner this panel and calculated from the Σ_{HII}/Σ_{H2} profile. The dashed lines represent the standard error, calculated as the ratio between the standard deviation of the Σ at each ring and the number of spaxels used to compute Σ.

For all galaxies, the ionized and molecular gas surface density profiles decrease with the distance to the nucleus, with the ionized gas showing a steeper gradient for most galaxies. The only exception is NGC 1068, that shows in increase in Σ_{H2} between 25 and 75 pc due to the presence of an expanding molecular gas ring (e.g. Müller-Sánchez et al. 2009; Riffel et al. 2014; Barbosa et al. 2014). The bottom panels for each galaxy shows the radial profile for $\frac{M_{HII}}{M_{H_2}}$, that confirm the trend that ionized gas shows an steeper decrease in surface mass density, as the $\frac{M_{HII}}{M_{H_2}}$ for most galaxies have the highest values at the nucleus or at small distances from it. The mean values of $<\frac{M_{HII}}{M_{H_2}}>$, indicated at the top-left corner of each panel, range from ∼200 for Mrk 607 to ∼8000 for NGC 5506.

Table 3 shows the total mass of ionized and hot molecular gas for each galaxy by summing up the masses from all spaxels with detected Brγ and $H_2\lambda2.12\,\mu$m emission. The uncertainties in the masses are not included in this table, but they are dominated by the uncertainty in flux calibration and can be up to 20 %. The mass of ionized gas is in the range $(3-440)\times10^4\,M_\odot$, while the hot molecular gas ranges from 50 to 3 000 $M_\odot$. The mean surface mass density for the ionized and molecular gas, shown in Table 3 are in the ranges $(0.2–35.9)\,M_\odot\,pc^{-2}$ and $(0.2–13.9)\times10^{-3}\,M_\odot\,pc^{-2}$. These values are in good agreement with those previously obtained, as for example, summarized by Schönel et al. (2017) in their Table 1.

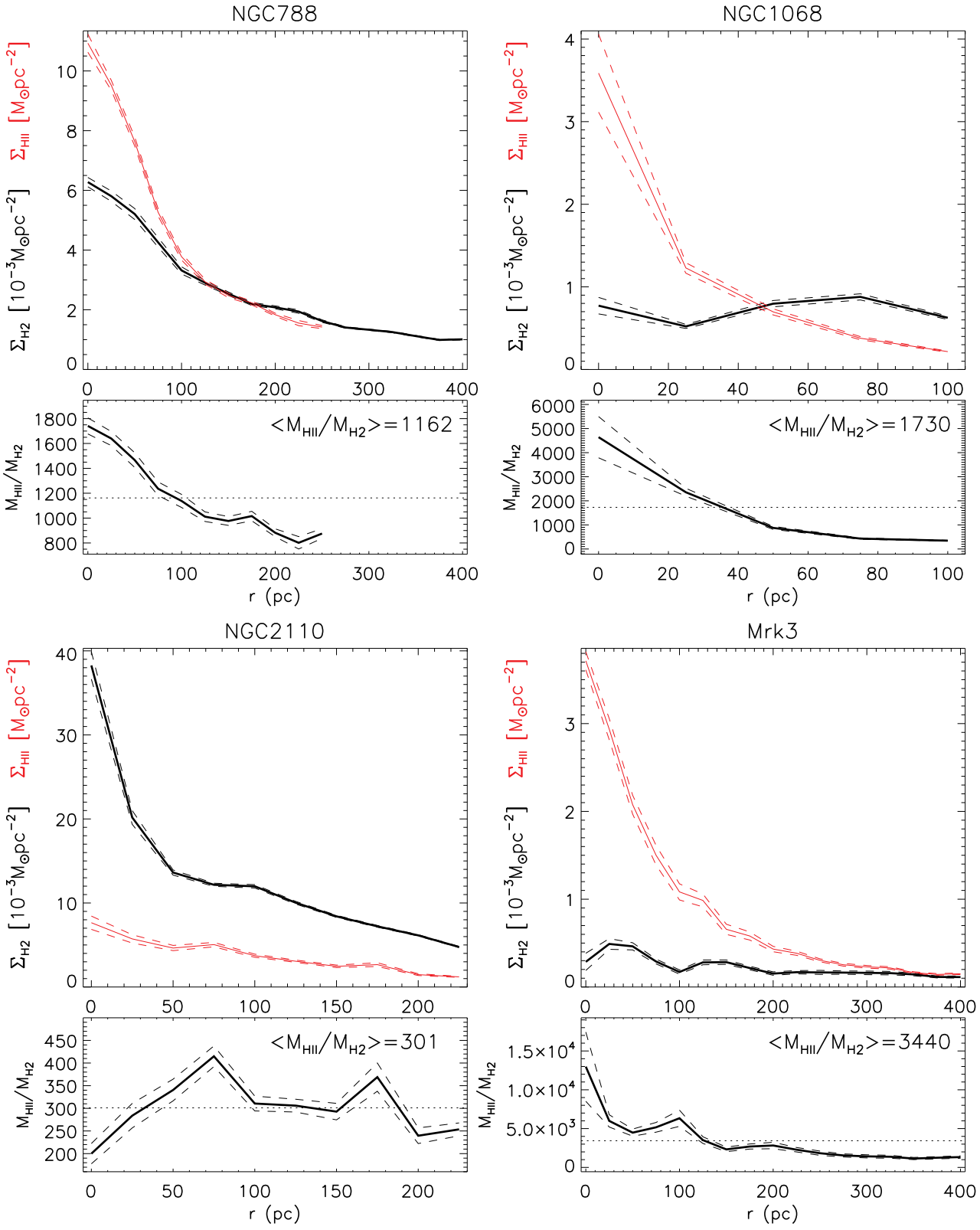

Figure 5. Surface mass density profiles for the hot molecular (top panels) and ionized (middle panels) for a radial bin of 25 pc at the plane of the galaxy. The profiles are shown as continuous lines and the dashed lines shows the standard error variation. The bottom panels show the ratio ratio between the mass of ionized and molecular gas variation for the same radial bin, considering only spaxels with measurements of both masses. The mean value of the ratio $< M_{HII}/M_HH2 >$ is shown at the top-right corner of the corresponding panel. The geometric parameters of the disk, used in the deprojection are shown in Table 3. In this figure, we show the profiles for NGC 788, NGC 1068, NGC 2110 and Mrk 3.

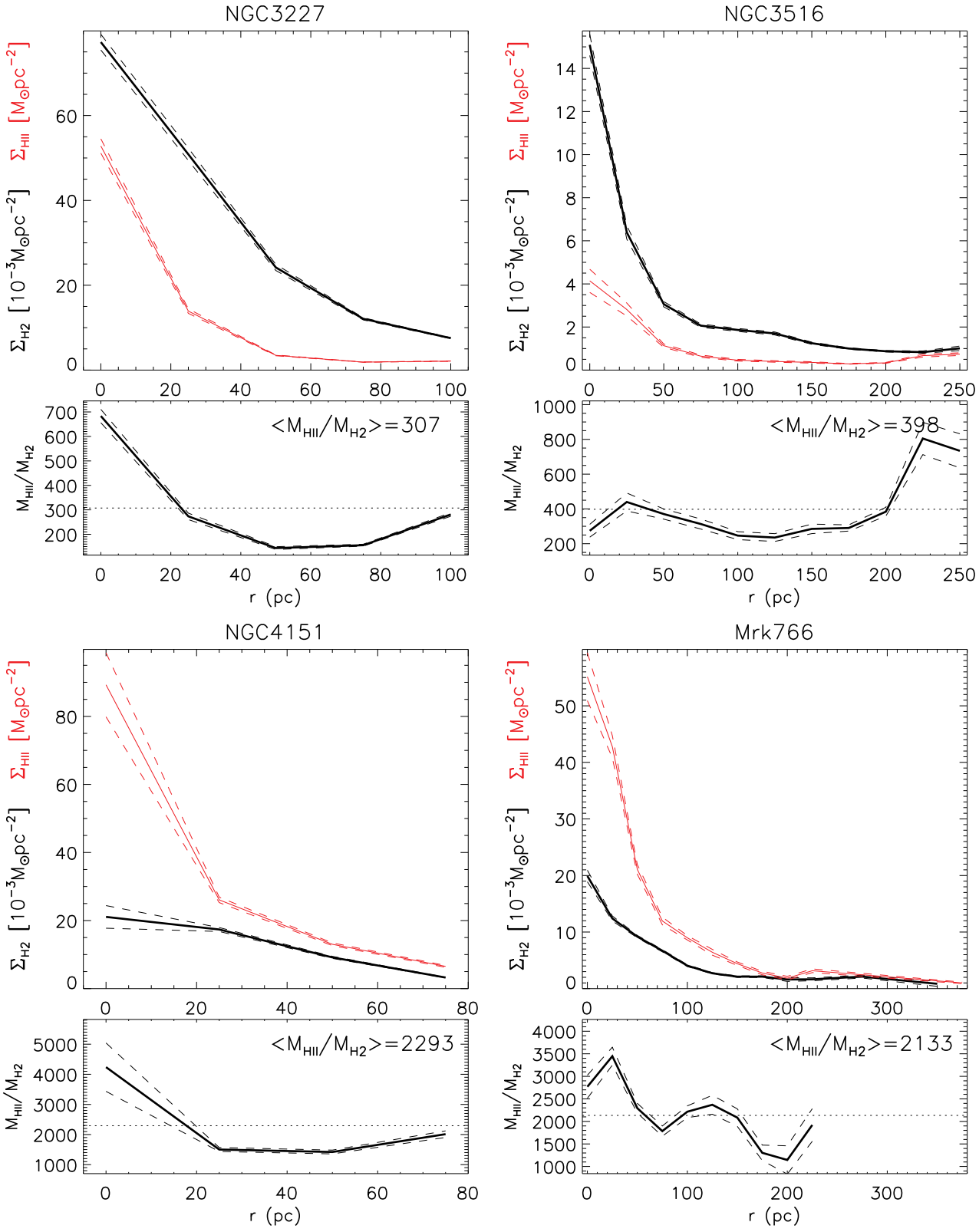

Figure 6. Same as Fig. 5 for NGC 3227, NGC 3516, NGC 4151 and Mrk 766.

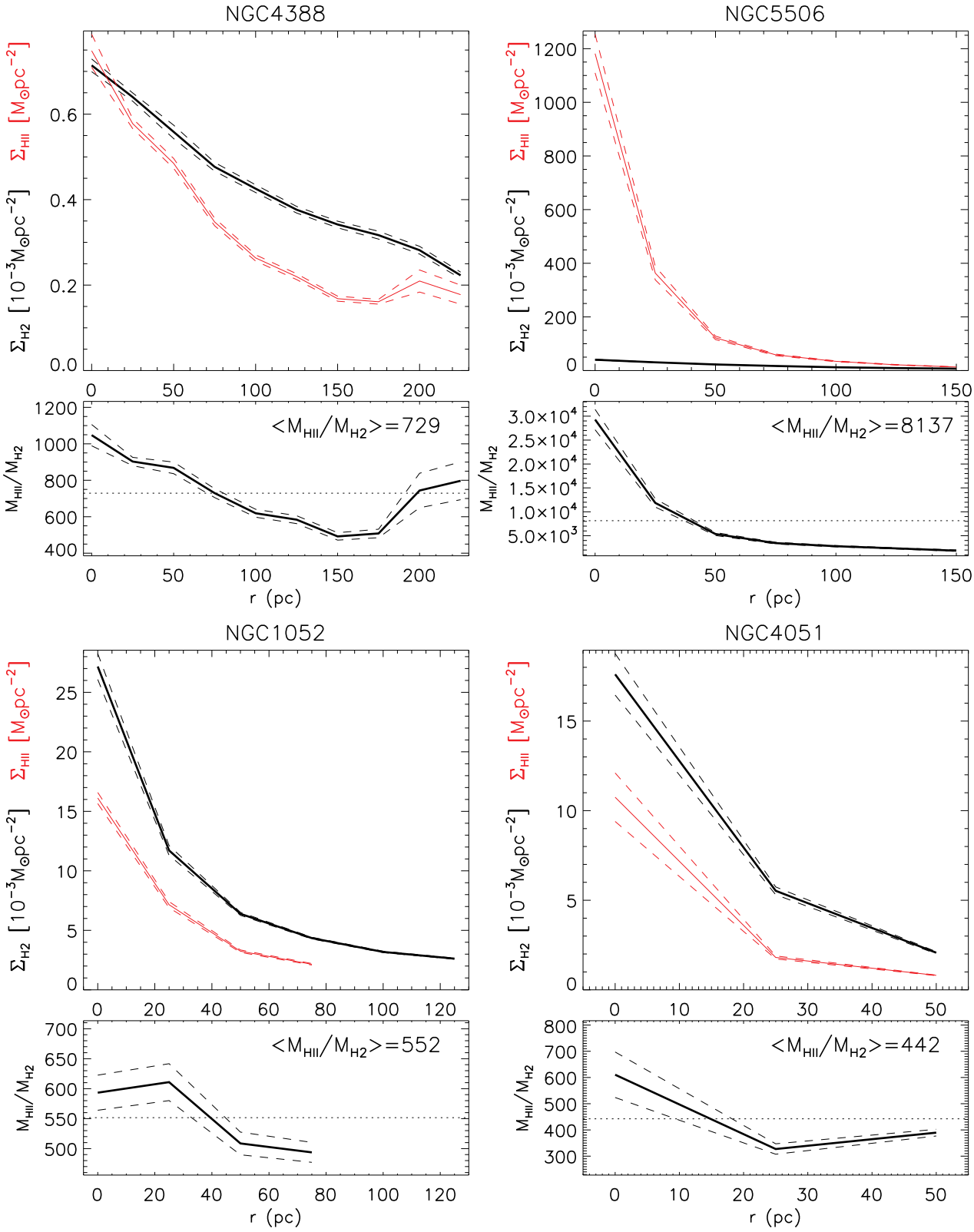

Figure 7. Same as Fig. 5 for NGC 4388, NGC 5506, NGC 1052 and NGC 4051.

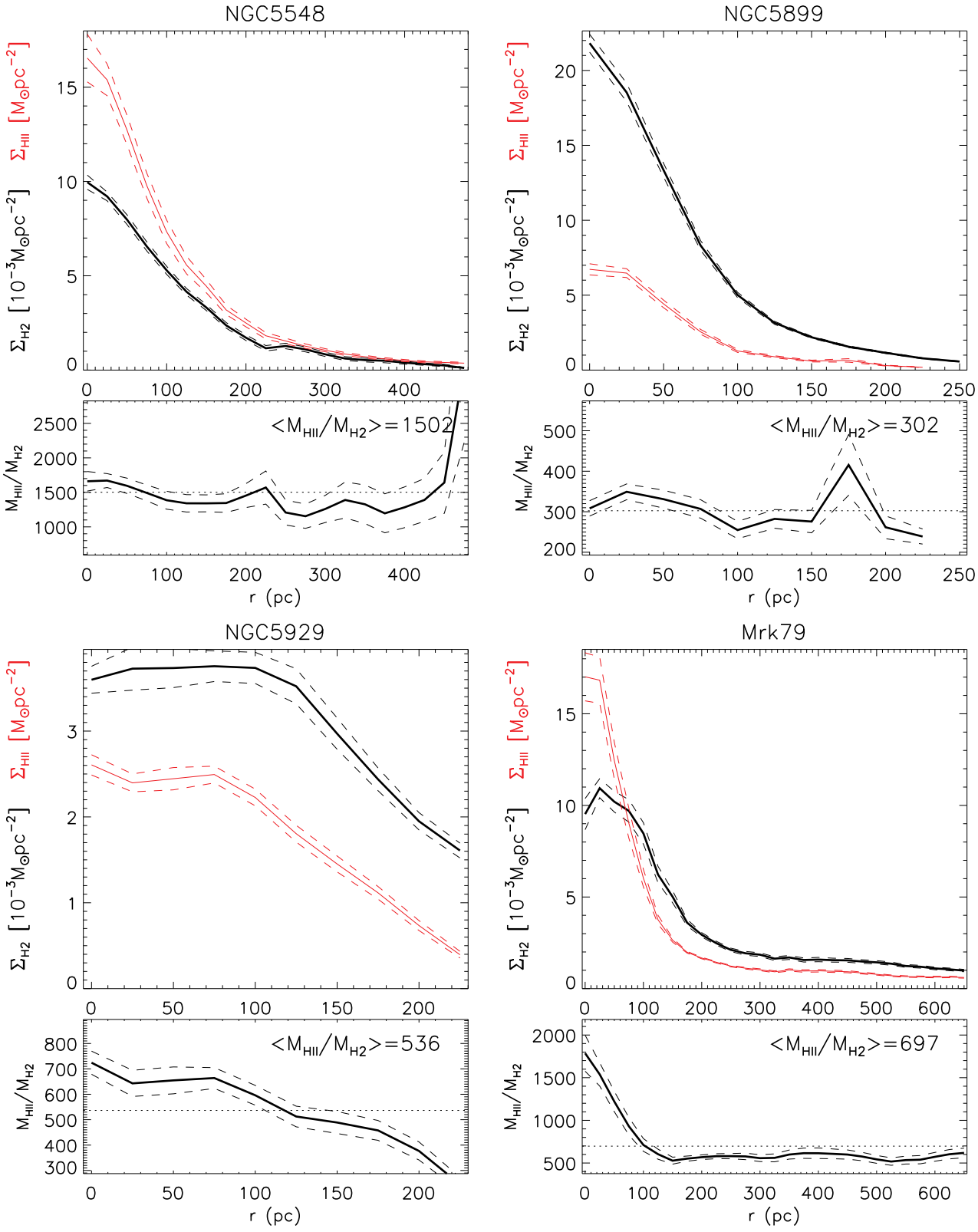

Figure 8. Same as Fig. 5 for NGC 5548, NGC 5899, NGC 5929 and Mrk 79.

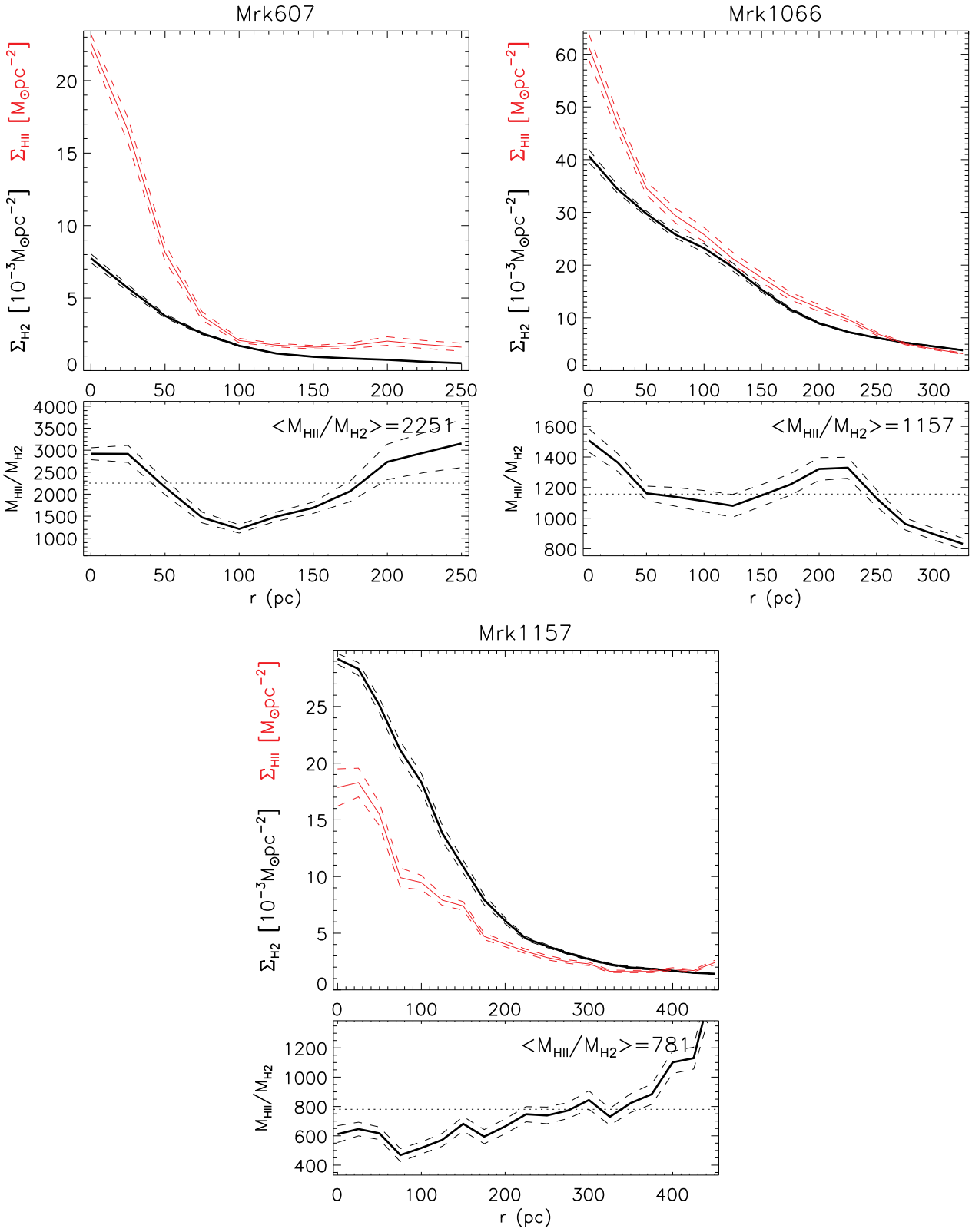

Figure 9. Same as Fig. 5 for Mrk 607, Mrk 1066 and Mrk 1157.

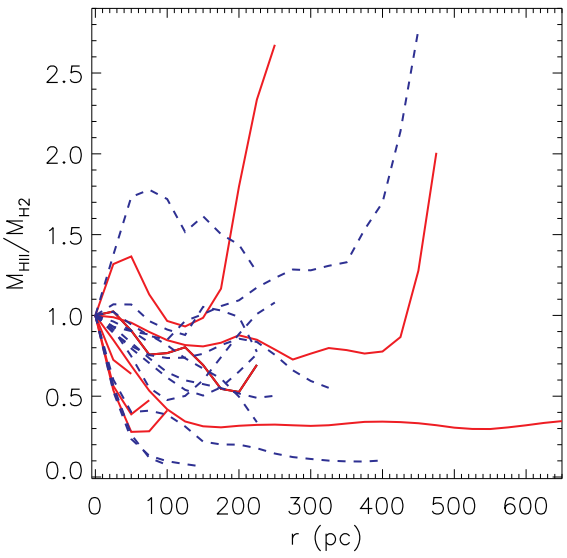

Figure 10. Normalized (by the nuclear value) radial profiles of M_{HII}/M_{H2}. Seyfert 1 galaxies are shown as continuous red lines and Seyfert 2 galaxies as dashed blue lines.

In order to further investigate the distribution of ionized and molecular gas in the inner few hundreds of parsercs of the galaxies of our sample, we constructed normalized radial profiles M_{HII}/M_{H2}, by dividing the M_{HII}/M_{H2} value at each radial bin by the nuclear value ($r < 25$ pc). These profiles are shown in Figure 10. Seyfert 1 galaxies (Mrk 766, Mrk 79, NGC 3227, NGC 3516, NGC 4051, NGC 4151 and NGC 5548) are shown as red continuous lines and Seyfert 2 galaxies (Mrk 1066, Mrk 1157, Mrk 3, Mrk 607, NGC 1052, NGC 1068, NGC 2110, NGC 4388, NGC 5506, NGC 5899, NGC 5929, NGC 788) as blue dashed lines. These profiles confirm the result already mentioned above that the ionized gas has an steeper surface mass profile, as for most galaxies the M_{HII}/M_{H2} decreases with the distance to the nucleus. In addition, Figure 10 shows that there is no significant difference for the distribution of ionized and molecular gas for Seyfert 1 and Seyfert 2 nuclei.

4 FEEDING THE AGN AND STAR FORMATION

We can estimate the accretion rate ($\dot{m}$) to the AGN in each galaxy by

$$\dot{m} = \frac{L_{\rm bol}}{c^2 \eta}, \quad (3)$$

where $L_{\rm bol}$ is the AGN bolometric luminosity, c is the light speed and η is the efficiency of conversion of the rest mass energy of the accreted material into radiation. The AGN bolometric luminosity can be estimated from the hard X-ray luminosity by (Marconi et al. 2004)

$$\log L_{\rm bol} = 0.0378(\log L_X)^2 - 2.03 \log L_X + 61.6, \quad (4)$$

where L_X is the hard X-ray (14-195 keV) luminosity. The resulting $\dot{m}$ values using the X-ray luminosities from Table 3 and assuming $\eta \approx 0.1$ (e.g. Frank, King & Raine 2002), are show in Table 1. The $\dot{m}$ for our sample ranges from 10^{-4} (for Mrk 607) to 10^{-1} $M_\odot$ yr^{-1} (for Mrk 79), with a mean value of $<\dot{m}> \sim 0.03$ $M_\odot$ yr^{-1}.

The surface mass density profiles of Figs. 5–9 show that most of the ionized e molecular gas masses listed in Table 3 are concentrated within the inner ~300 pc of the galaxies. The ionized gas alone would be enough to feed the central AGN for an activity cycle of $10^7 - 10^8$ yr. The hot molecular gas mass is typically 3 order of magnitudes lower than that of the ionized gas, but this gas is just the heated surface of a probably much larger molecular gas reservoir of colder molecular gas, that may be $10^5 - -10^7$ times more massive (Dale et al. 2005; Müller-Sánchez et al. 2006; Mazzalay et al. 2013), implying that the masses of the cold molecular gas probably range from $10^7 - -10^9$ $M_\odot$. Thus, the observed gas masses provide enough material to feed the SMBH of the galaxies of our sample.

We conclude that, within the inner 300 pc of our sample, there are $\sim 10^2$ times more gaseous mass than the necessary to feed the AGN. Most of this mass will not feed the AGN and might be consumed by star formation. The pioneer work by Schmidt (1959) showed that the star formation rate (SFR) is directly related to the gas density, while Kennicutt (1998) derived a relation between the SFR surface density (Σ_{SFR}) and the ionized gas mass surface density (Σ_{HII}) so that the former can be obtained from the latter as

$$\frac{\Sigma_{SFR}}{M_\odot yr^{-1} kpc^{-2}} = (2.5 \pm 0.7) \times 10^{-4} \left(\frac{\Sigma_{HII}}{M_\odot pc^{-2}} \right)^{1.4}, \quad (5)$$

where Σ_{HII} is the surface mass density.

Using the equation above, we obtain the mean values of the star formation density $<\Sigma_{SFR}>$ for each galaxy, shown in Table 3, which varies from 3×10^{-5} to 3.8×10^{-2} $M_\odot yr^{-1} kpc^{-2}$. Considering area of the Brγ emission quoted in Table 3 we obtain a wide range of total star formation rate of 10^{-6}–10^{-3} $M_\odot$ yr^{-1} (shown in Table 3). These values of SFR are smaller than that obtained for star-forming galaxies and circumnuclerar star forming regions ($SFR \sim 10^{-3}$ $M_\odot$ yr^{-1}) (e.g. Wold & Galliano 2006; Shi, Gu & Peng 2006; Dors et al. 2008; Galliano & Alloin 2008; Falcón-Barroso et al. 2014; Riffel et al. 2016). Considering a scenario in which the total mass would be used to form stars, the estimated masses for our sample would allow the star formation for about 10^9 yr at the current star formation rate.

Thus, considering the derived mass accretion rate, the star formation rate and the mass of molecular and ionized gas, we conclude that the mass reservoirs of the galaxies of our sample are much larger than that needed to power the central AGN and star formation, thus allowing the co-existence of recent star formation as evidenced by low-stellar velocity dispersion structures seen in some galaxies (Riffel et al. 2017) and the nuclear activity.

5 CONCLUSIONS

We characterize a sample of 20 nearby X-ray selected Seyfert galaxies being observed with the NIFS instrument of the Gemini North Telescope plus a complementary sample of

Table 3. Molecular and ionized gas masses and surface densities. (1) Name of the galaxy; (2) Total mass of ionized gas; (3) Area for the Brγ emission; (4) Average surface mass density for the ionized gas; (5) Total mass of hot molecular gas; (6) Area for the $H_2\,\lambda2.12$ emission; (7) Average surface mass density for the hot molecular gas; (8) Average star formation density; (9) total star formation rate; (10) and (11) orientation of the major axis and inclination of the disk, used in the deprojection from Riffel et al. (2017), except for Mrk 3 and Mrk 79 [from Hyperleda database – Makarov et al. (2014)], NGC 1068 (from Davies et al. 2007) and NGC 4151 (from Onken et al. 2014); (12) AGN bolometric luminosity estimated from the 14-195 keV luminosity; (13) mass accretion rate onto the SMBH; (14) Reference for the $H_2\,\lambda2.12$ and Brγ flux maps.

(1) Galaxy	(2) M_{HII} $10^4 M_\odot$	(3) A_{HII} 10^4pc^2	(4) $<\Sigma_{HII}>$ $M_\odot$/pc^2	(5) M_{H2} $10^2 M_\odot$	(6) A_{H2} 10^4pc^2	(7) $<\Sigma_{H2}>$ $10^{-3} M_\odot$/pc^2	(8) $<\Sigma_{SFR}>$ $10^{-3} M_\odot$/yrkpc^2	(9) SFR $10^{-4} M_\odot$/yr	(10) Ψ_0 deg	(11) i deg	(12) log$L_{\rm bol}$ erg/s	(13) $\dot{m}$ 10^{-3} $M_\odot$/yr	(14) Ref.
Main Sample													
NGC788	36.11	8.30	4.35	10.90	70.25	1.55	1.96	1.63	120	20.8	44.4	49.2	a
NGC1068	3.47	15.59	0.22	0.54	15.86	0.34	0.03	0.05	145	40.0	42.8	1.1	b
NGC2110	28.17	11.00	2.56	15.66	23.79	6.59	0.93	1.03	156	42.5	43.6	65.4	c
Mrk3	22.39	59.90	0.37	0.47	31.03	0.15	0.06	0.38	15	31.7	44.7	87.2	d
NGC3227	17.87	2.69	6.64	7.81	5.95	13.12	3.54	0.95	156	45.4	43.4	4.1	a
NGC3516	11.62	15.94	0.73	3.87	30.63	1.26	0.16	0.26	54	12.8	44.2	27.9	a
NGC4151	59.22	5.93	9.99	2.87	5.72	5.02	6.27	3.72	85	23.0	44.0	16.0	e
Mrk766	51.60	2.93	17.60	3.75	6.53	5.74	13.85	4.06	66	18.2	44.0	16.0	f
NGC4388	4.36	18.37	0.24	0.67	22.31	0.30	0.03	0.06	96	27.7	44.6	65.4	a
NGC5506	439.64	12.26	35.86	8.89	12.00	7.41	37.53	46.01	96	58.7	44.3	37.0	a
Complementary Sample													
NGC1052	6.18	0.92	6.70	3.00	7.56	3.96	3.58	0.33	114	47.5	42.9	1.4	g
NGC4051	3.64	2.13	1.71	0.86	2.91	2.94	0.53	0.11	24	37.3	42.5	0.5	h
NGC5548	74.49	85.30	0.87	3.80	15.70	2.42	0.21	1.76	108	60.9	44.7	87.2	i
NGC5899	8.10	3.81	2.12	3.60	23.45	1.53	0.72	0.27	24	62.7	43.1	2.4	a
NGC5929	14.70	23.77	0.62	3.94	28.86	1.37	0.13	0.30	30	60.7	42.3	0.4	j
Mrk79	169.24	163.24	1.04	26.90	179.32	1.50	0.26	4.29	73	35.6	44.8	116.4	k
Mrk607	51.85	20.30	2.55	2.06	28.49	0.72	0.93	1.89	138	58.2	41.7	0.1	a
Mrk1066	305.89	31.45	9.73	30.11	45.02	6.69	6.04	19.0	120	50.2	42.0	0.2	l
Mrk1157	188.70	65.13	2.90	28.24	89.60	3.15	1.11	7.22	114	45.1	42.0	0.2	m

a: Schonell et al., in prep.; b: Riffel et al. (2014); c: Diniz et al. (2015) ; d: Fischer et al., in prep.; e: Storchi-Bergmann et al. (2009)
f: Schönel et al. (2014); g: Dahmer-Hahn et al, in prep.; h: Riffel et al. (2008); i: Schönel et al. (2017); j: Riffel, Storchi-Bergmann & Riffel (2015);
k: Riffel, Storchi-Bergmann & Winge (2013); l: Riffel, Storchi-Bergmann & Nagar (2010); m: Riffel & Storchi-Bergmann (2011b)

9 additional galaxies already observed with NIFS. We also present and discuss mean radial profiles within the inner kiloparsec for the ionized and molecular gas surface mass densities for the galaxies already observed: 11 from the main X-ray sample and the 9 galaxies from the complementary sample. Our main conclusions are:

- The average values of X-ray luminosities are $< logL_X >= 42.6 \pm 0.1$ erg s^{-1} for the main sample and $< logL_X >= 42.4 \pm 0.1$ erg s^{-1} for the main plus complementary sample. The [O III]5007 luminosities are in the range $L_{[OIII]} = (0.2 - 155) \times 10^{40}$ erg s^{-1}, with a mean value of $< logL_{[OIII]} >= 41.0 \pm 0.2$ erg s^{-1}.
- The M_B and M_H distributions for the restricted BAT sample (all galaxies with $L_X \geq 10^{41.5}$ ergs s^{-1} and $z \leq 0.015$ from the 60 month BAT catalogue) and our sample are very similar, indicating that the additional criteria used in the definition of our sample does not include any bias in terms of these properties. The mean values for our sample are $< M_B >= -20.75 \pm 0.16$ and $< M_H >= -23.83 \pm 0.13$.
- The mean value of the central stellar velocity dispersion of the total sample is 154 ± 11 km s^{-1}, being essentially the same as that of the X-ray sample only.
- The axial ratio b/a of the total sample (similar also to that for the X-ray sample only) ranges from 0.2 (corresponding to a disk inclination of $i \sim 80°$, almost edge-on) to 0.9 ($i \sim 25°$, almost face-on).
- We contructed mean radial profiles for the surface mass density of the ionized (Σ_{HII}) and hot molecular (Σ_{H2}) gas for the 20 galaxies already observed, derived from the Brγ and $H_2\lambda2.12\mu m$ fluxes. Both profiles decrease with the distance from the nucleus most galaxies, with the ionized gas showing a steeper gradient. The only exception is NGC 1068, which shows an increase in Σ_{H2} at 25–75 pc from the nucleus due to the presence of a molecular gas ring.

- The mean surface mass density for the ionized and molecular gas are in the ranges (0.2–35.9) $M_\odot$ pc^{-2} and (0.2–13.9)$\times 10^{-3}$ $M_\odot$ pc^{-2}, while the ratio between them ranges from ∼200 for Mrk 607 to ∼8000 for NGC 5506. The mean star formation density is $< \Sigma_{SFR} >= (4.09 \pm 0.44) \times 10^{-3} M_\odot$/yrkpc^2, the star formation rates range from 10^{-6} to 10^{-3} $M_\odot$ yr^{-1}, while the accretion rate onto the SMBH ranges from 10^{-4} to 10^{-1} $M_\odot$ yr^{-1}.

- The total mass of ionized gas within the inner $\sim 100 - 500$ pc is in the range $(3 - 440) \times 10^4 M_\odot$, while that of hot molecular gas ranges between 50 and 3000 $M_\odot$. Considering also that the mass of cold molecular gas is usually $\sim 10^5$ times larger than that of hot molecular gas for AGN in general, we estimate a total mass of gas in the region ranging from 10^6 to 10^8 $M_\odot$. Comparing these masses with the typical accretion rates above, it can be concluded that they are much larger than that necessary to feed a typical AGN cycle of of $10^7 - 10^8$ yr. The fate of this gas is probably the formation of new stars in the region (the AGN-Starburst connection).

ACKNOWLEDGMENTS

Based on observations obtained at the Gemini Observatory, which is operated by the Association of Universities for Research in Astronomy, Inc., under a cooperative agreement with the NSF on behalf of the Gemini partnership: the National Science Foundation (United States), the Science and Technology Facilities Council (United Kingdom), the National Research Council (Canada), CONICYT (Chile), the Australian Research Council (Australia), Ministério da Ciência e Tecnologia (Brazil) and south-eastCYT (Argentina). This research has made use of the NASA/IPAC Extragalactic Database (NED) which is operated by the Jet Propulsion Laboratory, California Institute of Technology, under contract with the National Aeronautics and Space Administration. We acknowledge the usage of the HyperLeda database (http://leda.univ-lyon1.fr). This publication makes use of data products from the Two Micron All Sky Survey, which is a joint project of the University of Massachusetts and the Infrared Processing and Analysis Center/California Institute of Technology, funded by the National Aeronautics and Space Administration and the National Science Foundation.

R.A.R. acknowledges support from FAPERGS (project N0. 2366-2551/14-0) and CNPq (project N0. 470090/2013-8 and 302683/2013-5).

REFERENCES

Aalto, S. et al. 2012, A&A, 573, 44
Ajello, M., Alexander, D. M., Greiner, J., Madejski, G. M., Gehrels, N., Burlon, D., 2012, ApJ, 749, 21.
Audibert, A., Riffel, R., Sales, D. A., Pastoriza, M. G., Ruschel-Dutra, D., 2017, MNRAS, 464, 2139.
Barbosa, F. K. B., Storchi-Bergmann, T., Cid Fernandes, R., Winge, C., & Schmitt, H. 2006, MNRAS, 371, 170.
Barbosa, F. K., Storchi-Bergmann, McGregor, P., Vale, T. B., Riffel, R. A.., 2014, MNRAS, 455, 2353.
Bigiel, F., Leroy, A., Walter, F., Brinks, E., de Blok, W. J. G., Madore, B., Thornley, M. D., 2008, AJ, 136, 2846.
Bradt, H. V., Burke, B. F., Canizares, C. R., Greenfield, P. E., Kelley, R. L., McClintock, J. E., van Paradijs, J. & Koski, A. T., 1978, ApJ, 226, 111.
Cid Fernandes, R. et al. 2004, MNRAS, 355, 273
Dale, D. A., Sheth, K., Helou, G., Regan, M. W., & Hüttemeister, S., 2005, ApJ, 129, 2197.
Davies, R. I. et al. 2007, ApJ, 671, 1388
Davies, R. I., Maciejewski, W., Hicks, E. K. S., Tacconi, L. J., Genzel, R., Engel, H., 2009, ApJ, 702, 114.
Davies, R. I, et al., 2015, ApJ, 806, 127.
Davies, R. I, et al., 2017, MNRAS, 466, 4917.
de Vaucouleurs, G., de Vaucouleurs, A., Corwin, H. G., Jr., et al. 1991, Third Reference Catalogue of Bright Galaxies, Volume I: Explanations and references, Volume II: Data for galaxies between 0h and 12h, Volume III: Data for galaxies between 12h and 24h (New York: Springer)
Diniz, M. R., Riffel, R. A., Stochi-Bergmann, T., Winge, C., 2015, MNRAS, 453, 1727.
Dors, O. L., Storchi-Bergmann, T., Riffel, R. A., Schmidt, A. A, 2008, A&A, 482, 59.
Durré M. & Mould J., 2014, ApJ, 784, 79.
Croton D., et al., 2006, MNRAS, 365, 11
Falcoón-Barroso, J., Ramos Almeida, C., Böker, T., Schinnerer, E., Knapen, J. H., Lanǫn, A., Ryder, S., 2014, MNRAS, 438, 329.
Ferrarese, L., & Merritt, D., 2000, ApJ, 539, L9.
Ferrarese, L. & Ford, H. 2005, SSRv, 116, 523
Ferruit, P., Mundell, C. G., Nagar, N. M., Emsellem, E., Pécontal, E., Wilson, A. S., Schinnerer, E. 2004, MNRAS, 352, 1180.
Frank, J, King, A. & Raine, D. J., 2002, Accretion Power in Astrophysics, Cambridge Univ. Press
Ciotti, L., et al. 2010, ApJ 717, 707
Elvis, M. 2000, ApJ, 545, 63
Fabian, A. 2012, ARA&A, 50, 455
Frank, J., King, A. R., & Raine, D. J. 2002, Accretion Power in Astrophysics (3rd ed.; Cambridge: Cambridge Univ. Press)
Galliano, E., & Alloin, D. 2008, A&A, 487, 519.
Gebhardt, K., Bender, R., Bower, G., Dressler, A., Faber, S. M., Filippenko, A. V., Green, R., Grillmair, C., Ho, L. C., Kormendy, J., Lauer, T. R., Magorrian, J., Pinkney, J., Richstone, D., & Tremaine, S., 2000, ApJ, 539, L13.
González Delgado, R.M., Heckman, T. & Leitherer, C. 2001, ApJ, 546, 845.
González Delgado, R. M., Arribas, S., Pérez, E., Heckman, T., 2002, ApJ, 579, 188.
Graham, A. W., Onken, C. A., Athanassoula, E., Combes, F., 2011, MNRAS, 412, 2211.
Gu, Q., Melnick, J., Cid Fernandes, R., Kunth, D., Terlevich, E., Terlevich, R., 2006, MNRAS, 366, 480.
Heckman, T. M. & Best, P. N. 2014, ARA&A
Hicks, E. K. S., Davies, R. I., Maciejewski, W., Emsellem, E., Malkan, M. A., Dumas, G., Müller-Sánchez, F., Rivers, A., 2013, ApJ, 768, 107.
Hopkins & Quataert 2010, MNRAS, 407, 1529
Hopkins, P. F. 2012, MNRAS, 420, 8.
Kauffmann & Heckman 2009, MNRAS, 397, 135
Kennicutt, R. C., 1998, ARAA, 36, 189.
Kennicutt, R. C. et al., 2007, ApJ, 671, 333.
Kormendy, J. & Ho, L. C, 2013, ARA&A, 51, 511
Makarov, D., Prugniel, P., Terekhova, N., Courtois, H., Vauglin, I., 2014, A&A, 570, 13
Malkan, M. A., Gorjian, V. & Tam, R., 1998, ApJS, 117,25.
Martini, P., et al. 2013, MNRAS, 420, 2249
Mazzalay, X. et al., 2013, MNRAS, 428, 2389.
Mazzalay, X. et al., 2014, MNRAS, 438, 2036.
Marconi, A., Risaliti, G., Gilli, R., Hunt, L. K., Maiolino, R., Salvati, M., 2004, MNRAS, 351, 169.
McGregor, P. J., Hart, J., Conroy, P. G., Pfitzner, M. L., Bloxham, G. J., Jones, D. J., Downing, M. D., Dawson, M., Young, P., Jarnyk, M., &Van Harmelen, J. 2003, Proceedings of the SPIE, 4841, 1581.
Mulchaey, J. S., Wilson, A. S., Bower, G. A., Heckman, T. M., Krolik, J. H., Miley, G. K., 1994, ApJ, 433, 625.
Müller-Sánchez F., Davies R. I., Eisenhauer F., Tacconi L. J., Genzel R., Sternberg A., 2006, A&A, 454, 492.
Müller-Sánchez, F., Davies, R. I., Genzel, R., Tacconi, L. J., Eisenhauer, F., Hicks, E. K. S., Friedrich, S., & Sternberg, A., 2009, ApJ, 691, 749.
Müller Sánchez, F. et al. 2011, ApJ, 739, 69
Nagar, N. M., Wilson, A. S., Mulchaey, J. S. & Gallimore, J. F., 1999, ApJS, 120, 209.
Noguchi, K., Terashima, Y., Ishino, Y., Hashimoto, Y., Koss, M., Ueda, Y., Awaki, H., 2010, ApJ, 711, 144.
Onken, C. et al., 2014, ApJ, 791, 37.
Osterbrock, D. E. & Ferland, G. J., 2006, Astrophysics of Gaseous Nebulae and Active Galactic Nuclei, Second Edition, University Science Books, Mill Valley, California.
Ramos Almeida, C. et al., 2014, MNRAS, 445, 1130.
Riffel, R. A.., Sorchi-Bergmann, T., Winge, C., Barbosa, F. K. B., 2006, MNRAS, 373, 2.
Riffel, R. A., Storchi-Bergmann, T., Winge, C., McGregor, P., Beck, T. & Schmitt, H., 2008, MNRAS, 385, 1129

Riffel, R. A., Storchi-Bergmann, T., McGregor, P., 2009, ApJ, 698, 1767
Riffel, R. A.., Storchi-Bergmann, T. & Nagar, N. M., 2010, MNRAS, 404, 166.
Riffel, R. A.. & Storchi-Bergmann, T., Riffel, R., & Pastoriza, M. G., 2010, ApJ, 713, 469.
Riffel, R. A.. & Storchi-Bergmann, T., 2011, MNRAS, 411, 469.
Riffel, R. A.. & Storchi-Bergmann, T., 2011, MNRAS, 417, 2752.
Riffel, R. A., Storchi-Bergmann, T., Winge, C., 2013, 430, 2249.
Riffel, R. A., Vale, T. B., Storchi-Bergmann, T., McGregor, P. J., 2014, MNRAS, 442, 656.
Riffel, R. A., Storchi-Bergmann, T., Riffel, R., ApJ, 2014, 780, 24.
Riffel, R. A., Storchi-Bergmann, T., Riffel, R., 2015, MNRAS, 451, 3587.
Riffel, R. A. et al. 2016, MNRAS, 461, 4192.
Riffel, R. A. et al. 2017, MNRAS, submitted
Riffel, R., Rodríguez-Ardila, A. & Pastoriza, M. G., 2006, A&A, 457, 61.
Riffel, R., Pastoriza, M. G., Rodríguez-Ardila, A., Bonatto, C., 2009, MNRAS, 400, 273.
Riffel, R., Riffel, R. A.., Ferrari, F., Storchi-Bergmann, T., 2011. MNRAS, 416, 493.
Rosario D. J., Whittle M., Nelson C. H. & Wilson A. S., 2010, MNRAS, 408, 565.
Schmidt, M., 1959, ApJ, 129, 243.
Schmitt, H. R., Ulvestad, J. S., Antonucci, R. R. J., Kinney, A. L., 2001, ApJS, 132, 199.
Schmitt, H. R., Donley, J. L., Antonucci, R. R. J., Hutchings, J. B., Kinney, A. L., 2003, ApJS, 148, 327.
Scoville, N. Z., Hall, D. N. B., Kleinmann, S. G., & Ridgway, S. T. 1982, 253, 136.
Shankar, F. et al. 2009, ApJ, 690, 20
Sakamoto, K.et al. 2010, ApJ, 725, L228
Schnorr-Müller A., Storchi-Bergmann T., Nagar N. M., Robinson A., Lena D., Riffel R. A. & Couto G. S., 2014, MNRAS, 437, 1708,
Schonel, A. J., Riffel, R. A., Stochi-Bergmann, T., Winge, C., 2014, MNRAS, 445, 414.
Schonel, A. J., Riffel, R. A., Stochi-Bergmann, T., Riffel, R., 2017, MNRAS, 464, 1771.
Simoes Lopes et al. 2007, ApJ, 655, 718
Shi, L., Gu, Q. S., & Peng, Z. X. 2006, A&A, 450, 15.
Skrutskie, M., F. et al., AJ, 131, 1163.
Somerville et al. 2008, MNRAS, 391, 481
Springel et al. 2005, MNRAS, 361, 776
Storchi-Bergmann, T., Winge, C., Ward, M. & Wilson, A. S., 1999, MNRAS, 304, 35.
Storchi-Bergmann et al. 2000, ApJ, 544, 747.
Storchi-Bergmann et al. 2001, ApJ, 559, 147
Storchi-Bergmann, T., McGregor, P. J., Riffel, R. A., Simões Lopes, R., Beck, T., Dopita, M., 2009, MNRAS, 394, 1148.
Storchi-Bergmann, T., Simões Lopes, R., McGregor, P. Riffel, R. A.., Beck, T., Martini, P., 2010, MNRAS, 402, 819.
Storchi-Bergmann, T., Riffel, R. A.., Riffel, R., Diniz, M. R., Borges Vale, T., McGregor, P. J., 2012, ApJ, 755, 87.
Terlevich E. et al. 1990, MNRAS, 242, 271.
Tremaine, S., Gebhardt, K., Bender, R., Bower, G., Dressler, A., Faber, S. M., Filippenko, A. V., Green, R., Grillmair, C., Ho, L. C., Kormendy, J., Lauer, T. R., Magorrian, J., Pinkney, J., & Richstone, D., 2002, ApJ, 574, 740.
Ulvestad J. S. & Wilson A. S., 1983, ApJl, 264, L7.
Veilleux, S. et al. 2013, ApJ, 776, 27
Zhu, G., Zaw, I., Blanton, M. R., Greenhill, L. J., 2011, ApJ, 742, 73.
Weaver, K. A., Mushotzky, R. F., Serlemitsos, P. J., Wilson, A. S., Elvis, M. & Briel, U., 1995, ApJ, 442, 597.
Whittle, M. 1992, ApJS, 79,49
Wold, M., Galliano, E., 2006, MNRAS, 369, 47.

This paper has been typeset from a TEX/LATEX file prepared by the author.

3 *Obtenção e redução dos dados*

Os dados foram obtidos através do telescópio Gemini-Norte no Observatório de Mauna Kea, Big Island, Havaí, com o espectrógrafo de campo integral NIFS.

3.1 O instrumento NIFS

O NIFS (McGregor et al., 2003) é um espectrógrafo de campo integral (IFU - Integral Field Unit) que atua no infra-vermelho próximo e está acoplado ao telescópio Gemini-Norte, construído pela *Australian National University's Research School of Astronomy and Astrophysics*. O NIFS fornece espectroscopia 3D (X e Y espaciais e Z espectral) com poder de resolução espectral (R=$\lambda/\Delta\lambda$, onde $\Delta\lambda$ corresponde ao tamanho de 2 pixeis espectrais e λ é o comprimento de onda central do filtro utilizado) de R$\sim$5000 sobre uma imagem de 3.0" x 3.0" (X e Y) para a banda K. Ele pode ser acoplado ao sistema de ótica adaptativa do Gemini Norte, ALTAIR, que é capaz de atingir uma resolução angular de $\approx$ 0.1". Na maioria das IFUs o transporte do detector até o espectrógrafo é feito através de fibras óticas, já no NIFS isto é feito através de espelhos. O projeto ótico do NIFS baseou-se no método AIS (Advanced Image Slicer) proposto originalmente por Content (1997), em que a imagem original bidimensional é dividida em subimagens que são reagrupadas lado a lado como se fossem várias "fendas longas" na entrada do espectrógrafo. Tal método está ilustrado na Fig. 3.1.

Como indicado na Fig. 3.1, os espelhos S1 seccionam a imagem bidimensional em subimagens tal qual teríamos para uma fenda longa. As imagens são refletidas nos espelhos S2 que as projetam em um conjunto de espelhos S3 localizados na superfície focal da entrada do espectrógrafo. As imagens são então são reorganizadas e formam uma pseudo-fenda, fazendo com que tenhamos uma conversão da imagem em uma "fenda-longa".

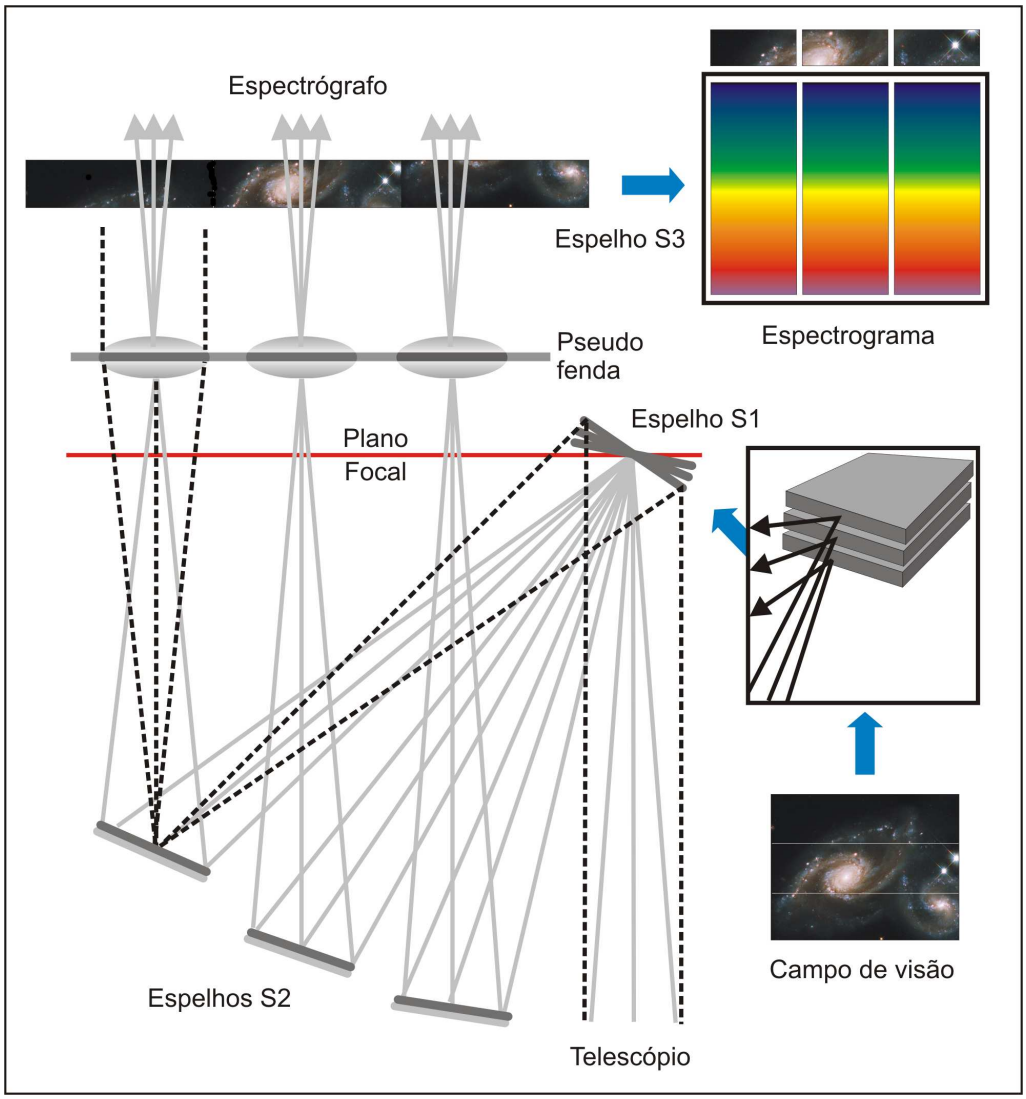

Figura 3.1: Ilustração do princípio do AIS equipado com três slices. Figura extraída de Allington-Smith et al. (2006) com algumas modificações.

3.2 Observações

As observações espectroscópicas de campo integral das galáxias da nossa amostra foram obtidas através do espectrógrafo NIFS do telescópio Gemini-Norte, operando com o uso de ótica adaptativa através do sistema ALTAIR. O NIFS tem um campo de visão quadrado de 3”×3”. As observações foram feitas nas bandas J e K(K_l), que compreendem os intervalos espectrais de 1.14 a 1.36μm para a banda J e 2.08 a 2.5μm para a banda K_l, com resoluções angulares variando de 0.12 a 0.20”, dependendo da performance dos sistema de ótica adaptativa. A resolução espectral varia de 1.7 a 2.0Åpara a banda J, que corresponde a 41 e 48 km/s no espaço de velocidades e para a banda K_l a resolução espectral varia de 3 a 3.7Å, que corresponde a 42 e 48 km/s no espaço de velocidades. A tabela 3.1 mostra dados das observações e reduções

Tabela 3.1: Observações. (1) Galaxia; (2) Identificação do Projeto; Resolução angular na banda (3) J e (4) K; Resolução espectral na banda (5) J e (6) K; Referência.

Galáxia	Programa	PSF_J (arcsec)	PSF_K (arcsec)	$FWHM_J$ (Å)	$FWHM_K$ (Å)	Ref.
Amostra principal						
NGC788	GN-2015B-Q-29	0.13	0.13	1.9	3.5	a
NGC1068	GN-2006B-C-9	0.14	0.11	1.7	3.0	b, c, d
NGC2110	GN-2015B-Q-29	0.13	-	1.9	-	a, e
Mrk3	GN-2010A-Q-5	?	?	2.0	3.2	-
NGC3227	GN-2016A-Q-6	0.13	0.12	1.8	3.5	a
NGC3516	GN-2015A-Q-3	0.17	0.15	1.8	3.5	a
NGC4151	GN-2006B-C-9	0.16	0.12	1.6	3.3	f, g, h
NGC4235	GN-2016A-Q-5	0.12	0.13	1.8	3.5	a
Mrk766	GN-2010A-Q-42	0.21	0.19	1.7	3.5	a, i
NGC4388	GN-2015A-Q-3	-	0.19	-	3.7	a
NGC5506	GN-2015A-Q-3	0.15	0.18	1.9	3.6	a
Amostra complementar						
NGC1052	GN-2010B-Q-25	-	0.15	1.7	-	a
NGC4051	GN-2006A-SV-123	-	0.18	-	3.2	a, j
NGC5548	GN-2012A-Q-57	0.28	0.20	1.7	3.5	a, k
NGC5899	GN-2013A-Q-48	0.13	0.13	1.8	3.4	a
NGC5929	GN-2011A-Q-43	0.12	0.12	1.7	3.2	a, l, m
Mrk79	GN-2010A-Q-42	0.25	0.25	1.8	3.5	n
Mrk607	GN-2012B-Q-45	0.14	0.14	2.0	2.2	a
Mrk1066	GN-2008B-Q-30	0.13	0.15	1.7	3.3	a, o, p, q, r
Mrk1157	GN-2009B-Q-27	0.11	0.12	1.8	3.5	a, s, t

Referências: a: Riffel et al. (2017 - submetido); b: Storchi-Bergmann et al. (2012); c: Riffel et al. (2014); d: Barbosa et al. (2014); e: Diniz et al. (2015); f: Storchi-Bergmann et al. (2009); g: Storchi-Bergmann et al. (2010); h: Riffel et al. (2009b); i: Schönell et al. (2014); j: Riffel et al. (2008); k: Schönell et al. (2017); l: Riffel et al. (2014); m: Riffel et al. (2015); n: Riffel et al. (2013); o: Riffel et al. (2010); p: Riffel et al. (2010); q: Riffel e Storchi-Bergmann (2011a); r: Ramos Almeida et al. (2014); s: Riffel e Storchi-Bergmann (2011b); t: Riffel e Storchi-Bergmann (2011c).

das galáxias da amostra.

3.3 Redução de Dados

A redução de dados se deu através do software IRAF (Image Reduction and Analysis facility) que é composto por vários pacotes de redução e análise de dados astronômicos. O processo de redução incluiu cada um dos itens que serão discutidos a seguir.

3.3.1 Remoção da corrente de escuro

"*Dark current*" ou "corrente de escuro" é o ruído térmico registrado pela matriz do detector mesmo quando o obturador está fechado. São feitas imagens com o obturador fechado com tempo de exposição equivalente ao tempo utilizado na obtenção da imagem bruta e esse conjunto de imagens *"darks"* é combinado obtendo uma imagem média de *darks*, a qual será subtraída das demais imagens obtidas.

3.3.2 Divisão por flat-field

As fotocélulas do detector possuem uma resposta ligeiramente diferente para a mesma quantidade de radiação incidente. Imagens Flat-field (ver Fig. 3.2) são usadas para corrigir essa variação de resposta ou sensitividade pixel a pixel. Para determinar essa variação do detector são feitas exposições de uma lâmpada que o ilumina uniformemente. Uma média das imagens flat-fields é feita usando a tarefa **gemcombine**, obtendo assim uma estimativa das variações pixel a pixel da sensitividade do detector, então o flat-field médio é normalizado com a tarefa **nreduce**. Todos os demais dados são divididos pelo flat-field normalizado, eliminando assim as diferenças de resposta pixel-a-pixel.

3.3.3 Correção por distorção espacial

Para esta correção usamos uma imagem de máscara Ronchi (Ronchi mask), que faz parte das calibrações padrão do NIFS, para corrigir a distorção espacial. Para o NIFS, a máscara de Ronchi (ver Fig. 3.3) é uma rede de dispersão de transmissão localizada no plano focal do instrumento, a qual é iluminada pela lâmpada de flat-field. Dessa maneira ela produz uma distribuição uniforme de fontes compactas artificiais ao longo de cada slice. Na direção espacial, a máscara de Ronchi produz nove traços espectrais para cada slice. Cada um desses traços pode ser pensado como o traço de uma fonte pontual em uma dada posição espacial de cada slice. Ajustando-se os traços de uma fonte para todas as slices remove-se uma pequena inclinação sistemática do traço espectral (que é de $\sim$ 1 pixel de ponta a ponta) e permite uma construção mais precisa da imagem bidimensional.

3.3.4 Calibração em comprimento de onda

Para fazer esta calibração utiliza-se espectros de lâmpadas de comparação, neste caso foi usada uma lâmpada de ArXe (ver Fig. 3.4). Lâmpadas de calibração são usadas porque possuem

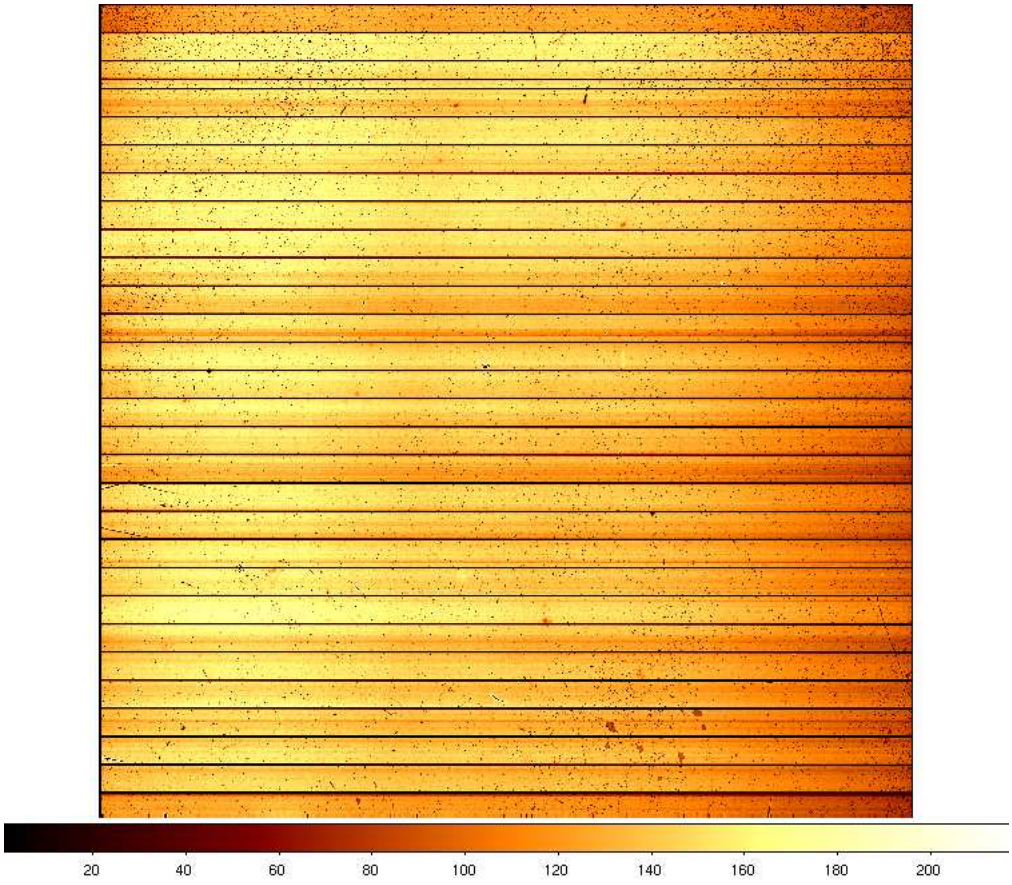

Figura 3.2: Imagem flat-field obtida com o NIFS.

um espectro de emissão cujas linhas têm de comprimentos de onda suficientemente espaçados e conhecidos. A partir de seus espectros conhecemos a relação exata entre o comprimento de onda e o pixel da imagem e por isso utiliza-se estas lâmpadas como espectros de referência.

3.3.5 Subtração do Céu

Foram realizadas observações do céu em regiões próximas ao objeto em intervalos entre as observações do mesmo. A sequência de observação para as duas bandas foi (objeto - céu - objeto - objeto - céu - objeto - objeto - céu - objeto). A subtração do céu foi realizada escolhendo-se a exposição mais próxima temporalmente de cada exposição do objeto.

3.3.6 Remoção de absorções telúricas

Foram obtidas observações de estrelas padrão telúricas. Estes espectros são usados para eliminar observações telúricas da atmosfera dividindo o espectro de ciência por um espectro normalizado da estrela padrão telúrica.

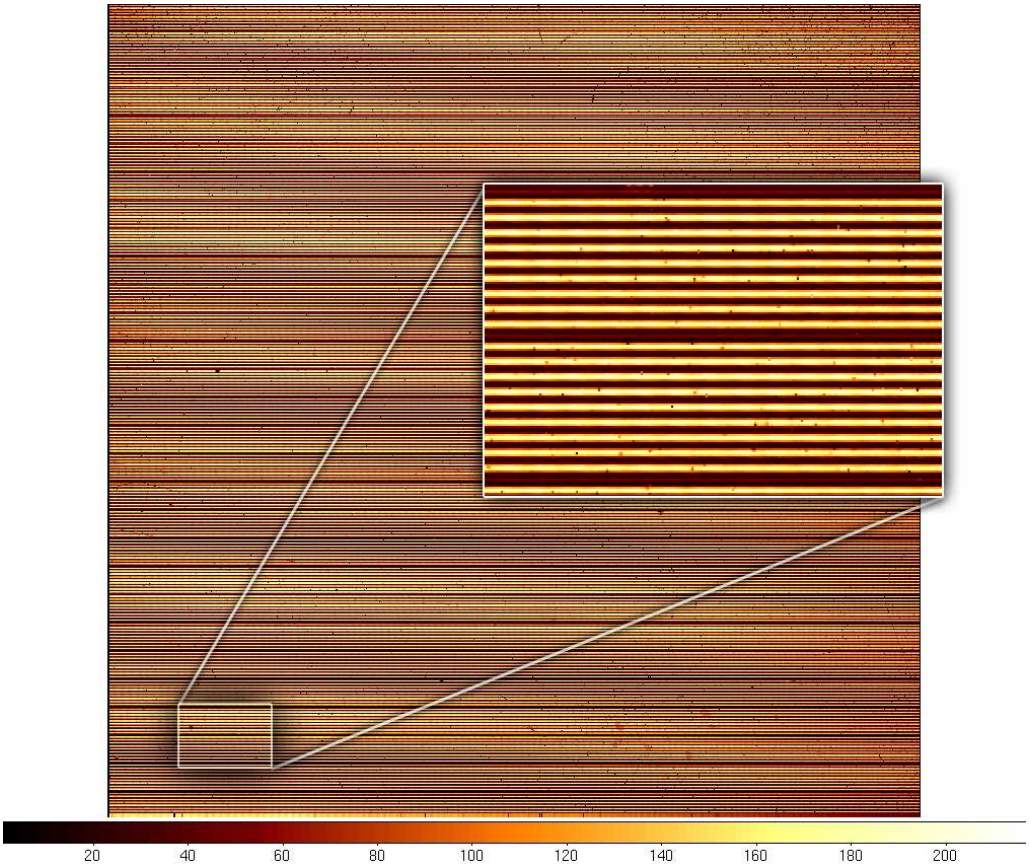

Figura 3.3: Imagem da máscara de Ronchi com detalhe para os 9 traços espectrais de fontes pontuais para cada slice.

3.3.7 Calibração em Fluxo

A calibração em fluxo consiste em converter os espectros de contagens detectadas pelo detector para unidades de fluxo. Para o infravermelho, usamos a estrela padrão telúrica e retiramos da base de dados SIMBAD (http://simbad.u-strasbg.fr/simbad/) a sua classificação espectral, e por consequência sua temperatura e sua magnitude em uma determinada banda. Tendo essas informações , criamos uma função de corpo negro que tenha o mesmo fluxo e a mesma temperatura da estrela. Esta função é usada para converter de contagens (espectro observado) a unidades de fluxo (erg s^{-1} cm^{-2} $Å^{-1}$).

3.3.8 Construção dos Cubos de Dados

Como resultado da redução obtemos 2 cubos de dados para cada galáxia, um para banda J e outro para a banda K_l.

As resoluções espectrais são obtidas através da largura a meia altura de linhas presentes na

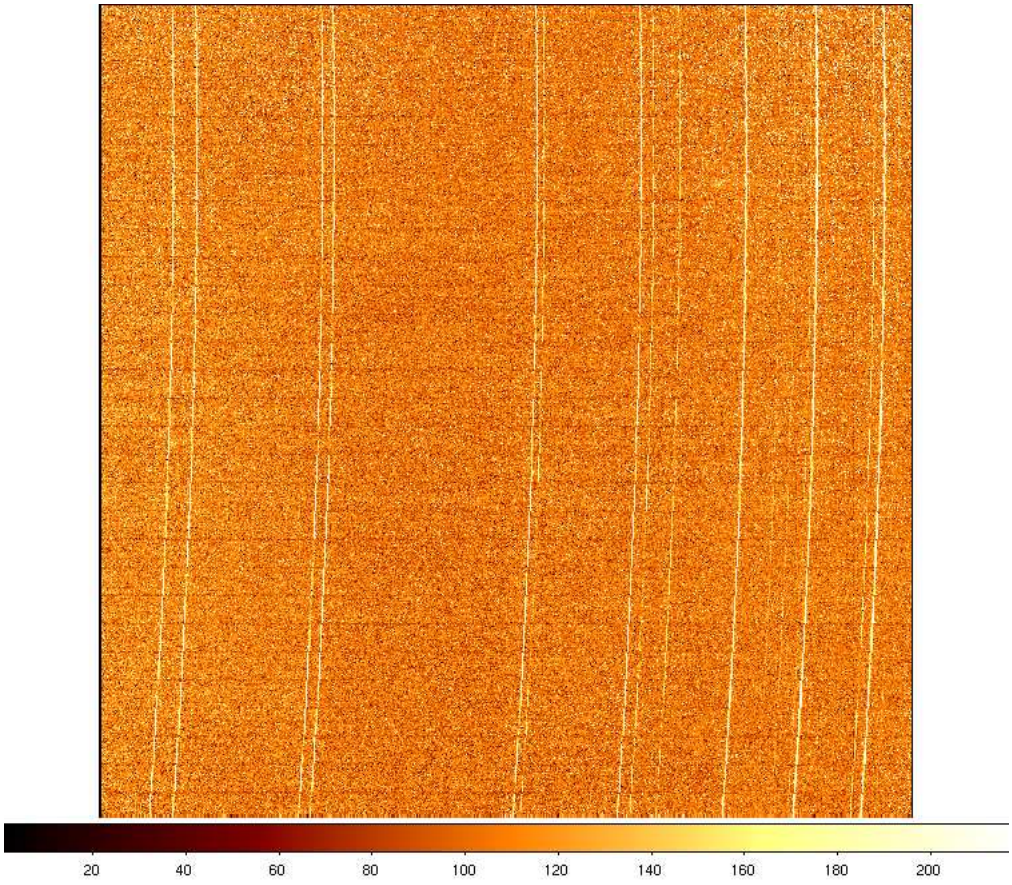

Figura 3.4: Imagem da lâmpada padrão - ArXe.

lâmpada de calibração e as resoluções espaciais a partir da largura a meia altura das distribuições espaciais de fluxo para a componente larga do Paβ para a banda J e o Brγ para a banda K_l.

Os cubos serão tornados públicos para a comunidade depois da publicação dos resultados pelo grupo.

4 *Metodologia*

Construímos mapas bidimensionais para o fluxo, velocidade radial, dispersão de velocidades, momentos de Gauss-Hermite h_3 e h_4 a partir do ajuste das principais linhas de emissão presentes nos espectros das galáxias através de Gaussianas ou séries de Gauss-Hermite.

Ajustamos os perfis das linhas de emissão do [P II]λ1.1886μm, [Si VII]λ1.2523μm, [Fe II]λ1.2570μm, Pa$\beta\lambda$1.2821μm, $H_2\lambda$2.1218μm e Br$\gamma\lambda$2.1661μm usando a rotina PROFIT (Emission-line PROfile FITting routine - Riffel (2010)). As séries de Gauss-Hermite possibilitam um melhor ajuste dos perfis quando comparado com ajustes por gaussianas, uma vez que, as curvas produzidas por séries de Gauss-Hermite podem ajustar melhor as asas dos perfis, bem como desvios simétricos em relação a uma gaussiana. Porém, como veremos na sequência desse trabalho, nem sempre as séries de Gauss-Hermite representam fisicamente o que observamos; percebemos que em alguns casos ela ajustava ruídos presentes nas proximidades da linha de emissão em questão, fazendo com que uma gaussiana fosse o melhor ajuste. Explicitamos como cada linha de emissão foi ajustada no decorrer do trabalho. Na Fig. 4.1 apresenta-se uma comparação entre séries de Gauss-Hermite com diferentes valores de h_3 e h_4 com curvas gaussianas.

4.1 Diferenciando séries de Gauss-Hermite de Gaussianas

Pode-se escrever séries de Gauss-Hermite da seguinte maneira (e.g. (van der Marel; Franx, 1993); (Gerhard, 1993); (Cappellari; Emsellem, 2004); (Riffel, 2010)):

$$GH = \frac{A\alpha(\omega)}{\sigma} \sum_{j=0}^{n} h_j H_j(\omega) \tag{4.1}$$

sendo

$$\omega \equiv \frac{\lambda - \lambda_c}{\sigma}, \tag{4.2}$$

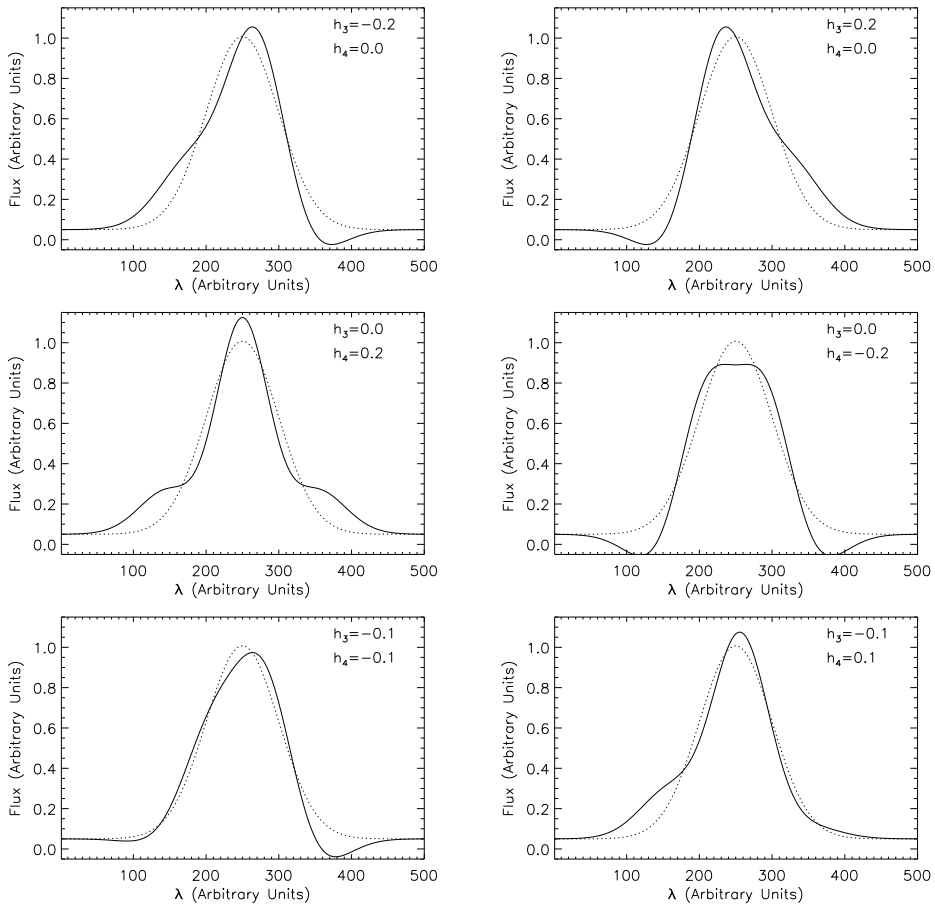

Figura 4.1: Comparação entre gaussianas (linhas pontilhadas) e séries de Gauss-Hermite (linhas contínuas) com os respectivos momentos h_3 e h_4 no canto superior direito de cada painel. Figura extraída de Riffel (2010).

e

$$\alpha(\omega) = \frac{1}{\sqrt{2\pi}} e^{-\omega^2/2}, \tag{4.3}$$

A a amplitude das séries de Gauss-Hermite, λ_c o comprimento de onda correspondente ao pico da série de Gauss-Hermite, h_j os momentos de Gauss-Hermite e $H_j(\omega)$ os polinômios de Hermite. Se o perfil da linha de emissão é similar a uma gaussiana podemos truncar a soma em $n = 4$ e assumir $h_0 = H_0(\omega) = 1$, $h_1 = h_2 = 0$ (van der Marel & Franx 1993). Essa é uma boa aproximação se a linha de emissão apresenta um perfil assimétrico assim como as asas azuis e vermelhas frequentemente observadas em linhas de emissão do gás ionizado na região de linhas estreitas de galáxias ativas (Riffel et al. 2009a, 2010; Komossa et al. 2008). Usando a aproximação acima, a Eq.(4) pode ser escrita como:

$$GH = \frac{A\alpha(\omega)}{\sigma}[1 + h_3 H_3(\omega) + h_4 H_4], \tag{4.4}$$

onde

$$H_3(\omega) = \frac{1}{\sqrt{6}}(2\sqrt{2}\omega^3 - 3\sqrt{2}\omega) \tag{4.5}$$

$$H_4(\omega) = \frac{1}{\sqrt{24}}(4\omega^4 - 12\omega^2 + 3) \tag{4.6}$$

O momento de Gauss-Hermite h_3 representa desvios assimétricos em relação a um perfil Gaussiano, tais como asas azuis ou vermelhas, enquanto o momento h_4 quantifica desvios simétricos em relação a uma gaussiana, com $h_4 > 0$ para um pico mais pontiagudo que uma gaussiana e $h_4 < 0$ para um perfil mais achatado que uma Gaussiana. Para chegarmos a uma gaussiana basta que $h_3 = h_4 = 0$.

4.2 Construção dos mapas bidimensionais

Os mapas bidimensionais para fluxos, velocidade radial, dispersão de velocidades, h_3 e h_4 foram construídos a partir dos parâmetros obtidos a partir do ajuste dos perfis das principais linhas de emissão por séries de Gauss-Hermite em todos os pixeis espaciais. Os mapas de fluxos são obtidos pela integral sob a curva de Gauss-Hermite. Os mapas de velocidades são obtidos a partir do comprimento de onda central ajustado pela equação do efeito Doppler:

$$V_p = c\,\frac{\lambda^2 - \lambda_0^2}{\lambda^2 + \lambda_0^2}, \tag{4.7}$$

sendo c o módulo da velocidade da luz no vácuo, λ_0 o comprimento de onda de repouso e λ o comprimento de onda observado. Os mapas de dispersão de velocidades e de momentos de Gauss-Hermite h_3 e h_4 foram obtidos diretamente dos parâmetros σ, h_3 e h_4 da equação (7) ajustados para cada pixel espacial.

Todos os mapas construídos são provenientes dos ajustes das funções e assumem um valor para cada pixel do mapa.

4.3 Construção dos *Channel Maps*

Os *Channel Maps* são mapas de densidade de fluxo construídos a partir de cortes ao longo dos perfis das linhas de emissão, ou seja, mapeiam o fluxo do gás em diferentes velocidades. Para a sua construção, fazemos um mapa de fluxo em um comprimento de onda que pertença ao perfil da linha, correspondente a um intervalo de velocidades δV. Escolhe-se duas faixas de contínuo ao lado do perfil (uma em cada lado) e faz-se uma média dos valores de contínuo nestas

faixas. O channel map correspondente a velocidade V será o resultado da subtração do mapa de fluxo pelo mapa do contínuo, restando assim, somente a emissão do gás em questão que possua uma velocidade V. Na Fig. 4.2, apresenta-se uma representação esquemática da construção dos *Channel Maps*, onde mostra-se três mapas de fluxo obtidos e um exemplo de espectro de onde se extrai a informação de velocidade.

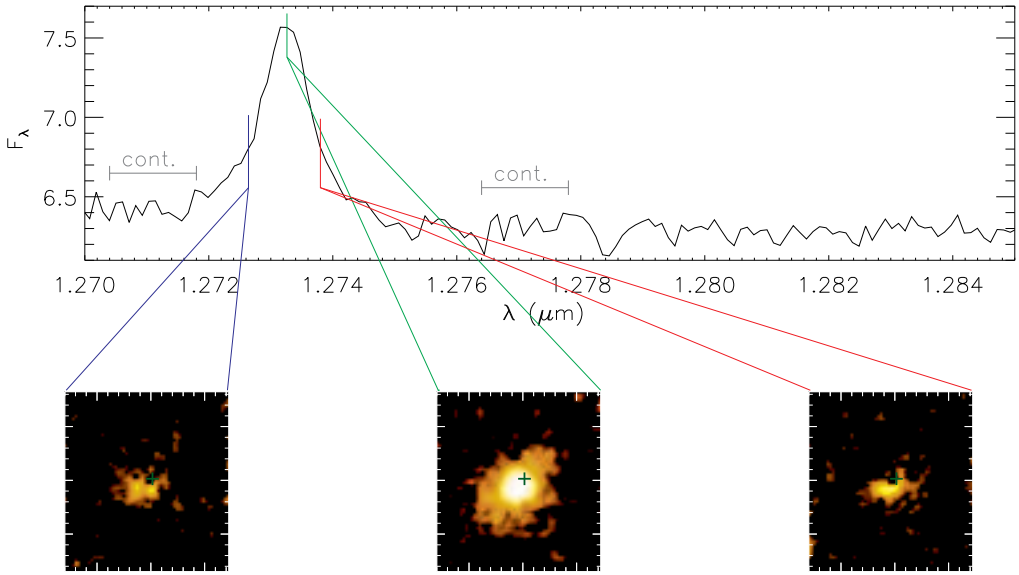

Figura 4.2: Cortes ao longo do perfil da linha do [Fe II] e seus respectivos mapas de fluxo.

4.4 Construção dos mapas de razões de fluxo

Foram contruídos mapas de razões de fluxos dividindo os mapas correspondentes: [Fe II]/Paβ, [Fe II]λ1.2570μm/[P II]λ1.8861μm e $H_2\lambda$2.1218μm/Brγ. Essas razões são importantes para estudar os mecanismos de excitação do H_2 e do [Fe II].

4.5 O modelo de rotação

Ajustamos os campos de velocidades do gás por um modelo de órbitas circulares no plano do disco sujeito a um potencial de Plummer, dado por Binney e Tremaine (1988):

$$\Phi = -\frac{GM}{\sqrt{r^2+a^2}}, \tag{4.8}$$

sendo a um comprimento de escala, r é a distância radial no plano da galáxia, M e a massa contida dentro do raio r e G é a constante gravitacional de Newton. A velocidade circular de matéria sujeita a este potencial é dada por:

$$v_c^2 = r\frac{d\Phi}{dr} = \frac{r^2 GM}{\sqrt{r^2+a^2}}. \tag{4.9}$$

Definindo as coordenadas do centro cinemático do sistema como X_0, Y_0 e assumindo que a matéria têm órbitas contidas no plano (i,Ψ_0), onde i é a inclinação do disco em relação ao plano do céu ($i = 0$ para a galáxia vista de frente e $i = 90^\circ$ para a galáxia vista de perfil) e Ψ_0 é o ângulo de posição da linha dos nodos, a velocidade radial na posição (R,Ψ), onde R é a distância radial ao núcleo projetada no plano do céu com o correspondente ângulo de posição Ψ [medido de N (0°) para E (90°)], é dada por (Barbosa et al., 2006, e.g.):

$$V_r = V_s + \sqrt{\frac{R^2 GM}{(R^2+A^2)^{3/2}}}\frac{\sin(i)\cos(\Psi-\Psi_0)}{\left(\cos^2(\Psi-\Psi_0)+\frac{\sin^2(\Psi-\Psi_0)}{\cos^2(i)}\right)^{3/4}} \tag{4.10}$$

onde V_s é a velocidade sistêmica e as relações entre e e R e entre a e A são: $r = \alpha R$ e $a = \alpha A$, sendo:

$$\alpha = \sqrt{\cos^2(\Psi-\Psi_0)+\frac{\sin^2(\Psi-\Psi_0)}{\cos^2(i)}}. \tag{4.11}$$

O modelo adotado gera curvas de isovelocidades que constituem o chamado "diagrama aranha". A equação (4.10) possui seis parâmetros livres, incluindo a posição do centro cinemático, que podem ser determinados pelo ajuste do modelo ao campo de velocidades observado. Os ajustes foram feitos utilizando um algorítimo de ajustes por mínimos quadrados não linear (Levenberg-Marquardt), no qual são dadas estimativas para os parâmetros livres. A inclinação do disco está acoplada a M pois $V_r^2 \propto M\sin(i)$ e, quando ambos os parâmetros forem livres, os valores fornecidos pelo ajuste apresentam esta degenerescência.

O modelo do campo de velocidades é feito a partir de uma série de procedimentos bem definidos e descritos abaixo:

Criamos um arquivo de texto com todas as medidas de velocidade do campo, ou seja, teremos um valor de velocidade para cada posição (X e Y) do campo (pixel-a-pixel) assim como mostra a Fig. 4.3, onde mostra-se um gráfico tridimensional com as posições em parsecs ao longo dos eixos da IFU e a velocidade está em km s^{-1} para a linha do Paβ. Esta tabela é

ajustada pela equação (4.10) usando-se o software GNUPLOT para se obter os valores dos parâmetros livres. Usa-se uma rotina em *fortran* para calcular o valor de V a partir da equação (4.10) em cada posição espacial fornecendo como entrada os parâmetros ajustados e criar uma tabela com posições (X e Y) e velocidade modelada. Finalmente, usa-se esta tabela como entrada da rotina *rtex* do IRAF para criar um arquivo *fits* com o campo de velocidades modelado.

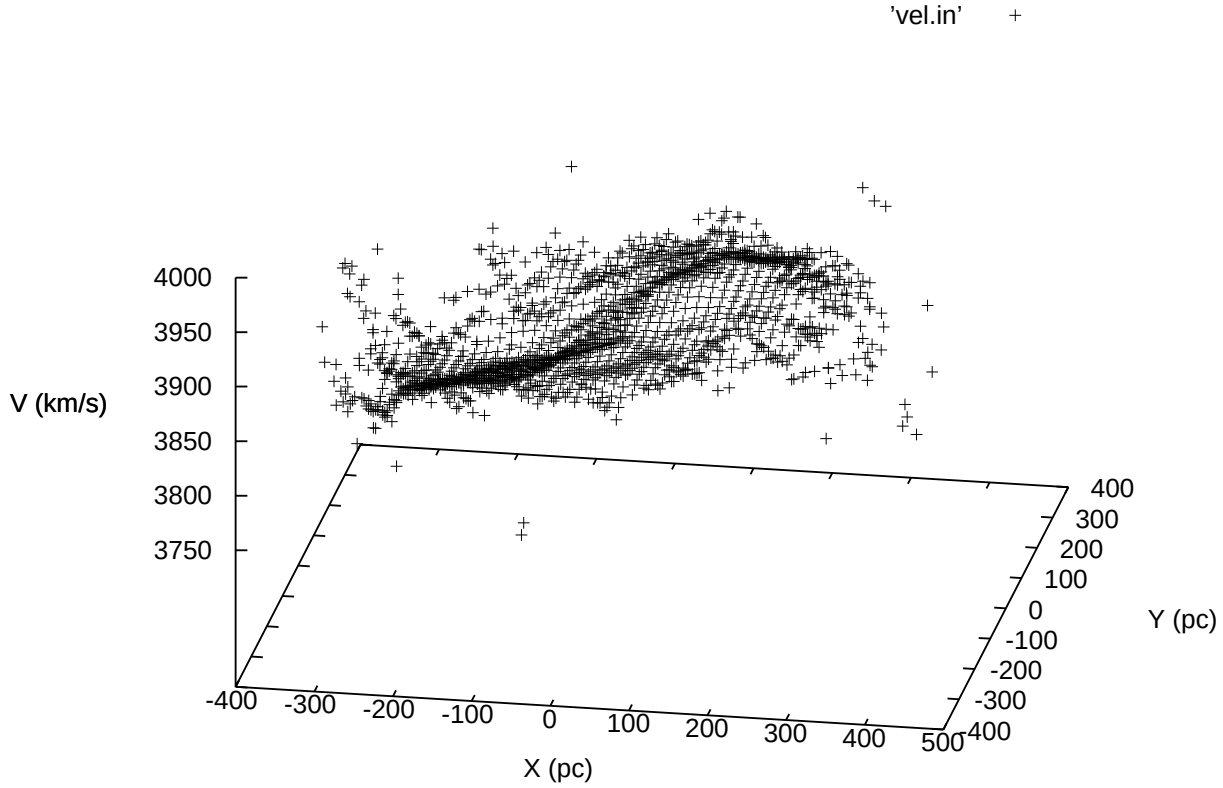

Figura 4.3: Gráfico de X por Y por V, onde X e Y são as posições em parsecs e V é a velocidade do gás no referido ponto.

4.6 Cálculos de Massas, distribuição de densidades superficiais e gradientes

A massa total de gás ionizado pode ser estimada através da equação (Scoville et al., 1982; Riffel et al., 2008; Storchi-Bergmann et al., 2009; Schönell et al., 2014, 2017):

$$M_{HII} \approx 5.1 \times 10^{16} \left(\frac{F_{Pa\beta}}{erg\,s^{-1}cm^{-2}} \right) \left(\frac{D}{Mpc} \right)^2 [M_\odot], \tag{4.12}$$

onde $F_{Pa\beta}$ é o fluxo integrado da linha de emissão $Pa\beta$ e D é a distância da galáxia. Assumimos uma temperatura eletrônica $T = 10^4 K$ e densidade eletrônica $N_e = 100\,\mathrm{cm}^{-3}$ (Osterbrock; Ferland, 2006).

A massa total de gás molecular quente pode ser obtida através de (Scoville et al., 1982):

$$M_{H_2} \approx 5.0776 \times 10^{13} \left(\frac{F_{H_2\lambda 2.1218}}{erg\,s^{-1}cm^{-2}} \right) \left(\frac{D}{Mpc} \right)^2 [M_\odot], \tag{4.13}$$

onde $F_{H_2\lambda 2.1218}$ é o fluxo da linha de emissão $H_2\lambda 2.1218\mu$m. Usamos uma temperatura vibracional $T = 2000K$ (Riffel et al., 2008, 2010; Storchi-Bergmann et al., 2009; Schönell et al., 2014, 2017).

A massa total de gás molecular frio pode ser obtida através da equação (Mazzalay et al., 2013):

$$M_{H_2\,\mathrm{cold}} \approx 1174 \left(\frac{L_{H_2\lambda 2.1218}}{L_\odot} \right), \tag{4.14}$$

onde $L_{H_2\lambda 2.1218}$ é a luminosidade da linha de emissão $H_2 2.12\mu$m.

Os mapas de distribuição de densidade superficial foram obtidos através da razão entre a massa de gás obtida pixel a pixel e a área de cada pixel em pc^2. A partir destes mapas, criamos os gradientes da distribuição de densidade superficiais de massa, através da média de quatro cortes (pseudo-fendas de 3 pixeis de largura) partindo do centro cinemático e indo ao longo do PA, PA+20°, PA+40° e PA+60°.

4.7 O código Starlight

Estudamos a população estelar das galáxias utilizando a técnica de síntese espectral, através do programa Starlight (Cid Fernandes et al., 2005) que permite obter idades e metalicidades das Single Stellar Populations (SSPs). Tal código é capaz de ajustar uma função ao espectro observado O_λ através de uma combinação de espectros de diferentes populações estelares, que fazem parte de uma base de elementos ($b_{j,\lambda}$). Essa base é utilizada pelo código que fornece, ao final da síntese, a idade, massa, metalicidade e extinção das populações estelares presentes.

O código ajustará o contínuo, linhas e bandas de absorção do espectro, se escolhermos uma

base adequada. A extinção do fluxo devido à poeira é modelada assumindo uma distribuição uniforme de poeira no meio interestelar, com lei de extinção dada por Cardelli et al. (1989). O código dá como resultado o espectro modelo M_λ composto de N_* espectros disponíveis na base de elementos, resolvendo a equação:

$$M_\lambda = M_{\lambda 0} \sum_{j=1}^{N_*} x_j b_{j,\lambda} r_\lambda \bigotimes G(v_*, \sigma_*), \tag{4.15}$$

onde $M_{\lambda 0}$ é o fluxo médio obtido em uma faixa livre de qualquer linha de absorção ou emissão; x_j (j=1...N_*) é a contribuição da j-ésima SSP da base de elementos com uma determinada idade t_j e metalicidade Z_j; $b_{j,\lambda}$ é o espectro da j-ésima população estelar normalizado em λ_0 sendo $r_\lambda = 10^{-0.4(A_\lambda - A_{\lambda 0})}$ a extinção no comprimento de onda λ; $\bigotimes$ é o operador convolução; os movimentos estelares na linha de visada são modelados por uma distribuição gaussiana $G(v_*, \sigma_*)$ centrada na velocidade v_*, com uma dispersão σ_*. Como todos os espectros de base são normalizados em λ_0, na verdade x_j corresponde à fração de luz em λ_0 devida à população j.

O melhor ajuste é obtido quando o código encontra um mínimo para χ^2, na seguinte equação:

$$\chi^2 = \sum_\lambda [(O_\lambda - M_\lambda)\omega_\lambda]^2, \tag{4.16}$$

onde $\omega_\lambda = 1/e_\lambda$ e e_λ corresponde aos erros associados ao espectro observado, sendo $\omega_\lambda = 0$ em regiões com linhas de emissão, pixeis com baixo S/N e com desvios maiores que 3σ.

De uma maneira geral, o Starlight usa uma combinação de métodos numéricos para determinar valores de massa estelar, extinção estelar (Av), idades estelares, metalicidades, σ_* e V_*. Ele busca quantificar a contribuição de cada SSP ao espectro integrado da galáxia. Para cada objeto da amostra que estamos interessados, teremos, após o processo de síntese espectral, uma lista de parâmetros e um espectro sintético resultante do ajuste ao espectro observado.

5 Resultados

O trabalho desenvolvido nesta tese resultou em 5 artigos publicados ou submetidos, incluindo o artigo da amostra (já discutido), um artigo com a cinemática estelar (que encontra-se no apêndice) e 3 outros artigos em que sou o primeiro autor. Neste capítulo apresentamos os resultados desses 3 artigos, listados a seguir.

5.1 Feeding versus feedback in AGN from near-infrared IFU observations: the case of Mrk 766

5.2 Feeding versus feedback in active galactic nuclei from near-infrared integral field spectroscopy - XII. NGC 5548

5.3 Gemini NIFS survey of feeding and feedback processes in nearby Active Galaxies: III - Gas distribution and excitation

Estes 3 artigos são apresentados a seguir.

Monthly Notices of the ROYAL ASTRONOMICAL SOCIETY

MNRAS **445,** 414–427 (2014) doi:10.1093/mnras/stu1685

Feeding versus feedback in AGN from near-infrared IFU observations: the case of Mrk 766

Astor J. Schönell Jr,[1]★ Rogemar A. Riffel,[1] Thaisa Storchi-Bergmann[2] and Claudia Winge[3]

[1]*Universidade Federal de Santa Maria, Departamento de Física, Centro de Ciências Naturais e Exatas, 97105-900, Santa Maria, RS, Brazil*
[2]*Instituto de Física, Universidade Federal do Rio Grande do Sul, Av. Bento Goncalves 9500, 91501-970 Porto Alegre, RS, Brazil*
[3]*Gemini Observatory, Southern Operations Center, c/o AURA, Casilla 603 La Serena, Chile*

Accepted 2014 August 15. Received 2014 August 15; in original form 2012 December 10

ABSTRACT

We have mapped the emission-line flux distributions and ratios as well as the gaseous kinematics of the inner 450 pc radius of the type 1 Seyfert galaxy Mrk 766 using integral field near-infrared *J*- and K_l-band spectra obtained with the Gemini Near Infrared Integral Field Spectrograph at a spatial resolution of 60 pc and velocity resolution of 40 km s^{-1}. Emission-line flux distributions in ionized and molecular gas extend up to ≈ 300 pc from the nucleus. Coronal [S IX] λ1.2523 μm line emission is resolved, being extended up to 150 pc from the nucleus. At the highest flux levels, the [Fe II] λ1.257 μm line emission is most extended to the south-east, where a radio jet has been observed. The emission-line ratios [Fe II] λ1.2570 μm/Paβ and $H_2\lambda$2.1218 μm/Brγ show a mixture of Starburst and Seyfert excitation; the Seyfert excitation dominates at the nucleus, to the north-west and in an arc-shaped region between 0.2 and 0.6 arcsec to the south-east at the location of the radio jet. A contribution from shocks at this location is supported by enhanced [Fe II]/[P II] line ratios and increased [Fe II] velocity dispersion. The gas velocity field is dominated by rotation that is more compact for H_2 than for Paβ, indicating that the molecular gas has a colder kinematics and is located in the galaxy plane. There is about 10^3 M$_\odot$ of hot H_2, implying ≈10^9 M$_\odot$ of cold molecular gas. At the location of the radio jet, we observe an increase in the [Fe II] velocity dispersion (150 km s^{-1}), as well as both blueshift and redshifts in the channel maps, supporting the presence of an outflow there. The ionized gas mass outflow rate is estimated to be ≈10 M$_\odot$ yr^{-1}, and the power of the outflow ≈0.08 $L_{\rm bol}$.

Key words: galaxies: active – galaxies: individual: Mrk 766 – galaxies: kinematics and dynamics – galaxies: nuclei – galaxies: Seyfert.

1 INTRODUCTION

The study of the extended emission in the narrow-line region (NLR) around nearby active galactic nuclei (AGN) allows the investigation of both the AGN feeding – via gas inflows (e.g. Fathi et al. 2006; Storchi-Bergmann et al. 2007; Davies et al. 2009; Müller Sánchez et al. 2009; Schnorr Müller et al. 2011) and feedback – via the interaction of the AGN radiation and mass outflow with the circumnuclear gas, affecting its kinematics and excitation (e.g. Wilson et al. 1993; Schmitt & Kinney 1996; Veilleux, Goodrich & Wilson 1997; Ferruit, Wilson & Mulchaey 2000; Veilleux, Cecil & Bland-Hawthorn 2005; Holt et al. 2006; Crenshaw & Kraemer 2007; Crenshaw et al. 2009, 2010a,b; Fischer et al. 2010, 2011; Müller-Sánchez et al. 2011).

Most studies on the feeding and feedback mechanisms of AGN presently available in the literature are based on optical observations, which are affected by dust obscuration, a problem that can be softened by the use of infrared (IR) observations. Another advantage of IR spectral region is that, besides observing ionized gas emission, we can also observe emission from molecular gas (H_2). Our group, AGN Integral Field Spectroscopy (AGNIFS), has been developing a project to map both the feeding and feedback in nearby AGN using near-infrared (NIR) integral field spectroscopic observations mostly with the instrument Near Infrared Integral Field Spectrograph (NIFS) at the Gemini North Telescope. The main findings of our group so far have been that the molecular gas – traced by *K*-band H_2 emission, and the ionized gas traced by H I recombination lines and [Fe II] emission, present distinct flux

★E-mail: juniorfisicoo@gmail.com

distributions and kinematics. Usually, the H_2 emitting gas is restricted to the plane of the galaxy, while the ionized gas extends also to high latitudes and is associated with the radio emission, when present (Riffel et al. 2006a, 2008, 2009, 2011; Storchi-Bergmann et al. 2009, 2010; Riffel, Storchi-Bergmann & Nagar 2010). The H_2 kinematics is usually dominated by rotation, including in some cases, streaming motions towards the nucleus, while the kinematics of the ionized gas, and in particular of the [Fe II] emitting gas, shows also, in many cases, a strong outflowing component associated with radio jets from the AGN. Similar results have been found using the Spectrograph for Integral Field Observations in the Near Infrared at the Very Large Telescope. Davies et al. (2009) found molecular gas inflows towards the nucleus of NGC 1097 and Müller Sánchez et al. (2009) mapped similar H_2 inflows feeding and obscuring the active nucleus of NGC 1068, while Müller-Sánchez et al. (2011) mapped outflows in ionized gas around seven AGN.

In this work, we present the gaseous distribution and kinematics of the inner 450 pc radius of the narrow-line type 1 Seyfert (Seyfert 1) galaxy Mrk 766 (NGC 4253) a barred spiral galaxy (SBa), located at a distance of 60.6 Mpc, for which 1 arcsec corresponds to 294 pc at the galaxy. The *Hubble Space Telescope* (*HST*) images of this galaxy show some irregular dust filaments around the nucleus (Malkan, Gorjian & Tam 1998). Kukula et al. (1995) show that the radio source appears to be extended to south-east (SE) in position angle (PA) $\approx$150° (on a scale of $\approx$1.0 arcsec). The optical emission is extended beyond the radio structure (González Delgado & Pérez 1996). The NIR spectrum is well described by Rodríguez-Ardila, Contini & Viegas (2005a), showing a large number of permitted lines of H I, He I, He II and Fe II, and by forbidden lines of [S II], [S III] and [Fe II]. High-ionization lines like [Si IX], [Si X], [S IX] and [Mg VIII] are also observed. The X-ray observations of this galaxy show that it is a strong variable source, with evidences of the amplitude being larger at $\approx$2 kev. The mass of the supermassive black hole has been accurately measured via reverberation mapping by Bentz et al. (2009), resulting in a mass of $1.76^{+1.56}_{-1.40} \times 10^6$ $M_\odot$. There are no CO observations for this galaxy in the literature.

Mrk 766 was selected for this study because: (i) it presents strong NIR emission lines (e.g. Rodríguez-Ardila et al. 2005a), allowing the mapping of the gaseous distribution and kinematics; and (ii) it has radio emission, allowing the investigation of the role of the radio jet (Kukula et al. 1995) in the gas excitation and kinematics. This paper is organized as follows: In Section 2, we describe the observations and data reduction procedures. The results are presented in Section 3 and discussed in Section 4. We present our conclusions in Section 5.

2 OBSERVATIONS AND DATA REDUCTION

The observations of Mrk 766 were obtained using the NIFS (McGregor et al. 2003) operating with the Gemini North Adaptive Optics system ALTAIR in 2010 June under the programme GN-2010A-Q-42, following the standard Sky-Object–Object-Sky dither sequence. Observations were obtained in the *J* band using the *J_G5603* grating and *ZJ_G0601* filter, and in the K_l band using the *K1_G5607* grating and *HK_G0603* filter.

On-source and sky position observations were both obtained with individual exposure times of 550 s. Two sets of observations with six on-source individual exposures were obtained: the first, in the *J* band, was centred at 1.25 μm and covered the spectral range 1.14 to 1.36 μm, and the second, in the K_l band, was centred at 2.3 μm and covered the spectral range 2.10 to 2.53 μm.

The data reduction procedure included trimming of the images, flat-fielding, sky subtraction, wavelength and spatial distortion calibrations. We also removed the telluric bands and flux calibrated the frames by interpolating a blackbody function to the spectrum of the telluric standard star. These procedures were executed using tasks contained in the NIFS software package which is part of GEMINI IRAF package, as well as generic IRAF tasks. In order to check our flux calibration, we extracted a nuclear spectrum with the same aperture of a previous spectrum of the galaxy by Rodríguez-Ardila et al. (2004). The two spectra are very similar to each other (considering the difference in spectral resolution), with the largest difference in flux being about 5 per cent at 2.2 μm. The final integral field unit (IFU) data cube for each band contains ~4200 spectra, with each spectrum corresponding to an angular coverage of 0.05 arcsec × 0.05 arcsec, which translates into $\approx$15 × 15 pc^2 at the galaxy and covering the inner 3 arcsec × 3 arcsec($\approx$ 900 × 900 pc^2) of the galaxy.

The full width at half-maximum (FWHM) of the arc lamp lines in the *J* band is 1.65 Å, corresponding in velocity space to 40 km s^{-1}, while in the K_l band the FWHM of the arc lamp lines is 3.45 Å, corresponding to 45 km s^{-1}. The angular resolution obtained from the FWHM of the spatial profile of the flux distribution of the broad component of the Paβ and Brγ lines and is 0.21 arcsec ± 0.03 arcsec for the *J* band and 0.19 arcsec ± 0.03 arcsec for the K_l band, corresponding to 60 and 55 pc at the galaxy, respectively.

3 RESULTS

In the top-left panel of Fig. 1, we present an optical image of Mrk 766 obtained with the Lick observatory Nickel telescope (Hunt et al. 1999). In the top-right panel, we present an optical image of Mrk 766 obtained with the *HST* Wide Field Planetary Camera 2 (WFPC2) through the filter *F606W* (Malkan et al. 1998). In the bottom panels we present, to the left, a zoom of the *HST* image within the field of view (FOV) covered by the NIFS observations and to the right an image obtained from the NIFS data cube within a continuum window centred at 2.22 μm. In Fig. 2, we present two IFU spectra integrated within a 0.25 arcsec × 0.25 arcsec aperture: one at the nucleus and the other at 0.5 arcsec east of it (Position A), chosen randomly with the purpose of just presenting a characteristic extranuclear spectrum. The nucleus was defined to be the location of the peak flux in the continuum.

We list in Table 1 the emission-line fluxes we could measure from these two spectra, which comprise 20 emission lines from the species [P II], [Fe II], He II, H I, H_2, [S IX] and [Ca VIII]. They were measured with the *splot* task in IRAF and the uncertainties were estimated as the standard deviation of the average of six measurements.

3.1 Emission-line flux distributions

In order to map the flux distributions as well as the centroid velocity and velocity dispersion fields, we used the PROFIT routine (Riffel 2010) to fit the profiles of [P II] λ1.1886 μm, [S IX] λ1.2523 μm, [Fe II] λ1.2570 μm, Paβλ1.2822 μm, H_2λ2.1218 μm and Brγλ2.1661 μm emission lines at each pixel over the whole FOV. These emission lines were chosen because they have the highest signal-to-noise ratio (S/N) among their species (coronal, ionized and molecular gas). The flux values (as well as those of the central wavelength and width of the profile, see next sections) were obtained by the fit of the profiles using both Gaussian and Gauss–Hermite (GH) series. We found out that the latter gave better fits to most lines, except for the [S IX] line, for which the GH

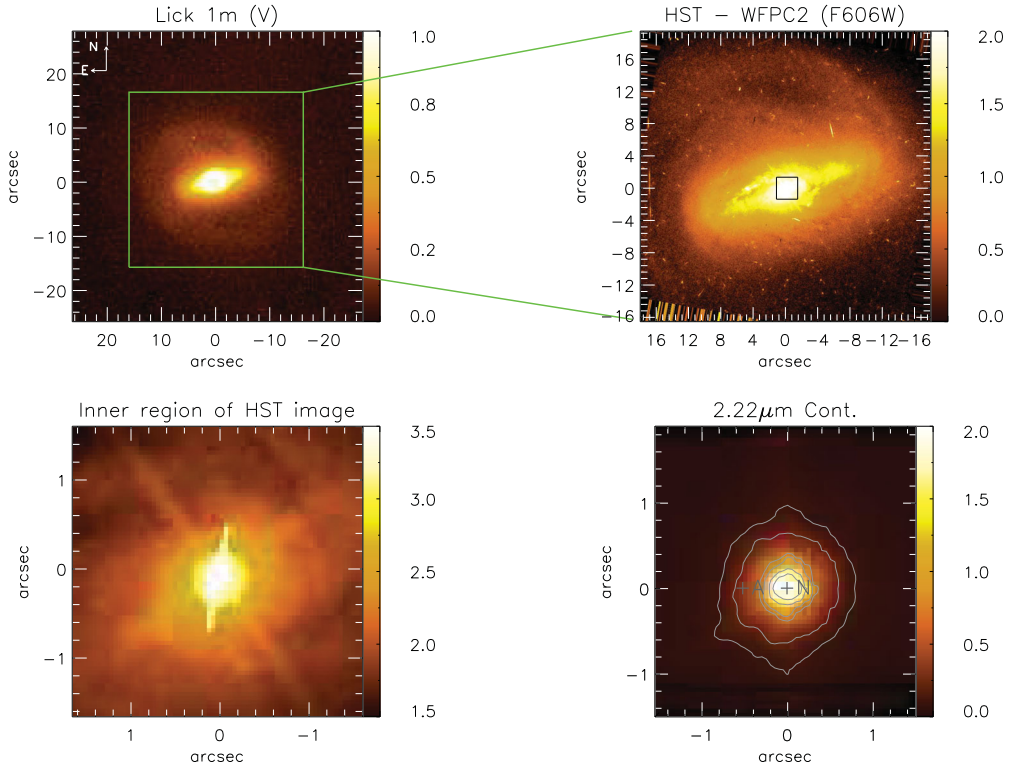

Figure 1. Top-left panel: Lick 1 m telescope *V*-band image of Mrk 766 (Hunt et al. 1999) in arbitrary flux units. Top-right panel: *HST*-WFPC2 continuum image of Mrk 766 obtained through the filter *F*606*W* (Malkan et al. 1998). Bottom-left panel: zoom of the inner 3.0 arcsec × 3.0 arcsec of the *HST*-WFPC2 image. The colour bars for the *HST* images show the flux in arbitrary units. Bottom-right panel: 2.22 μm continuum image obtained from the NIFS data cube with fluxes shown in units of 10^{-17} erg s^{-1} cm^{-2}. The position angle of the major axis of the galaxy is PA = 73° and the bar is oriented along PA = 105°. The box in the *HST* image shows the NIFS FOV. The labels A and N mark the position where the spectra of Fig. 2 have been extracted.

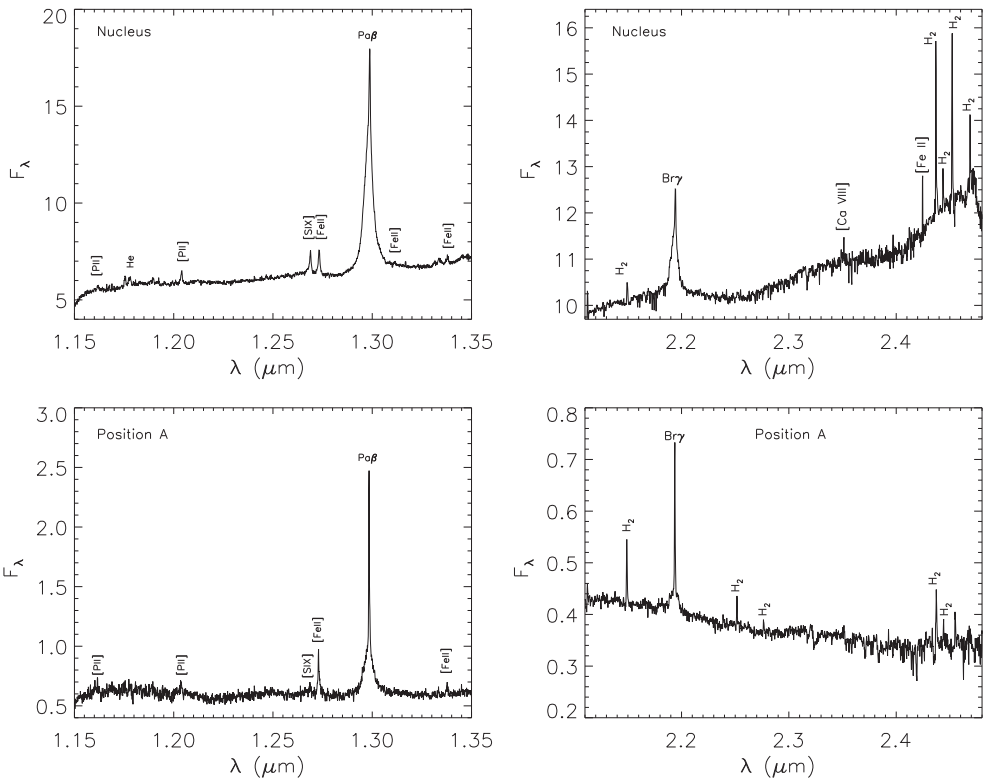

Figure 2. Spectra obtained within a 0.25 arcsec × 0.25 arcsec aperture centred at the nucleus and at 0.5 arcsec east from it (Position A, marked in Fig. 1). The flux is in 10^{-17} erg s^{-1} cm^{-2} Å^{-1} units.

Table 1. Measured emission-line fluxes (in units of 10^{-16} erg s^{-1} cm^{-2}) for the two positions identified in Fig. 1.

λ_{vac}(μm)	ID	Nucleus F(10^{-16} erg s^{-1} cm^{-2})	Position A F(10^{-16} erg s^{-1} cm^{-2})
1.18861	[P II]$^1D_2 - {}^3P_2$	4.89 ± 0.2	–
1.25235	[S IX]$^3P_1 - {}^3P_2$	10.45 ± 0.6	0.39 ± 0.05
1.25702	[Fe II]$a^4D_{7/2} - a^6D_{9/2}$	12.98 ± 0.6	2.59 ± 0.2
1.28216	H I Paβ(narrow)	34.1 ± 2	6.39 ± 0.82
1.28216	H I Paβ(broad)	421.7 ± 20	6.39 ± 0.82
1.32092	[Fe II]$a^4D_{7/2} - a^6D_{7/2}$	1.28 ± 0.1	0.51 ± 0.03
2.12183	H_2 1-0S(1)	5.66 ± 0.03	1.21 ± 0.17
2.15420	H_2 2-1S(2)	–	–
2.16612	H I Brγ(narrow)	8.46 ± 0.3	2.21 ± 0.45
2.16612	H I Brγ(broad)	90.0 ± 4	2.21 ± 0.45
2.18911	He II 10-7	1.96 ± 0.12	–
2.22344	H_2 1-0 S(0)	–	0.41 ± 0.09
2.24776	H_2 2-1 S(1)	–	0.25 ± 0.02
2.32204	[Ca VIII]$^2P^0_{3/2} - {}^2P^0_{1/2}$	1.56 ± 0.80	–
2.36760	[Fe II]$a^4G_{9/2} - a^4H_{9/2}$	52.2 ± 0.83	–
2.39396	[Fe II]$b^4D_{7/2} - a^2F_{7/2}$	10.6 ± 1.76	–
2.40847	H_2 1-0 Q(1)	23.70 ± 2.24	1.02 ± 0.19
2.41367	H_2 1-0 Q(2)	22.6 ± 1.30	0.32 ± 0.02
2.42180	H_2 1-0 Q(3)	36.70 ± 2.01	–
2.43697	H_2 1-0 Q(4)	75.7 ± 1.12	–

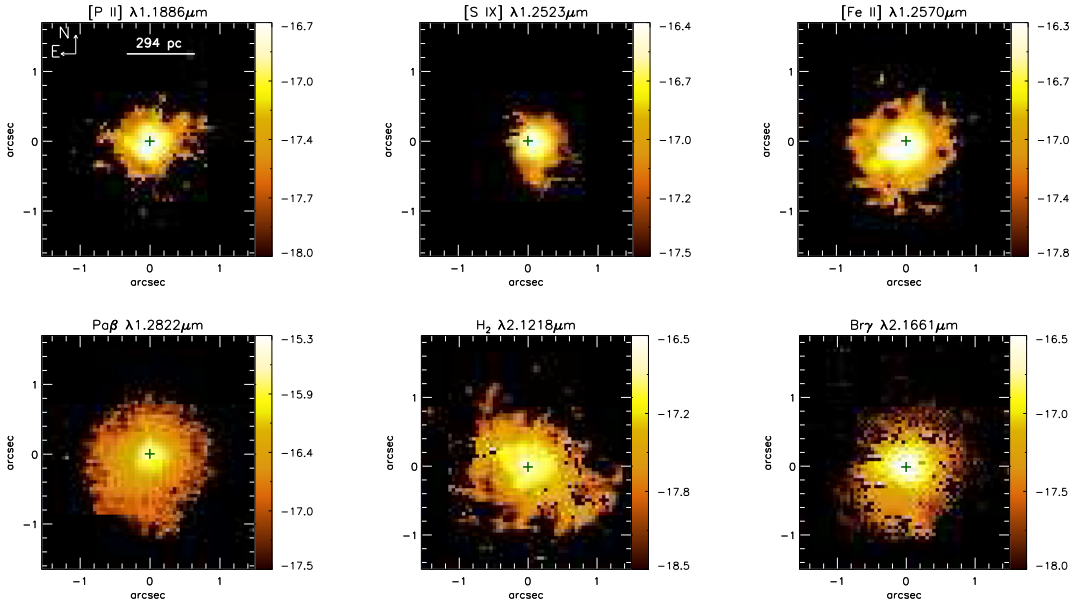

Figure 3. Emission-line flux distributions. Flux levels are shown according to the colour bar in logarithmic units (erg s^{-1} cm^{-2}).

fits introduced extra wings in some regions where the line was weak. We decided then to adopt the paramenters of the fit obtained from the GH for all lines except for [S IX], for which we adopted the fit with Gaussians. In the case of Paβ and Brγ, we have also fitted a broad component to the line. This was done via a modification of the *profit* routine to fit the broad component and subtract its contribution from the profiles in order to generate a data cube only with the narrow component. The steps in this procedure were: (i) fit only one Gaussian to the broad component; (ii) subtract it from the spectra where it is present, and (iii) fit the narrow component.

In Fig. 3, we present the resulting flux distribution maps, where we have masked out the bad fits by using the χ^2 map, which is an output from the *profit* routine. All maps have their peak fluxes at the same position, which also coincides with that of the peak of the continuum: the nucleus.

The [P II] and [S IX] flux distributions are the most compact, reaching about 0.5 arcsec from the nucleus in all directions in the case of the former, and being more extended to the south-west in the case of the latter. Another coronal line (not shown in the figure), [Ca VIII] λ2.3220 μm, also shows a similarly compact flux distribution, indicating that the coronal line region is compact but resolved, extending up to 150 pc from the nucleus, what is a typical radius for this region (e.g. Rodríguez-Ardila et al. 2006; Storchi-Bergmann et al. 2009; Mazzalay, Rodríguez-Ardila & Komossa 2010; Riffel et al. 2011).

The highest levels of the [P II] flux distribution are more elongated towards the SE. This elongation is also observed in the [Fe II] emission, which reaches 0.8 arcsec (240 pc) from the nucleus in that direction. The Paβ flux distribution is the most extended in all directions, reaching up to 1 arcsec from the nucleus. The Brγ flux distribution is very similar to that of Paβ, although noisier due to its lower flux. The H_2 flux distribution is somewhat distinct, being elongated from north-east to south-west, thus approximately perpendicular to the elongation of the [Fe II] flux distribution, reaching 1.5 arcsec (440 pc) from the nucleus towards the south-west.

3.2 Emission-line ratios

In Fig. 4, we present line-ratio maps obtained from the flux maps, where regions with bad fits were masked out. The average uncertainties in the line-ratio values are ≈10 per cent. In the left-hand panel, we present the [Fe II] λ 1.2570 μm/Paβ ratio map, which can be used to investigate the excitation mechanism of [Fe II] (e.g. Rodríguez-Ardila et al. 2004; Rodríguez-Ardila, Riffel & Pastoriza 2005b; Storchi-Bergmann et al. 2009; Riffel et al. 2011). The values of [Fe II]/Paβ for Mrk 766 range from 0.2 (most locations) to 1.0 with the highest values – between 0.6 and 1 – being observed between 0.2 and 0.6 arcsec to the SE of the nucleus. Another line ratio that can be used to investigate the [Fe II] excitation mechanism is [Fe II] λ1.2570 μm/[P II] λ1.8861 μm. Values larger than 2 indicate that shocks have passed through the gas destroying the dust grains, releasing the Fe and enhancing its abundance and emission (e.g. Oliva et al. 2001; Storchi-Bergmann et al. 2009; Riffel et al. 2010, 2011). We present this ratio map in the central panel of Fig. 4. The lowest values, (≤2), are observed to the north and north-west of the nucleus while the highest values of ≈7.0 are observed in a narrow strip at ≈0.6 arcsec to the SE of the nucleus, approximately at the border of the region with the highest values of [Fe II]/Paβ.

In the right-hand panel of Fig. 4, we present the H_2λ2.1218 μm/Brγ ratio map, which is useful to investigate the excitation of the H_2 emission line (e.g. Rodríguez-Ardila et al. 2004, 2005b; Riffel, Rodríguez-Ardila & Pastoriza 2006b; Riffel et al. 2008, 2009; Storchi-Bergmann et al. 2009). In Mrk 766, the values of this ratio range from 0.2 to 2.0. The lowest values are observed at the nucleus and in most regions to the south and SE, except for the region between 0.2 and 0.6 arcsec to the SE where the values increase to ≈0.8 (where both [Fe II]/Paβ and [Fe II]/[P II] show larger values). Such increased values are also observed to the north where they reach ≈1.25. At approximately 1 arcsec to the south-west, the values reach up to ≈2, although the fit of the lines is not so good and the uncertainty is high there.

3.3 Gas kinematics

The *profit* routine (Riffel 2010) that we have used to obtain the flux of the emission lines, provide also the centroid velocity (V), velocity dispersion (σ) and higher order GH moments (h_3 and h_4), which have been used to map the gas kinematics. In Fig. 5, we present the centroid velocity fields after subtraction of the heliocentric systemic velocity of $3853 \pm 17\,\mathrm{km\,s^{-1}}$, which was obtained through a model fitted to the Paβ velocity field, as discussed in Section 4.3. The uncertainties in the velocity maps range from 5 to $20\,\mathrm{km\,s^{-1}}$ depending on the S/N of the spectra (which decrease from the centre towards the border of the mapped region). The white regions in the figures represent locations where the S/N was not high enough to allow the fitting of the line profiles. All velocity fields show blueshifts to the east (left in the figures) and redshifts to the west, with the line of nodes oriented at a position angle (PA) of approximately 80° (see Section 4.3), with the isovelocity lines showing an approximate 'spider diagram' characteristic of rotation.

Fig. 6 shows the velocity dispersion maps corresponding to the centroid velocity maps of Fig. 5. As in the case of the centroid velocities, the uncertainties in the velocity dispersion maps range from 5 to $20\,\mathrm{km\,s^{-1}}$ depending on the S/N of the spectra. The white regions in the figures represent locations where the S/N was not high enough to allow the fitting of the line profiles. The [Fe II] σ map shows the highest values of up to $150\,\mathrm{km\,s^{-1}}$ to the SE of the nucleus and lowest values, down to $75\,\mathrm{km\,s^{-1}}$, to the north-west. The [P II] σ map has medium values with soft deviations. The Paβ σ map shows high values at the nucleus and also 0.4 arcsec to the south and 0.6 arcsec to the north and lower values to the east, south and west of this central region. The higher values at the nuclear region may be due to residual contamination from the broad component of the line. The H_2 emitting gas presents the lowest σ values, which are smaller than $70\,\mathrm{km\,s^{-1}}$ at most locations. We do not show the h_3 and h_4 maps because their values are low and do not present any systematic behaviour.

3.4 Channel maps

Channel maps along the emission-line profiles are shown in Figs 7–10 for the [S IX], [Fe II], Paβ and H_2 emission lines, respectively. Each panel presents the flux distribution in logarithmic units

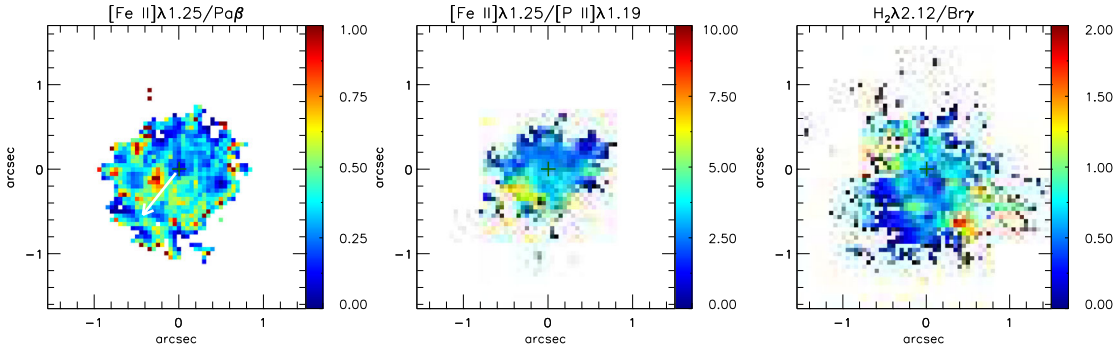

Figure 4. Emission-line ratio maps. In the left-hand panel, we show the [Fe II] λ1.2570 μm/Paβ ratio map, in the central panel the [Fe II] λ1.2570 μm/[P II] λ1.8861 μm ratio map and in the right-hand panel the H_2λ2.1218 μm/Brγ ratio map. The central cross marks the position of the nucleus. The white arrow in [Fe II]/Paβ panel shows the extent of the radio structure (Kukula et al. 1995).

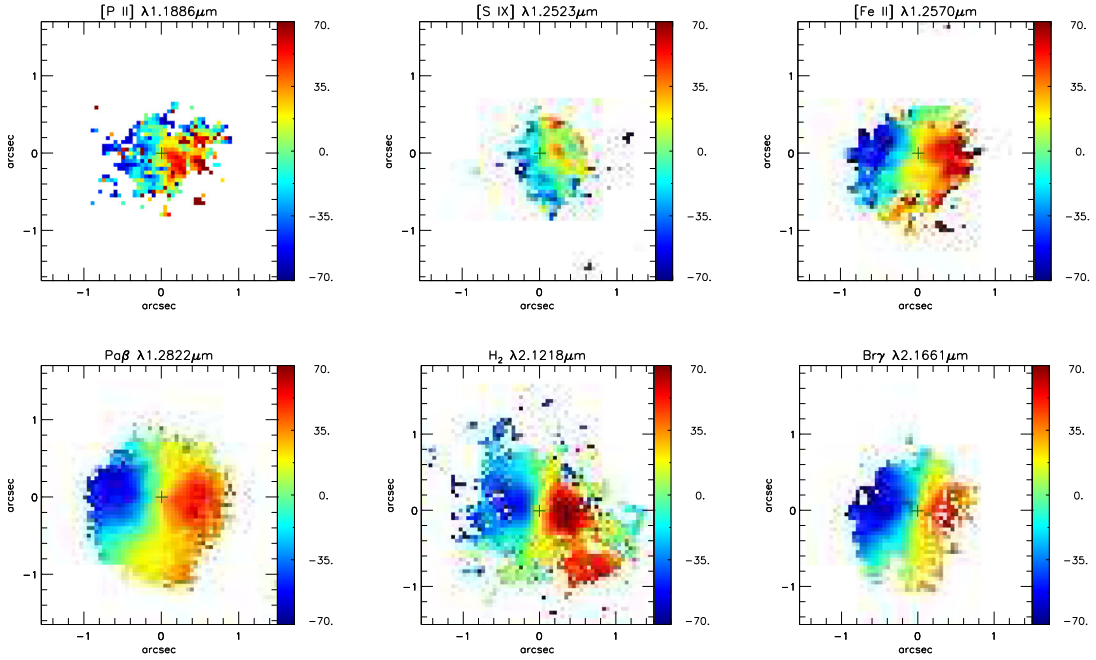

Figure 5. Centroid velocity field for the [P II] λ1.1886 μm (top left), [S IX] λ1.2523 μm (top middle), [Fe II] λ1.2570 μm (top right), Paβ (bottom left), $H_2\lambda$2.1218 μm (bottom middle) and Brγ (bottom right) emitting gas. The central cross marks the position of the nucleus. The colour bar shows the velocities in units of km s^{-1}.

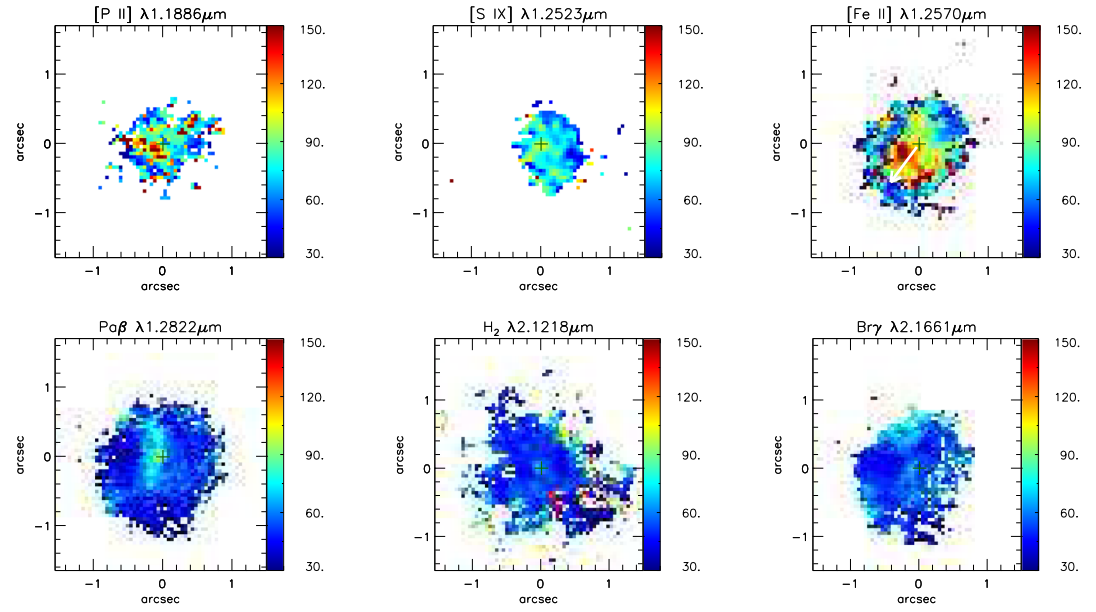

Figure 6. σ maps for the same emission lines of Fig. 5. The central cross marks the position of the nucleus. The colour bars show the σ values in units of km s^{-1}. The white arrow in [Fe II] panel shows the extent of the radio structure (Kukula et al. 1995).

integrated in velocity bins centred at the velocity shown in the top-left corner of each panel (relative to the systemic velocity of the galaxy). The central cross marks the position of the nucleus. We do not show channel maps for [P II] and Brγ because the [P II] maps are similar to those of [Fe II] and those for Brγ are similar to those of Paβ but noisier.

In Fig. 7, the channel maps along the [S IX] emission-line profile show the flux distributions integrated within velocity bins of 25 km s^{-1} (corresponding to one spectral pixel). At the highest velocities the emission is extended 0.5 arcsec to the south/south-west, and at the lowest velocities, the [S IX] is concentrated in the nucleus.

In Fig. 8, the channel maps along the [Fe II] emission-line profile show the flux distributions integrated within velocity bins of 105 km s^{-1} (corresponding to three spectral pixels) for the highest velocities and 50 km s^{-1} for the central panels (corresponding to two spectral pixels). All [Fe II] channel maps present flux distributions which are elongated towards the SE, up to ≈0.9 arcsec (270 pc)

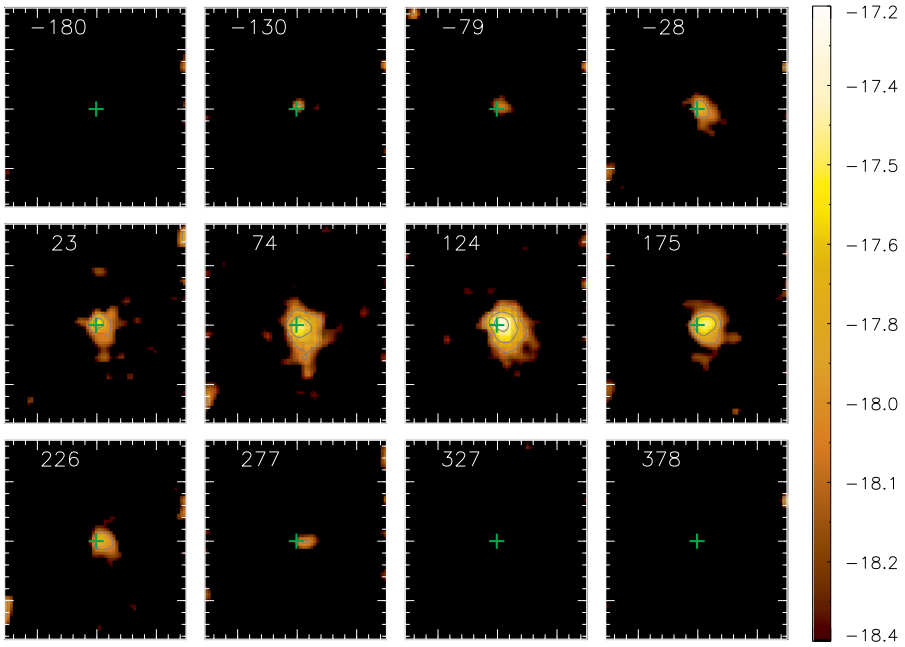

Figure 7. Channel maps along the [S IX] emission-line profile, centred at the velocity shown in the upper-left corner of each panel in km s^{-1}. The long tick marks are separated by 1 arcsec and the cross marks the position of the nucleus.

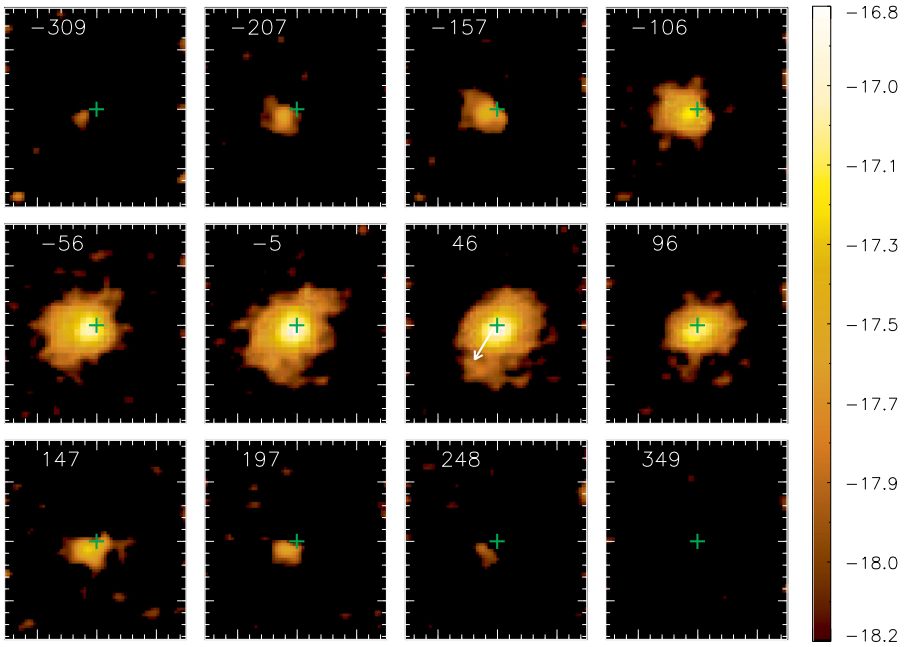

Figure 8. Channel maps along [Fe II] emission-line profile. Description as in Fig. 7, with a white arrow showing the extent of the radio structure (Kukula et al. 1995).

from the nucleus. Both the highest blueshifts and highest redshifts, which reach 250 km s^{-1}, are also observed to the SE of the nucleus.

Fig. 9 shows the channel maps for the Paβ emitting gas for the same velocity bins as for [Fe II]. The highest blueshifts and redshifts are observed mostly at the nucleus, but are probably due to residuals of a broad component to the line which was fitted and subtracted. The flux distributions are more extended and more symmetrically distributed around the nucleus than those of the [Fe II] channel maps.

Fig. 10 shows the channel maps for the H_2 emitting gas, for velocity bins of 30 km s^{-1}. The highest blueshifts and redshifts, reaching $\approx$130 km s^{-1}, are observed to the north-east and south-west of the nucleus, respectively, following the line of nodes of the

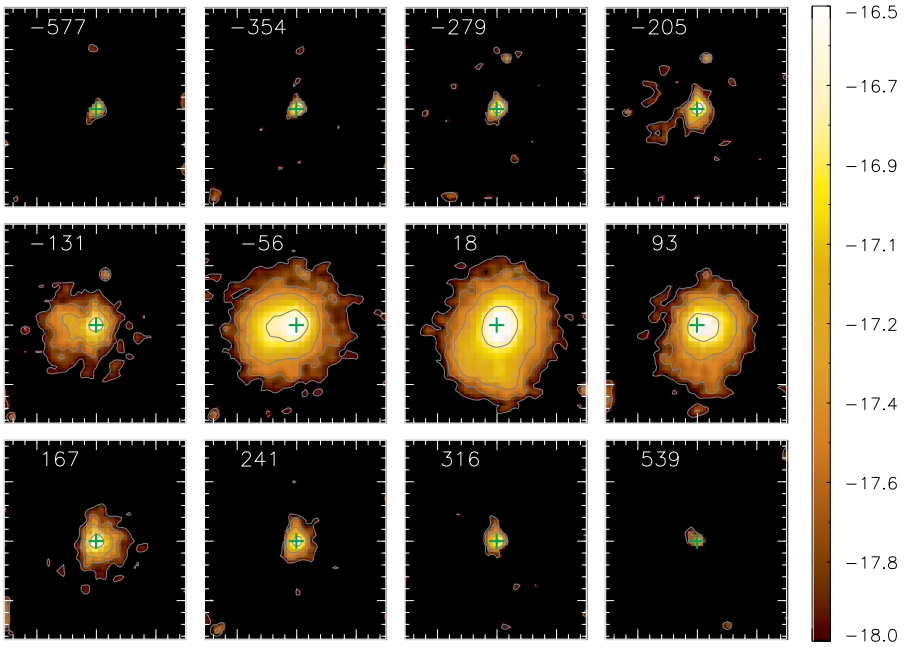

Figure 9. Channel maps along Paβ emission-line profile. Description as in Fig. 7.

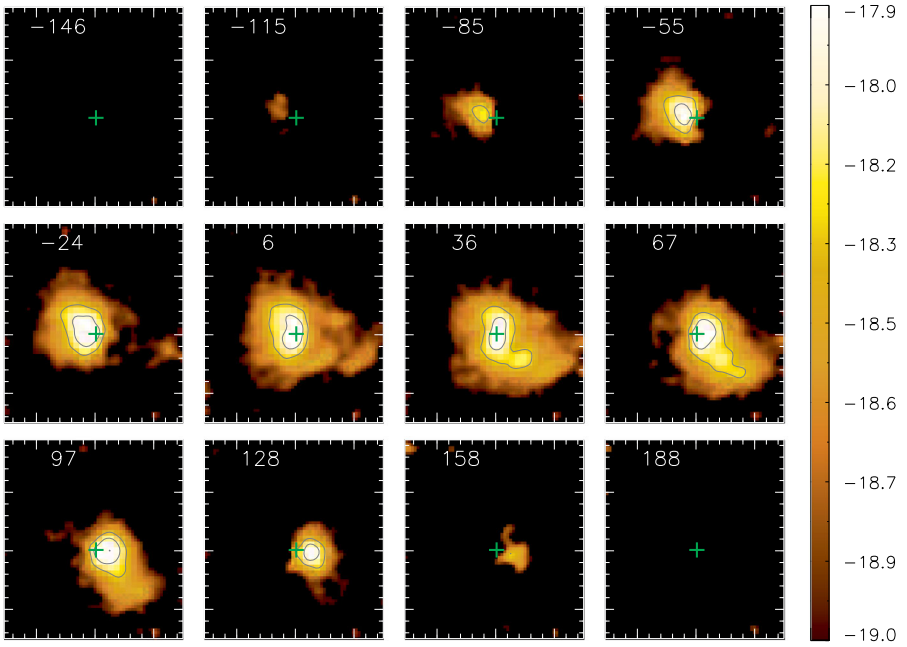

Figure 10. Channel maps along H_2 emission-line profile. Description as in Fig. 7.

galaxy, as seen in Fig. 5. For zero and positive velocities there is a structure extending from the nucleus to the south-west.

4 DISCUSSION

4.1 Gaseous excitation

4.1.1 Diagnostic diagram

In order to further map the excitation of the circumnuclear line-emitting region, we constructed a spectral diagnostic diagram with the ratios [Fe II] λ1.2570 µm/*Pa*β versus $H_2\lambda$2.1218 µm/Brγ (Larkin et al. 1998; Rodríguez-Ardila et al. 2004, 2005b; Riffel et al. 2010), shown in Fig. 11. Typical values for the nuclei of Seyfert galaxies range between 0.6 and 2.0 for both ratios (Rodríguez-Ardila et al. 2005b), while for Starbursts the values are smaller than 0.6 and for low-ionization nuclear emission-line regions (LINERs) the values are larger than 2, as shown in the top panel of Fig. 11. In this figure, the black filled circles represent Seyfert ratios, the blue open circles Starbursts ratios and red crosses represent ratios of LINERs. Most ratios present Starburst and Seyfert values, with a few LINER values. The locations from where the distinct line ratios

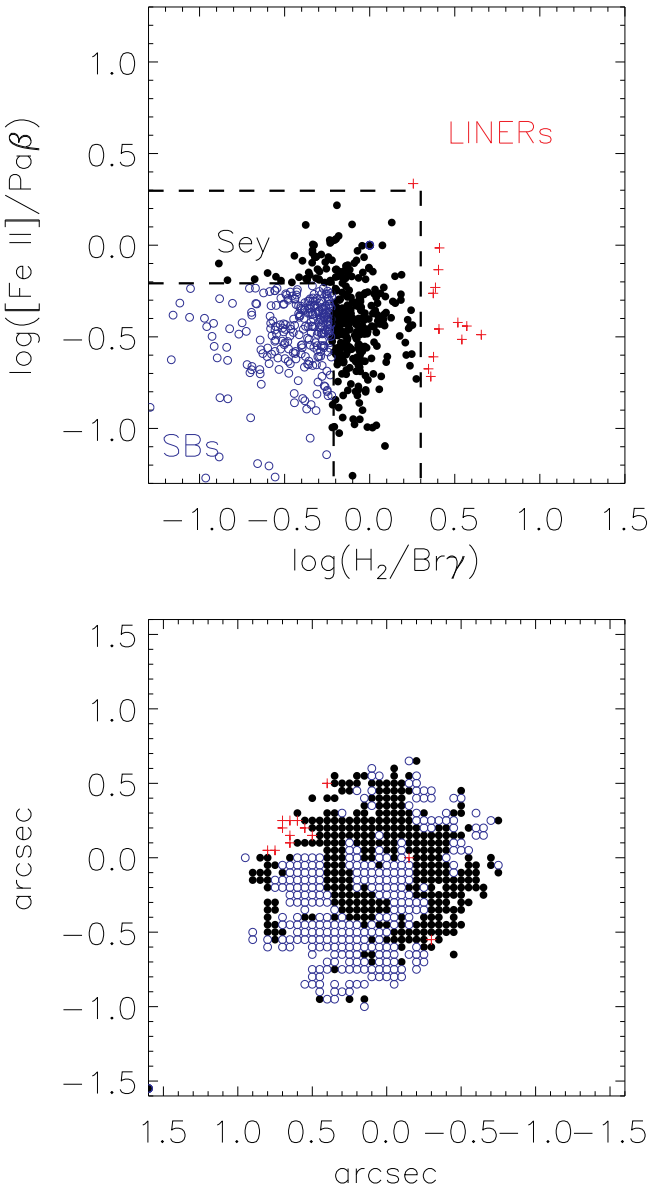

Figure 11. Top panel: [Fe II] λ1.25 μm/Paβ versus H_2λ2.12 μm/Brγ line-ratio diagnostic diagram. The dashed lines delimit regions with ratios typical of Starbursts (blue open circles), Seyferts (black filled circles) and LINERS (red crosses). Bottom panel: spatial position of each point from the diagnostic diagram.

originate are shown in the bottom panel of Fig. 11. Seyfert ratios are found at the nucleus, in most regions to the north and between 0.2 and 0.6 arcsec to the SE. In a few locations to the north of the nucleus, between the nucleus and the region of enhanced ratios (at 0.2–0.6 arcsec) and beyond this region, Starburst ratios are found. LINER ratios are only found at the south-west border of the mapped region.

4.1.2 *The* H_2 *emission*

The excitation of warm H_2 has been the subject of many previous studies (e.g. Black & van Dishoeck 1987; Hollenbach & McKee 1989; Storchi-Bergmann et al. 1999, 2009; Reunanem, Kotilainem & Prieto 2002; Rodríguez-Ardila et al. 2004; Davies et al. 2005; Rodríguez-Ardila et al. 2005b; Riffel, Rodríguez-Ardila & Pastoriza 2006b; Riffel et al. 2008, 2009, 2010; Guillard et al. 2010; Mazzalay et al. 2013; Riffel, Storchi-Bergmann & Winge 2013). Summarizing, these studies have shown that the H_2 emission lines can be excited by two mechanisms: (i) fluorescent excitation through absorption of soft-UV photons (912–1108 Å) in the Lyman and Werner bands (Black & van Dishoeck 1987) and (ii) collisional excitation due to heating of the gas by shocks, in the interaction of a radio jet with the interstellar medium (Hollenbach & McKee 1989) or heating by X-rays from the central AGN (Maloney, Hollenbach & Tielens 1996). The second mechanism is usually referred to as thermal process since it involves the local heating of the emitting gas, while the first is usually called a non-thermal process. Previous studies have verified that non-thermal processes are not important for most galaxies studied so far (e.g. Rodríguez-Ardila et al. 2004, 2005b; Riffel et al. 2010).

In the case of Mrk 766, the H_2/Brγ ratio (Fig. 4) is larger than 0.6 to the north-east of the nucleus and in the arc-shaped region between 0.2 and 0.5 arcsec to the SE supporting Seyfert excitation there. The origin of the H_2 excitation could be fluorescence or thermal excitation. One possible evidence for fluorescence (a non-thermal process) is a ratio between the H_2 lines 2.24/2.12 μm higher than 0.6 (Storchi-Bergmann et al. 2009). We could measure this ratio at position A, where the value is ∼0.2, favouring thermal excitation. At a number of other positions, the 2.24 μm line is fainter, but wherever it could be measured, the line ratio is smaller than 0.2. This line ratio thus seems to favour thermal excitation due to heating by X-rays or shocks from a radio jet (which seems to be present to the SE) in the region with 'Seyfert excitation', although there is no clear signature of shocks such as an increase in velocity dispersion as observed in the [Fe II] emission.

In the remaining regions, the H_2/Brγ ratio is smaller than 0.6, supporting starburst excitation via heating from shocks in supernovae (SNe) winds and/or by UV radiation from young stars. The presence of starbursts in the nuclear region is in agreement with the results of Rodríguez-Ardila & Viegas (2003), who reported the observation of the polycyclic aromatic hydrocarbon 3.3 μm feature in the IR spectrum of Mrk 766 within the inner 150 pc, suggesting the presence of recent star formation there. The mixed Seyfert and Starburst excitation is also seen in the diagnostic diagram of Fig. 11.

4.1.3 *The [Fe II] emission*

Using the [Fe II] λ1.2570 μm/*Paβ* and [Fe II] λ1.2570 μm/[P II] λ1.8861 μm line-ratio maps shown in Fig. 4, we can investigate the excitation mechanism of [Fe II]. The first ratio [Fe II] λ1.2570 μm/*Paβ* is controlled by the ratio between the volumes of partially to fully ionized gas regions, as the [Fe II] emission is excited in partially ionized gas regions. In AGNs, such regions can be created by X-ray (e.g. Simpson et al. 1996) and/or shock (e.g. Forbes & Ward 1993) heating of the gas. For Starburst galaxies, [Fe II]/Paβ ≤ 0.6 and for SNe for which shocks are the main excitation mechanism, this ratio is larger than 2 (Rodríguez-Ardila et al. 2004, 2005b).

The values of [Fe II]/Paβ range from ≈0.2 to the north-west to ≈1.0 in the arc-shaped region between 0.2 and 0.6 arcsec to the SE of the nucleus. Kukula et al. (1995) have obtained a 3.6 cm radio image of Mrk 766 and found an extended emission to the SE, at the location of the arc-shaped region where there is an enhancement of the [Fe II]/Paβ ratio. The variation of this line ratio, and its correlation with the radio structure suggest that excitation by shocks from the

radio jet is indeed important at this location. On the other hand, we cannot rule out the possible contribution from SNe as well.

The above conclusion is also supported by the [Fe II] λ1.2570 μm/[P II] λ1.1886 μm line-ratio map (central panel of Fig. 4). These two lines have similar ionization temperatures, and their parent ions have similar ionization potentials and relative recombination coefficients. Values larger than 2 indicate that the shocks have passed through the gas destroying the dust grains, releasing the Fe and enhancing its abundance and thus emission (Oliva et al. 2001; Storchi-Bergmann et al. 2009; Riffel et al. 2010). For SNe remnants, where shocks are the dominant excitation mechanism, [Fe II]/[P II] is typically higher than 20 (Oliva et al. 2001). For Mrk 766, to the SE of the nucleus, where there is the radio structure, [Fe II]/[P II] values reach ≈10 (Fig. 4), suggesting that shocks are indeed important in agreement with the highest values obtained for the [Fe II]/Paβ at the same locations. In other regions, typical values are [Fe II]/[P II] ≤ 2, indicating almost no contribution from shocks.

Finally, the diagnostic diagram of Fig. 11 confirms Seyfert excitation in the nucleus and in the SE arc and regions surrounding the nucleus and non-Seyfert values in the other regions. And the low [Fe II]/[P II] ratios in these other regions suggest also that SNe winds should not be important, favouring ionization by young stars instead.

4.2 Mass of ionized and molecular gas

The mass of ionized gas in the inner 900×900 pc^2 of the galaxy can be estimated using (e.g. Scoville et al. 1982; Riffel et al. 2008; Storchi-Bergmann et al. 2009)

$$M_{\rm H\,II} \approx 3 \times 10^{17} \left(\frac{F_{\rm Br\gamma}}{\rm erg\,s^{-1}\,cm^{-2}}\right) \left(\frac{D}{\rm Mpc}\right)^2 ({\rm M}_\odot), \quad (1)$$

where $F_{\rm Br\gamma}$ is the integrated flux for the $Br\gamma$ emission line and D is the distance to Mrk 766. We have assumed an electron temperature $T = 10^4$ K and electron density $N_{\rm e} = 100\,{\rm cm}^{-3}$ (Osterbrock & Ferland 2006).

The mass of warm molecular gas can be obtained using (Scoville et al. 1982)

$$M_{\rm H_2} \approx 5.0776 \times 10^{13} \left(\frac{F_{\rm H_2\lambda2.1218}}{\rm erg\,s^{-1}\,cm^{-2}}\right) \left(\frac{D}{\rm Mpc}\right)^2 ({\rm M}_\odot), \quad (2)$$

where $F_{\rm H_2\lambda2.1218}$ is the integrated flux for the H$_2\lambda$2.1218 μm emission line and we have used the vibrational temperature $T = 2000$ K (Riffel et al. 2008, 2010; Storchi-Bergmann et al. 2009).

We used the Brγ/Paβ line ratio in order to estimate the effect of the reddening in the observed fluxes for these lines. We constructed a reddening map using the Paβ/Brγ line ratio. The resulting map is very noisy with an additional uncertainty relative to other line ratios because the lines are in different spectral bands (K and J). The $E(B-V)$ values are also mostly very small. Thus, instead of using this map to correct the whole Brγ flux distribution for reddening – as we would introduce too much noise – we have estimated an average value for $E(B-V) = 0.3 \pm 0.1$ using the integrated fluxes for Brγ and Paβ emission lines over the whole FOV, following Storchi-Bergmann et al. (2009) and adopting the extinction law of Cardelli, Clayton & Mathis (1989).

Adopting this $E(B-V)$ value, the fluxes for the emission lines in the K band increase by about 10 per cent. The effect of the reddening is negligible for the line ratios of Fig. 4, since the lines are from the same band and the reddening has no effect on the discussion of the gas excitation presented above. On the other hand, its effect is not negligible for the estimate of the ionized and molecular gas masses, which have thus been corrected. Integrating over the whole IFU field, we obtain the following reddening-corrected values: $F_{\rm Br\gamma} \approx 6.82 \pm 0.35 \times 10^{-15}$ erg s^{-1} cm^{-2} and $F_{\rm H_2\lambda2.1218} \approx 7.3 \pm 0.37 \times 10^{-15}$ erg s^{-1} cm^{-2}. The resulting masses are $M_{\rm H\,II} \approx 7.6 \pm 0.4 \times 10^6$ M$_\odot$ and $M_{\rm H_2} \approx 1.32 \pm 0.07 \times 10^3$ M$_\odot$.

The above values are similar to those we have obtained in previous studies, which are in the range 0.1×10^6 M$_\odot \leq M_{\rm H\,II} \leq 1.7 \times 10^6$ M$_\odot$ and 66 M$_\odot \leq M_{\rm H_2} \leq 3300$ M$_\odot$, respectively.

The mass of molecular gas is thus 10^3 times smaller than that of the ionized gas but, as discussed in Storchi-Bergmann et al. (2009), this H$_2$ mass represents only that of warm gas emitting in the NIR. The total mass of molecular gas is dominated by the cold gas, and the usual proxy to estimate the cold H$_2$ mass has been the CO emission. A number of studies have derived the ratio between the cold and warm H$_2$ gas masses by comparing the masses obtained using the CO and NIR emission. Dale et al. (2005) obtained ratios in the range 10^5–10^7; using a larger sample of 16 luminous and ultraluminous IR galaxies, Müller-Sánchez et al. (2006) derived a ratio $M_{\rm cold}/M_{\rm warm} = 1$–$5 \times 10^6$. More recently, Mazzalay et al. (2013) compiled from the literature values of $M_{\rm cold}$ derived from CO observations and H$_2$2.12 μm luminosities for a larger number of galaxies, covering a wider range of luminosities, morphological and nuclear activity types. From that, an estimate of the cold H$_2$ gas mass can be obtained from

$$M_{\rm H_2\,cold} \approx 1174 \left(\frac{L_{\rm H_2\lambda2.1218}}{\rm L_\odot}\right), \quad (3)$$

where $L_{\rm H_2\lambda2.1218}$ is the luminosity of the H$_2$2.12 μm line. The resulting mass value is $M_{\rm H_2\,cold} \approx 9.8 \times 10^8$ M$_\odot$.

4.3 Gaseous kinematics

All the velocity fields shown in Fig. 5 suggest rotation in the inner 450 pc of Mrk 766. In order to obtain the systemic velocity, orientation of the line of nodes and an estimate for the enclosed mass, we fitted a model of circular orbits in a plane to the Paβ and H$_2\lambda$2.1218 μm velocity fields. The expression for the circular velocity is given by (Barbosa et al. 2006; Riffel et al. 2006b, 2011)

$$V_r = V_{\rm s} + \sqrt{\frac{R^2 G M}{(R^2+A^2)^{3/2}}} \frac{\sin(i)\cos(\Psi-\Psi_0)}{\left(\cos^2(\Psi-\Psi_0) + \frac{\sin^2(\Psi-\Psi_0)}{\cos^2(i)}\right)^{3/4}} \quad (4)$$

where R is the projected distance from the nucleus in the plane of the sky, Ψ is the corresponding PA, M is the mass inside R, G is the Newton's gravitational constant, $V_{\rm s}$ is the systemic velocity, i is the inclination of the disc ($i = 0$ for a face-on disc), Ψ_0 is the PA of the line of nodes and A is a scalelength projected in the plane of the sky.

The location of the kinematical centre was not allowed to vary, being fixed to the position of the peak of the continuum. The equation above contains five free parameters, which can be determined by fitting the model to the observations. This was done using the Levenberg–Marquardt least-squares fitting algorithm, in which initial guesses are given for the free parameters. The best-fitting model for Paβ is shown in Fig. 12 (top-left panel) and the best-fitting model for H$_2\lambda$2.1218 μm in Fig. 13. In both figures, we show the residual maps (observed velocity field – model) for [Fe II] (bottom-left panel), H$_2$ (bottom-right panel) and Paβ (top-right panel).

The parameters derived from the fit of the Paβ are: the systemic velocity corrected to the heliocentric reference frame $V_{\rm s} = 3853 \pm 17$ km s^{-1}, $\Psi_0 = 80^\circ \pm 3^\circ\!.36$, $M = 8.72 \pm 0.63 \times 10^8$ M$_\odot$,

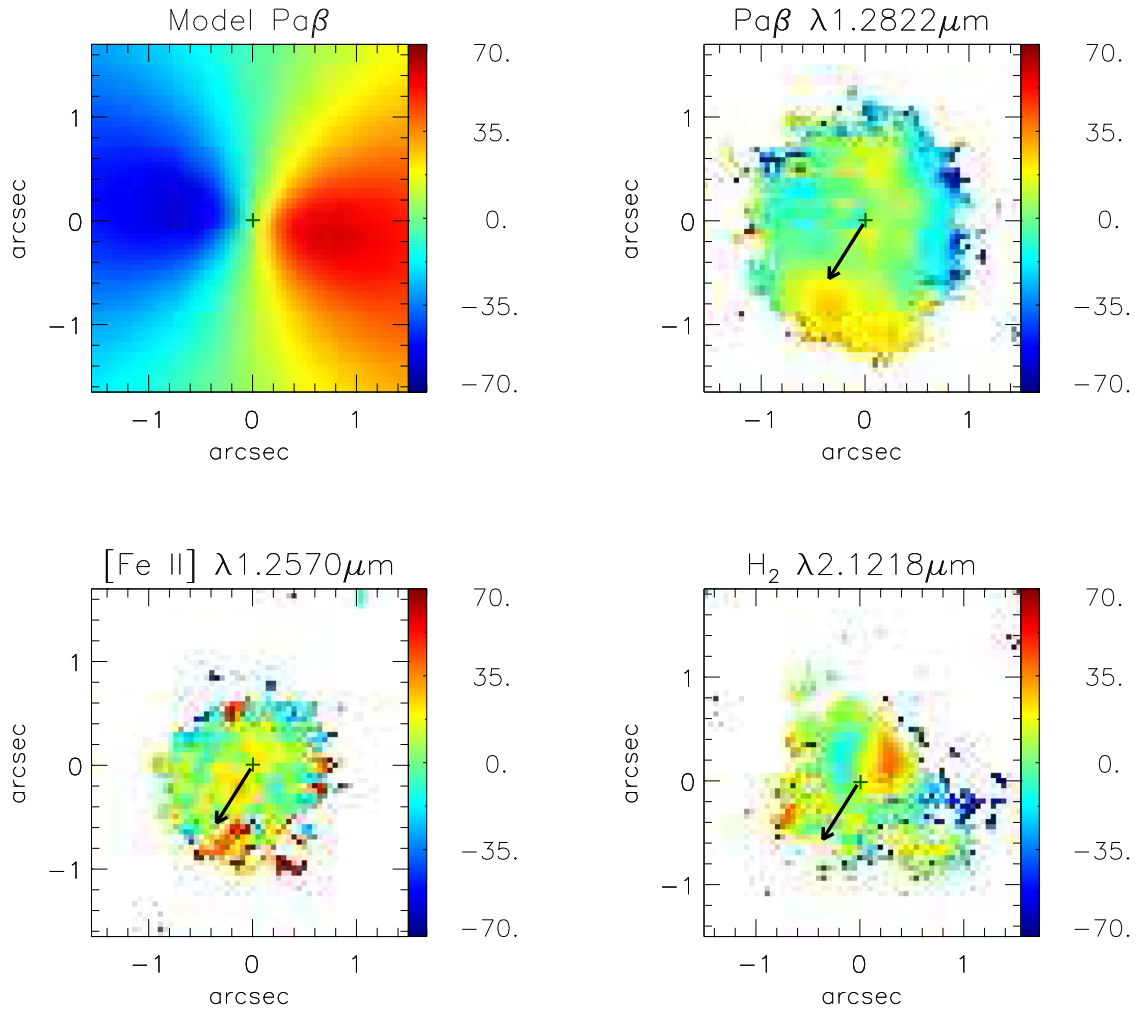

Figure 12. Rotating disc model fitted to the Paβ velocity field, together with the residuals of its subtraction from the observed velocity fields of Paβ, [Fe II] λ 1.2570 μm and $H_2\lambda$ 2.1218 μm. The black arrows show the extent of the radio structure (Kukula et al. 1995).

$i = 30^\circ \pm 4^\circ$ and $A = 163.4 \pm 10$ pc. We can compare the NIR line-emitting gas kinematics with results obtained in the optical at larger scales. González Delgado & Pérez (1996) present long-slit spectroscopy of Mrk 766 at kpc scales with the slit oriented along PA = 55°. They found that the kinematic of the high-excitation gas (traced by the [O III] λ5007 emission) is more perturbed than that of the low-ionization gas (traced by Hα and Hβ), showing radial motions consistent with gas outflows from the nucleus. The low-ionization gas seems to be dominated by rotation in the plane of the galaxy with a velocity amplitude of $\sim$130 km s^{-1}. At distances smaller than 1.5 arcsec from the nucleus, the velocity amplitude is $<$50 km s^{-1}, which is somewhat smaller than the amplitude that we have derived. This is expected, since the slit used by González Delgado & Pérez (1996) was not oriented along the major axis of the galaxy. González Delgado & Pérez (1996) quote a photometric major axis orientation of 105°, based on a large-scale continuum image at λ5960 Å. The PA of the line of nodes Ψ_0 that we have found is 25° smaller than this value. On the other hand, our Ψ_0 is in reasonable agreement with the value listed at the Hyperleda ($\Psi_0 \approx 73^\circ$; Paturel et al. 2003). Fig. 1 shows that Mrk 766 presents a bar with size of 4.5 kpc. The orientation of the bar is similar to that of the photometric major axis considered by González Delgado & Pérez (1996). As the bar is broad and luminous and the outer parts of the galaxy are faint, we believe they have mistakenly concluded that the direction of the bar was that of the major axis. The systemic velocity and i are in reasonable agreement with the values listed at the Hyperleda (Paturel et al. 2003) and NED data bases ($V_s \approx 3876$ km s^{-1} and $i \approx 36^\circ$ and M and A are similar to values found for other Seyfert galaxies using the same model (e.g. Barbosa et al. 2006). For the $H_2\lambda$2.1218 μm fit, we found a much more compact velocity field than that of Paβ, with a scalelength $A = 41.1 \pm 4$ pc. The other parameters were practically the same. This signature of a more compact rotating disc in H_2 than in Paβ, is similar to that we have found for Mrk 1066 (Riffel & Storchi-Bergmann 2010), indicating that H_2 presents a colder and more ordered kinematics. An exception is the region to the south-west, which seems to show a detached kinematics. This region is probably a molecular cloud that is not in the galaxy disc.

The residuals shown in Fig. 12 show blueshifts in the borders of the measured field in Paβ to the north–north-east of the nucleus which we attribute to poor fits of the lines in this region. More significant are the redshift residuals to the south–SE, a region where the largest residuals in the [Fe II] velocity field are also observed. There is where the enhanced [Fe II] velocity dispersion and the radio structure are also located. In addition, in this same region, the [Fe II] flux distributions in the channel maps of Fig. 8 show both

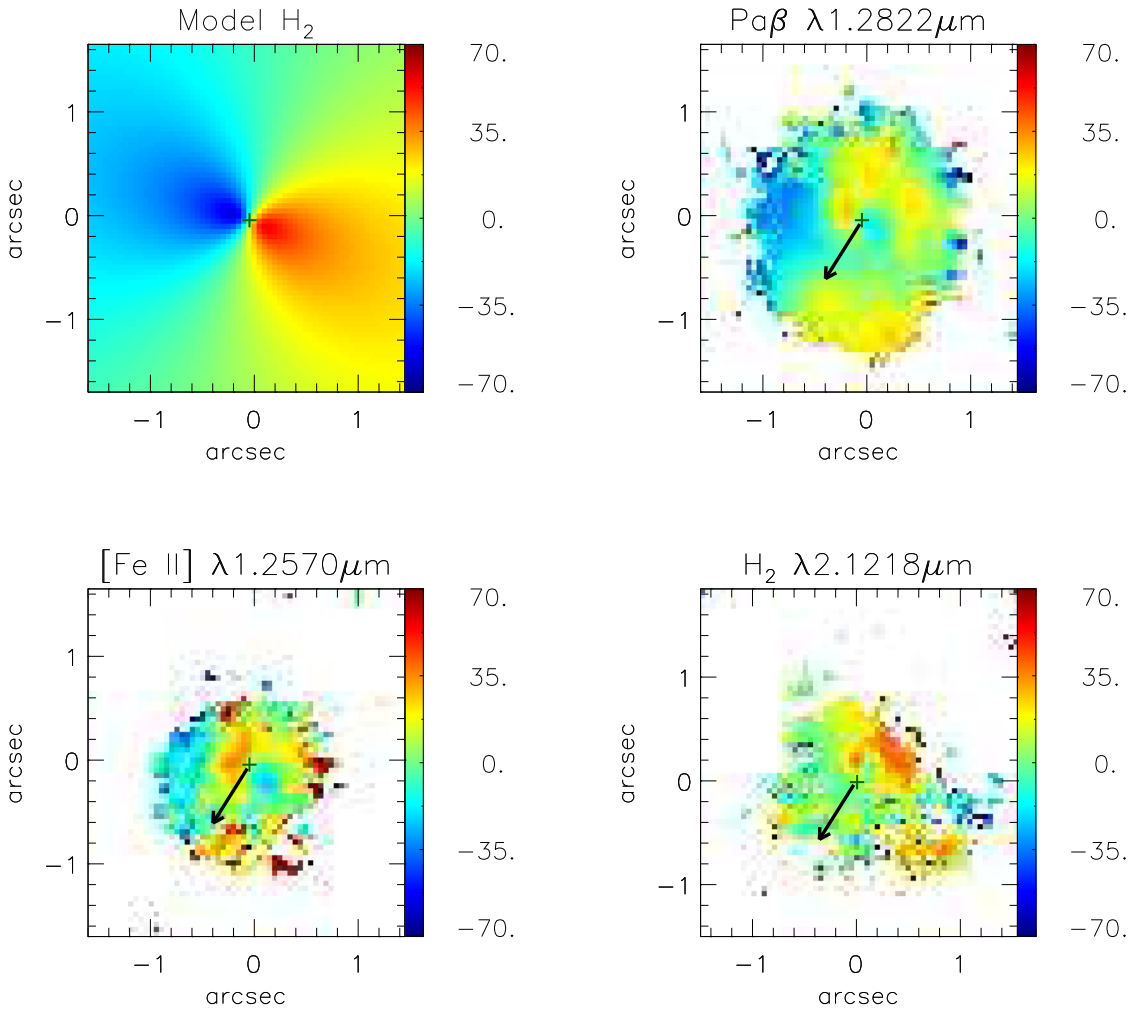

Figure 13. Rotating disc model fitted to the $H_2\lambda2.1218$ μm velocity field, together with the residuals of its subtraction from the observed velocity fields of Paβ, [Fe II] λ 1.2570 μm and $H_2\lambda$ 2.1218 μm. The black arrows show the extent of the radio structure (Kukula et al. 1995).

blueshifts and redshifts, with velocities of up to 250 km s^{-1}. We interpret these results as being due to emission of gas in a one-sided outflow oriented along the PA $\approx$ 135°. The observation of both blueshifts and redshifts in the channel maps supports that its axis lies approximately in the plane of the sky. The main residuals in the H_2 velocity field that are not in the borders of the field (where the line fits are poorer) are the redshifts observed to the north–north-west. As this is the near side of the galaxy, we speculate that these residuals could be due to inflows in the plane of the galaxy. These residuals are seen along the direction of the bar at PA $\approx -60°$. We speculate that they may be associated with inflows along the bar, as predicted by theoretical models (e.g. Combes 2004) and as measured in a few cases (e.g. Mundell & Shone 1999). In previous studies, we have found inflows along nuclear dusty spirals (Riffel et al. 2008, 2013; Schnorr Müller et al. 2011). Indeed, numerical simulations by Maciejewski (2004a,b) have shown that if a central SMBH is present, shocks can extend all the way to the vicinity of the SMBH and generate gas inflows consistent with the accretion rates inferred in local AGN. Similar residuals are also seen in the Paβ and [Fe II] residual maps: redshifts to north–north-west, also suggesting inflows. We rule out the possibility of these redshifts being due to a counterpart of the SE outflow once it is observed in redshift over the far side of the galaxy. A possible counterpart should be in blueshift and behind the near side of the galaxy plane. We do not see such a component; one possibility is that it is hidden by the galaxy plane.

The residuals shown in Fig. 13, after the subtraction of the circular velocity model fitted to the H_2 velocity field shows similar residuals to the south–SE for Paβ and [Fe II], but show additional residuals in the northern part of the field. In the case of the H_2 residuals, redshifts are observed also in the region to the south-west, that we have interpreted as due to a detached cloud, that is probably not in the galaxy plane.

4.3.1 Mass outflow rate

With the goal of quantifying the feedback from the AGN in Mrk 766, we estimate the ionized-gas mass outflow rate through a circular cross-section with radius $r = 0.25$ arcsec $\approx$ 75 pc located at a distance of $h = 0.4$ arcsec from the nucleus to the SE. This geometry corresponds to a conical outflow with an opening angle of $\approx$64°, estimated from Fig. 8. The mass outflow rate can be obtained using

$$\dot{M}_{\rm out} = m_{\rm p}\, N_{\rm e}\, v\, f\, A \qquad (5)$$

and the filling factor (f) can be obtained from

$$f = \frac{L_{\mathrm{Pa}\beta}}{j_{\mathrm{Pa}\beta}\, V} \quad (6)$$

where m_{p} is the proton mass, N_{e} the electron density, v_{out} is velocity of the outflowing gas and $L_{\mathrm{Pa}\beta}$ and $j_{\mathrm{Pa}\beta}$ are the luminosity and the emission coefficient of Paβ (Riffel et al. 2011).

We have assumed that $N_{\mathrm{e}} = 500\,\mathrm{cm^{-3}}$, $L_{\mathrm{Pa}\beta} = 1.43\times10^{39}\,\mathrm{erg\,s^{-1}}$, $j_{\mathrm{Pa}\beta} = 4.07\times10^{-22}\,\mathrm{erg\,cm^{-3}\,s^{-1}}$ and $v_{\mathrm{out}} = 147\,\mathrm{km\,s^{-1}}/\sin\theta \approx 277\,\mathrm{km\,s^{-1}}$, where θ is the angle between the wall of the cone (from where we observe the line-of-sight velocity component of $147\,\mathrm{km\,s^{-1}}$) and the plane of sky. The latter velocity value was obtained directly from the channel maps considering that the structure seen to SE is due to the emission of the walls of the cone. As described above, the axis of the cone seems to lie close to the plane of the sky. From the estimated aperture of the cone, we adopt a maximum angle between the cone and the plane of the sky of 32°. Under these assumptions we obtain $f = 0.18$ and then $\dot{M}_{\mathrm{out}} \approx 10\,\mathrm{M_\odot\,yr^{-1}}$. The value found here for $\dot{M}_{\mathrm{out}}$ is in good agreement with those found in Veilleux et al. (2005), which range from 0.1 to $10\,\mathrm{M_\odot\,yr^{-1}}$, it is of the same order of that obtained by Riffel et al. (2011), of $8\,\mathrm{M_\odot\,yr^{-1}}$, and is also within the range of the values found by Müller-Sánchez et al. (2011), which range from 2.5 to $120\,\mathrm{M_\odot\,yr^{-1}}$.

Following Storchi-Bergmann et al. (2010), we can use the above mass outflow rate to estimate the kinetic power of the outflow using

$$\dot{E} \approx \frac{\dot{M}_{\mathrm{out}}}{2}(v_{\mathrm{out}}^2 + \sigma^2), \quad (7)$$

where $v_{\mathrm{out}} = v_{\mathrm{obs}}/\sin\theta$ is the velocity of the outflowing gas and σ is its velocity dispersion. Using $\sigma \approx 100\,\mathrm{km\,s^{-1}}$ (from Fig. 6) and $v_{\mathrm{out}} = v_{\mathrm{obs}}/\sin\theta = 277\,\mathrm{km\,s^{-1}}$, we obtain $\dot{E} \approx 2.9\times10^{41}\,\mathrm{erg\,s^{-1}}$ which is in good agreement with the values obtained for Seyfert galaxies and compact radio sources (Morganti, Tadhunter & Oosterloo 2005). This value is also similar to that obtained for Mrk 1157 (Riffel et al. 2011), of $\dot{E} \approx 5.7\times10^{41}\,\mathrm{erg\,s^{-1}}$, it is within the range of those found by Müller-Sánchez et al. (2011), between 0.6 and $50\times10^{41}\,\mathrm{erg\,s^{-1}}$.

In order to compare the above value of $\dot{E}$ with the bolometric luminosity, we estimate the latter as 10 times the X-ray luminosity, of $3.5\times10^{41}\,\mathrm{erg\,s^{-1}}$ (Boller et al. 2001), resulting in $\dot{E} \approx 0.08\,L_{\mathrm{Bol}}$.

Finally, we can calculate the mass accretion rate to feed the active nucleus from (Riffel et al. 2011)

$$\dot{m} = \frac{L_{\mathrm{bol}}}{c^2\eta}, \quad (8)$$

where L_{bol} is the nuclear bolometric luminosity, η is the efficiency of conversion of the rest mass energy of the accreted material into radiation and c is the light speed. The bolometric luminosity was already estimated as $3.5\times10^{42}\,\mathrm{erg\,s^{-1}}$. Assuming $\eta \approx 0.1$, which is a typical value for a geometrically thin, optically thick accretion disc (Frank, King & Raine 2002), we obtain an accretion rate of $\dot{m} \approx 1.4\times10^{-2}\,\mathrm{M_\odot\,yr^{-1}}$, which is about three orders of magnitude smaller than the mass outflow rate, a ratio compared with those found in our previous studies.

5 CONCLUSIONS

We have mapped the gas flux distribution, excitation and kinematics from the inner ≈450 pc radius of the Seyfert 1 galaxy Mrk 766 using NIR J- and K-band integral-field spectroscopy at a spatial resolution of ≈60 pc (0.20 arcsec). The main conclusions of this work are as follows.

(i) The emission-line flux distributions of molecular hydrogen H_2 and low-ionization gas are extended to at least ≈300 pc from the nucleus.

(ii) The H_2 line emission is most extended along PA = 70°, which is close to the PA of the line of nodes of the gas kinematics.

(iii) The [Fe II] emission is most extended approximately along the perpendicular direction to the line of nodes of the gas kinematics.

(iv) The coronal line [S IX] emission is resolved and extends up to ≈150 pc from the nucleus.

(v) The emission-line ratios [Fe II]/Paβ and H_2/Brγ show a mixture of Starburst and Seyfert type excitation; the Seyfert values dominate at the nucleus, to the north-west and in an arc-shaped region between 0.2 and 0.6 arcsec to the SE where a radio jet has been observed, while Starburst values are present at the nucleus and other regions.

(vi) The enhancement of the [Fe II]/[P II] line ratio at the location of the radio jet, as well as the corresponding increase in the [Fe II] flux and velocity dispersion support a contribution from shocks to the gas excitation in the arc-shaped region to the SE; in the remaining regions, the favoured excitation mechanism is UV radiation from young stars.

(vii) The H_2 gas kinematics is dominated by rotation in a compact disc with a velocity amplitude of $140\,\mathrm{km\,s^{-1}}$ and low velocity dispersion (40–60 $\mathrm{km\,s^{-1}}$, consistent with orbital motion in the plane of the galaxy).

(viii) The kinematics of the ionized gas is also dominated by rotation, but channel maps in [Fe II] show in addition an outflowing component to the SE, with an axis lying close to the plane of the sky reaching velocities of $\sim300\,\mathrm{km\,s^{-1}}$, probably associated with the radio jet.

(ix) The mass outflow rate in ionized gas is estimated to be $\approx10.7\,\mathrm{M_\odot\,yr^{-1}}$ and the power of the outflow estimated to be $\approx0.08\,L_{\mathrm{Bol}}$.

(x) The mass of ionized gas is $M_{\mathrm{H\,II}} \approx 7.6\times10^6\,\mathrm{M_\odot}$ while the mass of the hot molecular gas is $M_{\mathrm{H_2}} \approx 1.3\times10^3\,\mathrm{M_\odot}$ and the estimated cold molecular gas mass is $M_{\mathrm{H_2\,cold}} \approx 9.8\times10^8\,\mathrm{M_\odot}$.

The distinct flux distributions and kinematics of the H_2 and [Fe II] emitting gas, with the first more restricted to the plane of the galaxy and in compact rotation and the second related with the radio jet and in outflow are common characteristics of eight Seyfert galaxies (ESO428-G14, NGC 4051, NGC 7582, NGC 4151, Mrk 1066, Mrk 1157, Mrk 79 and Mrk 766) we have studied so far using similar integral-field observations and two others (Circinus and NGC 2110) using long-slit observations. These results again suggest – as those found in previous studies – that the H_2 emission is tracer of the AGN feeding, while the [Fe II] is a tracer of its feedback.

ACKNOWLEDGEMENTS

This work is based on observations obtained at the Gemini Observatory, which is operated by the Association of Universities for Research in Astronomy, Inc., under a cooperative agreement with the NSF on behalf of the Gemini partnership: the National Science Foundation (USA), the Science and Technology Facilities Council (UK), the National Research Council (Canada), CONICYT (Chile), the Australian Research Council (Australia), Ministério da Ciência e Tecnologia (Brazil) and south-east CYT (Argentina). This research has made use of the NASA/IPAC Extragalactic Database (NED) which is operated by the Jet Propulsion Laboratory, California Institute of Technology, under contract with the National

Aeronautics and Space Administration. We acknowledge the usage of the HyperLeda data base (http://leda.univ-lyon1.fr). This work has been partially supported by the Brazilian institutions CNPq, CAPES and FAPERGS.

REFERENCES

Barbosa F. K. B., Storchi-Bergmann T., Cid Fernandes R., Winge C., Schmitt H., 2006, MNRAS, 371, 170
Bentz M. C. et al., 2009, ApJ, 705, 199
Black J. H., van Dishoeck E. F., 1987, ApJ, 322, 412
Boller T., Keil R., Trümper J., O'Brien P. T., Reeves J., Page M., 2001, A&A, 365, 146
Cardelli J. A., Clayton G. C., Mathis J. S., 1989, ApJ, 345, 245
Combes F., 2004, in Storchi-Bergmann T., Ho L. C., Schmitt H. R., eds, Proc. IAU Symp. 222, The Interplay among Black Holes, Stars and ISM in Galactic Nuclei. Cambridge Univ. Press, Cambridge, p. 383
Crenshaw D. M., Kraemer S. B., 2007, ApJ, 659, 250
Crenshaw D. M., Kraemer S. B., Schmitt H. R., Kaastra J. S., Arav N., Gabel J. R., Korista K. T., 2009, ApJ, 698, 281
Crenshaw D. M., Kraemer S. B., Schmitt H. R., Jaffé Y. L., Deo R. P., Collins N. R., Fischer T. C., 2010a, ApJ, 139, 871
Crenshaw D. M., Schmitt H. R., Kraemer S. B., Mushotsky R. F., Dunn J. P., 2010b, ApJ, 708, 419
Dale D. A., Sheth K., Helou G., Regan M. W., Hüttemeister S., 2005, AJ, 129, 2197
Davies R. I. I., Sternberg A., Lehnert M. D., Tacconi-Garman L. E., 2005, ApJ, 633, 105
Davies R. I., Maciejewski W., Hicks E. K. S., Tacconi L. J., Genzel R., Engel H., 2009, ApJ, 702, 114
Fathi K., Storchi-Bergmann T., Riffel R. A., Winge C., Axon D. J., Robinson A., Capetti A., Marconi A., 2006, ApJ, 641, L25
Ferruit P., Wilson A. S., Mulchaey J., 2000, ApJS, 128, 139
Fischer T. C., Crenshaw D. M., Kraemer S. B., Schmitt H. R., Trippe M. L., 2010, AJ, 140, 577
Fischer T. C., Crenshaw D. M., Kraemer S. B., Schmitt H. R., Mushotsky R. F., Ward M. J., 2011, ApJ, 727, 71
Forbes D. A., Ward M. J., 1993, ApJ, 416, 150
Frank J., King A. R., Raine D. J., 2002, Accretion Power in Astrophysics, 3rd edn. Cambridge Univ. Press, Cambridge
González Delgado R. M., Pérez E., 1996, MNRAS, 278, 737
Guillard P., Boulanger F., Cluver M. E., Appleton P. N., Pineau Des Forêts G., Ogle P., 2010, A&A, 518, 59
Hollenbach D., McKee C. F., 1989, ApJ, 342, 306
Holt J., Tadhunter C., Morganti R., Bellamy M., González Delgado R. M., Tzioumis A., Inskip K. J., 2006, MNRAS, 370, 1633
Hunt L. K., Malkan M. A., Rush B., Bicay M. D., Nelson B. O., Stanga R. M., Webb W., 1999, ApJS, 125, 349
Kukula M. J., Pedlar A., Baum S. A., O'Dea C. P., 1995, MNRAS, 276, 1262
Larkin J. E., Armus L., Knop R. A., Soifer B. T., Matthews K., 1998, ApJS, 114, 59
McGregor P. J. et al., 2003, Proc. SPIE, 4841, 1581
Maciejewski W., 2004a, MNRAS, 354, 883
Maciejewski W., 2004b, MNRAS, 354, 892
Malkan M. A., Gorjian V., Tam R., 1998, ApJS, 117, 25
Maloney P. R., Hollenbach D. J., Tielens A. G. G. M., 1996, ApJ, 466, 561
Mazzalay X., Rodríguez-Ardila A., Komossa S., 2010, MNRAS, 405, 1315
Mazzalay X. et al., 2013, MNRAS, 428, 2389
Morganti R., Tadhunter C. N., Oosterloo T. A., 2005, A&A, L9, L13
Müller-Sánchez F., Davies R. I., Eisenhauer F., Tacconi L. J., Genzel R., Sternberg A., 2006, A&A, 454, 492
Müller-Sánchez F., Davies R. I., Genzel R., Tacconi L. J., Eisenhauer F., Hicks E. K. S., Friedrich S., Sternberg A., 2009, ApJ, 691, 749
Müller-Sánchez F., Prieto M. A., Hicks E. K. S., Vives-Arias H., Davies R. I., Malkan M., Tacconi L. J., Genzel R., 2011, ApJ, 739, 69
Mundell C. G., Shone D. L., 1999, MNRAS, 304, 475
Oliva E. et al., 2001, A&A, 369, L5
Osterbrock D. E., Ferland G. J., 2006, Astrophysics of Gaseous Nebulae and Active Galactic Nuclei, 2nd edn. University Science Books, Mill Valley, California
Paturel G., Petit C., Prugniel P., Theureau G., Rousseau J., Brouty M., Dubois P., Cambrésy L., 2003, A&A, 412, 45
Reunanen J., Kotilainen J. K., Prieto M. A., 2002, MNRAS, 331, 154
Riffel R. A., 2010, Ap&SS, 327, 239
Riffel R. A., Storchi-Bergmann T., 2010, MNRAS, 411, 469
Riffel R. A., Sorchi-Bergmann T., Winge C., Barbosa F. K. B., 2006a, MNRAS, 373, 2
Riffel R., Rodríguez-Ardila A., Pastoriza M. G., 2006b, A&A, 457, 61
Riffel R. A., Storchi-Bergmann T., Winge C., McGregor P. J., Beck T., Schmitt H., 2008, MNRAS, 385, 1129
Riffel R. A., Storchi-Bergmann T., Dors O. L., Winge C., 2009, MNRAS, 393, 783
Riffel R. A., Storchi-Bergmann T., Nagar N. M., 2010, MNRAS, 404, 166
Riffel R., Riffel R. A., Ferrari F., Storchi-Bergmann T., 2011, MNRAS, 416, 493
Riffel R. A., Storchi-Bergmann T., Winge C., 2013, MNRAS, 430, 2249
Rodríguez-Ardila A., Viegas S. M., 2003, MNRAS, 340, 33
Rodríguez-Ardila A., Pastoriza M. G., Viegas S., Sigut T. A. A., Pradhan A. K., 2004, A&A, 425, 457
Rodríguez-Ardila A., Contini M., Viegas S. M., 2005a, MNRAS, 357, 220
Rodríuez-Ardila A., Riffel R., Pastoriza M. G., 2005b, MNRAS, 364, 1041
Rodríguez-Ardila A., Prieto M. A., Viegas S., Gruenwald R., 2006, ApJ, 653, 1098
Schmitt H. R., Kinney A. L., 1996, ApJ, 463, 498
Schnorr Müller A., Storchi-Bergmann T., Riffel R. A., Ferrari F., Steiner J. E., Axon D. J., Robinson A., 2011, MNRAS, 413, 149
Scoville N. Z., Hall D. N. B., Kleinmann S. G., Ridgway S. T., 1982, ApJ, 253, 136
Simpson C., Forbes D. A., Baker A. C., Ward M. J., 1996, MNRAS, 283, 777
Storchi-Bergmann T., Winge C., Ward M., Wilson A. S., 1999, MNRAS, 304, 35
Storchi-Bergmann T., Dors O., Jr, Riffel R. A., Fathi K., Axon D. J., Robinson A., 2007, ApJ, 670, 25
Storchi-Bergmann T., McGregor P., Riffel R. A., Simões Lopes R., Beck T., Dopita M., 2009, MNRAS, 394, 1148
Storchi-Bergmann T., Simões Lopes R., McGregor P., Riffel R. A., Beck T., Martini P., 2010, MNRAS, 402, 819
Veilleux S. A., Goodrich R. W., Hill G. J., 1997, ApJ, 477, 631
Veilleux S., Cecil G., Bland-Hawthorn J., 2005, ARA&A, 43, 769
Wilson A. S., Braatz J. A., Heckman T. M., Krolic J. H., Miley G. K., 1993, ApJ, 419, L61

This paper has been typeset from a TEX/LATEX file prepared by the author.

Monthly Notices
of the
ROYAL ASTRONOMICAL SOCIETY

MNRAS **464,** 1771–1782 (2017)
Advance Access publication 2016 September 8

doi:10.1093/mnras/stw2263

Feeding versus feedback in active galactic nuclei from near-infrared integral field spectroscopy – XII. NGC 5548

Astor J. Schönell, Jr,[1]★ Thaisa Storchi-Bergmann,[1] Rogemar A. Riffel[2]★ and Rogério Riffel[1]

[1]*Instituto de Física, Universidade Federal do Rio Grande do Sul, Av. Bento Goncalves 9500, 91501-970 Porto Alegre, RS, Brazil*
[2]*Universidade Federal de Santa Maria, Departamento de Física, Centro de Ciências Naturais e Exatas, 97105-900 Santa Maria, RS, Brazil*

Accepted 2016 September 7. Received 2016 September 5; in original form 2016 June 1

ABSTRACT

We map the gas excitation and kinematics, and the stellar population properties of the Seyfert 1 galaxy NGC 5548 using Gemini Near Infrared Integral Field Spectrograph in the *J* and *K* bands at a spatial and velocity resolution of 105 pc and 45 km s^{-1}, respectively. Emission-line flux distributions in ionized and molecular gas extend up to ≈400 pc from the nucleus, where they are found to peak. The mass of H II is 4.8±0.6 × 10^6 M$_\odot$ and the mass of warm H_2 is 1.1±0.2 × 10^3 M$_\odot$, while the mass of cold H_2 is estimated as 5.8±1.2 × 10^8 M$_\odot$. The Pa β emission shows two kinematic components: one in blueshift, with velocity reaching ≈−300 km s^{-1} and another showing a velocity field characteristic of rotation in the galaxy plane. The blueshifted component is also observed in the coronal line [S IX]λ1.2523 μm, while the rotational component is also observed in the molecular gas. We interpret this velocity field as due to gas rotating in the galaxy plane plus an outflow, and estimate a mass outflow rate of 6.8±0.75 M$_\odot$ yr^{-1}. Spectral synthesis of the continuum shows nuclear emission dominated by a featureless AGN continuum combined with hot dust emission attributed to a dusty torus. The stellar population is dominated by an old (2 Gyr < t ≤ 15 Gyr) component between 160 and 300 pc, while closer to the nucleus, an intermediate age (50 Myr < t ≤ 2 Gyr) component contributes at levels ranging from ≈40 per cent to ≈100 per cent to the flux at 2.12 μm.

Key words: galaxies: active – galaxies: individual: NGC 5548 – galaxies: kinematics and dynamics – galaxies: nuclei – galaxies: Seyfert.

1 INTRODUCTION

The study of the narrow-line region of nearby active galactic nuclei (AGN) allows the mapping of the processes of feeding of a nuclear supermassive black hole – via gas inflows (e.g. Fathi et al. 2006; Storchi-Bergmann et al. 2007; Davies et al. 2009; Müller Sánchez et al. 2009; Schnorr Müller et al. 2011) and its feedback – via the interaction of the AGN radiation and outflows with the circumnuclear gas, affecting its kinematics and excitation (Wilson et al. 1993; Schmitt & Kinney 1996; Veilleux, Goodrich & Wilson 1997; Ferruit, Wilson & Mulchaey 2000; Veilleux, Cecil & Bland-Hawthorn 2005; Holt et al. 2006; Crenshaw & Kraemer 2007; Crenshaw et al. 2009, 2010; Fischer et al. 2010; Müller-Sánchez et al. 2011).

Our group, AGN integral field spectroscopy, has been mapping the feeding and feedback processes in nearby AGN using near-infrared (NIR) integral field spectroscopic observations mostly with the instrument Near Infrared Integral Field Spectrograph (NIFS) at the Gemini North Telescope. Studies in the NIR have the advantage of being less affected by dust obscuration, allowing also the observation of the properties of the molecular gas.

The main findings of our group so far have been that the molecular gas- traced by *K*-band H_2 emission, and the ionized gas traced by H I recombination lines and [Fe II] emission, present distinct flux distributions and kinematics. Usually, the H_2 emitting gas is restricted to the plane of the galaxy, while the ionized gas extends also to high latitudes and is associated with the radio emission, when present (Riffel et al. 2006, 2008, 2009a, 2011b; Storchi-Bergmann et al. 2009, 2010; Riffel, Storchi-Bergmann & Nagar 2010a). The kinematics of the ionized gas, and in particular of the [Fe II] emitting gas shows, in many cases (but not always), a strong outflowing component associated with radio jets from the AGN, while the H_2 kinematics is usually dominated by rotation, including streaming motions towards the nucleus. Davies et al. (2009), using the instrument SINFONI (Spectrograph for Integral Field Observations in the Near Infrared) at the Very Large Telescope, found similar results – molecular gas inflows towards the nucleus of NGC 1097, while

★ E-mail: juniorfisicoo@gmail.com (AJS); rogemar@ufsm.br (RAR)

Müller Sánchez et al. (2009) mapped similar inflows feeding and obscuring the active nucleus of NGC 1068. Müller-Sánchez et al. (2011) mapped outflows in ionized gas around seven AGN, and Davies et al. (2014) analysed molecular and ionized gas inflows and outflows in five active galaxies, both also using SINFONI.

In this study, we present the gaseous distribution, excitation, kinematics, and stellar population (SP) distribution of the inner ≈500 pc radius of the Seyfert 1.5 galaxy NGC 5548 (Mrk 1509), a spiral galaxy (S0/a) at a distance of 79.1 Mpc, where 1.0 arcsec corresponds to 384 parsecs at the galaxy.

This paper is organized as follows: in Section 2, we describe the observations and data reduction procedures. The results are presented in Section 3 and discussed in Section 4. We present our conclusions in Section 5.

2 OBSERVATIONS AND DATA REDUCTION

Observations of the inner region of NGC 5548 were obtained with the instrument NIFS (McGregor et al. 2003) using the Gemini North Adaptive Optics system ALTAIR, in 2012 July under the programme GN-2012A-Q-57. The exposures followed the standard Sky-Object-Object-Sky dither sequence and were obtained in the *J* band using the J_G5603 grating and ZJ_G0601 filter, and in the K_l band using the Kl_G5607 grating and HK_G0603 filter.

On-source and sky position observations were both obtained with individual exposure times of 450 s. Two sets of observations were obtained: the first, in the *J* band, was centred at 1.25 μm and covered the spectral range 1.14–1.36 μm, and the second, in the K_l band, was centred at 2.3 μm and covered the spectral range 2.10–2.53 μm. The total on source exposure was 90 min (45 min in each band).

The data reduction procedure included trimming of the images, flat-fielding, sky subtraction, wavelength and spatial distortion calibrations. We also removed the telluric bands and flux calibrated the frames by interpolating a blackbody function to the spectrum of the telluric standard star. These procedures were executed using tasks contained in the NIFS software package which is part of GEMINI IRAF package, as well as generic IRAF tasks.

The final integral field unit (IFU) data cube for each band contains ≈4000 spectra, with each spectrum corresponding to an angular coverage of 0.05 arcsec × 0.05 arcsec, which translates into ≈20 × 20 pc^2 at the galaxy and covering the inner 3.0 arcsec × 3.0 arcsec (≈1.1 × 1.1 kpc^2) of the galaxy.

We have replaced each spatial pixel by the median of its value and that of its first eight neighbours as well as we used the Butterworth filter (Riffel et al. 2016) to increase the signal-to-noise (S/N) ratio and allow the fitting of the emission-line profiles. The full width at half-maximum (FWHM) of the arc lamp lines in the *J* band is 1.65 Å, corresponding in velocity space to 40 km s^{-1}, while in the K_l band the FWHM of the arc lamp lines is 3.45Å, corresponding to 45 km s^{-1}. The angular resolution in *J* band obtained from the FWHM of the spatial profile of the flux distribution of the broad component of the Pa β is 0.28 arcsec corresponding to 105 pc at the galaxy. The spatial resolution in the K_l band is 0.2 arcsec, corresponding to 75 pc at the galaxy and was obtained from the profile of the nuclear source which is dominated by the contribution of the unresolved AGN.

3 RESULTS

In the top-left panel of Fig. 1, we show a *z*-band image of NGC 5548 obtained from the SDSS (Sloan Digital Sky Survey; Baillard et al. 2011). In the top-right panel, we present an optical image of NGC 5548 obtained with *HST* (*Hubble Space Telescope*) through the filter *F*606*W* (Malkan, Gorjian & Tam 1998). In the bottom panels, we display in the left a *J*-band continuum image constructed by collapsing the spectra within a 100 Å window centred at 1.23 μm, and in the right a *K*-band continuum image centred at 2.22 μm. In Fig. 2, we present two IFU spectra integrated within 0.25 arcsec × 0.25 arcsec aperture. One of them is at the nucleus and the other at 0.4 arcsec south-east of it (position A), which was randomly chosen just to present a characteristic extranuclear spectrum. The nucleus was defined to be the location of the peak of the continuum.

3.1 Emission-line flux distributions

In order to map the flux distributions as well as the centroid velocity and velocity dispersion of the emission lines observed in the *J* and *K* bands ([P II]λ1.1886 μm, [S IX]λ1.2523 μm, [Fe II]λ1.2570 μm, Pa βλ1.2822 μm and H_2λ2.1218 μm), we have used the PROFIT routine (Riffel 2010) to fit the profiles at each pixel over the whole field-of-view. The integrated flux, centroid velocity and velocity dispersion values were obtained by the fit of the emission-line profiles using both Gaussian and Gauss–Hermite (GH) series. The Pa β emission line needed to be fitted with a broad component and this was made using a modified PROFIT routine in three steps: (i) fit two Gaussians to the broad component; (ii) subtract it from the spectra where it is present, and (iii) fit the narrow component.

The narrow component of Pa β emission-line profile was also fitted with two Gaussians because at many locations it shows two peaks. In Fig. 3, we show the fits of the broad and narrow components for the central pixel (peak of the continuum in *J* band) to demonstrate the need of a two-component fit for Pa β. The remaining lines were fitted with a single component of GH series. We do not show the GH moments h_3 and h_4 because they are very noisy, not adding relevant information.

In Fig. 4, we present the flux distribution maps for all the lines fitted. We have masked out the bad fits (using the relative χ^2 parameter of the fit, which is an output from the PROFIT routine) and regions with S/N ratio lower than 3. All maps have their peak fluxes at the same position, which coincides with the peak of the continuum and is adopted as the position of the nucleus.

The [P II]λ1.1886 μm and [S IX]λ1.2523 μm flux distributions are very compact, reaching ≈0.4 arcsec from the nucleus in all directions. The flux distribution of these two coronal lines are thus barely resolved, extending to ≈150 pc from the nucleus, which is typical for coronal lines (e.g. Rodríguez-Ardila et al. 2006; Mazzalay, Rodríguez-Ardila & Komossa 2010; Riffel et al. 2011b; Schönell et al. 2014). The [Fe II]λ1.2570 μm flux distribution is more extended than the coronal lines, reaching almost 0.6 arcsec (230 pc) in all directions.

The blue component of Pa β is extended in all directions up to ≈0.8 arcsec (≈300 pc) (region with S/N ≥ 3) and is the brightest among the observed lines.

We have concluded that the Pa β has two components only within 0.8 arcsec (≈300 pc) from the nucleus. Beyond this region, a good fit is obtained with a single GH component. Therefore, we combined the fluxes of the red component from the inner region with the single GH component from the surrounding region, which extents up to ≈1.2 arcsec (≈500 pc) from the nucleus.

The H_2 line is the only K_l band line that we were able to fit due to the low S/N ratio (S/N < 3) of the other lines present there. The H_2 flux is extended in all directions reaching ≈0.6 arcsec (≈230) from the nucleus.

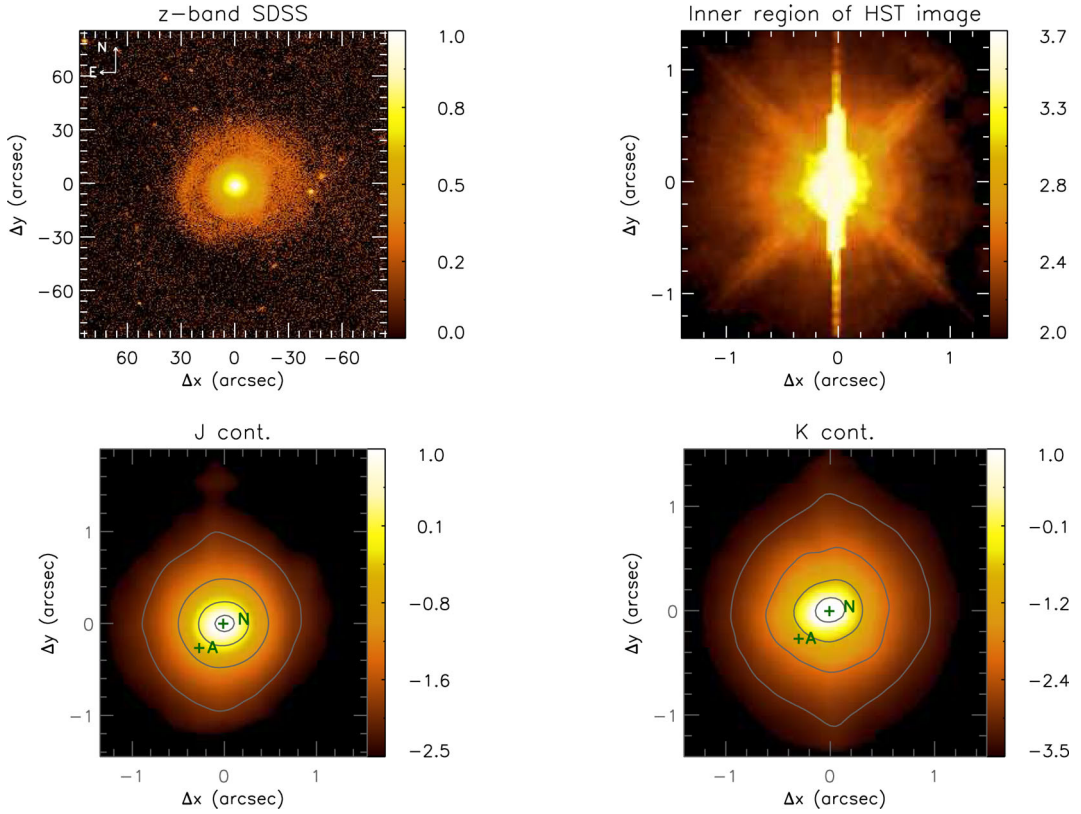

Figure 1. Images of NGC 5548. Top-left panel: SDSS z-band image centred at 8932 Å (Baillard et al. 2011) in arbitrary flux units. Top-right panel: *HST* optical image obtained through the filter *F606W* (Malkan et al. 1998). Botton-left panel: 1.23 μm continuum image obtained from the NIFS data cube with fluxes shown in logarithmic units of 10^{-17} erg s^{-1} cm^2. Bottom-Right panel: 2.22 μm continuum image obtained from the NIFS data cube with fluxes shown in logarithmic units of 10^{-17} erg s^{-1} cm^2.The label N marks the position of the continuum peak and the label A marks the extranuclear position where the spectra of Fig. 2 was obtained.

3.2 Gas kinematics

The PROFIT routine (Riffel 2010) also provides the centroid velocity (v), velocity dispersion (σ) and higher order GH moments (h_3 and h_4), that can be used to map the gas kinematics. In Fig. 5, we present the centroid velocity fields after subtraction of the heliocentric systemic velocity of 5160 ± 10 km s^{-1}, which was obtained through a model fitted to the H_2 velocity field and will be discussed in the next section. The white regions in the figures represent locations where the S/N ratio was too low for a reliable fit.

In Fig. 5 we can see the [P II] velocity field with low centroid velocities, most of them close to zero reaching no more than ≈60 km s^{-1}. The [S IX] velocity field is entirely blueshifted, reaching up to −250 km s^{-1} in most regions. The [Fe II] velocity field is similar to that of [P II]. The Pa β velocity field for the blue component shows velocities in the range −250 to −100 km s^{-1}, while the red component shows a rotation pattern, with blueshifts to the south-east and redshifts to the north-west. The H_2 velocity field also presents a rotation pattern, similar to that of the red component of Pa β.

Fig. 6 shows the velocity dispersion maps for the same lines as for the velocity fields. The σ map for the [P II] shows most values close to ≈100 km s^{-1}, reaching ≈130 km s^{-1} to the west, while the [S IX] σ map is noisier showing values close to 200 km s^{-1}. The [Fe II] σ map has values ranging from ≈50 to ≈125 km s^{-1} with the higher values closer to the nucleus. The blue component of Pa β shows an increase in the σ values around the nucleus of up to 200 km s^{-1} just to the south of the nucleus (≈0.3 arcsec – 105 pc). The red component of Pa β shows lower values of σ, in the range 50–120 km s^{-1}). The H_2 map shows lower values of σ, in the range 50–100 km s^{-1}.

3.3 Channel maps

We have constructed channel maps along the emission-line profiles, but as most emission lines are barely resolved and do not have much kinematic information, we show only the $H_2\lambda2.1218$ μm channel maps in Fig. 7. The panels in the figure show the flux in logarithmic units integrated in velocity bins centred at the velocity shown in the top-left corner of each panel (relative to the systemic velocity of the galaxy). The central cross marks the position of the nucleus. The velocity bins are 30 km s^{-1} (corresponding to 1 spectral pixel) for all panels except the first and last panels, integrated in bins of 100 km s^{-1} (corresponding to 3 spectral pixels). The maps show blueshifts of up to −143 km s^{-1} to the south-east and redshifts of up to 128 km s^{-1} to the north-west. For velocities close to zero the flux distribution is more compact, reaching only 0.6 arcsec (230 pc) with no preferential direction.

3.4 Stellar population synthesis

In this subsection, for the first time, we map the SP properties within the inner 1.5 arcsec (≈600 pc) at a spatial resolution of ≈105 pc of a Seyfert 1 galaxy NGC 5548 derived from the NIR spectra. In order to do this, we simultaneously fit the stellar continuum of the

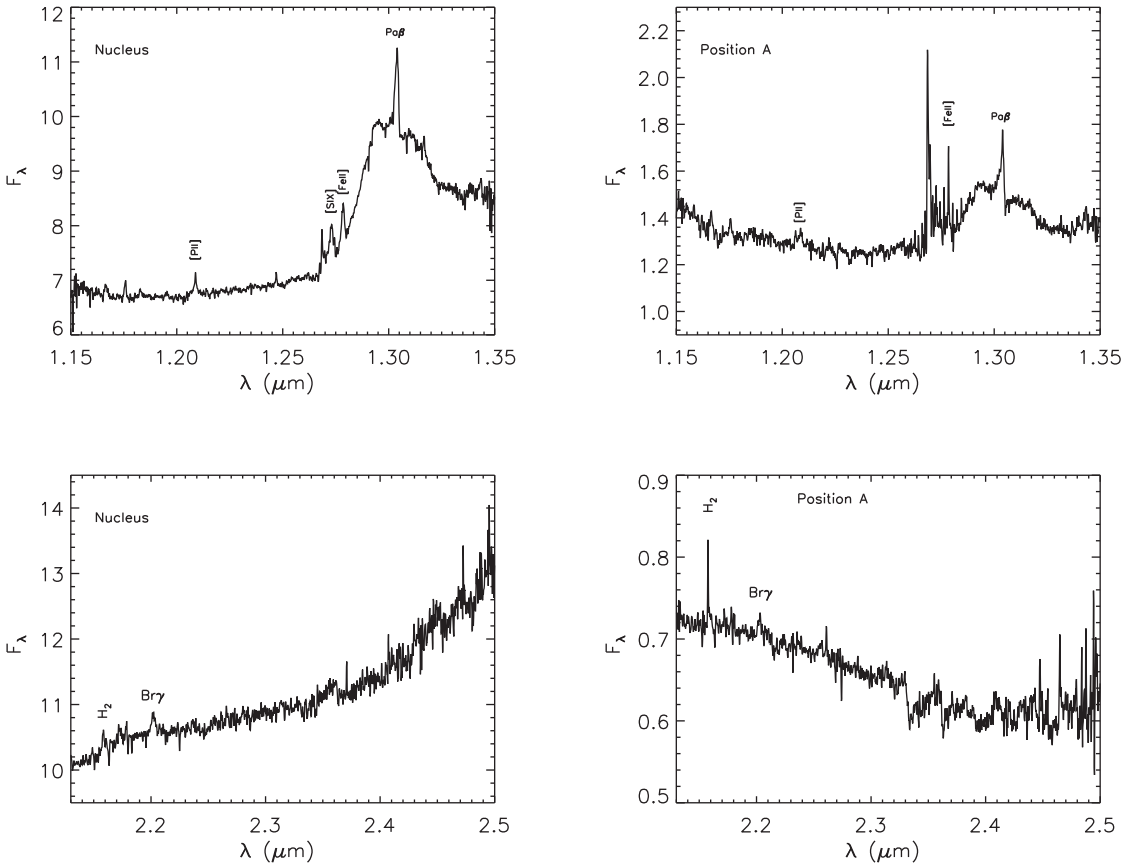

Figure 2. Spectra obtained with an aperture of 0.25 arcsec × 0.25 arcsec centred at the nucleus and at 0.4 arcsec south-east from it (position A, marked in Fig. 1). Flux units: 10^{-17} erg s^{-1} cm^{-2} Å^{-1}.

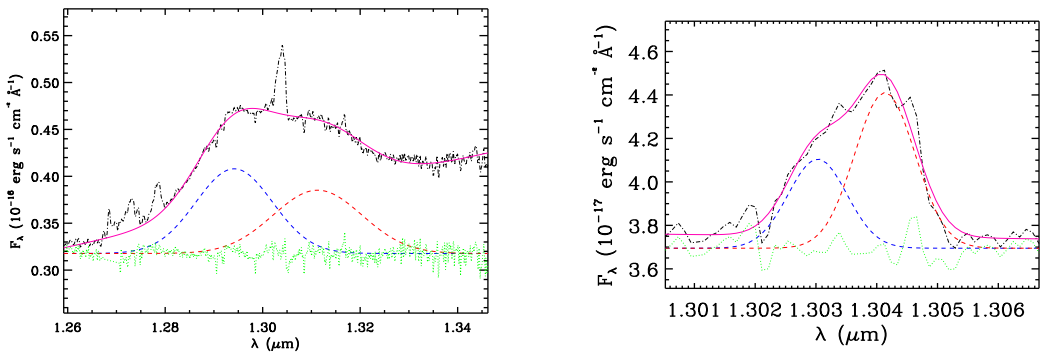

Figure 3. Left-hand panel: fit of the broad Pa β component with two Gaussians. Right-hand panel: fit of the narrow component also with two Gaussians.

J and *K* bands applying the method described in Riffel et al. (2009b) as follows.

Using the STARLIGHT code (Cid Fernandes et al. 2004, 2005, 2009; Asari et al. 2007; Mateus et al. 2011), we performed the SP synthesis. The code uses computational techniques originally developed for semi-empirical population synthesis with ingredients from evolutionary synthesis models (Cid Fernandes et al. 2004, 2005) to fit the whole spectrum, excluding emission lines and spurious data. To summarize, an observed spectrum (O_λ) is fitted with a combination, in different proportions, of N_* simple stellar populations (SSPs). Maraston (2005) provides the evolutionary population synthesis (EPS) models used here. The extinction of the SSPs is parametrized by the v-band extinction A_v and modelled by STARLIGHT as due to foreground dust, and the extinction law used was Cardelli, Clayton & Mathis (1989). The code solves the following equation to model a spectrum M_λ:

$$M_\lambda = M_{\lambda 0} \sum_{j=1}^{N_*} x_j b_{j,\lambda} r_\lambda \bigotimes G(v_*, \sigma_*), \quad (1)$$

where x is the population vector, whose components x_j ($j = 1,..., N_*$) represent the fractional contribution of each SSP in the base to the total synthetic flux at λ_0. The spectrum of the jth SSP of the base of elements normalized at λ_0 is represented by $b_{j,\lambda}$, the reddening term is given by $r_\lambda = 10^{-0.4(A_\lambda - A_{\lambda 0})}$, $M_{\lambda 0}$ is the synthetic flux at the normalization wavelength, $\bigotimes$ represents the convolution operator and $G(v_*, \sigma_*)$ gives the Gaussian distribution used to model the line-of-sight stellar motions, that has a dispersion σ_*, centred at a

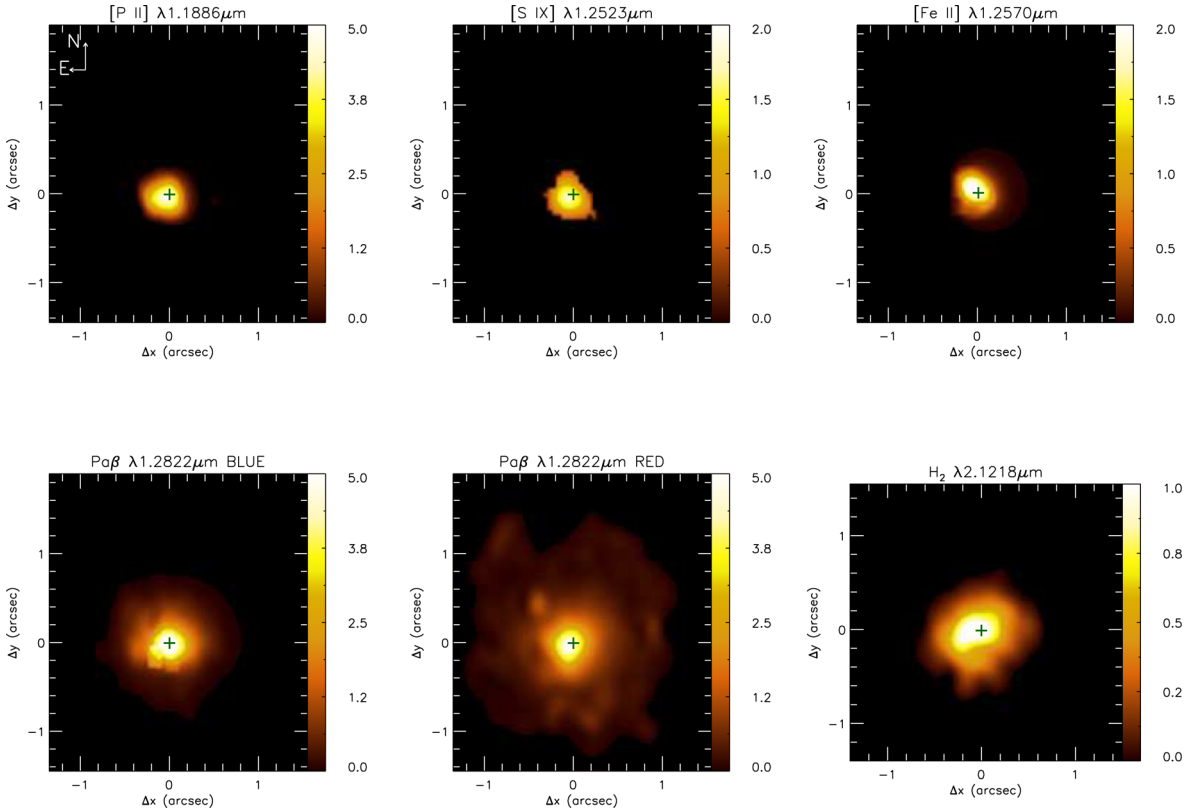

Figure 4. Emission-line flux distributions. The flux units are 10^{-17} erg s^{-1} cm^{-2} Å^{-1}.

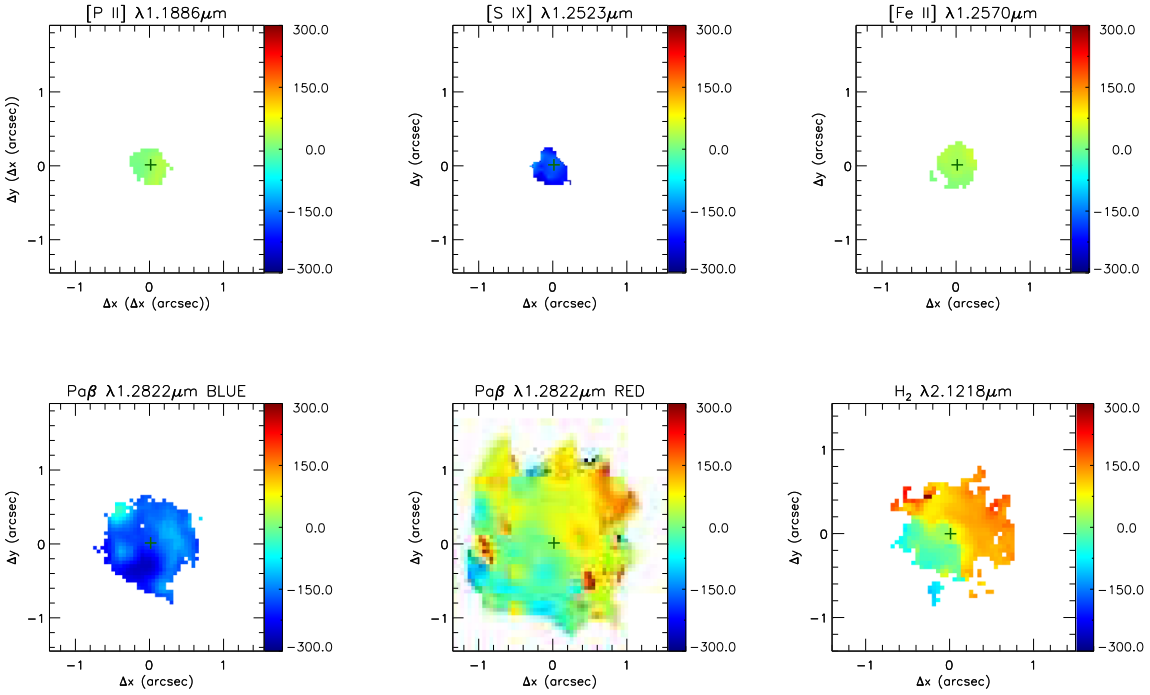

Figure 5. Centroid velocity fields for the [P II]λ1.1886 μm (top-left), [S IX]λ1.2523 μm (top-middle), [Fe II]λ1.2570 μm components (top-right), Pa β blue component (bottom-left), Pa β red component (bottom-middle), $H_2\lambda$2.1218 μm (bottom-right). The central cross marks the position of the nucleus. The colour bars show the velocities in units of km s^{-1}.

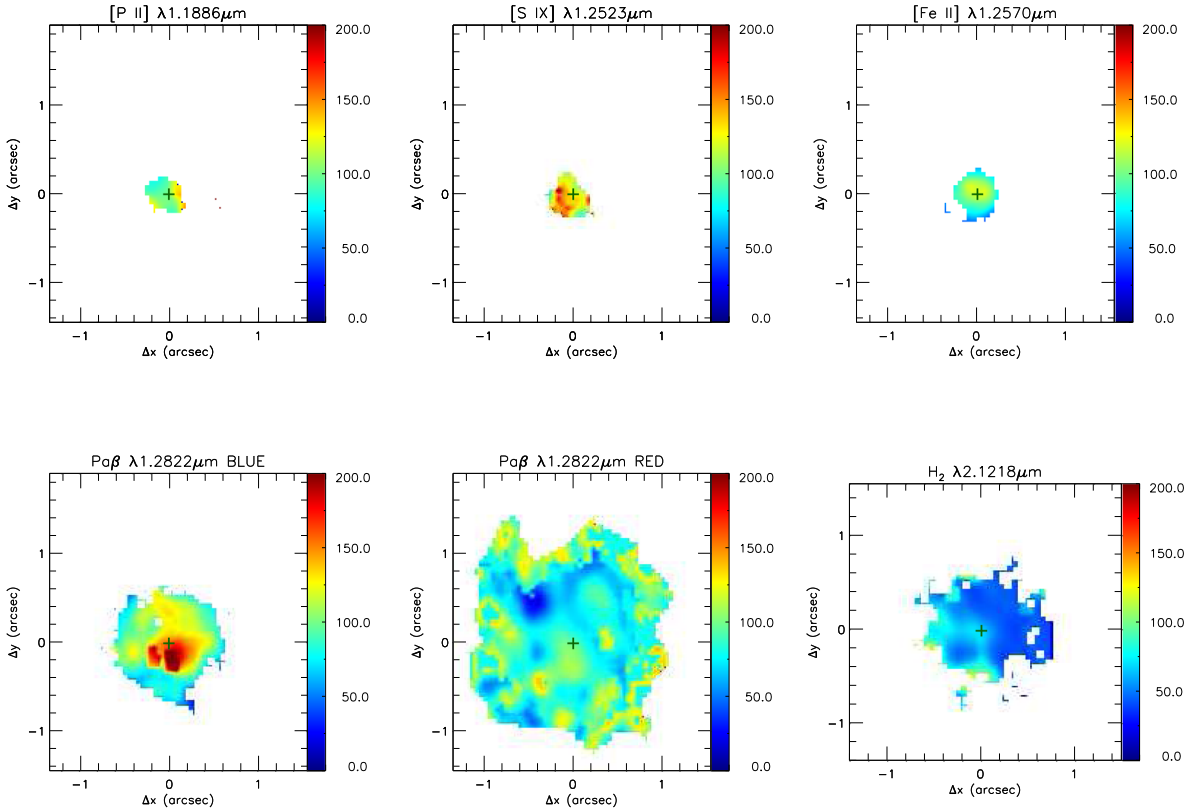

Figure 6. σ maps for the same emission lines of Fig. 5. The central cross marks the position of the nucleus. The colour bars show the σ values in units of km s^{-1}.

velocity v_*. For the NIR the values of σ_* cannot be derived with precision due the low spectral resolution of the EPS models, ergo, we do not use them. By minimizing the following equation we get the final fit

$$\chi^2 = \sum_{\lambda} [(O_\lambda - M_\lambda)\omega_\lambda]^2, \quad (2)$$

with spurious features and emission lines being excluded from the fit by fixing $\omega_\lambda = 0$.

The best fit for the observed spectrum should have the ideal base set of SSPs, since it should cover the range of spectral properties observed in the galaxy sample (Cid Fernandes et al. 2005) and provide enough resolution in age and metalicity. A library of integrated spectra of star clusters is a good base set, since they depend only on ages and metallicities of the stars being free from any assumptions on stellar evolution and initial mass function (Bica & Alloin 1986; Riffel et al. 2011a). So far, though, there is no such library available in the literature for the NIR spectral region. To get around this problem, we used the base set of theoretical SSPs covering this spectral region of Maraston (2005). The NIR carries fingerprints from evolved stars (Riffel et al. 2007; Ramos Almeida, Pérez García & Acosta-Pulido 2009; Martins et al. 2013) and these are crucial to model the absorption line spectra of the galaxies. They include empirical spectra of C- and O-rich stars and thus, are able to predict these features. The base comprises SSP synthetic spectra covering ages from 1 to 15 Gyr according to a grid of 67 models with four metallicities. The final base set comprises 31 ages, $t = 0.0010$, 0.0030, 0.0035, 0.0040, 0.0050, 0.0055, 0.0060, 0.0065, 0.0070, 0.0075, 0.0080, 0.0085, 0.0090, 0.010, 0.015, 0.020, 0.025, 0.030, 0.050, 0.080, 0.2, 0.3, 0.4, 0.5, 0.7, 0.8, 1,1.5, 2, 3, and 13 Gyr, and four metallicities, $Z = 0.02$, 0.5, 1, and 2 $Z_\odot$, with a final set of 124 SSPs.

We also included blackbody functions for temperatures in the range of 700–1400 K in steps of 100 K (Riffel et al. 2009b) and a power law ($F_\nu \propto \nu^{-1.5}$) in order to account for possible blackbody contributions from dust emission (BB) and from featureless continuum (FC), respectively, at the nucleus.

The resulting maps for the spectral synthesis are shown in Figs 8 and 9. Following Riffel et al. (2010b), we have binned the contribution of the SSPs into a reduced population vector with only three components that we call SPC (stellar population component) comprising three age ranges: young (x_y, $t \leq 50$ Myr); intermediate (x_i, 50 Myr $< t \leq 2$ Gyr) and old (x_o, 2 Gyr $< t \leq 15$ Gyr). In Fig. 8, we show the spatial distribution of the per cent flux contribution of each stellar component at 2.12 μm. In the top panels, we show the light-fraction of the SPC contributions and in the bottom panel the mass fraction contributions. Regarding the BB components, shown in Fig. 9 we have grouped them into a cold (BB$_c$, $700 < T < 1000$) and hot (BB$_h$, $1000 < T < 1400$) component.

The old SP flux contribution x_o dominates in a ring of radius ≈0.6 arcsec (230 pc), and in mass the ring extends inwards down to 0.3 arcsec (115 pc) from the nucleus, except for a small region to the east-southeast (E-SE) where the intermediate age component dominates. The largest contribution of the intermediate age SP x_i in light is observed between 0.3 arcsec (115 pc) and 0.5 arcsec (190 pc) and ranges from 40 to 100 per cent, the maximum contribution observed to the E-SE, where it also dominates the contribution in mass, as pointed out above. There is just a small contribution of young SP in light beyond the ring of old SP and around the nucleus (within 0.3 arcsec/115 pc).

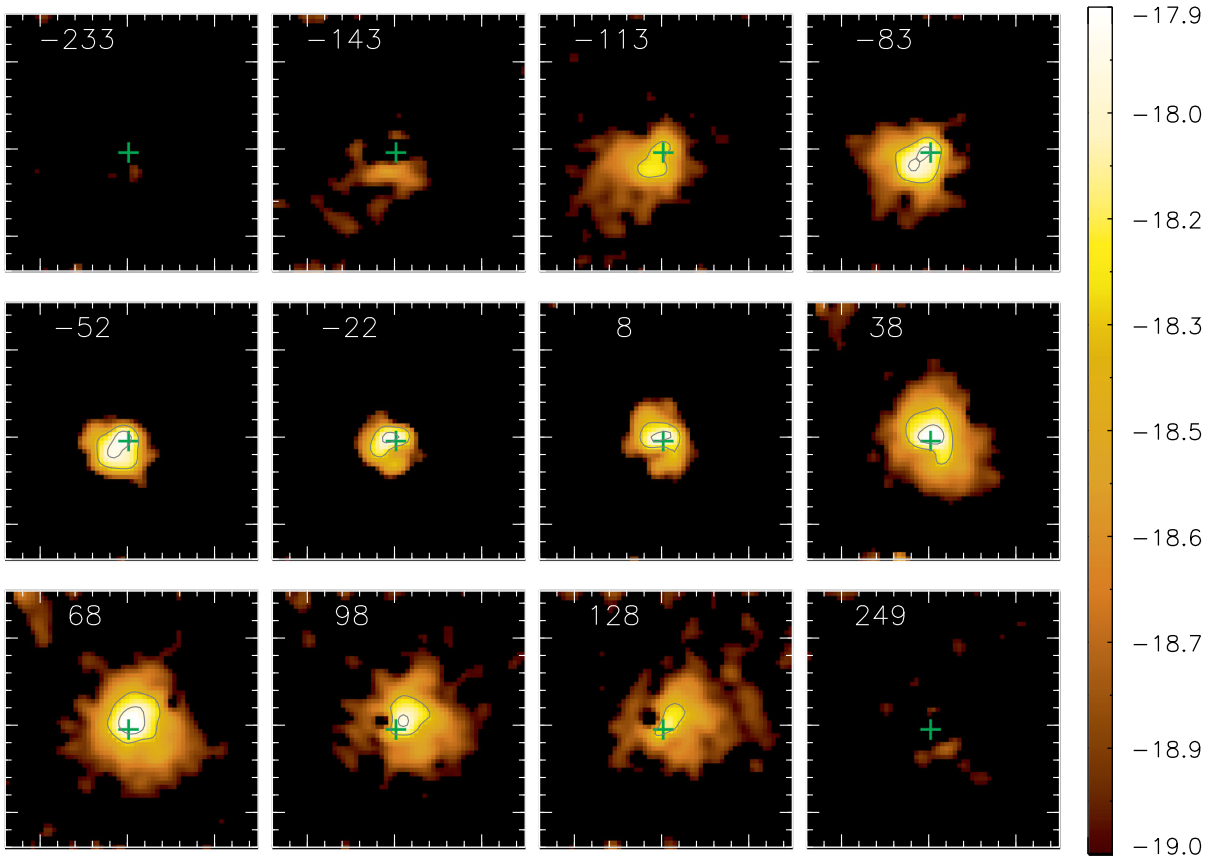

Figure 7. Channel maps along the H_2 emission-line profile, centred at the velocity shown in the upper-left corner of each panel in km s^{-1}. The cross marks the position of the nucleus.

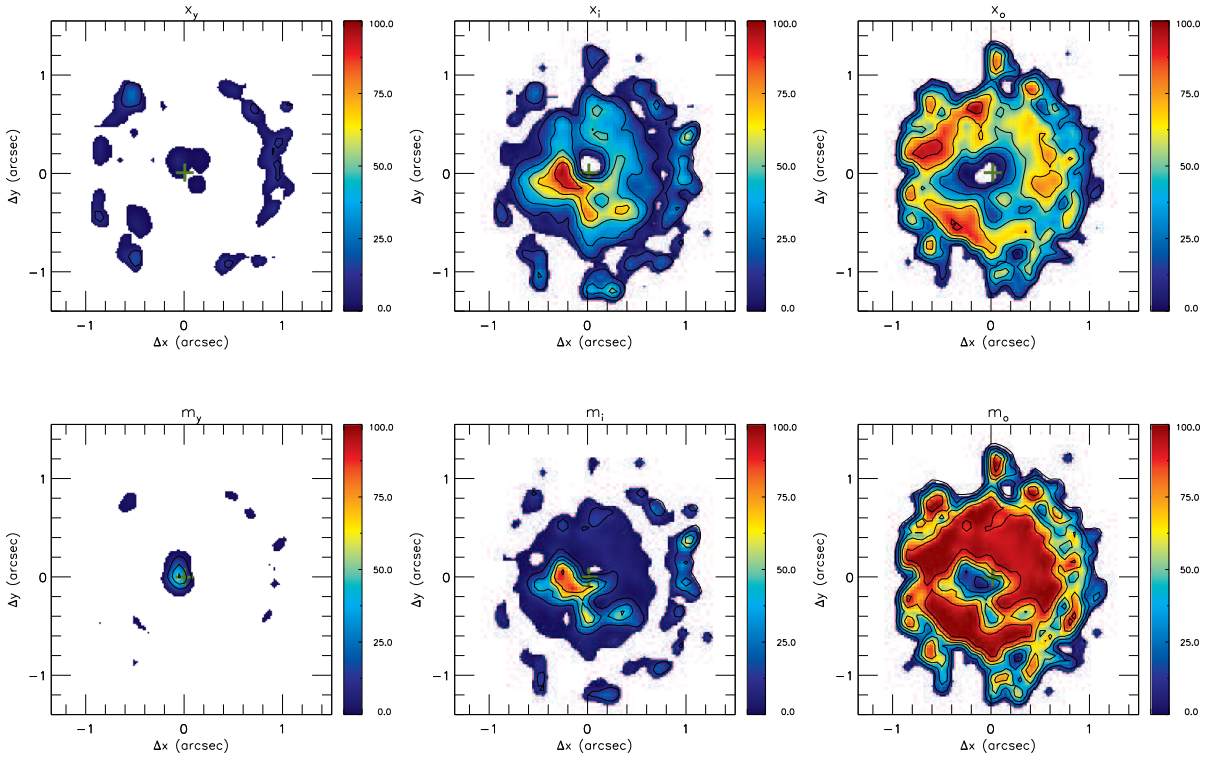

Figure 8. Spatial distributions of the per cent contribution of each SPC to the flux at $\lambda = 2.12$ μm (x_j) (top panels) and to the mass (m_j) (bottom panels), where j represents the age of the SPC: young ($t \leq 50$ Myr); intermediate (50 Myr $< t \leq 2$ Gyr) and old (2 Gyr $< t \leq 15$ Gyr).

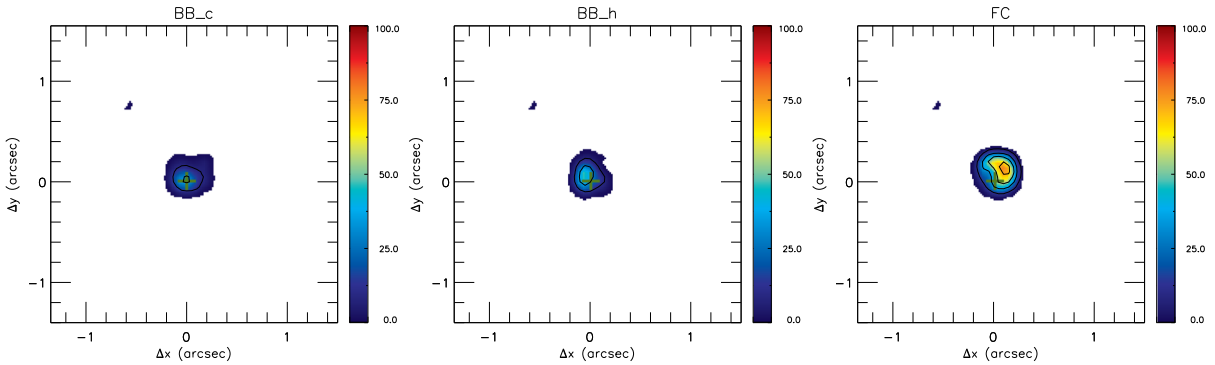

Figure 9. From left to right: spatial distribution of the cold dust emission (BB_c, 0 K < T < 1000 K); the hot dust emission (BB_h, 1000 K < T < 1400 K) and of the featureless continuum, FC.

In Fig. 9, we show the contributions of the BB and FC components. They are observed only at the nucleus and are essentially unresolved, with contributions reaching up to 20 per cent (±10 per cent) for both the hot (BB_h) and cold (BB_c) components and reaching up to 80 per cent (±10 per cent) for the FC.

4 DISCUSSION

4.1 Flux distributions and masses of ionized and molecular gas

The flux distribution is only barely resolved for [P II], [S IX], and [Fe II] emission lines, being more extended for Pa β and H_2, where it reaches 500 pc and 230 pc, respectively, from the nucleus, for a limiting S/N ratio ≈3. We have used the latter two to calculate the masses of the ionized and molecular gas within the inner 1×1 kpc.

The mass of ionized gas in the inner 1×1 kpc of the galaxy can be estimated using (e.g. Scoville et al. 1982; Riffel et al. 2008; Storchi-Bergmann et al. 2009; Schönell et al. 2014)

$$M_{\rm H\,II} \approx 5.1 \times 10^{16} \left(\frac{F_{\rm Pa\,\beta}}{\rm erg\,s^{-1}cm^{-2}}\right) \left(\frac{D}{\rm Mpc}\right)^2 [{\rm M}_\odot], \quad (3)$$

where, $F_{\rm Pa\,\beta}$ is the integrated flux for the Pa β emission line and D is the distance to NGC 5548. We have assumed an electron temperature $T = 10^4$ K and electron density $N_e = 100\,{\rm cm}^{-3}$ (Osterbrock & Ferland 2006).

The mass of warm molecular gas can be obtained using (Scoville et al. 1982)

$$M_{\rm H_2} \approx 5.0776 \times 10^{13} \left(\frac{F_{\rm H_2\lambda2.1218}}{\rm erg\,s^{-1}cm^{-2}}\right) \left(\frac{D}{\rm Mpc}\right)^2 [{\rm M}_\odot], \quad (4)$$

where $F_{\rm H_2\lambda2.1218}$ is the integrated flux for the $H_2\lambda2.1218$ μm emission line and we have used the vibrational temperature $T = 2000$ K (Riffel et al. 2008, 2010b; Storchi-Bergmann et al. 2009; Schönell et al. 2014).

Integrating over the whole IFU field, we obtain the following values for the masses: $M_{\rm H\,II} = 4.8\pm0.6 \times 10^6$ $M_\odot$ and $M_{\rm H_2} = 1.1\pm0.2 \times 10^3$ $M_\odot$, which are similar to those we have obtained in previous studies for other Seyfert galaxies, which are in the range 0.1×10^6 $M_\odot \leq M_{\rm H\,II} \leq 1.7 \times 10^6$ $M_\odot$ (Riffel et al. 2010a; Diniz et al. 2015) and 66 $M_\odot \leq M_{\rm H_2} \leq 3300$ $M_\odot$ (Riffel et al. 2008, 2010a), respectively.

The mass of molecular gas is thus 10^3 times smaller than that of the ionized gas but, as discussed in Storchi-Bergmann et al. (2009), this H_2 mass represents only that of warm gas emitting in the NIR. The total mass of molecular gas is dominated by the cold gas, and the usual proxy to estimate the cold H_2 mass has been the CO emission. A number of studies have derived the ratio between the cold and warm H_2 gas masses by comparing the masses obtained using the CO and NIR emission. Dale et al. (2005) obtained ratios in the range 10^5–10^7; using a larger sample of 16 luminous and ultraluminous infrared galaxies, Müller-Sánchez et al. (2006) derived a ratio $M_{\rm cold}/M_{\rm warm} = 1$–$5\times 10^6$. More recently, Mazzalay et al. (2013) compiled from the literature values of $M_{\rm cold}$ derived from CO observations and H_2 2.12 μm luminosities for a larger number of galaxies, covering a wider range of luminosities, morphological, and nuclear activity types. From that, an estimate of the cold H_2 gas mass can be obtained from

$$M_{\rm H_2\,cold} \approx 1174 \left(\frac{L_{\rm H_2\lambda2.1218}}{L_\odot}\right), \quad (5)$$

where $L_{\rm H_2\lambda2.1218}$ is the luminosity of the $H_2$2.12 μm line. The resulting mass value is $M_{\rm H_2\,cold} = 5.8\pm1.2 \times 10^8$ $M_\odot$.

In order to compare the masses obtained here with those of our previous studies of other galaxies, over different field-of-views, we have also calculated the mass surface density of the ionized and molecular gas distributions. Table 1 shows the integrated mass values, corresponding areas and resulting mass surface densities for NGC 5548 in comparison to those of previous studies by our group. Considering the extents of the flux distributions down to S/N ≈3, the surface densities in ionized and total (warm + cold) molecular gas in NGC 5548 are 7.2±0.8 and 3473±700 $M_\odot$ pc^{-2}, respectively. These values agree with those found in our previous studies, which range from 1.4 to 125 $M_\odot$ pc^{-2} for the mass surface density of ionized gas and 384 to 9600 $M_\odot$ pc^{-2} for the mass surface density of molecular gas as we can see in Table 1.

4.2 Gaseous kinematics

In Fig. 5 we show the centroid velocity fields of the observed emission lines, where the [P II]λ1.1886 μm and [Fe II]λ1.125 70 μm compact (barely resolved) velocity fields show values close to zero, while the [SIX]λ1.2523 μm velocity field is also compact but is all blueshifted to ≈−300 km s^{-1}. The velocity field of Pa β is more extended showing two components: one is all blueshifted, up to −400 km s^{-1}, and the other one shows a rotation pattern, similar to the velocity field observed also for H_2, which will be discussed in the following section.

4.2.1 *Rotation velocity model*

A rotation pattern is observed both for the Pa β red component and H_2 velocity fields (Fig. 5), but that for H_2 is more regular, and the

Table 1. Areas, masses (M) and mass surface densities (μ) for NGC 5548 and previous studied galaxies. The estimated errors are of the order of 20 per cent in the fluxes, and this propagates to the masses and surface mass densities. References: 1 – This work; 2 – Riffel & Storchi-Bergmann (2011); 3 – Riffel et al. (2014); 4 – Riffel et al. (2010a); 5 – Diniz et al. (2015); 6 – Riffel, Storchi-Bergmann & Winge (2013); 7 – Riffel et al. (2008); 8 – Storchi-Bergmann et al. (2009); 9 – Schönell et al. (2014); 10 – Riffel, Storchi-Bergmann & Riffel (2015).

Galaxies	Area (H_2)	Area (H II)	M $(H_2)_h$	M $(H_2)_c$	M (H II)	μ $(H_2)_h$	μ $(H_2)_c$	μ (H II)	Ref.
NGC 5548	1.7×10^5	6.7×10^5	2.3×10^2	1.7×10^8	2.2×10^6	6.6×10^{-3}	3473	7.2	1
Mrk 1157	2.8×10^5	1.8×10^5	2.3×10^3	1.6×10^9	5.4×10^6	8.2×10^{-3}	5714	45	2
NGC 1068	3.8×10^4	1.5×10^4	29	2×10^7	2.2×10^4	7.6×10^{-4}	526	1.5	3
Mrk 1066	2.5×10^5	1.9×10^5	3.3×10^3	2.4×10^9	1.7×10^7	1.3×10^{-2}	9600	89	4
NGC 2110	1.1×10^5	7×10^4	1.4×10^3	9.9×10^8	1.7×10^6	1.3×10^{-2}	9000	24	5
Mrk 79	9.8×10^5	7.8×10^5	3×10^3	2.2×10^9	7×10^6	3.1×10^{-3}	2245	9	6
NGC 4051	1.3×10^4	1.4×10^4	66	4.7×10^7	1.4×10^5	5.3×10^{-3}	3760	9.8	7
NGC 4151	2.4×10^4	1.9×10^4	240	1.7×10^8	2.4×10^6	1.8×10^{-2}	7083	125	8
Mrk 766	3×10^5	2.7×10^5	1.3×10^3	9.8×10^8	7.6×10^6	4.3×10^{-3}	3266	28	9
NGC 5929	1.2×10^5	7×10^4	471	3.5×10^8	1.3×10^6	3.9×10^{-3}	2966	18	10

Note. All mass (M) units are in $M_\odot$, area units in pc^2 and the mass surface densities (μ) in $M_\odot\ pc^{-2}$.

corresponding velocity dispersions are also lower, supporting that the H_2 is more confined to the galaxy plane (as we have observed also in previous studies of other galaxies). Aiming to obtain parameters such as the systemic velocity, orientation of the line of the nodes and the inclination of the disc, we fitted a rotation model for the H_2 centroid velocity field assuming that the emitting gas is rotating in a central potential (Barbosa et al. 2006). For this kinematic model (van der kruit & Allen 1978; Bertola et al. 1991), it is assumed that the gas has circular orbits in a plane, and the velocity field is given by

$$V_{\rm mod}(R, \Psi) = V_{\rm sys} + \frac{A R \cos(\Psi - \Psi_0) \sin\theta \cos^p\theta}{(R^2)(\sin^2(\Psi - \Psi_0) + \cos^2\theta \cos^2(\Psi - \Psi_0) + c_0^2 \cos^2\theta)^{p/2}}, \quad (6)$$

where $v_{\rm sys}$ is the systemic velocity, A is the centroid velocity amplitude, Ψ_0 is the major axis position angle, c_0 is a concentration parameter, θ is the angle between the disc plane and the sky plane, p is a model fitting parameter (which is ≈1 for infinite masses in a Plummer potential) and R and Ψ are the coordinates of each pixel in the plane of the sky.

In the fit, the location of the kinematical centre was not allowed to vary, being fixed to the position of the peak of the continuum, adopted to be the nucleus of the galaxy. In Fig. 10 we show the centroid velocity field of H_2 in the top-left panel, the resulting model from the fit in the top-right panel and residual maps (centroid velocity field of the emitting gas – model) in the bottom panels. The resulting parameters of the fit are: $v_{\rm sys} = 5160 \pm 52$ km s^{-1}, which is close to the systemic velocity reported in De Vaucouleurs et al. (1991) that is 5149 km s^{-1}, $\Psi_0 = 126^\circ$ being 16° higher than the one quoted in NED (Nasa Extragalactic Database), from a large-scale continuum image. The H_2 discs – observed within the inner 400 pc – thus seems to follow the orientation of the large scale disc. The fit also gives an inclination for the disc relative to the plane of the sky of $\theta = 10^\circ$. The best model shows a compact velocity curve, peaking at only ≈200 pc from the nucleus. We have found similarly steep velocity curves for H_2 in our previous studies of active galaxies (Riffel & Storchi-Bergmann 2011; Schönell et al. 2014). Although this velocity field seems not very well constrained in the outer parts (due to the limited coverage of the H_2 velocity field), the residual map for H_2 shows that at most locations the deviations from the model are smaller than ≈40 km s^{-1}. The residuals for the Pa β velocity field are larger, and could be due to the presence of other components and/or a less steep velocity field for this line as we found also in our previous studies of other galaxies.

4.2.2 *Mass outflow rate*

The blueshift observed in the Pa β emission line can be interpreted as due to an outflow and can be used to estimate the gas mass outflow rate. We have assumed a conical geometry in which we considered a possible range for the height (h) of the cone between 1.0 arcsec (384 pc) to 2.0 arcsec (768 pc) – under the assumption that the height of the cone is of the order of the diameter of its base, as we cannot observe this height.

With this range of heights we have the resulting opening angles of ≈27°.5, and ≈53°. The outflow is thus calculated at a distance from the nucleus of 1.0 arcsec and 2.0 arcsec, through a circular area of radius $r = 0.5$ arcsec estimated from Fig. 5. The mass outflow rate can then be estimated by

$$\dot{M}_{\rm out} = m_{\rm p}\, N_{\rm e}\, v\, f\, A \quad (7)$$

and the filling factor (f) can be obtained from

$$f = \frac{L_{\rm Pa\,\beta}}{j_{\rm Pa\,\beta}\, V}, \quad (8)$$

where $m_{\rm p}$ is the proton mass, $N_{\rm e}$ the electron density, v is velocity of the outflowing gas and $L_{\rm Pa\,\beta}$ and $j_{\rm Pa\,\beta}$ are the luminosity and the emission coefficient of Pa β, respectively (Riffel et al. 2011b; Schönell et al. 2014), and the volume of the outflowing region is $v = A \times (h/3)$.

We have assumed that $N_{\rm e} = 500$ cm^{-3} and measured $L_{\rm Pa\,\beta} = 3.89 \pm 0.43 \times 10^{39}$ erg s^{-1}, for $j_{\rm Pa\,\beta} = 4.07 \times 10^{-22}$ erg cm^{-3} s^{-1} (Osterbrock & Ferland 2006) and $v_{\rm out} = 280$ km s^{-1}. The value for the velocity of the outflow ($v = 280$ km s^{-1}) was obtained as the average velocity of the blueshifted component of Pa β. With the geometry described above we obtain $\dot{M}_{\rm out} = 9 \pm 1\ M_\odot\ {\rm yr}^{-1}$ for $h = 1.0$ arcsec and $\dot{M}_{\rm out} = 4.5 \pm 0.5\ M_\odot\ {\rm yr}^{-1}$ for $h = 2.0$ arcsec. The values found here for $\dot{M}_{\rm out}$ are somewhat larger than those we have found in our previous studies of other Seyfert galaxies but are in good agreement with those found in Veilleux et al. (2005) for outflows observed in other active galaxies, which range from 0.1 to 10 $M_\odot\ {\rm yr}^{-1}$, as well as with those found by Müller-Sánchez et al. (2011), which range from 2.5 to 120 $M_\odot\ {\rm yr}^{-1}$.

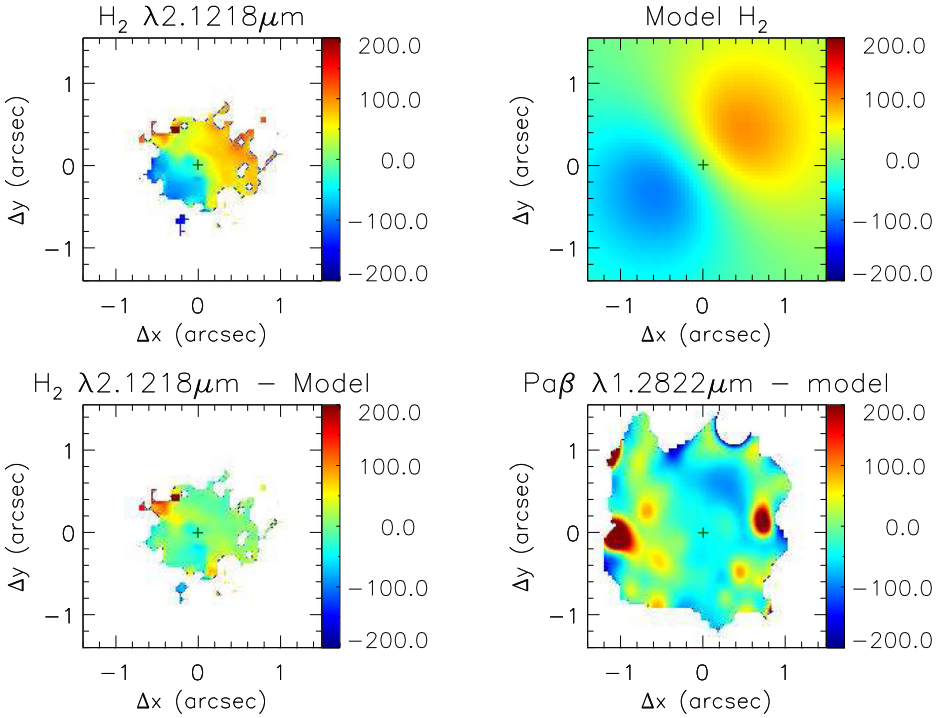

Figure 10. Top panels: H_2 velocity field and fitted rotating disc model; bottom panels: residual maps between the observed velocity fields of H_2 and Pa β and the model.

To estimate the kinetic power of the outflow we can use the following relation (Storchi-Bergmann et al. 2010; Schönell et al. 2014):

$$\dot{E} \approx \frac{\dot{M}_{\rm out}}{2}(v^2 + \sigma^2), \quad (9)$$

where v is the velocity of the outflowing gas and σ is its velocity dispersion. Using $\sigma \approx 130$ km s^{-1} and $v = 280$ km s^{-1}, we obtain $\dot{E} \approx 2.1 \times 10^{41}$ erg s^{-1}. The value found for $\dot{E}$ is in good agreement with those found for Seyfert galaxies and compact radio sources (Morganti, Tadhunter & Oosterloo 2005). This value is similar to that obtained for Mrk 1157 (Riffel & Storchi-Bergmann 2011), of $\dot{E} \approx 5.7 \times 10^{41}$ erg s^{-1} and for Mrk 766 (Schönell et al. 2014), of $\dot{E} \approx 2.9 \times 10^{41}$ erg s^{-1}, it is also within the range of those found by Müller-Sánchez et al. (2011), between 0.6 and 50×10^{41} erg s^{-1}. To compare the $\dot{E}$ value with the bolometric luminosity, we estimate the latter as 10 times the X-ray luminosity of 5.1×10^{42} erg s^{-1} (Rivers, Markowitz & Rothschild 2011), resulting in $\dot{E} \approx 0.004\ L_{\rm Bol}$. This value is about the one quoted in galaxy evolution simulations by Di Matteo, Springel & Hernquist (2005) and Hopkins & Elvis (2010) – 0.5 per cent $L_{\rm Bol}$ – as the necessary power of the outflow to have a significant impact on the evolution of the galaxy.

4.3 Stellar population

From the spectral synthesis we conclude that, at the unresolved nucleus (within ≈0.2 arcsec), the main components contributing to the continuum flux in the NIR are the featureless contribution from the AGN (≈70 per cent) followed by the blackbody components – 20 per cent for both the hot (BB_h) and cold (BB_c) that can be attributed to the dusty torus. Some minor contribution in flux from the young stellar component (≈10 per cent) was also found there.

Moving outwards, in a ring extending from 0.2 arcsec (80 pc) to 0.5 arcsec (190 pc) there is a ≈50 per cent contribution in flux from the intermediate age component that increases to almost 100 per cent in flux and also in mass in a patch to the E-SE of the nucleus. The rest is contributed by the old component that dominates outward from the ring, both in flux and mass.

In general, our results for the SP synthesis are similar to those of our previous works (Riffel et al. 2011b; Storchi-Bergmann et al. 2012) in other Seyfert galaxies, where we have found 100–300 pc circumnuclear rings with increased contribution of young to intermediate age SP.

Results from other authors also support the presence of young to intermediate age stellar populations in circumnuclear rings around AGN. In Davies et al. (2007), for example, the authors investigated the star formation history in the circumnuclear region of a sample of nine Seyfert galaxies using the SINFONI NIR integral field spectrograph with adaptive optics at the Very Large Telescope. With measurements of the Br γ emission-line equivalent widths, supernova rates and mass-to-light ratios, they found circumnuclear discs of typical diameters of tens of pc with a 'characteristic' age in the range 10–300 Myr, corresponding closely to our 'intermediate' age range, therefore agreeing with our results.

5 CONCLUSIONS

We have mapped the gas flux distribution, excitation, and kinematics as well as the SP from the inner ≈500 pc radius of the Seyfert 1 galaxy NGC 5548 using NIR *J*- and *K*-band integral field spectroscopy. The conclusions of this work are listed below.

(i) The emission-line flux distributions of [P II], [S IX], and [Fe II] are barely resolved, extending to ≈150 pc from the nucleus.

(ii) The emission-line flux distributions of Pa β and H_2 are more extended, reaching up to ≈450 pc and ≈300 pc from the nucleus, respectively, observed only in blueshift, at ≈300 km s^{-1}, as due to an outflow approximately perpendicular to the plane of the sky.

(iii) The Pa β emission line has a second component observed in blueshift within ≈300 pc from the nucleus, with velocities ranging from −100 to −400 km s^{-1}. The [S IX] emission is observed only in blueshift , at ≈−300 km s^{-1}. These components have been interpreted as due to an outflow oriented approximately perpendicularly to the plane of the sky.

(iv) The mass outflow rate in ionized gas is estimated to be ≈6.8±0.75 M$_\odot$ yr^{-1}.

(v) The power of the outflow is 0.4 per cent $L_{\rm Bol}$, which is of the order of the minimum necessary to significantly influence (by pushing gas out of the galaxy) the evolution of the galaxy.

(vi) The velocity fields of H_2 and the red component of Pa β show a rotation pattern.

(vii) Fitting a rotation model to the H_2 velocity field, we derived a systemic velocity for the galaxy of 5160±52 km s^{-1}.

(viii) The mass of ionized gas is $M_{\rm H\,II} = 4.8\pm0.6 \times 10^6$ M$_\odot$;

(ix) The mass of the hot molecular gas is $M_{\rm H_2} = 1.1\pm0.2 \times 10^3$ M$_\odot$ and the estimated cold molecular gas mass is $M_{\rm H_2} = 5.8\pm1.2 \times 10^8$ M$_\odot$.

(x) The surface densities in ionized and cold molecular gas are 7.2±0.8 and 3473±700 M$_\odot$ pc^{-2}, respectively.

(xi) Spectral synthesis of the continuum reveals that, at the nucleus, a featureless power-law continuum dominates the flux, with some contribution from blackbody components attributed to a dusty torus and a minor contribution from a young SP.

(xii) Outwards from the nucleus, an intermediate age component contributes with ≈40 per cent in flux in a ring extending from 0.2 arcsec (80 pc) to 0.5 arcsec (190 pc) with an increased contribution in a patch to the E-SE that reaches almost 100 per cent both in flux and in mass, while the remainder contribution is attributed to the old component that dominates also outwards.

ACKNOWLEDGEMENTS

We thank an anonymous referee for useful suggestions which helped to improve the paper. This work is based on observations obtained at the Gemini Observatory, which is operated by the Association of Universities for Research in Astronomy, Inc., under a cooperative agreement with the NSF on behalf of the Gemini partnership: the National Science Foundation (United States), the Science and Technology Facilities Council (United Kingdom), the National Research Council (Canada), CONICYT (Chile), the Australian Research Council (Australia), Ministério da Ciência e Tecnologia (Brazil) and southeastCYT (Argentina). This research has made use of the NASA/IPAC Extragalactic Database (NED) which is operated by the Jet Propulsion Laboratory, California Institute of Technology, under contract with the National Aeronautics and Space Administration. This work has been partially supported by the Brazilian institution CNPq.

REFERENCES

Asari N. V., Cid Fernandes R., Stasínska G., Torres-Papaqui J. P., Mateus A., Sodré L., Schoenell W., Gomes J. M., 2007, MNRAS, 381, 263
Barbosa F. K. B., Storchi-Bergmann T., Cid Fernandes R., Winge C., Schmitt H., 2006, MNRAS, 371, 170
Barillard A. et al., 2011, A&A, 532, 74
Bertola F., Bettoni D., Danziger J., Sadler E., Sparke L., de Zeeuw T., 1991, ApJ, 373, 369
Bica E., Alloin D., 1986, A&A, 162, 21
Cardelli J. A., Clayton G. C., Mathis J. S., 1989, ApJ, 345, 245
Cid Fernandes R., Gu Q., Melnick J., Terlevich E., Terlevich R., Kunth D., Rodrigues Lacerda R., Joguet B., 2004, MNRAS, 355, 273
Cid Fernandes R., Mateus A., Sodré Laerte, Stasínska G., Gomes J. M., 2005, MNRAS, 358, 363
Cid Fernandes R. et al., 2009, Rev. Mex. Astron. Astrofis. Ser. Conf., 35, 127
Crenshaw D. M., Kraemer S. B., 2007, ApJ, 659, 250
Crenshaw D. M., Kraemer S. B., Schmitt H. R., Kaastra J. S., Arav N., Gabel J. R., Korista K. T., 2009, ApJ, 698, 281
Crenshaw D. M., Schmitt H. R., Kraemer S. B., Mushotsky R. F., Dunn J. P., 2010, ApJ, 708, 419
Dale D. A., Sheth K., Helou G., Regan M. W., Hüttemeister S., 2005, AJ, 129, 2197
Davies R. I., Sánchez F. M., Genzel R., Tacconi L. J., Hicks E. K. S., Friedrich S., Sternberg A., 2007, ApJ, 671, 1388
Davies R. I. et al., 2014, ApJ, 792, 101
Davies R. I., Maciejewski W., Hicks E. K. S., Tacconi L. J., Genzel R., Engel H., 2009, ApJ, 702, 114
de Vaucouleurs G., de Vaucouleurs A., Corwin H. G. Jr Buta R. J., Paturel G., Fouqué P., 1991, Third Reference Catalogue of Bright Galaxies. Springer, New York
Di Matteo T., Springel V., Hernquist L., 2005, Nature, 433, 604
Diniz M. R., Riffel R. A., Storchi-Bergmann T., Winge C., 2015, MNRAS, 453, 1727
Fathi K., Storchi-Bergmann T., Riffel R. A., Winge C., Axon D. J., Robinson A., Capetti A., Marconi A., 2006, ApJ, 641, L25
Ferruit P., Wilson A. S., Mulchaey J., 2000, ApJS, 128, 139
Fischer T. C., Crenshaw D. M., Kraemer S. B., Schmitt H. R., Mushotsky R. F., Ward M. J., 1993, ApJ, 727, 71
Fischer T. C., Crenshaw D. M., Kraemer S. B., Schmitt H. R., Trippe M. L., 2010, AJ, 140, 577
Holt J., Tadhunter C., Morganti R., Bellamy M., González Delgado R. M., Tzioumis A., Inskip K. J., 2006, MNRAS, 370, 1633
Hopkins P. F., Elvis M., 2010, MNRAS, 401, 7
McGregor P. J. et al., 2003, in Iye M., Moorwood A. F. M., eds, Proc. SPIE Conf. Ser. Vol. 4841, Instrument Design and Performance for Optical/Infrared Ground-based Telescopes. SPIE, Bellingham, p. 1581
Malkan M. A., Gorjian V., Tam R., 1998, ApJS, 117, 25
Maraston C., 2005, MNRAS, 362, 799
Martins L. P., Rodríguez-Ardila A., Diniz S., Riffel R., de Souza R., 2013, MNRAS, 435, 2861
Mateus A., Sodré L., Cid Fernandes R., Stasínska G., Schoenell W., Gomes J. M., 2006, MNRAS, 370, 721
Mazzalay X., Rodríguez-Ardila A., Komossa S., 2010, MNRAS, 405, 1315
Mazzalay X. et al., 2013, MNRAS, 428, 2389
Morganti R., Tadhunter C. N., Oosterloo T. A., 2005, A&A, L9, L13
Müller-Sánchez F., Davies R. I., Eisenhauer F., Tacconi L. J., Genzel R., Sternberg A., 2006, A&A, 454, 492
Müller Sánchez F., Davies R. I., Genzel R., Tacconi L. J., Eisenhauer F., Hicks E. K. S., Friedrich S., Sternberg A., 2009, ApJ, 691, 749
Müller-Sánchez F., Prieto M. A., Hicks E. K. S., Vives-Arias H., Davies R. I., Malkan M., Tacconi L. J., Genzel R., 2011, ApJ., 739, 69
Osterbrock D. E., Ferland G. J., 2006, Astrophysics of Gaseous Nebulae and Active Galactic Nuclei, 2nd edn. University Science Books, Mill Valley, CA
Ramos Almeida C., Pérez García A. M., Acosta-Pulido J. A., 2009, ApJ, 694, 1379
Riffel R. A., 2010, Ap&SS, 327, 239
Riffel R. A., Storchi-Bergmann T., 2011, MNRAS, 411, 469
Riffel R. A., Sorchi-Bergmann T., Winge C., Barbosa F. K. B., 2006, MNRAS, 373, 2
Riffel R., Pastoriza M. G., Rodríguez-Ardila A., Maraston C., 2007, ApJ, 659, 103
Riffel R. A., Storchi-Bergmann T., Winge C., McGregor P. J., Beck T., Schmitt H., 2008, MNRAS, 385, 1129
Riffel R. A., Storchi-Bergmann T., Dors O. L., Winge C., 2009a, MNRAS, 393, 783
Riffel R., Pastoriza M. G., Rodríıguez-Ardila A., Bonatto C., 2009b, MNRAS, 400, 273
Riffel R. A., Storchi-Bergmann T., Nagar N. M., 2010a, MNRAS, 404, 166

Riffel R. A., Storchi-Bergmann T., Riffel R., Pastoriza M. G., 2010b, ApJ, 713, 469
Riffel R., Ruschel-Dutra D., Pastoriza M. G., Rodríguez-Ardila A., Santos J. F. C., Jr, Bonatto C. J., Ducati J. R., 2011a, MNRAS, 410, 2714
Riffel R., Riffel R. A., Ferrari F., Storchi-Bergmann T., 2011b, MNRAS, 416, 493
Riffel R. A., Storchi-Bergmann T., Winge C., 2013, MNRAS, 430, 2249
Riffel R. A., Tibério V. B., Storchi-Bergmann T, McGregor P. J., 2014, MNRAS, 442, 656
Riffel R. A., Storchi-Bergmann T., Riffel R., 2015, MNRAS, 451, 3587
Riffel R. A. et al., 2016, MNRAS, 461, 4205
Rivers E., Markowitz A., Rothschild R., 2011, ApJS, 193, 3
Rodríguez-Ardila A., Prieto M. A., Viegas S., Gruenwald R., 2006, ApJ, 653, 1098
Schmitt H. R., Kinney A. L., 1996, ApJ, 463, 498
Schnorr Müller A., Storchi-Bergmann T., Riffel R. A., Ferrari F., Steiner J. E., Axon D. J., Robinson A., 2011, MNRAS, 413, 149
Schönell A. J. J., Riffel R. A., Storchi-Bergmann T., Winge C., 2014, MNRAS, 445, 427
Scoville N. Z., Hall D. N. B., Kleinmann S. G., Ridgway S. T., 1982, ApJ, 253, 136
Storchi-Bergmann T., Dors O., Jr, Riffel R. A., Fathi K., Axon D. J., Robinson A., 2007, ApJ, 670, 25
Storchi-Bergmann T., McGregor P., Riffel R., Rogemar A., Simões Lopes R., Beck T., Dopita M., 2009, MNRAS, 394, 1148
Storchi-Bergmann T., Simões Lopes R., McGregor P. Riffel, Rogemar A., Beck T., Martini P., 2010, MNRAS, 402, 819
Storchi-Bergmann T., Riffel R. A., Riffel R., Diniz M. R., Borges V. T., McGregor P. J., 2012, ApJ, 755, 87
van der Kruit P. C., Allen R. J., 1978, ARA&A, 16, 103
Veilleux S. A., Goodrich R. W., Hill G. J., 1997, ApJ, 477, 631
Veilleux S., Cecil G., Bland-Hawthorn J., 2005, ARA&A, 43, 769
Wilson A. S., Braatz J. A., Heckman T. M., Krolic J. H., Miley G. K., 1993, ApJ, 419, L61

This paper has been typeset from a TEX/LATEX file prepared by the author.

Mon. Not. R. Astron. Soc. **000**, 1–19 (2017) Printed 6 September 2017 (MN LATEX style file v2.2)

Gemini NIFS survey of feeding and feedback processes in nearby Active Galaxies: III - Gas distribution and excitation

Astor J. Schönell Jr.[1⋆], Thaisa Storchi-Bergmann[1], Rogemar A. Riffel[2], Rogério Riffel[1], Luis G. Dahmer-Hahn[1], Marlon R. Diniz[2], Natacha Z. Dametto[1]
[1] *Instituto de Física, Universidade Federal do Rio Grande do Sul, Av. Bento Goncalves 9500, 91501-970 Porto Alegre, RS, Brazil*
[2] *Universidade Federal de Santa Maria, Departamento de Física, Centro de Ciências Naturais e Exatas, 97105-900, Santa Maria, RS, Brazil*

19/04/2017

ABSTRACT

We used the Gemini Near-Infrared Field Spectrograph (NIFS) to map the gas distribution, kinematics and excitation of the inner few hundreds parsecs of a sample of 6 active nearby galaxies: NGC 788, Mrk 607, NGC 3227, NGC 3516, NGC 5506, NGC 5899. Molecular and ionized gas present distinct flux distributions: while the first is usually distributed uniformly and spread over the whole galaxy plane, the latter is more collimated along a direction that corresponds to the ionization axis of its Active Galactic Nucleus (AGN).

The molecular and ionized gases are also different in their kinematics: while the molecular gas is mostly rotating in the galaxy plane with low velocity dispersion, the ionized gas usually shows other components – usually outflows – associated with higher velocity dispersions.

The integrated mass of hot molecular gas ranges from 182 to 1400 $M_\odot$, while the cold molecular mass is estimated to range from 1.3×10^7 to 1×10^9 $M_\odot$. In the case of the ionized gas, the integrated mass is in the range 3×10^5 – 3.2×10^7 $M_\odot$. We have also obtained average surface mass densities for the hot (cold) molecular gas in the range 1.6×10^{-3} – 1.4×10^{-2} $M_\odot/pc^2$ (1319 – 20682 $M_\odot/pc^2$), while for the ionized gas the range is 4.8 – 244 $M_\odot/pc^2$. Average profiles of the surface mass density distributions show a steeper decrease with distance from the nucleus for the ionized gas than for the molecular gas, due to the distinct nature of the excitation of the lines. The diagnostic diagram [Fe II]λ1.252/Paβ *vs* H_2 λ 2.122/Brγ show in three cases Starburst-like excitation values at the nucleus (within 100-200 pc), surrounded by Seyfert-like values and then outwards LINER like values, while the other cases show Seyfert values close to the nucleus, surrounded by LINER excitation outwards.

Key words: Galaxies: active – Galaxies: Seyfert – Galaxies: nuclei – Galaxies: excitation

1 INTRODUCTION

The excitation and the gas distribution around Active Galactic Nuclei (AGN) provide important information to understand the physics involved in the AGN feeding and feedback processes. The Near-IR integral field spectroscopy (IFS) of nearby galaxies is an effective method to better understand these processes. With 8-10 m telescopes IFS can provide two-dimensional coverage with spatial resolution of a few to tens of parsecs at a spectral resolution capable to resolve isolated inflows and outflows in the vicinity of the central engine (Müller Sánchez et al. 2009; Davies et al. 2009, 2014). In the Near-IR wavelenghts the dust extinction at the central regions of galaxies is less important than at the optical band, plus, strong absorption CO bands are present in the galaxies spectra, originated in giant and super-giant

⋆ E-mail: juniorfisicoo@gmail.com

stars that dominate the continuum emission for the central regions. Also, adaptative optics systems are available mainly in the Near-IR, another reason to chose this spectral band to resolve the central regions down to a few parsecs or tens of parsecs.

The growth of the super-massive black holes (SMBH) and their host galaxies are deeply related to the AGN feeding and feedback processes, which can explain the correlation between the mass of the SMBH and the mass of the galaxy bulge (Ferrarese & Ford 2005; Somerville et al. 2008; Kormendy & Ho 2013). To trigger the nuclear activity the feeding processes are required, while the feedback processes are fundamental to constrain galaxy evolution models, since without the AGN feedback, the models do not reproduce the properties of the massive galaxies (massive galaxies end up forming too many stars ;Springel et al. (2005); Fabian et al. (2012); Terrazas et al. (2016)).

The ionized and molecular gas have distinct flux distributions and kinematics in the inner kpc of active galaxies. The Near-IR line-emission at ≈ 100 pc scales is originated by the heating and ionization of the ambient gas by the AGN radiation and shocks produced by radio jets (Riffel et al. 2006a, 2010). Recent observations by our group and others show that the ionized and molecular gas have distinct flux distributions and kinematics at these scales. The molecular emitting gas is usually more restricted to the plane of galaxies, with the kinematics being dominated by rotation and inflows from the disk in most cases. The ionized gas emission traces a more disturbed medium, usually associated to outflows from the AGN, but frequently showing also a rotation component from the disk of the galaxy (Riffel et al. 2010; Mazzalay et al. 2014).

In this paper we show the gas distribution and excitation, as well as the gas kinematics of the inner $3\farcs3$ of a sample of 6 nearby Seyfert galaxies. In the present paper we discuss mostly the gas distribution and masses as well as its excitation. Although we present measurements of the gas kinematics, its modeling and analysis will be discussed in a forthcoming paper.This work is the third paper with the results of a large Gemini proposal in which our group AGNIFS (AGN Integral Field Spectroscopy) aims to map and quantify the feeding and feedback processes of a sample of 30 nearby Seyfert galaxies, selected for their proximity and X-ray luminosity, as described bellow. Our goal is to investigate possible correlations among measured properties and with the AGN luminosity. The gas distribution and excitation of this X-ray sample galaxies plus those of a complementary sample (not selected from X-rays) have been discussed in previous papers by our group: NGC 4051 (Riffel et al. 2008, 2017), NGC 4151 (Storchi-Bergmann et al. 2009, 2010; Riffel et al. 2009), Mrk 1066 (Riffel et al. 2010; Riffel & Storchi-Bergmann 2011; Ramos Almeida et al. 2009; Riffel et al. 2017), Mrk 1157 (Riffel & Storchi-Bergmann 2011; Riffel et al. 2011b, 2017), NGC 1068 (Storchi-Bergmann et al. 2012; Riffel et al. 2014; Barbosa et al. 2014), Mrk 79 (Riffel et al. 2013), Mrk 766 (Schönell et al. 2014; Riffel et al. 2017), NGC5929 (Riffel et al. 2014, 2015, 2017), NGC 2110 (Diniz et al. 2015; Riffel et al. 2017), NGC 5548 (Schönell et al. 2017; Riffel et al. 2017), NGC 788, NGC 3227, NGC 3516, NGC 4235, NGC 4388, NGC 5506, NGC 1052, NGC 5899 and Mrk 607 (Riffel et al. 2017).

This paper is organized as follows. Section 2 presents the sample; section 3 the description of the observations and data reduction procedure, while the measurement of the emission lines is presented in sec. 4. The results are presented in section 5, the discussion of each individual galaxy is presented in section 6, and in Section 7, we present our conclusions.

2 SAMPLE

Our sample of AGN was selected from the Swift-BAT 60-month catalogue adopting three principal criteria: (I) have 14195 keV luminosities $L_X \geqslant 10^{41.5}$ erg s^{-1}, (II) redshift z$\leqslant$0.015, and (III) being accessible for NIFS ($30^o < \delta < 73^o$). The hard (14195 keV) band of the Swift-BAT survey measures direct emission from the AGN rather than scattered or re-processed emission, and is much less sensitive to obscuration in the line-of-sight than soft X-ray or optical wavelengths, allowing a selection based only on the AGN properties. In order to assure that we will be able to probe the feeding and feedback processes we further selected the galaxies for having previously observed extended gas emission (Schmitt & Kinney 2000) and [O III]λ5007 luminosities. We have excluded from the sample a few galaxies that had guiding problems in the observations and included all aditional targets from our previous NIFS observations to be used to complement the sample. The total sample is composed by 30 galaxies. A complete characterization of the sample will be presented in a forthcoming paper (Riffel et al., in preparation, hereafter Rif17). The observations are still in progress and will probably be concluded in 2017. So far, 20 galaxies have already been observed and this work shows the gas distribution and excitation for 6 of them.

3 OBSERVATIONS AND DATA REDUCTION

We used observations obtained with the Gemini Near-Infrared Integral-Field Spectrograph (NIFS; McGregor et al. (2003)) with the Adaptive Optics system ALTAIR between 2008 and 2016. The observations of the targets listed in Tab. 1 followed the standard Object-Sky-Sky-Object dither sequence, with off-source sky positions since all targets are extended and the individual exposure times varied according to the target. Observations were obtained in the J band using the J_G5603 grating and ZJ_G0601 filter, centered at 1.25μm and covering the spectral range from 1.14 to 1.36μm and in the K and K$_l$ band the filter used was HK_G0603 and the gratings Kl_G5607 and K_G5605, where K band was centred at 2.2μm and the K$_l$ band centred at 2.3μm, covering the spectral range from 1.98 to 2.4 μm for the K band and from 2.08 to 2.5μm for the K$_l$ band. The spectral resolution in J band ranges between 1.7 and 1.8 Å, and from 3.2 to 3 Å for the K and K$_l$ band. These spectral resolutions were obtained from the measurement of the full width at half maximum (FWHM) of ArXe lamp lines, used to wavelength calibrate the spectra, close to the central wavelength. This translates to resolutions in the velocity space in the range 41 to 43 km s^{-1} for the J band and from 42 to 47 km s^{-1} for the K and K$_l$ band. The angular resolution for the J band is in the range $0\farcs13$ to $0\farcs17$ and for the K and K$_l$ band from

0.″12 to 0.″20 derived from the FWHM of flux distribution of the standard stars, corresponding to few tens of parsecs at the distance of most galaxies.

The data reduction followed the standard procedure and was accomplished using tasks specifically developed for NIFS data reduction, contained in the nifs package, which is part of gemini IRAF package, as well as generic iraf tasks and IDL scripts. The data reduction procedure included the trimming of the images, flatfielding, sky subtraction, wavelength and s-distortion calibrations. The telluric absorptions have been removed using observations of telluric standard stars with A spectral type. These stars were used to flux calibrate the spectra of the galaxies by interpolating a black body function to their spectra. Finally, datacubes were created for each individual exposure at an angular sampling of 0.″05×0.″05 and combined in a final datacube for each galaxy. All datacubes cover the inner ≈ 3.″0×3.″0 and have typical spectra as shown in Fig. 1.

4 MEASUREMENTS

In order to obtain the flux, centroid velocity, velocity dispersion and the Gauss-Hermite moments h_3 and h_4 we, we used the PROFIT routine (Riffel 2010) to fit the profiles of [P II]λ1.1886μm, [Fe II]λ1.2570μm, Pa$\beta\lambda$1.2822μm, $H_2\lambda$2.1218μm and Br$\gamma\lambda$2.1661μm emission lines at each pixel over the whole field-of-view (FOV) using Gauss-Hermite series. The fit of Gauss Hermite series was chosen because it preserves the velocity information of the emitting gas by fitting the wing of the emission line profiles. This information could be lost in the fit of a single Gaussian curve due to an asymmetric emission line profile. The h_3 Gauss-Hermite moment measures asymmetric deviation from a Gaussian profile, such as blue (negative values) or red (positive values) wings, while the h_4 moment quantify the peakness of the profile, with positive values of h_4 for a more peaked profile and negative values of h_4 for a broader profile than a Gaussian curve. The erros in the parameters are the formal 1-sigma errors, computed from the covariance matrix.

In the case of NGC 3227, NGC 3516 and NGC 5506 we also fitted a broad component to the Paβ and Brγ emission line profiles. This was done via a modification of the PROFIT routine to fit the broad component and subtract its contribution from the profiles in order to generate a data cube only with the narrow components. The steps to do such task were: (I) fit only one Gaussian to the broad component; (II) subtract it from the spectra in which it is present, and (III) fit the narrow component.

5 RESULTS

The results of the fit are shown as maps of: flux distributions, centroid velocities, velocity dispersion, h_3 and h_4 moments as well as E(B-V) and emission line ratio maps, presented in Fig. 2 for NGC 788, Fig. 3 for Mrk 607, Fig. 4 for NGC 3227, Fig. 5 for NGC 3516, Fig. 6 for NGC 5506 and Fig. 7 for NGC 5899. We chose to show the results only for [Fe II]λ1.2570μm, Pa$\beta\lambda$1.2822μm (or Br$\gamma\lambda$2.1661μm in one case) and $H_2\lambda$2.1218μm because these are the strongest emission lines allowing the mapping of the ionized gas properties via the [Fe II] and Paβ (Brγ) emission lines, and the hot molecular gas properties via the H_2 emission line. The results for each mapped property are going to be discussed in the next subsections separately.

In the maps discussed below, we have masked out bad fits, flagged as follows: (i) when the line flux error is larger than 50%; (ii) when the error in the velocity or velocity dispersion is larger than 50 km s^{-1}; (iii) when the χ^2 is larger than 0.6. For the line ratios and h_3 and h_4 moments a further masking was used: these maps were restricted to regions where the flux in the line was higher than tree times the standard deviation of the sky value. This was necessary because the errors in the line ratios are "amplified" relative to those in the line fluxes while the wings of the profile that determine the h_3 and h_4 values are faint and less constrained than the other profile parameters.

5.1 Flux Distributions

The flux distribution maps are shown in the first row of Figs. 2, 3, 4, 5, 6 and 7, where we have ploted the PA of the major axis of the galaxy as given in HYPERLEDA database (Prugniel et al. 2001) over the continuum galaxy images (leftmost panel) and H_2 flux maps. All maps have their peak fluxes at the same position, which coincides with that of the peak of the continuum, that we identify as the galaxy nucleus. Most line fluxes cover the whole FOV corresponding to a maximum distance from the nucleus variyng from 100 pc for NGC 3227 to 410 pc for NGC 788.

The largest extent of the [Fe II] flux distribution usually follows the major axis of the galaxy. Exceptions are the cases of NGC 788 where it is colimated and oriented at a small angle relative to the major axis, and NGC 5506, where its largest extent is perpendicular to the major axis.

The Paβ flux distribution is also more extended along the major axis of the galaxy, except in the case of NGC 788, where it shows a similar colimation to that of [Fe II].

A similar behavior – concentration along the major axis – is observed for the H_2 flux distribution which are however usually more extended in all directions than the ionized gas. The only exception is NGC 788, for which the H_2 emission is perpendicular to the major axis.

5.2 Emission Line-ratios

The emission line-ratios maps are shown in the first column of Figs. 2, 3, 4, 5, 6 and 7, below the galaxy image, together with the E(B-V) map.

E(B-V) values range from 0 to 3 (except for NGC 5506), reaching the highest values at the nucleus for NGC 5506 (E(B-V) ≈ 5) and NGC 5899 (E(B-V) ≈ 3) while for the others the highest values are observed outwards.

The [Fe II]λ1.2570μm/Paβ ratio map show values in the range 0 – 2 for most cases, except for NGC 3227 and NGC 5899 for which it reaches ≈ 10. The usual behavior is an increase of the line ratio from the center outwards.

The [Fe II]λ1.2570μm/[P II]λ1.8861μm values range from 0 to ≈ 10 for most maps, except for 2 cases: NGC 3227 and NGC 5899 where its superior limit reaches ≈ 30, again outwards from the center.

Table 1. (1) Galaxy name; (2) Project ID (3) Exposure Time(s); (4) Distance (Mpc); (5) Nuclear Activity; (6) Hubble type as quoted in NED.

1 Galaxies	2 Project ID	3 Exp. T.	4 D	5 Act.	6 Hub. type
NGC788	GN-2015B-Q-29	4400	56.1	Sy2	SA0/a(s)
Mrk607	GN-2012B-Q-45	6000	36.1	Sy2	Sa edge-on
NGC3227	GN-2016A-Q-6	2400	14.8	Sy1.5	SAB(s)a pec
NGC3516	GN-2015A-Q-3	4500	38.0	Sy1.5	(R)SB0^0(s)
NGC5506	GN-2015A-Q-3	4000	24.9	Sy1.9	Sa pec edge-on
NGC5899	GN-2013A-Q-48	4600	36.8	Sy2	SAB(rs)c

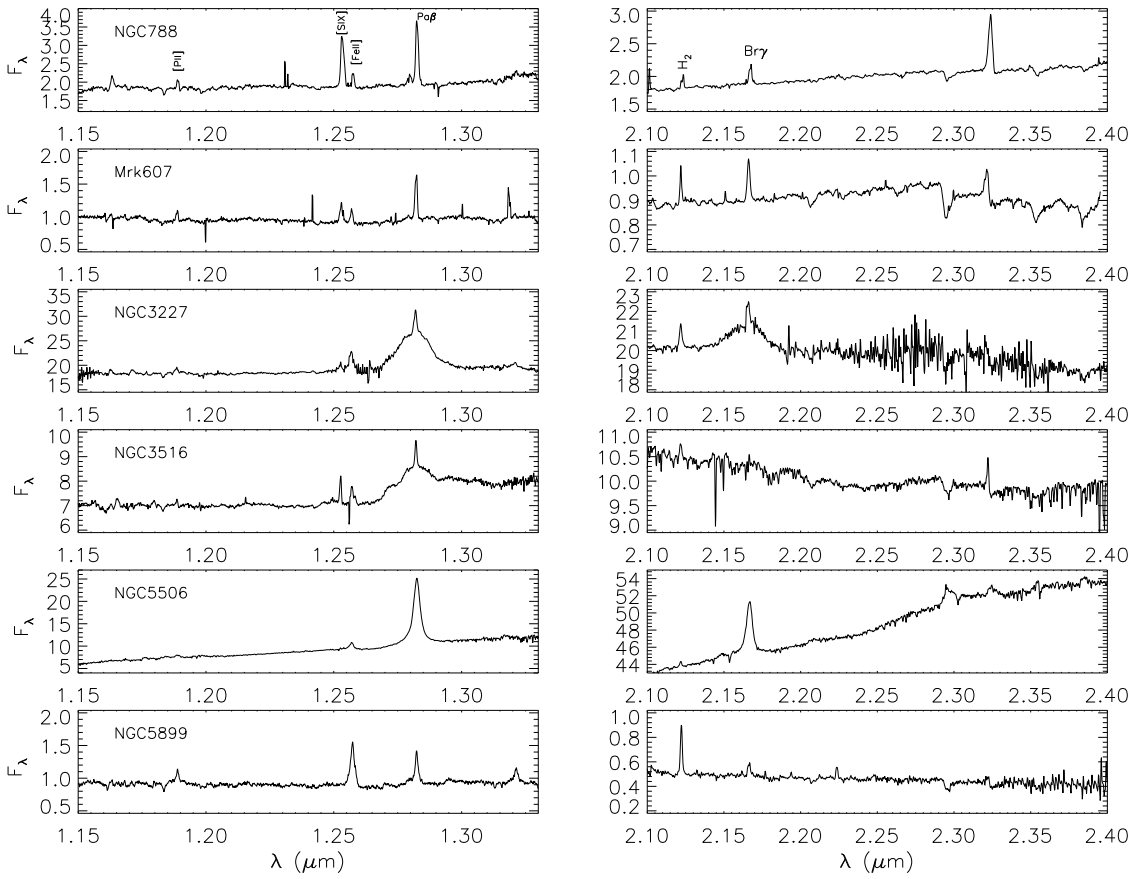

Figure 1. Spectra obtained within a 0.″25x0.″25 aperture at the nucleus of the galaxies indicated in the top lef of each spectra. The flux units are 10^{-16} erg s^{-1} cm^{-2} Å^{-1}.

The last ratio map is $H_2\lambda2.1218\mu$m/Brγ, which is usefull to investigate the excitation of the H_2 emission line (Rodríguez-Ardila et al. 2004, 2005; Riffel, Rodríguez-Ardila & Pastoriza 2006; Riffel et al. 2008b, 2009; Storchi-Bergmann et al. 2009). Values for this ratio are observed from 0 to 15, reaching the highest values for NGC 3227 and NGC 5899. The smallest values – in the range 0-2 – are observed for NGC 788 and NGC 5506. For all cases we observe the higher values outside the nucleus.

5.3 Centroid Velocities

The centroid velocity fields are shown in the second line of the figures after the subtraction of the heliocentric systemic velocity of each galaxy, which were obtained through the fit of a rotating disk model to the H_2 velocity field and will be discussed in a forthcoming paper (Schönell et al., in preparation, hereafter Sch17). Most [Fe II] and Paβ velocity fields show a disturbed rotation pattern (i.e. we see the signature of a "spider diagram" but it is distorted). The exception is NGC 5899 where we do not see a rotation pattern. The H_2 velocity fields, on the other hand, show a clearer (less

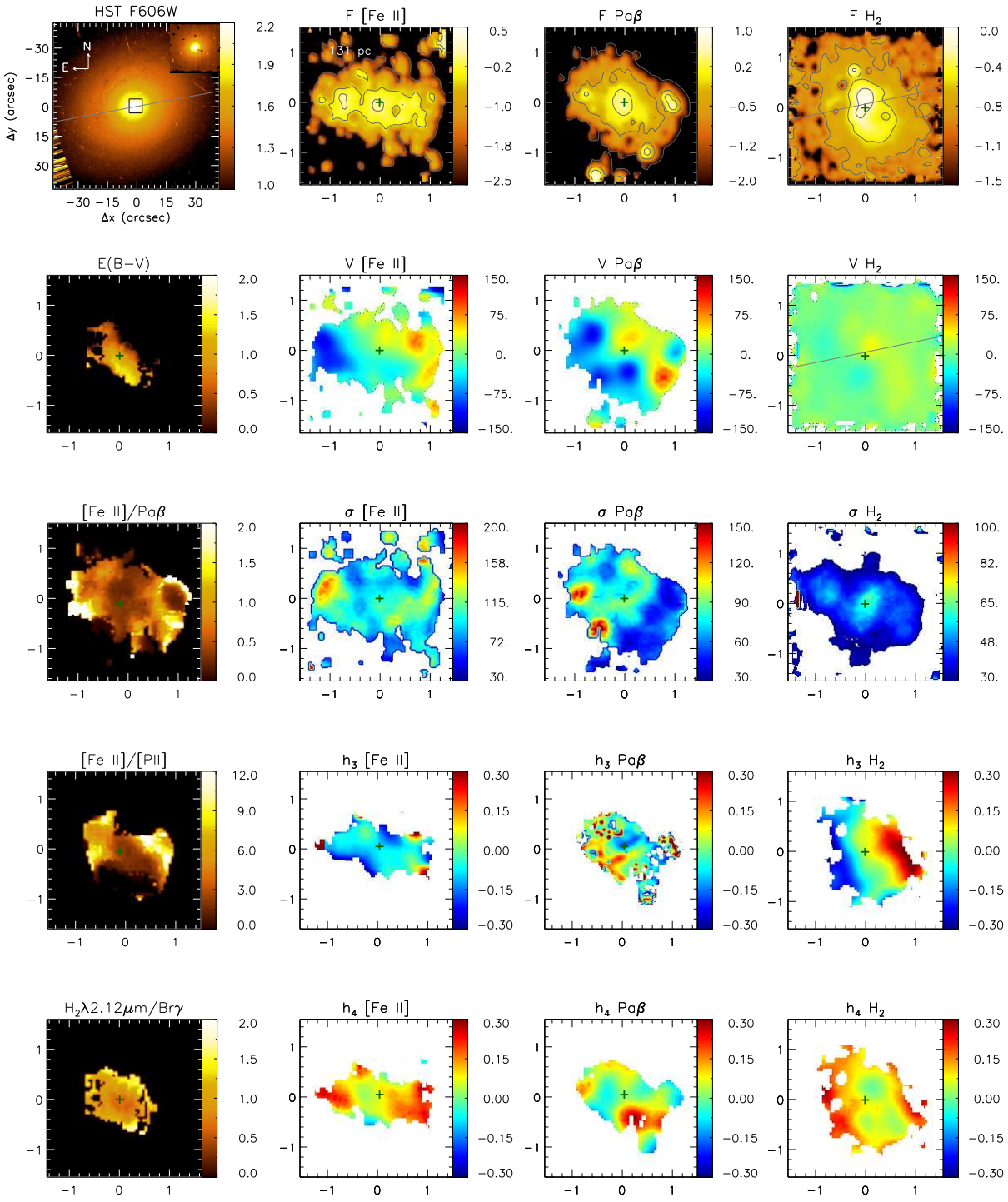

Figure 2. First row: HST-WFPC2 continuum image of NGC 788 obtained through the filter F606W (Malkan et al. 1998) the grey line is the photometric major axis (108.1° - from HYPERLEDA); reddening E(B-V) was obtained from Paβ/Brγ line ratio; [Fe II]λ1.2570μm/Paβ line ratio map; [Fe II]λ1.2570μm/[P II]λ1.1886μm line ratio map; $H_2\lambda$2.1218μm/Brγ line ratio map. Second row: Flux (F), centroid velocity (V), velocity dispersion (σ), h_3 Gauss-hermite moment and h_4 Gauss-hermite moment, consecutively, for [Fe II]λ1.2570μm emission line. Third row: Flux (F), centroid velocity (V), velocity dispersion (σ), h_3 Gauss-hermite moment and h_4 Gauss-hermite moment, consecutively, for [Pa$\beta\lambda$1.2821μm emission line. Fourth row: Flux (F), centroid velocity (V), velocity dispersion (σ), h_3 Gauss-hermite moment and h_4 Gauss-hermite moment, consecutively, for $H_2\lambda$2.1218μm emission line.

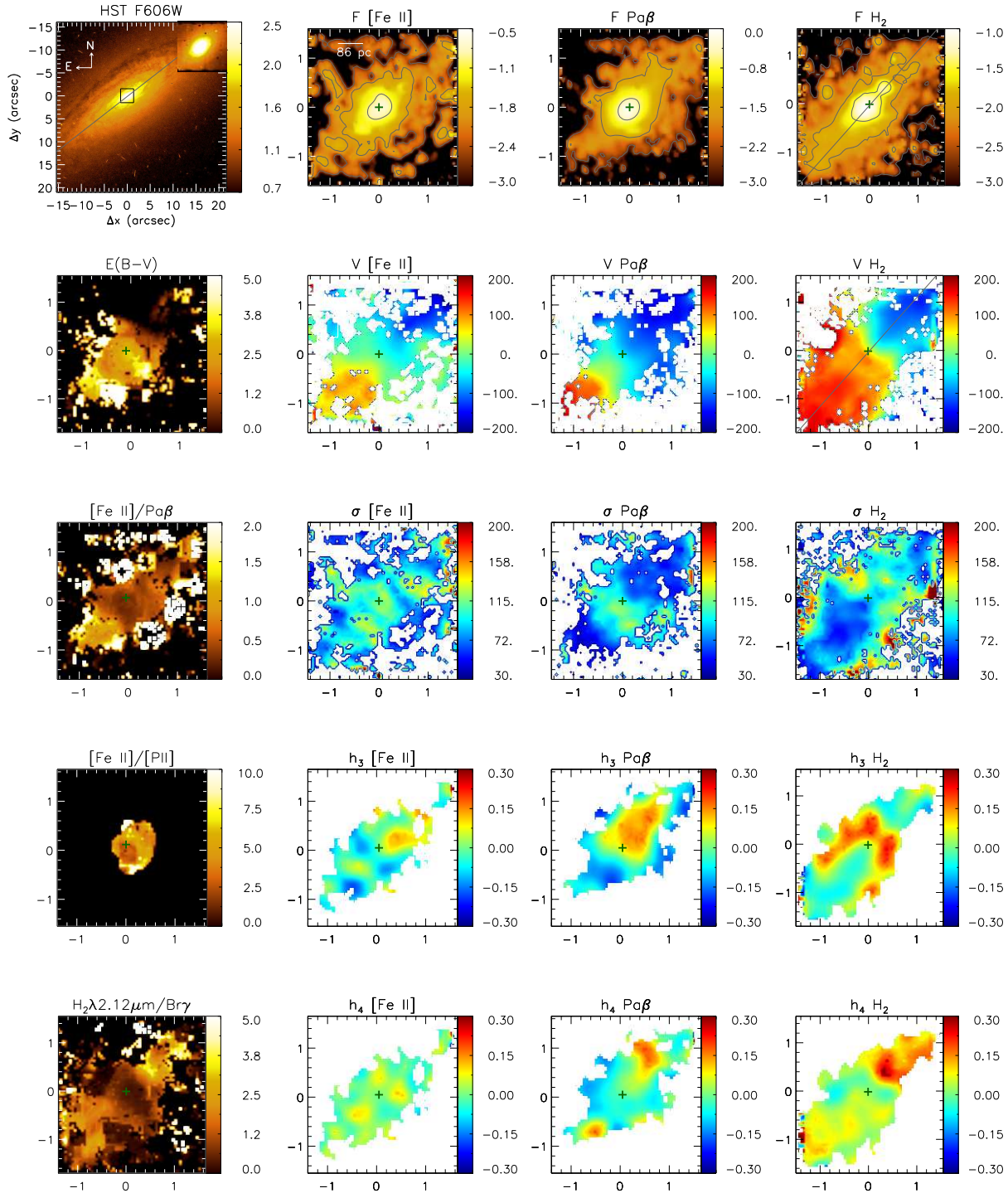

Figure 3. First row: HST-WFPC2 continuum image of Mrk 607 obtained through the filter F606W (Malkan et al. 1998) the grey line is the photometric major axis (137.3° - from HYPERLEDA); reddening E(B-V) was obtained from Paβ/Brγ line ratio; [Fe II]λ1.2570μm/Paβ line ratio map; [Fe II]λ1.2570μm/[P II]λ1.1886μm line ratio map; H_2λ2.1218μm/Brγ line ratio map. Second row: Flux (F), centroid velocity (V), velocity dispersion (σ), h_3 Gauss-hermite moment and h_4 Gauss-hermite moment, consecutively, for [Fe II]λ1.2570μm emission line. Third row: Flux (F), centroid velocity (V), velocity dispersion (σ), h_3 Gauss-hermite moment and h_4 Gauss-hermite moment, consecutively, for [Paβλ1.2821μm emission line. Fourth row: Flux (F), centroid velocity (V), velocity dispersion (σ), h_3 Gauss-hermite moment and h_4 Gauss-hermite moment, consecutively, for H_2λ2.1218μm emission line.

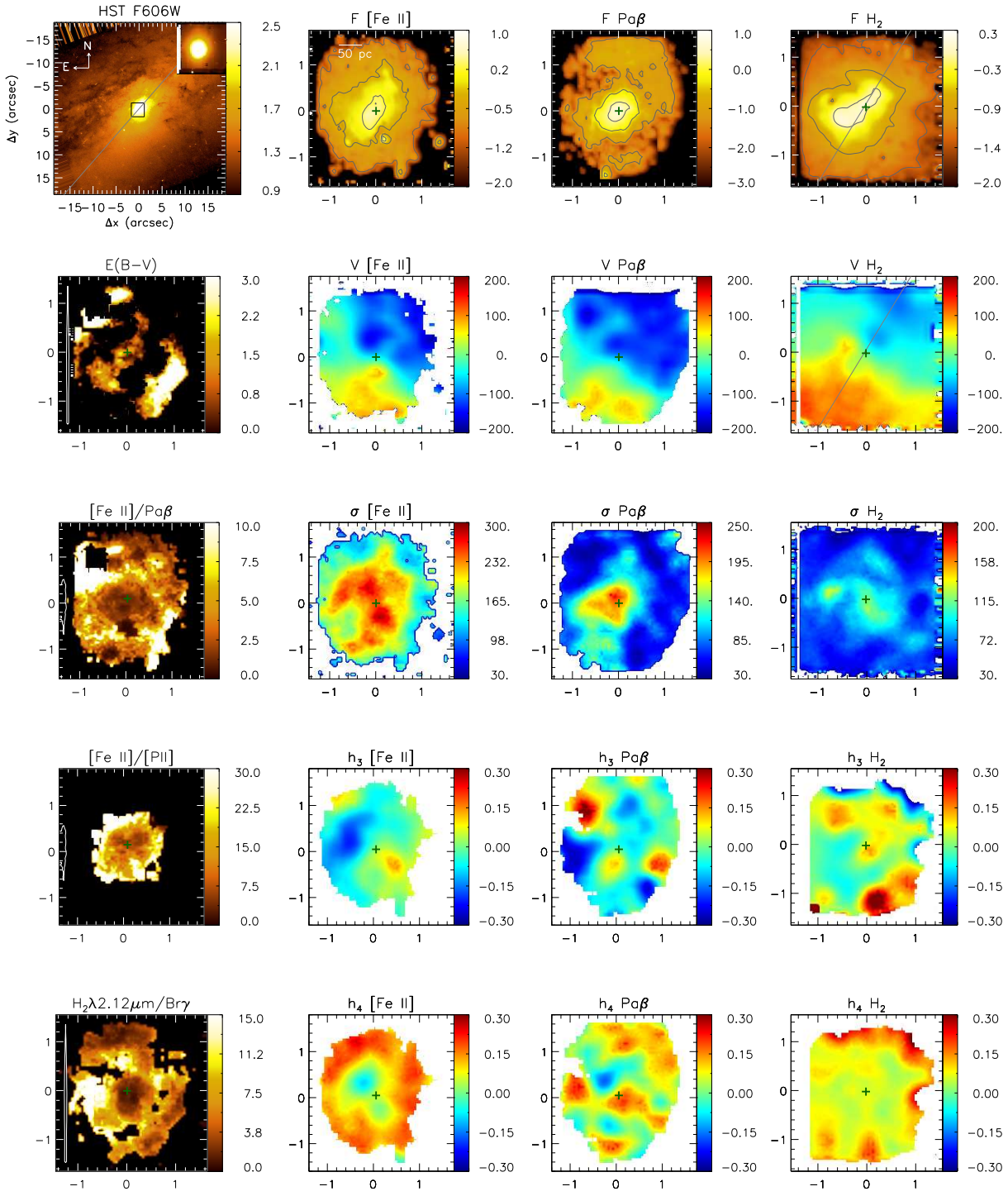

Figure 4. First row: HST-WFPC2 continuum image of NGC 3227 obtained through the filter F606W (Malkan et al. 1998) the grey line is the photometric major axis (156° - from HYPERLEDA); reddening E(B-V) was obtained from Paβ/Brγ line ratio; [Fe II]λ1.2570μm/Paβ line ratio map; [Fe II]λ1.2570μm/[P II]λ1.1886μm line ratio map; $H_2\lambda$2.1218μm/Brγ line ratio map. Second row: Flux (F), centroid velocity (V), velocity dispersion (σ), h_3 Gauss-hermite moment and h_4 Gauss-hermite moment, consecutively, for [Fe II]λ1.2570μm emission line. Third row: Flux (F), centroid velocity (V), velocity dispersion (σ), h_3 Gauss-hermite moment and h_4 Gauss-hermite moment, consecutively, for [Pa$\beta\lambda$1.2821μm emission line. Fourth row: Flux (F), centroid velocity (V), velocity dispersion (σ), h_3 Gauss-hermite moment and h_4 Gauss-hermite moment, consecutively, for $H_2\lambda$2.1218μm emission line.

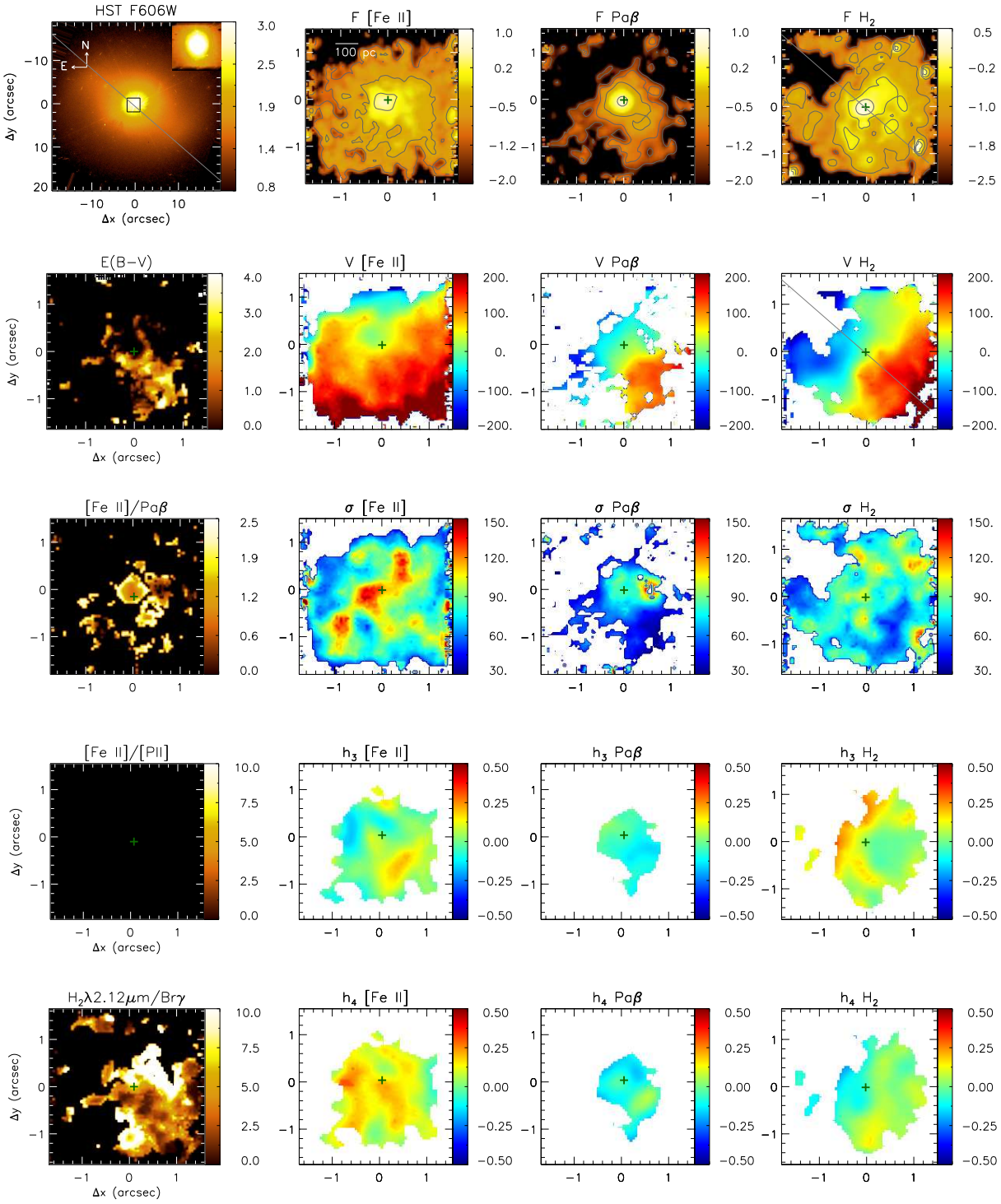

Figure 5. First row: HST-WFPC2 continuum image of NGC 3516 obtained through the filter F606W (Malkan et al. 1998) the grey line is the photometric major axis (55° - from HYPERLEDA); reddening E(B-V) was obtained from Paβ/Brγ line ratio; [Fe II]λ1.2570μm/Paβ line ratio map; [Fe II]λ1.2570μm/[P II]λ1.1886μm line ratio map; $H_2\lambda$2.1218μm/Brγ line ratio map. Second row: Flux (F), centroid velocity (V), velocity dispersion (σ), h_3 Gauss-hermite moment and h_4 Gauss-hermite moment, consecutively, for [Fe II]λ1.2570μm emission line. Third row: Flux (F), centroid velocity (V), velocity dispersion (σ), h_3 Gauss-hermite moment and h_4 Gauss-hermite moment, consecutively, for [Pa$\beta\lambda$1.2821μm emission line. Fourth row: Flux (F), centroid velocity (V), velocity dispersion (σ), h_3 Gauss-hermite moment and h_4 Gauss-hermite moment, consecutively, for $H_2\lambda$2.1218μm emission line.

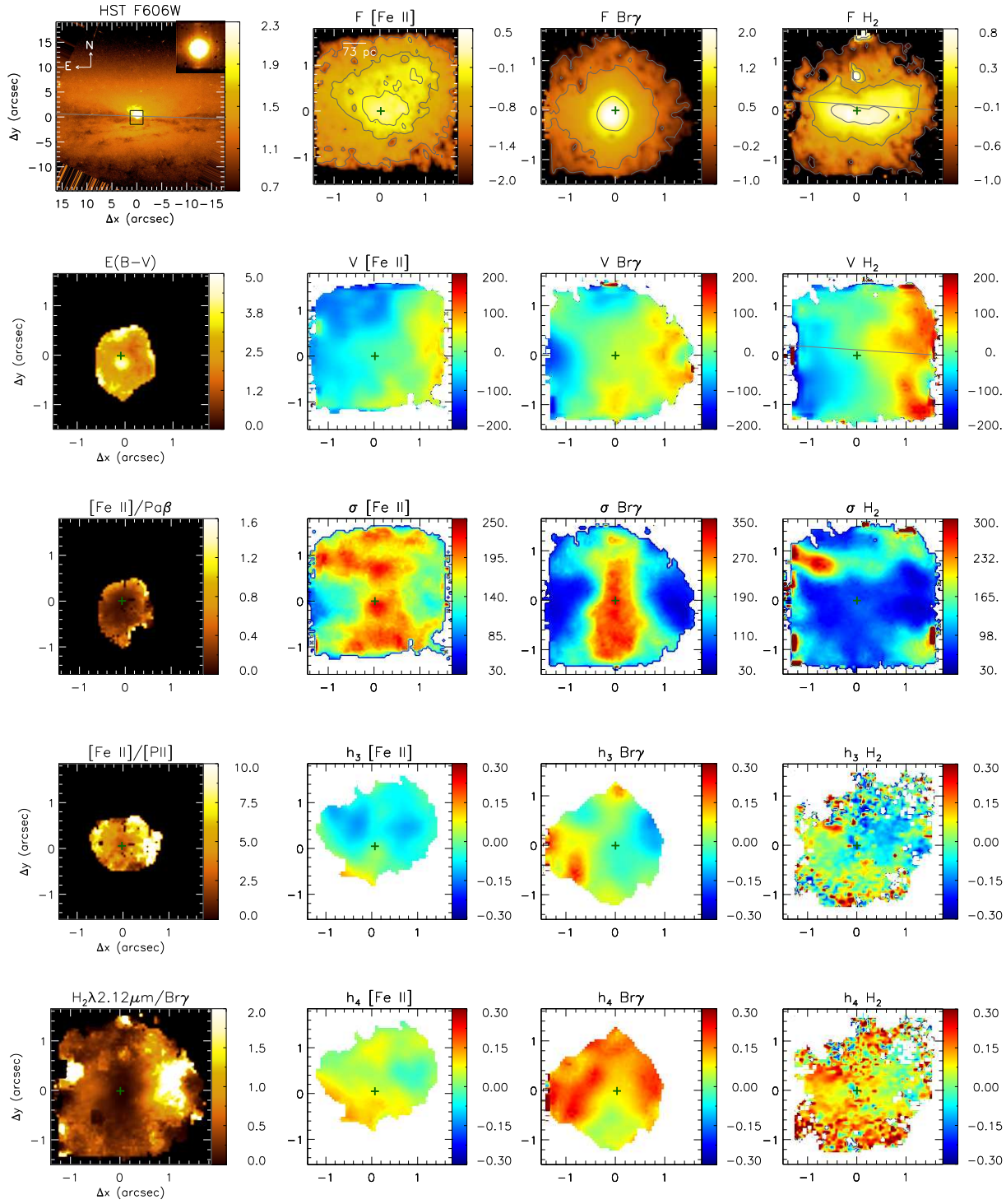

Figure 6. First row: HST-WFPC2 continuum image of NGC 5506 obtained through the filter F606W (Malkan et al. 1998) the grey line is the photometric major axis (88° - from HYPERLEDA); reddening E(B-V) was obtained from Paβ/Brγ line ratio; [Fe II]λ1.2570μm/Paβ line ratio map; [Fe II]λ1.2570μm/[P II]λ1.1886μm line ratio map; $H_2\lambda$2.1218μm/Brγ line ratio map. Second row: Flux (F), centroid velocity (V), velocity dispersion (σ), h_3 Gauss-hermite moment and h_4 Gauss-hermite moment, consecutively, for [Fe II]λ1.2570μm emission line. Third row: Flux (F), centroid velocity (V), velocity dispersion (σ), h_3 Gauss-hermite moment and h_4 Gauss-hermite moment, consecutively, for [Pa$\beta\lambda$1.2821μm emission line. Fourth row: Flux (F), centroid velocity (V), velocity dispersion (σ), h_3 Gauss-hermite moment and h_4 Gauss-hermite moment, consecutively, for $H_2\lambda$2.1218μm emission line.

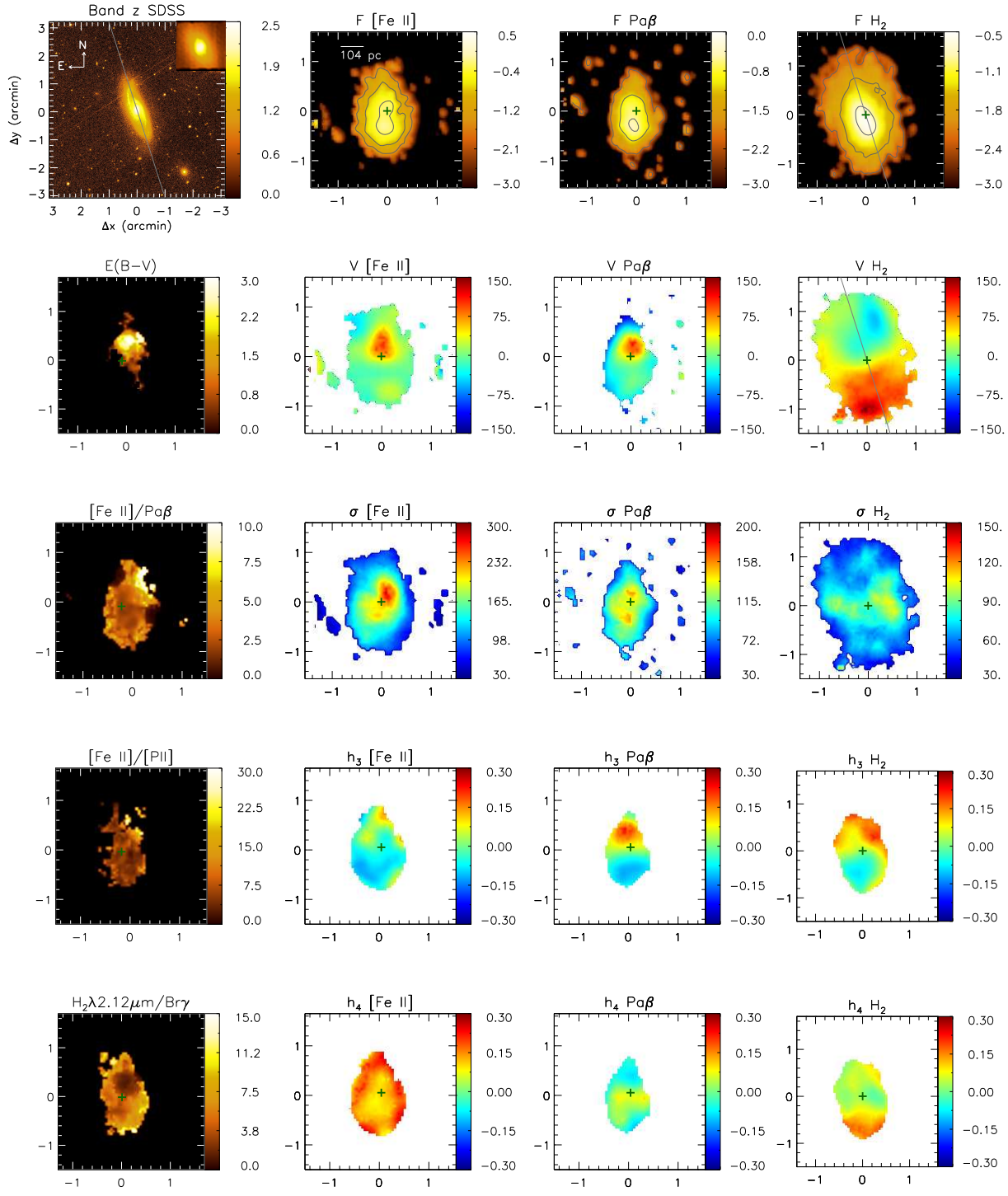

Figure 7. First row: SDSS band-z image of NGC 5899 (Baillard et al. 2011) the grey line is the photometric major axis (20.8° - from HYPERLEDA); reddening E(B-V) was obtained from Paβ/Brγ line ratio; [Fe II]λ1.2570μm/Paβ line ratio map; [Fe II]λ1.2570μm/[P II]λ1.1886μm line ratio map; H_2λ2.1218μm/Brγ line ratio map. Second row: Flux (F), centroid velocity (V), velocity dispersion (σ), h_3 Gauss-hermite moment and h_4 Gauss-hermite moment, consecutively, for [Fe II]λ1.2570μm emission line. Third row: Flux (F), centroid velocity (V), velocity dispersion (σ), h_3 Gauss-hermite moment and h_4 Gauss-hermite moment, consecutively, for [Paβλ1.2821μm emission line. Fourth row: Flux (F), centroid velocity (V), velocity dispersion (σ), h_3 Gauss-hermite moment and h_4 Gauss-hermite moment, consecutively, for H_2λ2.1218μm emission line.

disturbed) rotation pattern for all galaxies. In the case of NGC 788 the H_2 rotation amplitude is smaller than those of [Fe II] and Paβ.

5.4 Velocity dispersion

The [Fe II] velocity dispersion maps show the highest values, reaching $\approx$ 300 km s^{-1} for NGC 3227 and NGC 5899, while the H_2 maps show the lowest values, ranging from $\approx$ 40 km s^{-1} to $\approx$ 300 km s^{-1} (only in one case - NGC 5506). The Paβ velocity dispersion maps are similar to those of [Fe II] although reaching somewhat lower values, in the range $\approx$ 40 km s^{-1} to $\approx$ 250 km s^{-1}. An exception is the case of NGC 5506 that shows a region of enhanced σ ($\approx$ 350 km s^{-1}) for all emission lines.

5.5 Gauss-Hermite moment h_3

The h_3 maps show values ranging from -0.30 to 0.30 for all emission lines. For all emission lines there is an anti-correlation between the h_3 map and the velocity fields: positive values of h_3 are seen at the locations where blueshifts are observed in the velocity fields, while negative values are seen where redshifts are observed. This means that red wings are observed for blueshifted emission lines, while blue wings are observed for redshifted emission lines.

5.6 Gauss-Hermite moment h_4

The h_4 maps show values ranging from -0.30 to 0.30 for all emission lines. We also see an anti-corelation, this time between the h_4 and the velocity dispersion maps. Positive values of h_4 are seen at the locations showing the lowest velocity dispersion values, while negative values of h_4 are seen at the locations with the highest velocity dispersion values.

5.7 Total gas mass and surface mass density distributions

In Fig. 8 we show the surface mass density distributions of ionized and hot molecular gas, as well as the corresponding estimated gradients, obtained as described below. The ionized gas mass, in units of solar masses ($M_\odot$) was estimated using (e.g. Scoville et al. 1982; Riffel et al. 2008; Storchi-Bergmann et al. 2009; Schönell et al. 2014, 2017):

$$M_{HII} \approx 5.1 \times 10^{16} \left(\frac{F_{Pa\beta}}{erg\,s^{-1}cm^{-2}} \right) \left(\frac{D}{Mpc} \right)^2 [M_\odot], \quad (1)$$

where $F_{Pa\beta}$ is the integrated flux for the $Pa\beta$ emission line and D is the distance to the galaxies. We have assumed an electron temperature $T = 10^4 K$ and electron density $N_e = 100\,\mathrm{cm}^{-3}$ (Osterbrock & Ferland 2006).

The mass of the hot molecular gas (in $M_\odot$) was obtained using (Scoville et al. 1982):

$$M_{H_2} \approx 5.0776 \times 10^{13} \left(\frac{F_{H_2\lambda 2.1218}}{erg\,s^{-1}cm^{-2}} \right) \left(\frac{D}{Mpc} \right)^2 [M_\odot], \quad (2)$$

where $F_{H_2\lambda 2.1218}$ is the flux for the $H_2\lambda 2.1218\mu$m emission line and we have used the vibrational temperature $T = 2000K$ (Riffel et al. 2008, 2010; Storchi-Bergmann et al. 2009; Schönell et al. 2014, 2017).

In Table 2 we show the integrated gas mass values (for the whole FOV) as well as the average surface mass densities (in units of $M_\odot$ pc^{-2}), obtained as the ratio between the integrated masses and the area over which they are distributed, listed also in the Table.

The maps of the gas surface mass density distributions shown in Fig. 8 reveal that the ionized gas mass density distribution is more compact when compared with those of the hot molecular gas. In most cases the hot molecular gas extends farther from the nucleus than the ionized gas, which is more restricted to the center of the field.

A number of studies have derived the ratio between the cold and hot H_2 gas masses by comparing the masses obtained using the CO and near-IR H_2 line emission. Dale et al. (2005) obtained ratios in the range 10^5–10^7; using a larger sample of 16 luminous and ultraluminous infrared galaxies, Müller-Sánchez et al. (2006) derived a ratio M_{cold}/M_{warm} = 1-5$\times 10^6$. More recently, Mazzalay et al. (2013) compiled from the literature values of M_{cold} derived from CO observations and $H_2 2.12\mu$m luminosities for a larger number of galaxies, covering a wider range of luminosities, morphological and nuclear activity types. From that, an estimate of the cold H_2 gas mass can be obtained from

$$M_{H_2\,\mathrm{cold}} \approx 1174 \left(\frac{L_{H_2\lambda 2.1218}}{L_\odot} \right), \quad (3)$$

where $L_{H_2\lambda 2.1218}$ is the luminosity of the $H_2 2.12\mu$m line. The estimated masses for the cold molecular gas are also listed in Table 2.

The integrated mass of hot molecular gas (within typically 100 - 400 pc from the nucleus) ranges from 182 $M_\odot$ for Mrk 607 to 1400 $M_\odot$ for NGC 5506, while the mass of cold molecular gas ranges from $1.3\times10^7 M_\odot$ for Mrk 607 to 1×10^9 $M_\odot$ for NGC 5506. The mass of the ionized gas ranges from 3×10^5 $M_\odot$ for NGC 3516 to 3.2×10^7 $M_\odot$ for NGC 5506.

The average surface mass density of the hot molecular gas ranges from 1.6×10^{-3} $M_\odot$/pc^2 for NGC 788 to 1.4×10^{-2} $M_\odot$/pc^2 for NGC 3227, while for the estimated cold molecular gas the values range from 1319 $M_\odot$/pc^2 for NGC 788 to 20682 $M_\odot$/pc^2 for NGC 3227. In the case of the ionized gas, the average surface mass density range from 4.8 $M_\odot$/pc^2 for NGC 5899 to 244 $M_\odot$/pc^2 for NGC 5506.

5.8 Excitation maps

In Colina et al. (2015) we concluded that the [Fe II]$\lambda 1.2570\mu$m/$Pa\beta$ vs. $H_2\lambda 2.1218\mu$m/Brγ diagram approximately separates the gas excitation regions characteristic of Starburst, Seyfert and LINER excitation. Although the boundaries between the regions are not very well defined, we use Fig. 6 of Colina et al. (2015) to draw average boundaries that we have used to separate the regions in the central regions of the galaxies of our sample with these different excitations. These excitation maps are shown in Figs. 9, 10, 11, 12, 13 and 14. Typical values for the nuclei of Seyfert galaxies range between 0.6 and 2.0 for both ratios (Rodríguez-Ardila et al. 2005), while for Starbursts the values are smaller than 0.6 and for LINERs the values are larger than 2. In these figures, black filled

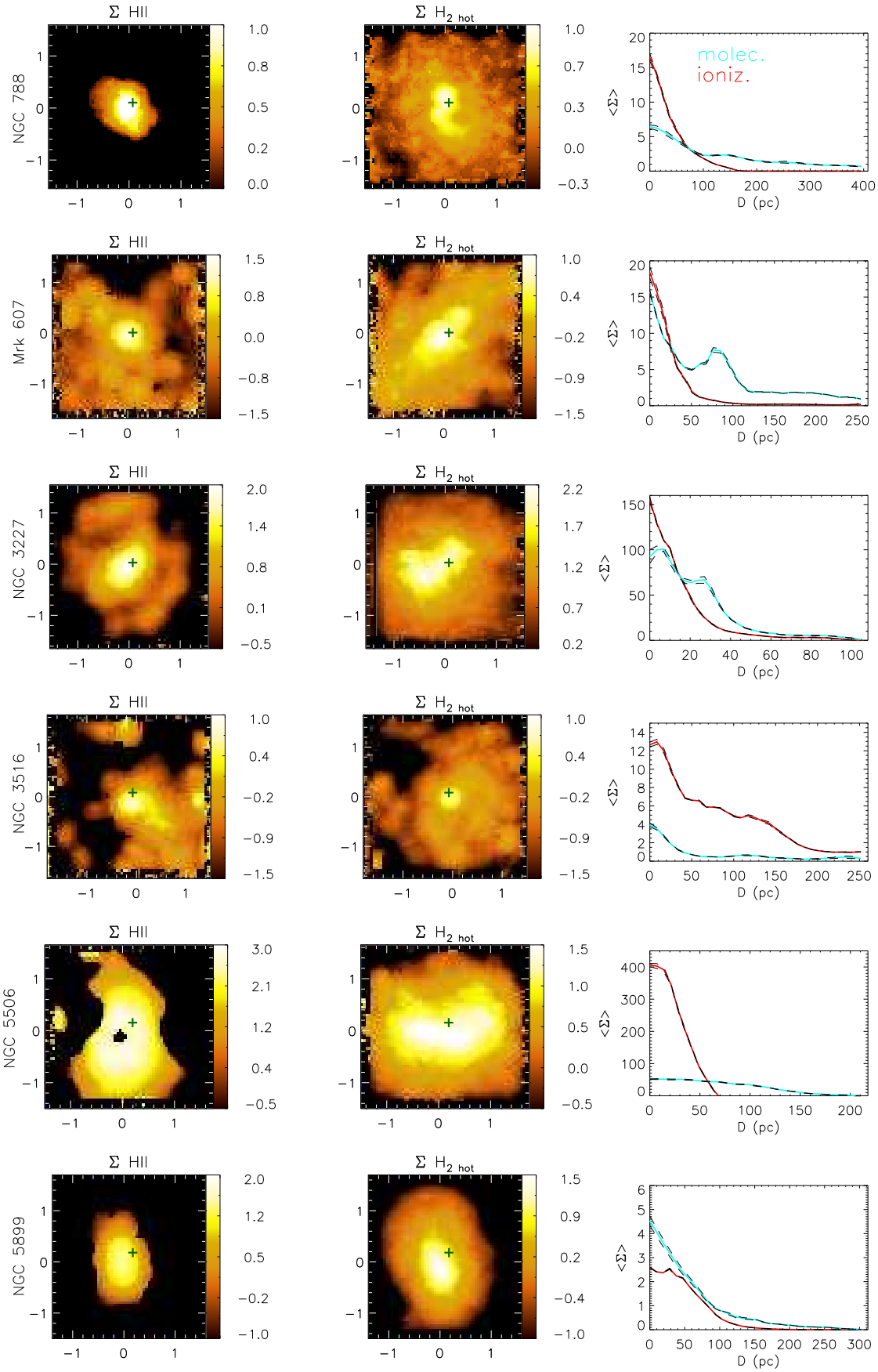

Figure 8. In the first column we show the surface mass density distribution of the ionized gas for each galaxy (units of $M_\odot$ pc^{-2}), in the second column that of the hot molecular gas (units of 10^{-3} $M_\odot$ pc^{-2}) and in the third the corresponding gradients.

Table 2. Total area, total mass and average surface mass density values for the ionized, hot and cold molecular gas for the 6 galaxies estudied in this work.

Galaxies	Area (H_2)	Area (HII)	M $(H_2)_h$	M $(H_2)_c$	M (HII)	Σ $(H_2)_h$	Σ $(H_2)_c$	Σ (HII)	Ref.
NGC788	6.2×10^5	5.5×10^5	1012	7.3×10^8	4.8×10^6	1.6×10^{-3}	1319	8.8	2
Mrk607	5.9×10^4	2.3×10^4	182	1.3×10^8	1.1×10^6	3×10^{-3}	5710	48	5
NGC3227	8.8×10^4	4.4×10^4	1274	9.2×10^8	1.7×10^6	1.4×10^{-2}	20682	39	8
NGC3516	8×10^4	6×10^4	517	3.7×10^8	3×10^5	6.4×10^{-3}	6168	5	9
NGC5506	1.4×10^5	1.2×10^5	1.4×10^3	1×10^9	3.2×10^7	9.7×10^{-3}	7951	244	13
NGC5899	1.9×10^5	8.7×10^4	559	4×10^8	4.2×10^5	2.9×10^{-3}	4624	4.8	15

All mass (M) units are in $M_\odot$, area units in pc^2 and the mass surface densities (Σ) in $M_\odot/pc^2$.

circles represent Seyfert ratios, blue open circles, Starbursts ratios and red crosses represent ratios of low-ionization nuclear emission-line regions (LINERs).

The diagnostic diagram of NGC 788 and Mrk 607 have excitation typical of Starburst within the inner 80 pc, surrounded up to 160 pc from the nucleus of Seyfert excitation, while outwards the excitation is typical of LINERs. In the cases of NGC 3227 and NGC 3516, the nuclear excitation is Seyfert-like and is surrounded by LINER-like excitation. In the case of NGC5506 the ratios suggest a dominance of Starburst excitation, and for NGC 5899 the ratios show only LINER-like excitation.

6 DISCUSSION

In this section we discuss individually each galaxy, making a brief review of the literature on their known properties, trying to relate our findings with these properties. Their kinematics are going to be modeled and further discussed in a forthcoming paper (Sch17).

6.1 NGC 788

NGC 788 was identified as a Seyfert galaxy by Huchra et al. (1982), and has been observed in the optical (Hamuy & Maza 1987; Wagner 1987; Kay 1994; Cruz-Gonzalez et al. 1994), radio (Ulvestad & Wilson 1989), and millimeter (Heckman et al. 1989) wave bands. Morphologically, the galaxy is a lenticular/early-type spiral with faint spiral arms visible ≈ 30" from the nucleus (Evans et al. 1996). The spiral arms are brightest to the northwest of the nucleus with a string of bright, compact HII regions that trace the spiral arm, together with a complex of fainter HII regions associated with the southern arm (Evans et al. 1996).

The PA can be determined from the centroid velocity fields seen in Fig. 2: $\approx 125°$, close to the value of $\approx 130°$ obtained by Rif17 for the stellar kinematics. The velocity amplitude observed for [Fez,II] and Paβ is much larger than that for H_2. These higher velocities are associated to a more collimated emission and higher velocity dispersion, suggesting the presence of a bipolar outflow along the east-west direction.

The excitation map shown in the bottom panel of fig. 9 reveals Starburst line ratios within the inner 140 pc, although they are close to the limit between Starburst and Seyfert excitation. As pointed out by Colina et al. (2015) these boundaries are not very well defined.

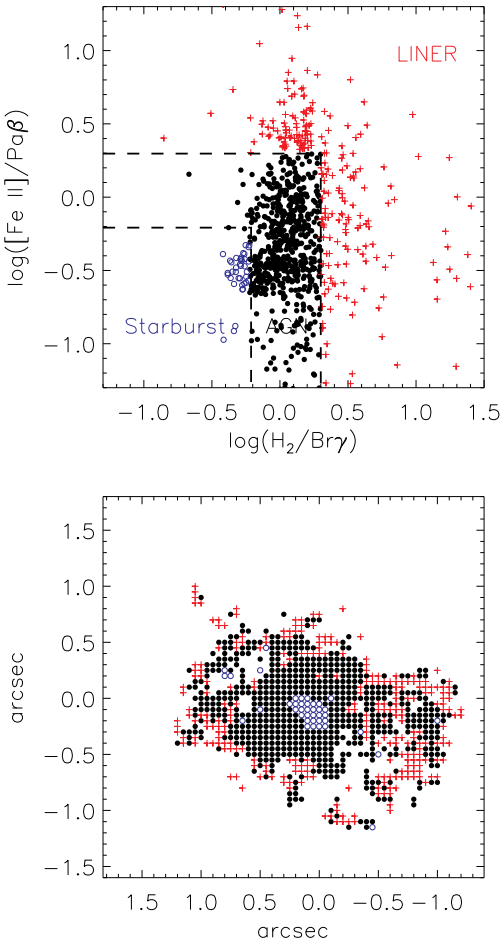

Figure 9. Diagnostic diagram and spatial position for NGC 788. Top panel: [Fe II]λ1.25μm/Paβ versus $H_2\lambda$2.12μm/Brγ lineratio diagnostic diagram. The dashed lines delimit regions with ratios typical of Starbursts (blue open circles), Seyferts (black filled circles) and LINERS (red crosses). Bottom panel: spatial position of each point from the diagnostic diagram.

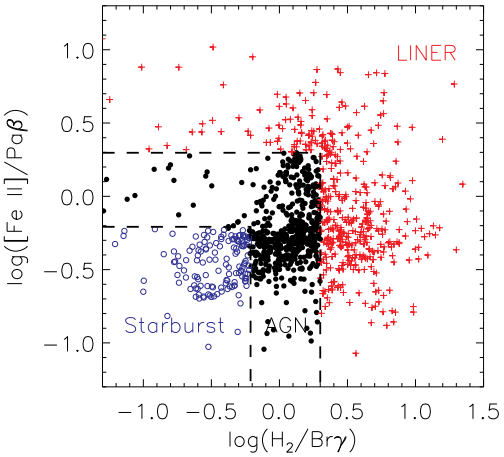

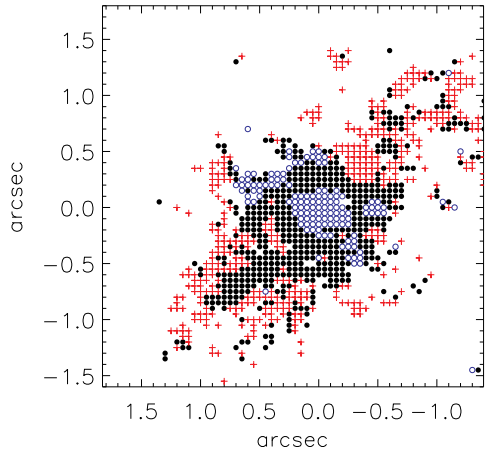

Figure 10. Diagnostic diagram and spatial position for Mrk 607. Top panel: [Fe II]λ1.25μm/Paβ versus H$_2\lambda$2.12μm/Brγ lineratio diagnostic diagram. The dashed lines delimit regions with ratios typical of Starbursts (blue open circles), Seyferts (black filled circles) and LINERS (red crosses). Bottom panel: spatial position of each point from the diagnostic diagram.

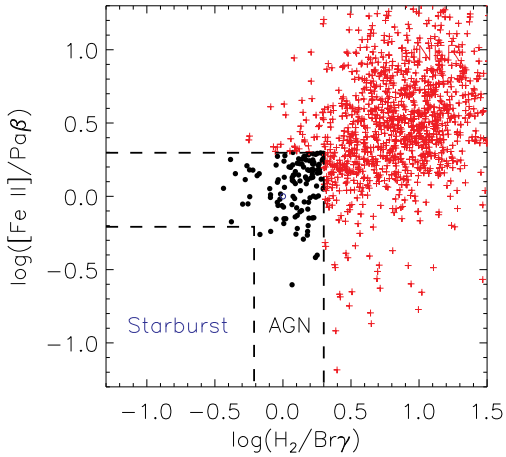

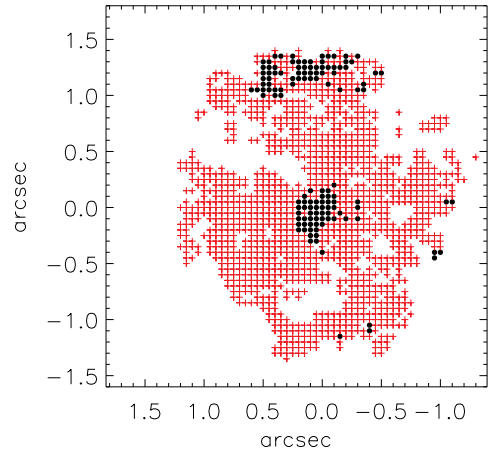

Figure 11. Diagnostic diagram and spatial position for NGC 3227. Top panel: [Fe II]λ1.25μm/Paβ versus H$_2\lambda$2.12μm/Brγ lineratio diagnostic diagram. The dashed lines delimit regions with ratios typical of Starbursts (blue open circles), Seyferts (black filled circles) and LINERS (red crosses). Bottom panel: spatial position of each point from the diagnostic diagram.

6.2 Mrk 607

Mrk 607 is an Sa galaxy hosting a Seyfert 2 nucleus. A continuum image from Ferruit et al. (2000), shows high inclination (ellipticity $\approx$ 0.60, yielding an inclination i $\approx$ 67°) with major axis PA of -43°, which agrees with our estimate of $\approx$ -38° from the H$_2$ velocity field. Our data shows that both [Fe II] and Paβ velocity fields also show what seems to be a rotation pattern, but less steep than that of H$_2$. Spiral dust lanes, are clearly visible in the F547 continuum image of the inner 8" (1.4 kpc) of the galaxy (Ferruit et al. 2000). The high inclination of the galaxy may explain the large velocity dispersions observed in the velocity field. In the central 5" (875 pc), it presents weak radio emission extended along P.A. $\approx$ 180° (Colbert et al. 1996; Nagar et al. 1999) which is not aligned with the emission-line region.

The excitation map (Fig. 10) shows that, within 90 pc from the nucleus, the excitation is Seyfert-like, surrounded by LINER-like excitation further out. As in the case of NGC 788, there is a trend for the region within 50 pc from the nucleus to present Starburst-like line ratios, even though previous studies in the optical (Zaw et al. 2009) report that this galaxy occupies the locus of Seyfert 2 galaxies in the BPT diagram.

6.3 NGC 3227

NGC 3227 is a well studied barred galaxy, with a Seyfert 1.5 nucleus (Ho et al. 1997) and in interaction with the dwarf elliptical galaxy NGC 3226 (Mundell et al. 2004). The galactic disc has an inclination of 56°, with an outer photometric major-axis at a position angle PA = 158° (Mundell et al. 1995), which agrees with the PA suggested by us of

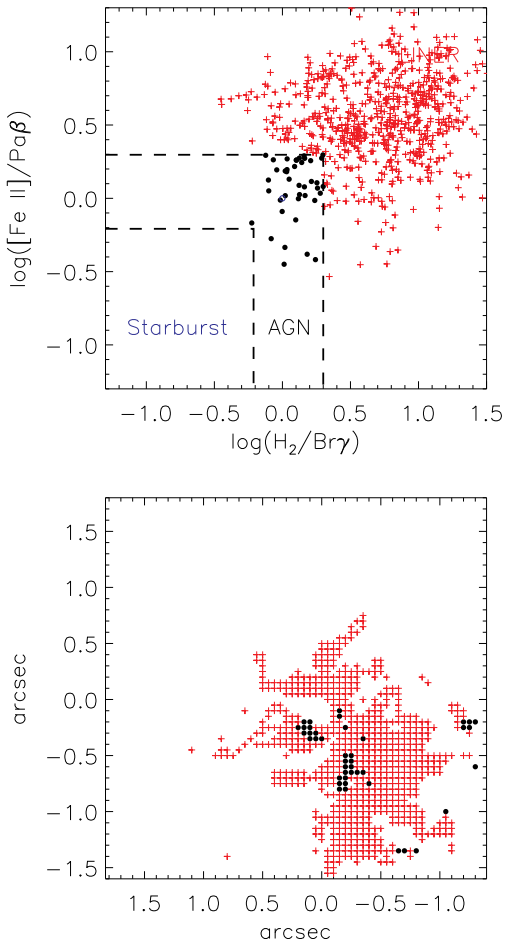

Figure 12. Diagnostic diagram and spatial position for NGC 3516. Top panel: [Fe II]λ1.25μm/Paβ versus $H_2\lambda$2.12μm/Brγ lineratio diagnostic diagram. The dashed lines delimit regions with ratios typical of Starbursts (blue open circles), Seyferts (black filled circles) and LINERS (red crosses). Bottom panel: spatial position of each point from the diagnostic diagram.

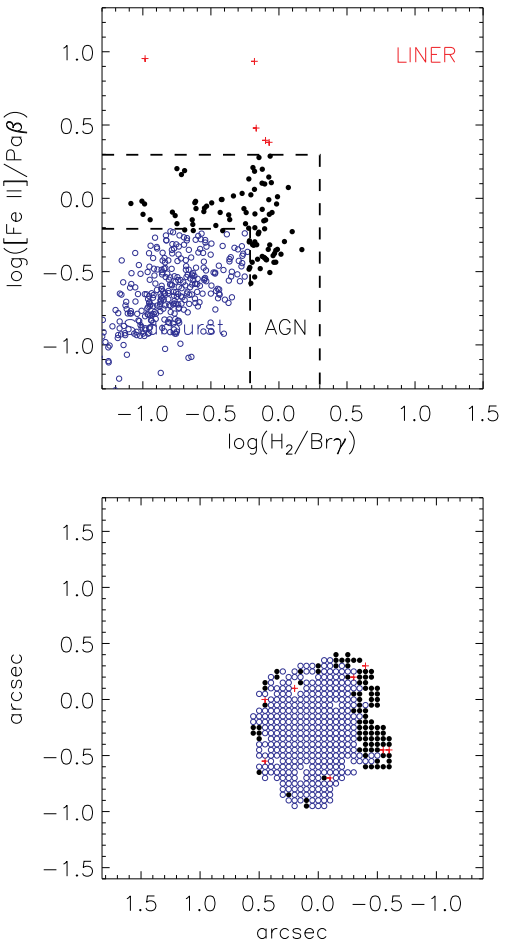

Figure 13. Diagnostic diagram and spatial position for NGC 5506. Top panel: [Fe II]λ1.25μm/Paβ versus $H_2\lambda$2.12μm/Brγ lineratio diagnostic diagram. The dashed lines delimit regions with ratios typical of Starbursts (blue open circles), Seyferts (black filled circles) and LINERS (red crosses). Bottom panel: spatial position of each point from the diagnostic diagram.

$\approx$ 155° (from the H_2 centroid velocity field) and with the value of 156° found by Rif17 from the stellar kinematics. The three emission-line velocity fields show a rotation pattern, but which is distorted in all cases, mainly to the noth-east and seen more clearly in [Fe II] and Paβ, in association with regions of enhanced velocity dispersion.

The central region has been mapped in ^{12}CO(1-0) and ^{12}CO(2-1) by Schinnerer et al. (2000), who detect molecular gas very close to the nucleus ($\approx$ 13 pc), in agreement with our results, that show a large molecular gas concentration towards the center (see the surface mass density profile in the third line of Fig. 8). Also, Schinnerer et al. (2000) found an asymmetric nuclear ring with a diameter of about 3.″0 (220 pc).

The inner kiloparsec hosts a radio jet at PA $\approx$ - 10° (Mundell et al. 1995) and a conical NLR outflow at a PA $\approx$ 15° (Mundell et al. 1995), while Arribas & Mediavilla (1994) report an Hα outflow at PA $\approx$ 50°. The extent of the [Fe II] mission to the north may be related to the radio emission, while the outflows observed at PAs between 15 and 50° can explain the deviation from rotation observed in the velocity fields of [Fe II] and Paβ to the norh-east. These features can also explain the high velocity dispersion regions seen in Fig. 4.

The excitation map (Fig. 11) shows a few Seyfert-like ratios at the nucleus but is dominated by LINER-like ratios, suggesting a contribution from shocks, in agreement with the high velocity dispersion observed for [Fe II] over most of the field-of-view.

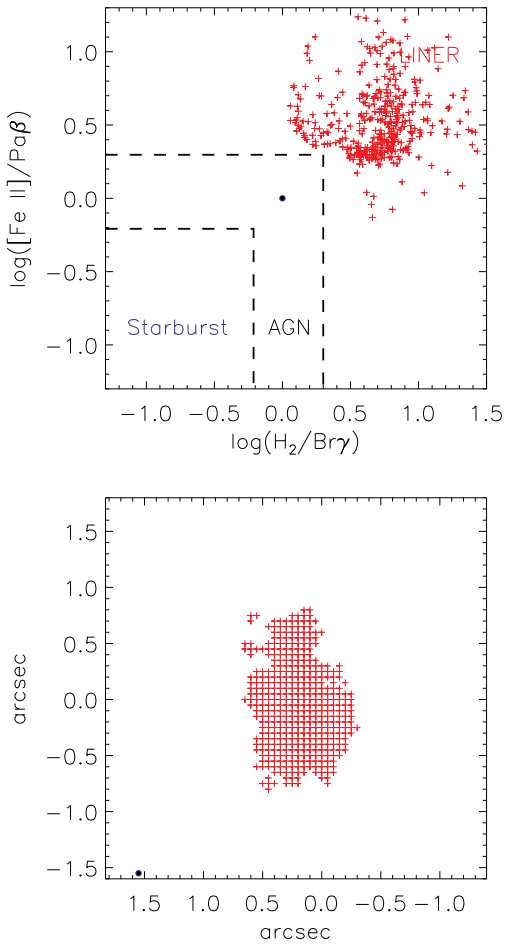

Figure 14. Diagnostic diagram and spatial position for NGC 5899. Top panel: [Fe II]λ1.25μm/Paβ versus H$_2\lambda$2.12μm/Brγ lineratio diagnostic diagram. The dashed lines delimit regions with ratios typical of Starbursts (blue open circles), Seyferts (black filled circles) and LINERS (red crosses). Bottom panel: spatial position of each point from the diagnostic diagram.

6.4 NGC 3516

The Seyfert 1 nucleus of this SB0 galaxy shows variable ultraviolet absorption lines (Voit et al. 1987; Kriss et al. 1996) and variable broad emission lines and continuum (Koratkar et al. 1996). Spectroscopic studies of the gaseous kinematics using either long-slit (Ulrich & Péquignot 1980; Goad & Gallagher 1987, 1988; Mulchaey et al. 1992) or integral field spectrographs (Veilleux et al. 1993; Aoki et al. 1994; Arribas & Mediavilla 1994) spectrographs have outlined multiple spectral components displaying strong deviations from "normal" galaxy rotation. Two general models have been proposed to explain the morphology and the kinematics of the emission-line gas that presents a Z-shaped structure that covers the inner 5.″0: a bent bipolar mass outflow model, first suggested by Goad & Gallagher (1987) and further developed by Mulchaey et al. (1992) and Veilleux et al. (1993), and a precessing twin-jet model by Veilleux et al. (1993).The stellar rotation curve obtained by Arribas et al. (1997) yields a systemic velocity of 2593±15 km s^{-1}, close to that one derived by Rif17 of ≈ 2631 km s^{-1}. The kinematic major axis obtained by Arribas et al. (1997) has P.A.= 53° ± 5° and is consistent with our results for the stellar kinematics (Rif17) and also to the aproximate orientation of the kinematic major axis of the molecular gas of ≈ 60°.

6.5 NGC 5506

The nucleus of this galaxy is classified as a Sy1.9 based on the detection of broad wings of the Paβ profile (Blanco et al. 1990). However, more recently, Nagar et al. (2002) presented evidence that NGC 5506 is an obscured narrow-line Sy1, as a result of the finding of the permitted O Iλ1.129μm line, together with a broad pedestal of Paβ and rapid X-ray variability. The galaxy nucleus is very compact in the mid-IR, with an apparent optical depth of $\tau_{10\mu m}^{app} \approx 1.4$ (Roche et al. 1991, 2007; Siebenmorgen et al. 2004), although NGC 5506 also shows variations in its silicate absorption depth on parsec scales (Roche et al. 2007). This galaxy has comparable X-ray and mid-IR absorbing columns, indicating that the dust-free absorption is lower than for a Sy2. The optical spectrum has strong [O III] and [N II] narrow lines (Zaw et al. 2009). The log([O III]/Hβ) and log([N II]/Hα) line ratios, 0.88 and -0.09 respectively (Kewley et al. 2001), place it firmly in the Seyfert 2 region of the BPT diagram, while in Fig. 13 we see starburst values in the central region surrounded by Seyfert-like values. It may be that we are reaching deeper regions in the galaxies in the near-IR, where Starburst excitation seems to be present.

This galaxy is close to edge-on (Maiolino et al. 1994), as also confirmed by Rif17, who found a PA ≈ 96° for the stellar kinematics, in agreement with that we obtain for the gas kinematics of ≈ 99° (Sch17). The model of Maiolino et al. (1994) has the disk plane inclined by 75°, above and below which ionized gas is outflowing in cones with opening angle of ≈ 80°. These outflows are consistent with the distribution of enhanced sigma values we observe in the ionized gas in a vertical structure crossing the galaxy plane and opening to the north and south of it (Fig. 6). The outflow to the north is also well traced by the [Fe II] flux distribution (approximately conical shape), while the H$_2$ flux distribution seems to better trace the gas in the galaxy plane.

6.6 NGC 5899

This inclined SAB(rs)c galaxy is reported to be in a pair and presents an optical Seyfert 2 spectrum (De Vaucouleurs et al. 1991). The stellar kinematics derived by Rif17 gives a PA ≈ 24°, that is somewhat distinct from that obtained for the molecular gas in Sch17, of ≈ 4°. The kinematics of the ionized gas is very different from that of the molecular gas (Fig. 7): while the later seems to be dominated by rotation in the inclined galaxy plane, with blueshifts to the north and redshifts to the south, the ionized gas kinematics shows a different orientation and velocities that are opposite to that observed in the H$_2$ velocity field. A possible interpretation is that the ionized gas is tracing an outflow at PA ≈ 0°,

as supported also by the north-south elongation observed mostly in the [Fe II] flux map and by the enhanced velocity dispersion also observed at these locations.

Although presenting a typical Seyfert 2 spectrum in the optical the near-IR line ratios indicate LINER excitation ever the whole field-of-view of our observations, what may be due to shocks produced by the outflows implied by the ionized gas kinematics.

6.7 Global properties

6.7.1 Kinematics

As already discussed many times along the paper, the H_2 velocity field is dominated by rotation in the plane of the galaxy. The ionized gas in most cases also show some rotation, but frequently shows distortions associated with an increase in the velocity dispersion that can be associated to outflows, that will be further discussed in Sch17. Signatures of outflows can be observed in most galaxies: NGC 788, along east-west; NGC 3227, towards the northeast, as suggested by distortions in the velocity field and patterns in h_3 and h_4; NGC 5506, along north-south, as suggested by the enhanced velocity dispersions; and NGC 5899, towards north-south, as indicated by the opposite velocity field between the ionized and molecular gas. The case of NGC 3516 is less clear, but it shows very disturbed gas velocity fields and enhanced velocity dispersion from the southeast to the northwest, suggesting the presence of an outflow along this direction.

6.7.2 Surface mass density distributions

Fig. 8 shows that the molecular gas seems to be more evenly distributed over the whole field of view, while the ionized gas is more concentrated towards the nucleus and shows a more patchy and collimated mass distribution. The more peaked distribution of the ionized gas is clearly seen in the average mass density profiles shown in the third column of Fig. 8 for the galaxies NGC 788, Mrk 607, NGC 3227 and NGC 5506. In the cases of NGC 3516 and NGC 5899, the profiles of the molecular and ionized gas surface mass distributions are similar to one another. The prevalence of the more concentrated ionized gas profiles can be understood as follows. The ionized gas emission traces better the collimated escape of ionized radiation, as expected in for the typical structure of an AGN. The H_2, on the other hand, has another source of excitation, like our previous works show, where the typical temperature is $\approx$ 2000K. The line ratios suggest thermal excitation for this region, and the heating can be attributed to X-rays originating in the AGN. These X-rays penetrate deep along the galaxy plane in every direction heating the H_2 gas. The different nature of the excitation of the ionized and the molecular gas can thus explain the diference in the gas surface mass density profiles of the ionized and molecular gas.

6.7.3 Excitation

The excitation maps $\log([\text{Fe II}]/\text{Pa}\beta)$ *versus* $\log(H_2/\text{Br}\gamma)$ show 3 main behaviors: i) nucleus with typical values of Seyfert excitation surrounded by typical values of LINER excitation (NGC 3227 and NGC 3516); ii) nucleus with typical values of Starburst excitation surrounded by typical values of Seyfert and/or LINER excitation (NGC 788, Mrk 607 and NGC 5506); iii) only LINER excitation values (NGC 5899).

The "i" behavior is frequently observed in active galaxies (Kraemer et al. 2008; Maksym et al. 2017). This behavior can be understood as the result of the ionization and excitation of the gas by ionizing radiation from the acretion disk which is collimated by a dust torus. The radiation that is not blocked by the dusty torus results in a Seyfert excitation of the gas along the ionization axis, resulting in a high ionization parameter along this direction. Radiation escaping at larger angles is filtered by the torus, but some of this radiation escapes, and the gas ionized and excited by it produces a LINER excitation due its lower ionization parameter.

7 CONCLUSIONS

We have mapped the ionized and molecular gas flux distributions, excitation and kinematics of the inner kiloparsec of 6 nearby active galaxies using NIR J- and K-band integral-field spectroscopy. The conclusions of this work are listed below.

- The flux distributions are usually distinct for the ionized and molecular gas: while the molecular gas emission is usually distributed approximately uniformly over the galaxy plane, the ionized gas is more collimated;
- The gas kinematics is also distinct: while the molecular gas is mostly rotating in the galaxy plane with low velocity dispersions, the ionized gas frequently shows other components associated with higher velocity dispersions;
- The additional components observed in the ionized gas velocity fields in most cases can be identified with outflows from the nucleus;
- There is usually an inverse correlation between the h_3 Gauss-Hermite moments and the velocity fields, in the sense that positive values (red wings) are associated to blueshifts and negative values (blue wings) are associated to redshifts;
- There is usually an inverse correlation between the h_4 Gauss-Hermite moment and the velocity dispersion maps, in the sense that high σ values (boxy profiles) correspond to negative values of h_4 and low values of σ (peaky profiles) correspond to positive values of h_4;
- The integrated mass of hot molecular gas ranges from 182 $M_\odot$ to 1400 $M_\odot$, while the estimated integrated mass of cold molecular gas ranges from $1.3\times10^7 M_\odot$ to 1×10^9 $M_\odot$.
- The integrated mass of the ionized gas ranges from 3×10^5 $M_\odot$ to 3.2×10^7 $M_\odot$.
- The average surface mass density of the hot molecular gas ranges from 1.6×10^{-3} $M_\odot/pc^2$ to 1.4×10^{-2} $M_\odot/pc^2$, while that estimated for the cold molecular gas ranges from 1319 $M_\odot/pc^2$ to 20682 $M_\odot/pc^2$.
- The ionized gas has average surface mass density ranging from 4.8 $M_\odot/pc^2$ to 244 $M_\odot/pc^2$.
- We have obtained azimuthally averaged gass mass density profiles and found that in 4 out of the 6 galaxies studied here, the profiles for the ionized gas are steeper that those for the molecular gas. We attribute this distinct behavior to the excitation mechanisms: while the ionized gas is excited by the AGN radiation in regions with temperatures

of about 10000K, the molecular gas is thermally excited in regions of lower temperatures of about 2000K, that extend farther from the nucleus;

• The near-IR diagnostic diagram [Fe II]/Paβ vs H_2/Brγ result in excitation maps with values characteristic of Starbursts surrounded first by Seyfert-like values and then outwards by LINER-like values for three galaxies of the sample, while for the other three, a mixture of Seyfert (usually at the nucleus) and LINER excitation (usually surrounding the Seyfert region) is observed.

REFERENCES

Adams T. F., 1977, ApJS, 33, 19.
Aoki K., Ohtani H., Yoshida M., Kosugi G., 1994, PASJ, 46, 539.
Arribas S., Mediavilla E., 1994, ApJ, 437, 149.
Arribas S., Mediavilla E., García-Lorenzo B., Del Burgo C., 1997, ApJ, 490, 227.
Barillard A., Bertin E., de Lapparent V., Fouqu P., Arnouts S., Mellier Y., Pell R., Leborgne J.-F., Prugniel P., Makarov D., Makarova L., McCracken H. J., Bijaoui A., Tasca L., 2011, A&A, 532, 74.
Barbosa F. K. B., Storchi-Bergmann T., McGregor P., Vale T. B., Riffel R. A., 2014, MNRAS, 445, 2353.
Blanco P. R., Ward M. J., Wright G. S., 1990 MNRAS, 242, 2.
Cruz-Gonzalez I., Carrasco L., Serrano A., Guichard J., Dultzin-Hacyan D., Bisiachhi G. F., 1994, ApJS, 94,47.
Colbert E. J. M., Baum S. A., Gallimore J. F., O'Dea C. P., Lehnert M. D., Tsvetanov Z. I., Mulchaey J. S., Caganoff S. 1996a, ApJS, 105, 75.
Colina L., Piqueras L. J, Arribas S, Riffel R., Riffel R. A., Rodriguez-Ardila A., Pastoriza M., Storchi-Bergmann T., Alonso-Herrero A., Sales D., 2015, A&A, 578, 48.
Dale D. A., Sheth K., Helou G., Regan M. W., Hüttemeister S., 2005, AJ, 129, 2197D.
Davies R. I., Maciejewski W., Hicks E. K. S., Tacconi L. J., Genzel R., Engel H., ApJ, 702, 114D.
Davies R. I., Maciejewski W., Hicks E. K. S., Emsellem E., Erwin P., Burtscher L., Dumas G., Lin M., Malkan M. A., Müller-Sánchez F., Orban de Xivry G., Rosario D. J., Schnorr-Mller A., Tran A., 2014, ApJ, 792, 101.
de Vaucouleurs G., de Vaucouleurs A., Corwin H. G. Jr., Buta R. J., Paturel G., Fouqué P., 1991, Third Reference Catalogue of Bright Galaxies (New York: Springer).
Diniz M. R., Riffel R. A., Storchi-Bergmann T., Winge C., 2015, MNRAS, 453, 1727.
Evans I. N., Koratkar A. P., Storchi-Bergmann T., Kirkpatrick H., Heckman T. M., Wilson, A. S., 1996, ApJS, 105, 93.
Fabian A. C., 2012, ARA&A, 50, 455.
Ferrarese L., Ford H., 2005, SSRv, 116, 523.
Ferruit, P., Wilson, A. S., & Mulchaey, J. 2000, ApJS, 128, 139.
Goad J. W., Gallagher J. S., 1987, AJ, 94, 640.
Goad J. W., Gallagher J. S., 1988, AJ, 95, 948.
Hamuy M., Maza J., 1987, A&AS, 68,383.
Heckman T. M., Blitz L., Wilson A. S., Armus L., Miley G. K., 1989, ApJ, 342,735.
Ho L. C., Filippenko A. V., Sargent W. L. W., 1997, ApJS, 112, 315.
Huchra J. P., Wyatt W. F., Davis H., 1982, AJ, 87,1628.
Kay L. E., 1994, ApJ, 430,196.
Kewley L. J., Heisler C. A., Dopita M. A., Lumsden S.m 2001, ApJS, 132, 37.
Kotilainen J. K., 1998, A&AS, 132, 197.
Kraemer S. B., Schmitt H. R., Crenshaw D. M., 2008, ApJ, 679, 1128.
Kriss G. A., Espey B. R., Krolik J. H., Tsvetanov Z., Zheng W., Davidsen A. F., 1996, ApJ, 467, 622.
Koratkar A., Goad M. R., O'Brien P. T., Salamanca I., Wanders I, Axon D., Crenshaw D. M., Robinson A., Korista, K., Rodriguez-Pascual P., Horne K., Blackwell J., Carini M., England M., Perez M., Pitts R., Rawley L., Reichert G., Shrader C., Wamsteker W., 1996, ApJ, 470, 378.
Kormendy J., Ho L. C., 2013, ARA&A, 51, 511.
Larkin J. E., Armus L., Knop R. A., Soifer B. T., Matthews K., 1998, ApJS, 114, 59.
Maiolino R., Stanga R., Salvati M., Rodriguez Espinosa J. M., 1994, A&A, 290, 40.
Maksym W. P., Fabbiano G., Elvis M., Karovska M, Paggi A., Raymond J., Wang J., Storchi-Bergmann T., 2017, ApJ, 844, 69.
Malkan M. A., Gorjian V., Tam R., 1998, ApJS, 117, 25.
Mazzalay X. et al., 2013, MNRAS, 428, 2389.
Mazzalay X., Maciejewski W., Erwin P., Saglia R. P., Bender R., Fabricius M. H., Nowak N., Rusli S. P., Thomas J., 2014, MNRAS, 438, 2036.
McGregor P. J. et al., 2003,Proc. SPIE, 4841, 1581.
Müller-Sánchez F., Davies R. I., Eisenhauer F., Tacconi L. J., Genzel R., Sternberg A., 2006, A&A, 454, 492.
Mulchaey J. S., Tsvetanov Z., Wilson A. S., Pérez-Fournon I., 1992, ApJ, 394, 91.
Müller Sánchez F., Davies R. I., Genzel R., Tacconi L. J., Eisenhauer F., Hicks E. K. S., Friedrich S., Sternberg A., 2009, ApJ, 691, 749.
Mundell C. G., James P. A., Loiseau N., Schinnerer E., Forbes D. A., 2004, ApJ, 614, 648.
Mundell C. G., Holloway A. J., Pedlar A., Meaburn J., Kukula M. J., Axon D. J., 1995, MNRAS, 275, 67.
Nagar N. M., Wilson A. S., Mulchaey J. S., Gallimore J. F., 1999, ApJS, 120, 209.
Nagar N. M., Oliva R., Marconi A., Maiolino R., 2002, A&A, 391, L21.
Oliva E. et al., 2001, A&A, 369, L5.
Osterbrock, D. E. & Ferland, G. J., 2006, Astrophysics of Gaseous Nebulae and Active Galactic Nuclei, Second Edition, University Science Books, Mill Valley, California.
Prugniel P., 2001, in Mining the Sky, ed. A. J. Banday, S. Zaroubi, & M. Bartelmann (Heidelberg: Springer), 683.
Pogge R. W., 1989, AJ, 98, 124.
Raluy F., Planesas P., Colina L., 1998, A&A, 335, 113.
Ramos Almeida C., Levenson N. A., Rodríguez Espinosa J. M., Alonso-Herrero A., Asensio Ramos A., Radomski J. T., Packham C., Fisher R. S., Telesco C. M., 2009, ApJ, 702, 1149.
Riffel R. A., 2010, Ap&SS, 327, 239.
Riffel R. A., Sorchi-Bergmann T., Winge C., Barbosa F. K. B., 2006a, MNRAS, 373, 2.
Riffel R. A., Storchi-Bergmann T., Winge C., McGregor P.

J., Beck T., Schmitt H., 2008, MNRAS, 385, 1129.
Riffel R., Pastoriza M. G., Rodríguez-Ardila A., Maraston C., 2008b, MNRAS, 388, 803.
Riffel R. A., Storchi-Bergmann T., Dors O. L., Winge C., 2009a, MNRAS, 393, 783.
Riffel R., Pastoriza M. G., Rodríguez-Ardila A., Bonatto C., 2009, MNRAS, 400, 273.
Riffel R. A., Storchi-Bergmann T., Riffel R., Pastoriza M. G., 2010, ApJ, 713, 469.
Riffel R. A., Storchi-Bergmann T., Nagar N. M., 2010, MNRAS, 404, 166.
Riffel R., Ruschel-Dutra D., Pastoriza M. G., Rodríguez-Ardila A., Santos J. F. C., Jr, Bonatto C. J., Ducati J. R., 2011a, MNRAS, 410, 2714.
Riffel R. Riffel A. R., Ferrari F., Storchi-Bergmann T., 2011, MNRAS, 416, 493.
Riffel R. A., Storchi-Bergmann T.,2011, MNRAS, 417, 2752.
Riffel R. A., Storchi-Bergmann T.,2011, MNRAS, 411, 469.
Riffel R. A., Storchi-Bergmann T., Winge, C. 2013, MNRAS, 430, 2249.
Riffel R. A., Vale T. B., Storchi-Bergmann T., McGregor P. J., 2014, MNRAS, 442, 656.
Riffel R. A., Storchi-Bergmann T., Riffel R., 2014, ApJL, 2014, 780, 24.
Riffel R. A., Storchi-Bergmann T., Riffel R., 2015, MNRAS, 451, 3587.
Riffel R. A., Storchi-Bergmann T., Riffel R., Dahmer-Hahn L. G., Diniz M. R., Schönell A. J. Jr., Dametto N. Z., 2017, MNRAS, 470, 992.
Roche, P. F., Packham, C., Aitken, D. K., & Mason, R. E. 2007, MNRAS, 375, 99.
Roche, P. F., Aitken, D. K., Smith, C. H. & Ward, M. J. 1991, MNRAS, 248, 606.
Rodríguez-Ardila A., Pastoriza M. G., Viegas S., Sigut T. A. A., Pradhan A. K., 2004, A&A, 425, 457.
Rodríguez-Ardila A., Contini M., Viegas S. M., 2005, MNRAS, 357, 220.
Rodríuez-Ardila A., Riffel R., Pastoriza M. G., 2005, MNRAS, 364, 1041.
Riffel R., Rodríguez-Ardila A., Pastoriza M. G., 2006b, A&A, 457, 61.
Scoville, N. Z., Hall, D. N. B., Kleinmann, S. G., & Ridgway, S. T. 1982, 253, 136..
Springel V, Di Matteo T., Hernquist L., 2005, MNRAS, 361, 776.
Siebenmorgen R., Krügel E., Spoon H. W. W., 2004b, A&A, 419, 49.
Somerville R. S., Hopkins P. F., Cox T. J., Robertson B. E., Hernquist L., 2008, MNRAS, 391, 481.
Schmitt H. R., Kinney A. L., 2000, ApJS, 128, 479.
Schinnerer E., Eckart A., Tacconi L. J., 2000, ApJ, 533, 826.
Schönell A. J. J., Riffel, R. A., Storchi-Bergmann T., Winge C., 2014, MNRAS, 445, 427.
Schönell A. J. J., Storchi-Bergmann T., Riffel, R. A, Riffel R., 2016, MNRAS, 464, 1771.
Storchi-Bergmann T., McGregor P., Riffel R., Rogemar A., Simões Lopes R., Beck T., Dopita M., 2009, MNRAS, 394, 1148.
Storchi-Bergmann T., Simões Lopes R., McGregor P. Riffel, Rogemar A., Beck T., Martini P., 2010, MNRAS, 402, 819.
Storchi-Bergmann T., Riffel R. A.; Riffel R., Diniz M. R., Borges V. T., McGregor P. J., 2012, ApJ, 755, 87.
Terrazas B. A., Bell E. F., Henriques B. M. B., White S. D. M., Cattaneo A., Woo J., 2016, ApJL, 830, 12.
Ulvestad J. S., Wilson A. S., 1989, ApJ, 343,659.
Ulrich M. H., Péquignot D., 1980, ApJ, 238, 45.
Veilleux S., Tully R. B., Bland-Hawthorn J., 1993, AJ, 105, 1318.
Voit G. M., Shull J. M., Begelman M. C., 1987, ApJ, 316, 573.
Wagner S. J., 1987, PASP, 100, 54.
Wrobel J. M., Heeschen D. S., 1988, ApJ, 335, 677.
Zaw I., Farrar G. R., Greene J. E., 2009, ApJ, 696, 1218.

6 *Discussão geral*

Neste capítulo discutimos os resultados obtidos nos trabalhos apresentados ao longo da Tese. Nas tabelas 6.1 e 6.2 listamos os parâmetros físicos obtidos para as galáxias já observadas da amostra extraídos de artigos já publicados ou em publicação.

6.1 Massas totais de gás e densidades superficiais médias de massa

6.1.1 Gás molecular

Na tabela 6.1 listamos os valores das massas de gás e correspondentes densidades superficiais de massa para seis galáxias trabalhadas em Schönell et al., submetido (a partir daqui Sch17) e mais 10 galáxias já previamente estudadas e com resultados publicados. As massas de hidrogênio molecular quente vão de 29 $M_{\odot}$ para a galáxia NGC 1068 (Riffel et al., 2014) até $3{,}3\times10^{3}$ $M_{\odot}$ para a galáxia Mrk1066 (Riffel et al., 2010). A partir dessas massas de gás molecular quente podemos estimar as massas de gás molecular frio, que vão de 2×10^{7} para a galáxia NGC 1068 (Riffel et al., 2014) até $2{,}4\times10^{9}$ $M_{\odot}$ para a galáxia Mrk 1157 (Riffel; Storchi-Bergmann, 2011d).

Estes valores de massas totais são da ordem dos calculados por Mazzalay et al. (2013), que estima valores de $\approx 10^{5-8}$ $M_{\odot}$ para o gás molecular frio numa região de 3"x 3", a partir de observações com o instrumento SINFONI do VLT (*Very Large Telescope*). Os valores moderadamente menores encontrados por Mazzalay et al. (2013) para o gás molecular frio, devem-se ao fato da área coberta por suas observações serem ligeiramente menores do que as usadas neste trabalho, uma vez que, mesmo tendo a mesma abertura angular (3"x3") as galáxias de Mazzalay et al. (2013) são mais próximas (10-16.5 Mpc). Já para o gás molecular quente, Mazzalay et al. (2013) encontra valores de 0.6 a 115 $M_{\odot}$, mais uma vez ligeiramente menores do que os encontrados neste trabalho, mas justificados da mesma maneira que para os valores de gás molecular frio.

Em um trabalho mais recente, Kakkad et al. (2017) observou com o ALMA (*Atacama Large Milimetric Array*) AGNs em z$\approx$ 1,5, e usou a linha de emissão CO[2-1] para encontrar massas para o hidrogênio molecular de 2,5 - 10×10^{10} $M_\odot$. Este valor é uma ou duas ordens de grandeza maior do que os valores encontrados nesta tese, mas temos que levar em conta a maior distância das galáxias de Kakkad et al. (2017) bem como a evolução das galáxias durante o tempo cósmico transcorrido, uma vez que a z$\approx$2, observamos o máximo da formação estelar e atividade nuclear no universo. A partir de linhas de emissões do CO observadas com o ALMA, Zschaechner et al. (2016) encontrou $\approx 2{,}9\times10^8$ $M_\odot$ de gás molecular nos 1.5 kpc centrais da galáxia Circinus, valor da ordem dos estimados nesta tese e em mais um trabalho usando as linhas do CO a partir de observações com o ALMA, Koay et al. (2016) estimaram a massa de gás molecular nos 2 kpc centrais da galáxia Mrk 590 em $\approx 10^7$ $M_\odot$, que é semelhante aos valores encontrados nesta tese para a massa do H_2 frio.

Na tabela 6.1 listamos também as densidades superficiais médias de massa (Σ) para cada galáxia, uma vez que temos observações cobrindo diferentes áreas nas galáxias, fazendo mais sentido discutirmos valores de massa por unidade de área do que valores absolutos de massa. Dessa maneira, vemos que a densidade superficial média de massa do gás molecular quente varia de $7{,}6\times10^{-4}$ a $1{,}3\times10^{-2}$ $M_\odot/pc^2$, enquanto que para o gás molecular frio estima-se uma Σ entre 526 e 20682 $M_\odot/pc^2$. Os valores de máximos e mínimos de Σ são mais próximos entre si do que os valores absolutos, confirmando a ideia de que a densidade superficial média de massa é um parâmetro melhor para comparações entre diferentes galáxias.

Na Fig 6.1 mostra-se os histogramas para as densidades superficiais médias de massa, onde pode-se ver também a linha verde que demarca a média desses valores: $7{,}1\times10^{-3}$ $M_\odot/pc^2$, $5{,}9\times10^3$ $M_\odot/pc^2$ e 44 $M_\odot/pc^2$ respectivamente para o gás molecular quente, molecular frio e gás ionizado. Para a galáxia Circinus, Zschaechner et al. (2016) chegaram a uma massa total de gás molecular de 2,9 $\times10^8$ $M_\odot$; estimando a área de emissão do CO e calculando a densidade supercifial média de massa para esse caso, encotra-se $\approx$ 2101 $M_\odot/pc^2$, valor na mesma ordem de grandeza da média do valores encontrados neste trabalho.

6.1.2 Gás ionizado

As massas de hidrogênio ionizado variam de $2{,}2\times10^4$ para a galáxia NGC 1068 (Riffel et al., 2014) a $3{,}2\times10^7$ para a galáxia NGC 5506 (Sch17). Quando comparamos estes valores aos de hidrogênio molecular quente chegamos a valores entre 10^3 e 10^4 vezes maiores para a massa de gás ionizado do que para a massa de gás molecular quente. Mas se usarmos a estimativa de gás molecular frio que é, pelo menos, 10^5 vezes maior do que a de gás quente (Mazzalay et al.,

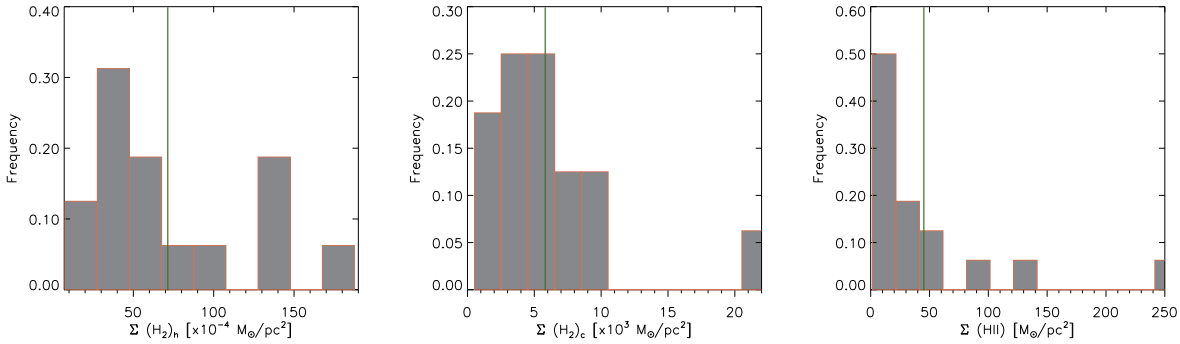

Figura 6.1: Histogramas para as densidades superficiais médias de massa para o gás molecular quente, molecular frio e gás ionizado, respectivamente. A linha verde que corta cada um dos histogramas determina a média das densidades.

2013; Dale et al., 2005), chegamos a valores mais altos para a massa de gás molecular do que de gás ionizado, com razões variando de 10^2 a 10^3 entre as massas de gás molecular frio e gás ionizado.

Novamente, é interessante considerar a densidade superficial média de massa de gás ionizado, que varia de 1,5 a 244 $M_{\odot}/pc^2$, 10^3 a 10^4 vezes maior do que a Σ para o hidrogênio molecular quente, mas 10 - 10^3 vezes menor do que a Σ estimada para o gás molecular frio.

Tabela 6.1: Área total, massa total e densidade superficial média de massa para o gás ionizado, molecular quente e molecular frio para 16 galáxias observadas da amostra.

Galaxies	Área (H_2)	Área (HII)	M $(H_2)_h$	M $(H_2)_c$	M (HII)	Σ $(H_2)_h$	Σ $(H_2)_c$	Σ (HII)	Ref.
Mrk1157	2.8×10^5	1.8×10^5	2.3×10^3	1.6×10^9	5.4×10^6	8.2×10^{-3}	5714	45	1
NGC788	6.2×10^5	5.5×10^5	1012	7.3×10^8	4.8×10^6	1.6×10^{-3}	1319	8.8	2
NGC1068	3.8×10^4	1.5×10^4	29	2×10^7	2.2×10^4	7.6×10^{-4}	526	1.5	3
Mrk1066	2.5×10^5	1.9×10^5	3.3×10^3	2.4×10^9	1.7×10^7	1.3×10^{-2}	9600	89	4
Mrk607	5.9×10^4	2.3×10^4	182	1.3×10^8	1.1×10^6	3×10^{-3}	5710	48	5
NGC2110	1.1×10^5	7×10^4	1.4×10^3	9.9×10^8	1.7×10^6	1.3×10^{-2}	9000	24	6
Mrk79	9.8×10^5	7.8×10^5	3×10^3	2.2×10^9	7×10^6	3.1×10^{-3}	2245	9	7
NGC3227	8.8×10^4	4.4×10^4	1274	9.2×10^8	1.7×10^6	1.4×10^{-2}	20682	39	8
NGC3516	8×10^4	6×10^4	517	3.7×10^8	3×10^5	6.4×10^{-3}	6168	5	9
NGC4051	1.3×10^4	1.4×10^4	66	4.7×10^7	1.4×10^5	5.3×10^{-3}	3760	9.8	10
NGC4151	2.4×10^4	1.9×10^4	240	1.7×10^8	2.4×10^6	1.8×10^{-2}	7083	125	11
Mrk766	3×10^5	2.7×10^5	1.3×10^3	9.8×10^8	7.6×10^6	4.3×10^{-3}	3266	28	12
NGC5506	1.4×10^5	1.2×10^5	1.4×10^3	1×10^9	3.2×10^7	9.7×10^{-3}	7951	244	13
NGC5548	1.7×10^5	6.7×10^5	2.3×10^2	1.7×10^8	2.2×10^6	6.6×10^{-3}	3473	7.2	14
NGC5899	1.9×10^5	8.7×10^4	559	4×10^8	4.2×10^5	2.9×10^{-3}	4624	4.8	15
NGC5929	1.2×10^5	7×10^4	471	3.5×10^8	1.3×10^6	3.9×10^{-3}	2966	18	16

Todas as massas estão em unidades de $M_\odot$, as unidades de área em pc^2 e as de densidade superficial média de massa (Σ) em $M_\odot/pc^2$.
Referências: 1 - (Riffel; Storchi-Bergmann, 2011d); 2 - Sch17; 3 - (Riffel et al., 2014); 4 - (Riffel et al., 2010); 5 - Sch17;
6 - (Diniz et al., 2015); 7 - (Riffel et al., 2013); 8 - Sch17; 9 - Sch17; 10 - (Riffel et al., 2008); 11 - (Storchi-Bergmann et al., 2009);
12 - (Schönell et al., 2014); 13 - Sch17; 14 - (Schönell et al., 2017); 15 - Sch17; 16 - (Riffel et al., 2015).

6.1.3 Distribuições de densidade superficial de massa

Em Sch17 mostramos que o gás molecular parece estar mais uniformemente distribuído pelo FOV, enquanto o gás ionizado está mais concentrado no núcleo. Essa diferença pode ser explicada: a emissão de gás ionizado traça melhor o escape colimado da radiação ionizante, o que é esperado para a estrutura típica de um AGN, em que a radiação do disco de acreção sai perpendicularmente ao disco, sendo mais fraca a ângulos grandes em relação à perpendicular ao disco, considerando também que a ângulos pequenos em relação ao disco, a radiação encontra o torus molecular de poeira. O gás molecular, por outro lado, tem outra fonte de excitação, as razões de linhas indicam excitação térmica nessas regiões e o aquecimento pode ser atribuído aos raios-X originados no AGN. Esses raios-X penetram no plano da galáxia em todas as direções aquecendo o gás molecular, produzindo assim, essa diferença na distribuição de densidade superficial de massa, que é atribuída, então, à diferente natureza de excitação dos gases ionizado e molecular.

6.2 Excitação

O diagrama diagnóstico no infravermelho próximo utilizado neste tese, que é um mapa com as razões de linhas log([Fe II]/Paβ) *versus* log(H_2/Brγ), nos permitem investigar a excitação na região central, onde os valores típicos destas razões variam entre 0,6 e 2,0 para núcleos Seyfet para as duas razões (Rodríguez-Ardila et al., 2005), enquanto para Starbursts os valores são menores que 0,6 e para LINERs os valores são maiores que 2,0. Mais recentemente, Colina et al. (2015) redefiniu o intervalo de valores correspondente à excitação Seyfert para a razão log(H_2/Brγ), ficando entre -0,3 e 0,9. Para a nossa amotra, os diagramas diagnóstico mostram 3 comportamentos principais: i) núcleo com valores típicos de Seyfert circundado por valores típicos de LINERS, como nos casos de Mrk 1157, NGC 3227 e NGC 3516; ii) núcleo com valores típicos de Starburst circundado por valores Seyfert e/ou LINER, como nos casos de NGC 788, NGC 607 e NGC 5506; iii) somente valores de Seyfert ou somente valores de LINER, como nos casos de NGC5929 e NGC 5899, respectivamente.

O comportamento "i"– uma região com excitação tipo Seyfert rodeada por uma região de excitação tipo LINER – é frequentemente observado em galáxias ativas (Maksym et al. 2017 para NGC 3393 e Kraemer et al. 2008 para NGC 4151). Este comportamento pode ser entendido como o resultado da ionzação e excitação do gás por radiação ionizante do disco de acreção colimada por um toróide de poeira. A radiação que sai livremente, sem ser bloqueada pelo toróide, resulta em excitação do tipo Seyfert devido seu alto parâmetro de ionização

enquanto que a radiação que sai rente ao toróide é parcialmente filtrada pelas suas bordas, produzindo excitação tipo LINER devido ao seu parâmetro de ionização mais baixo, assim como mostra a Fig. 6.2 para a NGC 3393.

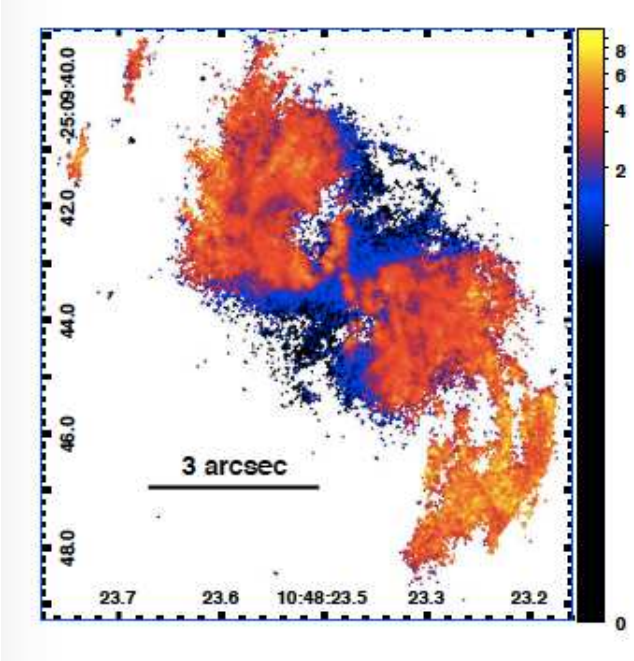

Figura 6.2: Mapa de razões de [O III]/Hα onde pontos azuis/pretos indicam razões baixas e amarelos/vermelhos indicam razões altas. Figura retirada de Maksym et al. (2017).

6.3 Cinemática do gás

A cinemática do gás é dominada por rotação, principalmente no caso do gás molecular, que ainda apresenta menor dispersão de velocidades ($\approx$ 100 km/s) e é interpretado como uma indicação de que o H_2 está mais restrito ao plano da galáxia. Em alguns casos, uma curva de rotação bem abrupta é observada, bem como discos moleculares compactos – estendendo-se somente algumas dezenas de parsecs do AGN – como nos casos de Mrk 1066 e Mrk 766, por exemplo. Em vários casos verificou-se a presença de inflows ao longo de braços espirais, com taxas de inflow da ordem de algumas massas solares por ano (ver discussão abaixo). Para o gás ionizado, que apresenta uma emissão mais colimada, observa-se também um padrão de rotação, porém, muitas vezes perturbado, com o gás parecendo se estender a altas latitudes. Esta perturbação somada à uma dispersão de velocidades muito mais alta ($>$ 100 km/s) quando comparada ao gás molecular, é frequentemente associada à outflows, que são observados principalmente para o [Fe II]λ1.2570μm. Esta linha de emissão parece traçar melhor os outflows do AGN do que a do [O III]λ5007Å usada em estudos anteriores, uma vez que a emissão do

[Fe II] é mais estendida que a do [O III], alcançando a região parcialmente ionizada (além da região totalmente ionizada). As taxas de outflow de massa calculadas a partir do [Fe II] ficam da ordem de algumas massas solares por ano (ver discussão abaixo).

6.3.1 Momentos h_3 e h_4

Para o H_2 e em alguns casos para o Paβ e Brγ encontramos uma anticorrelação entre o momento h_3 de Gauss-Hermite e a velocidade centróide, bem como uma anticorrelação entre o momento h_4 de Gauss-Hermite e a dispersão de velocidades σ. Isso significa que temos asas vermelhas em regiões de blueshift e asas azuis em regiões de redshift. Isto pode ser atribuído a um efeito conhecido como "asymmetric drift " (Westfall et al., 2007), que pode ser compreendido em termos da contribuição de um gás em rotação no plano – dando origem ao campo de velocidades "principal" (centróide da linha)– mais a contribuição de um gás mais tênue a mais alta latitude que gira com velocidade um pouco menor, dando origem às asas das linhas.

6.4 Cinemática Estelar

Obtivemos a cinemática estelar para 16 galáxias da amostra (Riffel et al., 2017). Encontramos que os mapas de velocidade para a maioria das galáxias é bem reproduzido por modelos de discos em rotação. Em Riffel et al. (2017) concluímos que as amplitudes encontradas nos mapas residuais de velocidade estão correlacionados com a luminosidade dos raios-X duros, sugerindo que os AGNs mais luminosos têm um impacto maior na dinâmica estelar da sua vizinhança. Para metade das galáxias, encontramos uma anticorrelação entre a velocidade e o momento h_3 de Gauss-Hermite, implicando em asas vermelhas no lado em blueshift e asas azuis no lado em redshit do campo de velocidades. Aqui vale a mesma interpretação para o fenômeno semelhante encontrado para o gás: o "*assimetric drift*". As estrelas do bojo, por terem uma maior dispersão de velocidades, tem uma velocidade de rotação menor, produzindo as asas observadas.

Duas das galáxias da amostra apresentam uma linha de velocidade nula com formato "S", o que foi atribuido ao potencial gravitacional de uma barra, como discutido em Riffel et al. (2017). Mapas de dispersão de velocidades mostraram anéis de baixa dispersão ($\approx$ 50 - 80 km/s) para 4 objetos e "caminhos" de baixa dispersão para 6 galáxias a 150 - 250 pc do núcleo, atribuídos a populações estelares jovens/intermediárias. Para mais informações sobre a cinemática estelar consulte o Apêndice I onde encontra-se o paper completo de Riffel et al. (2017).

6.5 Feeding e Feedback

6.5.1 Inflows

Inflows foram observados em gás molecular (quente), ao longo de braços espirais nucleares para as galáxias NGC 2110, Mrk 79 e NGC 4051, com taxas variando de 4×10^{-5} $M_\odot$ por ano para a galáxia NGC 4051 (Riffel et al., 2008) a 4×10^{-3} $M_\odot$ por ano para a galáxia Mrk 79 (Riffel et al., 2013). Em alguns casos não encontramos evidências cinemáticas de inflow, mas encontramos discos compactos em rotação, que devem estar alimentando o AGN, como é o caso de Mrk 766 (Schönell et al., 2014) e Mrk 1066 (Riffel et al., 2010). Em um estudo mais recente, Rodríguez-Ardila et al. (2017) encontram um limite superior para a taxa de inflow de ≈ 0.4 $M_\odot$ por ano para a galáxia NGC 1368.

Cabe aqui também a ressalva que temos levantado em nossos trabalhos de que o gás molecular quente deve ser somente um traçador do gás molecular total, que é dominado por gás frio. O gás frio emite em ondas de rádio em particular ondas milimétricas observadas com o ALMA. Assumindo uma razão típica de $> 10^5$ entre a massa de gás frio e quente também se aplica par a taxa de inflow, estas taxas poderiam chegar a dezenas de massas solares por ano.

6.5.2 Outflows

A grande maioria dos outflows encontrados foram em gás ionizado; valores para as taxas de outflow variam entre 6×10^{-2} $M_\odot$ por ano para a Mrk 1066 (Riffel et al., 2010) até 10,7 $M_\odot$ por ano para a Mrk 766 (Schönell et al., 2014), como podemos ver na tabela 6.2. Estes valores são compatíveis com os encontrados por Veilleux et al. (2005) e Müller-Sánchez et al. (2011), que vão de 0,1 até 120 $M_\odot$ por ano. Só foi encontrado outflow em gás molecular quente (2000 K) em um caso: NGC 2110 (Diniz et al., 2015) com taxas de outflow de $4{,}3\times10^{-4}$ $M_\odot$ por ano. Para a galáxia NGC 1368, Rodríguez-Ardila et al. (2017) encontram uma taxa de outflow de 11 $M_\odot$ por ano traçada pelo gás coronal.

Potência dos outflows

Os modelos de evolução de galáxias (Di Matteo et al., 2008) mostram que para o *outflow* de um AGN tenha um efeito (*feedback*) significativo na evolução de sua galáxia hospedeira, sua potência deve ser da ordem de 0,5% da luminosidade do AGN. Este valor é usado por ser da ordem da razão entre a energia de ligação das estrelas do bojo de uma galáxia e a energia típica de acreção do buraco negro supermassivo associado a este bojo, como explicado a seguir (Zu-

bovas; King, 2012). A energia de ligação das estrelas pode ser calculada através de E_b=$M_b\sigma^2$, onde M_b é a massa das estrelas do bojo da galáxia (para um bojo massivo $M_b \approx 10^{11}$ $M_\odot$) e σ é a dispersão de velocidades das estrelas, e a energia total disponível como resultado da acreção pode ser calculada através de E*acc*=$\eta M_{BH} c^2$, onde η é o coeficiente de eficiência de acreção, M_{BH} é a massa do buraco negro supermassivo (valor típico $\approx 10^8$ $M_\odot$ para $M_b \approx 10^{11}$ $M_\odot$) e c é a velocidade da luz. Fazendo essa razão encontramos um valor de ≈ 0.005. Isto significa que, se a potência do feedback/outflow for maior do que 0.5% L_{Bol}, o feedback pode causar "disrupção"no bojo.

A tabela 6.2 mostra os valores das potências dos outflows dos AGNs que foram encontradas entre as galáxias da amostra, bem como a razão percentual entre a potência do outflow e a luminosidade bolométrica do AGN. Podemos ver as potências dos outflows variando de 9.5×10^{37} ergs/s para a NGC 1066 a 5.7×10^{41} ergs/s para a NGC 1157 e que somente em um caso, para a NGC 1068, o valor da potência do outflow é maior do que 0,5% da luminosidade bolométrica do AGN, e somente para outros 2 casos chegamos a valores próximos a isso: 0.3 e 0.4 % para as galáxias NGC 4151 e Mrk 766 respectivamente.

Tabela 6.2: Distância, área observada, taxa de outflow, potência do outflow, razão percentual entre a potência do outflow e a luminosidade bolométrica do AGN e taxa de inflow para as galáxias correspondentes.

Galáxia	D (Mpc)	Área Obs (pc^2)	Outflow rate ($M_\odot$/ano)	Pot. (ergs/s $\times 10^{40}$)	% (Pot./L_{bol})	Inflow rate ($M_\odot$/ano)	Ref.
Mrk1157	61,1	900x900	6	57	-	-	1
NGC1068	15,2	200x200	1,9	28	4,4	-	2
Mrk1066	48,6	700x700	6×10^{-2}	0,0095	-	-	3
NGC2110	30,2	440x440	$4{,}3\times10^{-4}$†	16	0,08	$4{,}6\times10^{-4}$†	4
Mrk79	91,8	1350x1350	3,5	3,4	0,01	4×10^{-3}†	5
NGC4051	9,3	130x180	-	-	-	4×10^{-5}†	6
NGC4151	13,3	192x320	1	24	0,3	-	7
Mrk766	60,6	900x900	10,7	29	0,4	-	8
NGC5548	74,5	1050x1050	4,9	21	0.08	-	9
NGC5929	35,9	520x520	0,4	0,31	-	-	10

† Identifica as massas de outflow e inflow que foram calculadas a partir do gás molecular.
A luminosidade bolométrica do AGN foi estimada como sendo 10 vezes a luminosidade em raios-X do AGN. Casos sem o valor de porcentagem da razão entre potência do outflow e luminosidadade bolométrica do AGN se devem ao fato de não possuírem um valor para a luminosdidade em raios-X conforme a tabela encontrada no paper da Amostra (Seção 2).
Refs: 1 - (Riffel; Storchi-Bergmann, 2011d); 2 - (Riffel et al., 2014); 3 - (Riffel et al., 2010); 4 - (Diniz et al., 2015); 5 - (Riffel et al., 2013); 6 - (Riffel et al., 2008); 7 - (Storchi-Bergmann et al., 2009); 8 - (Schönell et al., 2014); 9 - (Schönell et al., 2017); 10 - (Riffel et al., 2015).

6.5.3 Populações estelares

Obtivemos populações estelares resolvidas até o momento para 4 galáxias da amostra. Destas 4, participei ativamente no estudo das populações estelares para a NGC 5548, onde encontramos uma componente de população estelar velha (2 Gyr $<$ t $\leq$ 15 Gyr) a distância variando entre 160 e 300 pc do núcleo, enquanto mais próximo do mesmo encontramos uma componente de idade intermediária (50 Myr $<$ t $\leq$ 2 Gyr) com contribuições variando de 40 a 100 % do fluxo em 2.12μm. Para as outras 3 galáxias, Mrk 1066, Mrk 1157 e NGC 1068, populações estelares jovens ($\leq$ 100 Myr) são vistas entre 200 a 300 pc, contribuindo com $\approx$ 20% no fluxo da banda K; populações estelares de idade intermediária estão mais afastadas, enquanto populações mais velhas dominam os 250 pc centrais.

7 *Conclusões*

Nesse capítulo sintetizamos as principais conclusões encontradas a partir do estudo de 20 galáxias ativas do universo próximo, usando espectroscopia de campo integral no infravermelho próximo, como parte de uma large proposal do telescópio Gemini usando o instrumento NIFS. As principais concluões são:

- A distribuição de fluxo do gás molecular é mais uniforme no plano da galáxia, enquanto que o gás ionizado é mais concentrado e/ou colimado ao longo da direção do eixo de ionização do AGN. Interpretamos essa diferença da seguinte maneira: a emissão do gás ionizado traça melhor o escape colimado da radiação ionizante, o que é esperado para a estrutura típica de um AGN, em que a radiação do disco de acreção sai perpendicularmente a ele, sendo mais fraca a ângulos grandes em relação à perpendicular ao disco, considerando também que a ângulos pequenos em relação ao disco, a radiação encontra o torus molecular de poeira. O gás molecular, por outro lado, é destruído pela radiação ionizante e portanto não é observado ao longo do eixo de ionização do AGN. O gás molecular tem outra fonte de excitação, as razões de linhas indicam excitação térmica nessas regiões e o aquecimento pode ser atribuído aos raios-X originados no AGN. Esses raios-X muitas vezes atravessam o próprio toro de poeira e penetram no plano da galáxia em todas as direções aquecendo o gás molecular, produzindo assim, essa diferença na distribuição do gás ionizado e molecular;

- A cinemática do gás também é distinta: enquanto o gás molecular está normalmente em rotação com baixa dispersão de velocidades, o gás ionizado frequentemente mostra outras componentes associadas a altas dispersões de velocidades. Essa diferença é uma indicação de que o gás molecular está mais restrito ao plano da galáxia – em alguns casos curvas de rotação abruptas são observadas, bem como discos moleculares compactos. Já o gás ionizado apresenta outras componentes cinemáticas além da rotação, em particular os outflows, que são observados principalmente para o [Fe II]λ1,2570μm;

- Há uma anticorrelação entre o momento de Gauss-Hermite h_3 e os campos de veloci-

dade, onde valores positivos (asas vermelhas) são associados a blueshifts e valores negativos (asas azuis) são associados a redshits, o que atribuímos ao efeito conhecido como "$assimetric\ drift$";

- Há uma anticorrelação entre o momento de Gauss-Hermite h_4 e os mapas de dispersão de velocidades onde altos valores de σ correspondem a valores negativos de h_4 e baixos valores de σ correspondem a valores positivos de h_4.

- Temos massas integradas de gás molecular quente variando de 29 $M_\odot$ a 3300 $M_\odot$ e de 2×10^7 a $2{,}4\times10^9$ $M_\odot$ para o gás molecular frio. Para o gás ionizado temos massas integradas indo de $2{,}2\times10^4$ a $3{,}2\times10^7$ $M_\odot$. Os valores citados são da mesma ordem dos encontrados em outras galáxias ativas por estudos semelhantes aos nossos.

- A densidade superficial média de massa de gás molecular quente varia de $7{,}6\times10^{-4}$ a 1.8×10^{-2} $M_\odot/pc^2$, enquanto para o gás molecular frio varia de 526 a 20682 $M_\odot/pc^2$. A densidade superficial média de massa para o gás ionizado varia de 4.8 a 244 $M_\odot/pc^2$. Quando comparamos os valores dessas densidades e estimamos a quantidade total de gás nos pc centrais ($\approx$ 100 - 500 pc) das galáxias, percebemos que as massas de gás presentes são muito maiores do que o necessário para a taxa de alimentação típica de um SMBH em ciclos de 10^7 - 10^8 anos. O destino deste gás é provavelmente a formação de estrelas.

- A excitação mostra 3 comportamentos principais: i) núcleo com valores típicos de Seyfert circundado por valores típicos de LINERS. Isto pode ser entendido como o resultado da ionzação e excitação do gás por radiação ionizante do disco de acreção colimada por um toróide de poeira. A radiação que sai livremente, sem ser bloqueada pelo toróide, resulta em excitação do tipo Seyfert devido seu alto parâmetro de ionização enquanto que a radiação que sai rente ao toróide é parcialmente filtrada pelas suas bordas, produzindo excitação tipo LINER devido ao seu parâmetro de ionização mais baixo; ii) núcleo com valores típicos de Starburst circundado por valores Seyfert e/ou LINER; iii) somente valores de Seyfert/somente valores de LINER;

- Encontramos evidências de inflow em gás quente para 3 galáxias, com as taxas variando de 4×10^{-5} a 4×10^{-3} $M_\odot$ por ano, que são valores comparáveis aos encontrados em estudos recentes para inflows em AGN próximos. Devemos lembrar que o gás molecular quente é somente um traçador do gás molecular total, que é dominado por gás frio. Se assumirmos uma razão típica de $\approx 10^5$ entre a massa de gás grio e quente, essas taxas poderiam chegar a dezenas de massas solares por ano;

- A maioria dos outflows encontrados foram em gás ionizado com valores para as taxas de outflow variando entre 6×10^{-2} a 10,7 $M_{\odot}$ por ano, o que vai ao encontro dos valores encontrados em estudos recentes da cinemática do gás na região central de galáxias ativas;

- A potência dos outflows foi estimada entre $9{,}5\times10^{37}$ ergs/s e $5{,}7\times10^{41}$ ergs/s. Somente em 3 galáxias encontramos potências da ordem de 0,5% L_{bol}, para as quais o feedback pode influenciar significativamente a evolução do bojo da galáxia;

- A cinemática estelar pode ser bem descrita através de modelos de discos em rotação e mais uma vez encontramos uma anticorrelação entre a velocidade e o momento h_3 de Gauss-Hermite, implicando em asas vermelhas no lado em blueshift e asas azuis no lado em redshit do campo de velocidades, atribuímos isso ao efeito do "$assimetric\ drift$. Duas galáxias mostram uma linha de velocidades nula com formato "S", que interpretamos como sendo graças ao potencial gravitacional de uma barra. Regiões distintas com "caminhos" de baixa dispersão foram atribuídas à populações estelares jovens/intermediárias;

- Encontramos populações estelares jovens (t $<$ 50 Myr) a distâncias do núcleo entre 200 e 300 pc, populações de idade intermediária (50 Myr $\leq$ t $<$ 2 Gyr) mais afastadas e populações mais velhas dominantes nos $\approx$ 250 pc centrais das galáxias.

Nesta busca de alimentação e retro-alimentação de AGNs, nossa maior contribuição foi resolver espacialmente os processos que ocorrem no kiloparsec central de galáxias ativas com espectroscopia de campo integral. As observações no infravermelho próximo permitiram observar as propriedades tanto do gás molecular – inacessíveis na banda ótica – como do gás ionizado. Mostramos que sim podemos observar episódios de alimentação do AGN, principalmente no gás molecular quente, com taxas de acreção que são da ordem ou um pouco maiores do que as taxas de acreção do SMBH, muito embora o mais provável seja que o inflow também ocorra em gás molecular frio, e portanto as taxas devem ser maiores. Quanto à retro-alimentação, esta é melhor observada no gás ionizado, mas as taxas de outflow são também baixas, bem como sua potência, e em somente $\approx$ 30% das galáxias ela é alta o suficiente para ter efeito significativo na evolução da galáxia.

Referências Bibliográficas

Aalto, S. et al. Winds of change - a molecular outflow in NGC 1377?. The anatomy of an extreme FIR-excess galaxy. *A&A*, v. 546, p. A68, out. 2012.

Allington-Smith, J. R. et al. New techniques for integral field spectroscopy - I. Design, construction and testing of the GNIRS IFU. *MNRAS*, v. 371, p. 380–394, set. 2006.

Antonucci, R. Unified models for active galactic nuclei and quasars. *ARA&A*, v. 31, p. 473–521, 1993.

Barbosa, F. K. B. et al. Gemini/GMOS Integral Field Unit stellar kinematics of the nuclear region of six nearby active galaxies. *MNRAS*, v. 371, p. 170–184, set. 2006.

Barbosa, F. K. B. et al. Modelling the [Fe II] λ1.644 μm outflow and comparison with H_2 and H^+ kinematics in the inner 200 pc of NGC 1068. *MNRAS*, v. 445, p. 2353–2370, dez. 2014.

Beckmann, V.; Shrader, C. R. *Active Galactic Nuclei*. [S.l.: s.n.], 2012.

Binney, J.; Tremaine, S. Book-Review - Galactic Dynamics. *SKYTEL*, v. 76, p. 45, jul. 1988.

Burtscher, L. et al. Dust Emission from a Parsec-Scale Structure in the Seyfert 1 Nucleus of NGC 4151. *ApJL*, v. 705, p. L53–L57, nov. 2009.

Cappellari, M.; Emsellem, E. Parametric Recovery of Line-of-Sight Velocity Distributions from Absorption-Line Spectra of Galaxies via Penalized Likelihood. *PASP*, v. 116, p. 138–147, fev. 2004.

Cardelli, J. A.; Clayton, G. C.; Mathis, J. S. The relationship between infrared, optical, and ultraviolet extinction. *ApJ*, v. 345, p. 245–256, out. 1989.

Cheung, E. et al. The Dependence of Quenching upon the Inner Structure of Galaxies at 0.5 <= z < 0.8 in the DEEP2/AEGIS Survey. *ApJ*, v. 760, p. 131, dez. 2012.

Cid Fernandes, R. et al. Semi-empirical analysis of Sloan Digital Sky Survey galaxies - I. Spectral synthesis method. *MNRAS*, v. 358, p. 363–378, abr. 2005.

Ciotti, L.; Ostriker, J. P.; Proga, D. Feedback from Central Black Holes in Elliptical Galaxies. III. Models with Both Radiative and Mechanical Feedback. *ApJ*, v. 717, p. 708–723, jul. 2010.

Colina, L. et al. Understanding the two-dimensional ionization structure in luminous infrared galaxies. A near-IR integral field spectroscopy perspective. *A&A*, v. 578, p. A48, jun. 2015.

Combes, F. Models of AGN feedback. In: Ziegler, B. L. et al. (Ed.). *Galaxies in 3D across the Universe*. [S.l.: s.n.], 2015. (IAU Symposium, v. 309), p. 182–189.

Content, R. New design for integral field spectroscopy with 8-m telescopes. In: Ardeberg, A. L. (Ed.). *Society of Photo-Optical Instrumentation Engineers (SPIE) Conference Series*. [S.l.: s.n.], 1997. (Society of Photo-Optical Instrumentation Engineers (SPIE) Conference Series, v. 2871), p. 1295–1305.

Cox, T. J. et al. The Kinematic Structure of Merger Remnants. *ApJ*, v. 650, p. 791–811, out. 2006.

Croton, D. J. et al. The many lives of active galactic nuclei: cooling flows, black holes and the luminosities and colours of galaxies. *MNRAS*, v. 365, p. 11–28, jan. 2006.

Dale, D. A. et al. Warm and Cold Molecular Gas in Galaxies. *AJ*, v. 129, p. 2197–2202, maio 2005.

Davies, R. I. et al. Stellar and Molecular Gas Kinematics Of NGC 1097: Inflow Driven by a Nuclear Spiral. *ApJ*, v. 702, p. 114–128, set. 2009.

Dekel, A.; Birnboim, Y. Galaxy bimodality due to cold flows and shock heating. *MNRAS*, v. 368, p. 2–20, maio 2006.

Di Matteo, T. et al. Direct Cosmological Simulations of the Growth of Black Holes and Galaxies. *ApJ*, v. 676, p. 33–53, mar. 2008.

Diniz, M. R. et al. Feeding versus feedback in AGN from near-infrared IFU observations XI: NGC 2110. *MNRAS*, v. 453, p. 1727–1739, out. 2015.

Elvis, M. A Structure for Quasars. *ApJ*, v. 545, p. 63–76, dez. 2000.

Faber, S. M. et al. Galaxy Luminosity Functions to z˜1 from DEEP2 and COMBO-17: Implications for Red Galaxy Formation. *ApJ*, v. 665, p. 265–294, ago. 2007.

Ferrarese, L.; Ford, H. Supermassive Black Holes in Galactic Nuclei: Past, Present and Future Research. *SSRv*, v. 116, p. 523–624, fev. 2005.

Ferrarese, L.; Merritt, D. A Fundamental Relation between Supermassive Black Holes and Their Host Galaxies. v. 539, p. L9–L12, ago. 2000.

Frank, J.; King, A.; Raine, D. J. *Accretion Power in Astrophysics: Third Edition*. [S.l.: s.n.], 2002. 398 p.

García-Burillo, S. et al. Molecular line emission in NGC 1068 imaged with ALMA. I. An AGN-driven outflow in the dense molecular gas. *A&A*, v. 567, p. A125, jul. 2014.

Gerhard, O. E. Line-of-sight velocity profiles in spherical galaxies: breaking the degeneracy between anisotropy and mass. *MNRAS*, v. 265, p. 213, nov. 1993.

Graham, A. W. et al. An expanded M_*bh*-σ diagram, and a new calibration of active galactic nuclei masses. *MNRAS*, v. 412, p. 2211–2228, abr. 2011.

Granato, G. L. et al. A Physical Model for the Coevolution of QSOs and Their Spheroidal Hosts. *ApJ*, v. 600, p. 580–594, jan. 2004.

Heckman, T. M. Peculiar nuclei and their relation to galaxy type. *PASP*, v. 90, p. 241–243, jun. 1978.

Heckman, T. M.; Best, P. N. The Coevolution of Galaxies and Supermassive Black Holes: Insights from Surveys of the Contemporary Universe. *ARA&A*, v. 52, p. 589–660, ago. 2014.

Hopkins, P. F. et al. Dissipation and Extra Light in Galactic Nuclei. III. "Core" Ellipticals and "Missing" Light. *ApJS*, v. 181, p. 486–532, abr. 2009.

Jaffe, W. et al. The central dusty torus in the active nucleus of NGC 1068. *Nat*, v. 429, p. 47–49, maio 2004.

Jesseit, R. et al. Specific angular momentum of disc merger remnants and the λ_R-parameter. *MNRAS*, v. 397, p. 1202–1214, ago. 2009.

Kakkad, D. et al. ALMA observations of cold molecular gas in AGN hosts at z 1.5 - evidence of AGN feedback? *MNRAS*, v. 468, p. 4205–4215, jul. 2017.

Kereš, D. et al. How do galaxies get their gas? *MNRAS*, v. 363, p. 2–28, out. 2005.

Khachikian, E. Y.; Weedman, D. W. An atlas of Seyfert galaxies. *ApJ*, v. 192, p. 581–589, set. 1974.

Khochfar, S.; Silk, J. Dry mergers: a crucial test for galaxy formation. *MNRAS*, v. 397, p. 506–510, jul. 2009.

Koay, J. Y. et al. ALMA probes the molecular gas reservoirs in the changing-look Seyfert galaxy Mrk 590. *MNRAS*, v. 455, p. 2745–2764, jan. 2016.

Kormendy, J.; Ho, L. C. Coevolution (Or Not) of Supermassive Black Holes and Host Galaxies. *ARA&A*, v. 51, p. 511–653, ago. 2013.

Kormendy, J.; Kennicutt JR., R. C. Secular Evolution and the Formation of Pseudobulges in Disk Galaxies. *ARA&A*, v. 42, p. 603–683, set. 2004.

Krywult, J. et al. The VIMOS Public Extragalactic Redshift Survey (VIPERS). The coevolution of galaxy morphology and colour to z 1. *A&A*, v. 598, p. A120, fev. 2017.

Magorrian, J. et al. The Demography of Massive Dark Objects in Galaxy Centers. *Aj*, v. 115, p. 2285–2305, jun. 1998.

Maksym, W. P. et al. CHEERS Results from NGC 3393. II. Investigating the Extended Narrow-line Region Using Deep Chandra Observations and Hubble Space Telescope Narrow-line Imaging. *ApJ*, v. 844, p. 69, jul. 2017.

Mancini, C. et al. Star formation and quenching among the most massive galaxies at z ̃1.7. *MNRAS*, v. 450, p. 763–786, jun. 2015.

Martin, D. C. et al. Quenching or Bursting: Star Formation Acceleration–A New Methodology for Tracing Galaxy Evolution. *ArXiv e-prints*, maio 2017.

Martini, P.; Dicken, D.; Storchi-Bergmann, T. The Origin of Dust in Early-type Galaxies and Implications for Accretion onto Supermassive Black Holes. *ApJ*, v. 766, p. 121, abr. 2013.

Mazzalay, X. et al. Molecular gas in the centre of nearby galaxies from VLT/SINFONI integral field spectroscopy - I. Morphology and mass inventory. *MNRAS*, v. 428, p. 2389–2406, jan. 2013.

McConnell, N. J. et al. Two ten-billion-solar-mass black holes at the centres of giant elliptical galaxies. *Nature*, v. 480, p. 215–218, dez. 2011.

McGregor, P. J. et al. Gemini near-infrared integral field spectrograph (NIFS). In: Iye, M.; Moorwood, A. F. M. (Ed.). *Society of Photo-Optical Instrumentation Engineers (SPIE) Conference Series*. [S.l.: s.n.], 2003. (Society of Photo-Optical Instrumentation Engineers (SPIE) Conference Series, v. 4841), p. 1581–1591.

Müller-Sánchez, F. et al. Outflows from Active Galactic Nuclei: Kinematics of the Narrow-line and Coronal-line Regions in Seyfert Galaxies. *ApJ*, v. 739, p. 69, out. 2011.

Naab, T.; Burkert, A. Statistical Properties of Collisionless Equal- and Unequal-Mass Merger Remnants of Disk Galaxies. *ApJ*, v. 597, p. 893–906, nov. 2003.

Nandra, K. et al. AEGIS: The Color-Magnitude Relation for X-Ray-selected Active Galactic Nuclei. *ApJL*, v. 660, p. L11–L14, maio 2007.

Oser, L. et al. The Two Phases of Galaxy Formation. *ApJ*, v. 725, p. 2312–2323, dez. 2010.

Osterbrock, D. E. Seyfert galaxies with weak broad H alpha emission lines. *ApJ*, v. 249, p. 462–470, out. 1981.

Osterbrock, D. E.; Ferland, G. J. Book Review: Astrophysics of Gaseous Nebulae and Active Galactic Nuclei (2ND Edition) / University Science Books, 2005. *Mercury*, v. 35, n. 1, p. 010000, jan. 2006.

Peterson, M. B. Book Review: An introduction to active galactic nuclei / Cambridge U Press, 1997. *The Observatory*, v. 117, p. 314, out. 1997.

Powell, L. C.; Slyz, A.; Devriendt, J. The impact of supernova-driven winds on stream-fed protogalaxies. *MNRAS*, v. 414, p. 3671–3689, jul. 2011.

Powell, M. C. et al. Morphology and the Color-mass Diagram as Clues to Galaxy Evolution at zãpprox1. *ApJ*, v. 835, p. 22, jan. 2017.

Ramos Almeida, C. et al. A mid-infrared view of the inner parsecs of the Seyfert galaxy Mrk 1066 using CanariCam/GTC. *MNRAS*, v. 445, p. 1130–1143, dez. 2014.

Riffel, R. A. PROFIT: a new alternative for emission-line profile fitting. *APSS*, v. 327, p. 239–244, jun. 2010.

Riffel, R. A.; Storchi-Bergmann, T. Compact molecular disc and ionized gas outflows within 350 pc of the active nucleus of Mrk 1066. *MNRAS*, v. 411, p. 469–486, fev. 2011.

Riffel, R. A.; Storchi-Bergmann, T. Compact molecular disc and ionized gas outflows within 350 pc of the active nucleus of Mrk 1066. *MNRAS*, v. 411, p. 469–486, fev. 2011.

Riffel, R. A.; Storchi-Bergmann, T. Feeding and feedback in the active nucleus of Mrk 1157 probed with the Gemini Near-Infrared Integral-Field Spectrograph. *MNRAS*, v. 417, p. 2752–2769, nov. 2011.

Riffel, R. A.; Storchi-Bergmann, T. Feeding and feedback in the active nucleus of Mrk 1157 probed with the Gemini Near-Infrared Integral-Field Spectrograph. *MNRAS*, v. 417, p. 2752–2769, nov. 2011.

Riffel, R. A. et al. AGN-starburst connection in NGC7582: Gemini near-infrared spectrograph integral field unit observations. *MNRAS*, v. 393, p. 783–797, mar. 2009.

Riffel, R. A.; Storchi-Bergmann, T.; McGregor, P. J. The Dusty Nuclear Torus in NGC 4151: Constraints from Gemini Near-Infrared Integral Field Spectrograph Observations. *ApJ*, v. 698, p. 1767–1770, jun. 2009.

Riffel, R. A.; Storchi-Bergmann, T.; Nagar, N. M. Near-infrared dust and line emission from the central region of Mrk1066: constraints from Gemini NIFS. *MNRAS*, v. 404, p. 166–179, maio 2010.

Riffel, R. A.; Storchi-Bergmann, T.; Riffel, R. An Outflow Perpendicular to the Radio Jet in the Seyfert Nucleus of NGC 5929. *ApJL*, v. 780, p. L24, jan. 2014.

Riffel, R. A.; Storchi-Bergmann, T.; Riffel, R. Feeding versus feedback in active galactic nuclei from near-infrared integral field spectroscopy - X. NGC 5929. *MNRAS*, v. 451, p. 3587–3605, ago. 2015.

Riffel, R. A. et al. Intermediate-age Stars as Origin of the Low-velocity Dispersion Nuclear Ring in Mrk 1066. *ApJ*, v. 713, p. 469–474, abr. 2010.

Riffel, R. A. et al. Gemini NIFS survey of feeding and feedback processes in nearby active galaxies - I. Stellar kinematics. *MNRAS*, v. 470, p. 992–1016, set. 2017.

Riffel, R. A.; Storchi-Bergmann, T.; Winge, C. Feeding versus feedback in AGNs from near-infrared IFU observations: the case of Mrk 79. *MNRAS*, v. 430, p. 2249–2261, abr. 2013.

Riffel, R. A. et al. Gemini near-infrared integral field spectroscopy of the narrow-line region of ESO428-G14: kinematics, excitation and the role of the radio jet. *MNRAS*, v. 373, p. 2–12, nov. 2006.

Riffel, R. A. et al. Mapping of molecular gas inflow towards the Seyfert nucleus of NGC4051 using Gemini NIFS. *MNRAS*, v. 385, p. 1129–1142, abr. 2008.

Riffel, R. A. et al. Feeding versus feedback in NGC 1068 probed with Gemini NIFS - I. Excitation. *MNRAS*, v. 442, p. 656–669, jul. 2014.

Robson, I. Book Review: Active galactic nuclei / Wiley/Praxis, 1996. *Journal of the British Astronomical Association*, v. 106, p. 164, jun. 1996.

Rodríguez-Ardila, A.; Mazzalay, X. The near-infrared spectrum of Mrk 1239: direct evidence of the dusty torus? *MNRAS*, v. 367, p. L57–L61, mar. 2006.

Rodríguez-Ardila, A. et al. Powerful outflows in the central parsecs of the low-luminosity active galactic nucleus NGC 1386. *MNRAS*, v. 470, p. 2845–2860, set. 2017.

Rodríguez-Ardila, A.; Riffel, R.; Pastoriza, M. G. Molecular hydrogen and [FeII] in active galactic nuclei - II. Results for Seyfert 2 galaxies. *MNRAS*, v. 364, p. 1041–1053, dez. 2005.

Rodríguez-Puebla, A. et al. Constraining the galaxy-halo connection over the last 13.3 Gyr: star formation histories, galaxy mergers and structural properties. *MNRAS*, v. 470, p. 651–687, set. 2017.

Sakamoto, K. et al. Vibrationally Excited HCN in the Luminous Infrared Galaxy NGC 4418. *ApJL*, v. 725, p. L228–L233, dez. 2010.

Sanchez, F. M. et al. *ApJ*, p. 691–749, 2009.

Sarzi, M. et al. The SAURON project - XVI. On the sources of ionization for the gas in elliptical and lenticular galaxies. *MNRAS*, v. 402, p. 2187–2210, mar. 2010.

Schawinski, K. et al. Observational evidence for AGN feedback in early-type galaxies. *MNRAS*, v. 382, p. 1415–1431, dez. 2007.

Schawinski, K. et al. Do Moderate-Luminosity Active Galactic Nuclei Suppress Star Formation? *ApJL*, v. 692, p. L19–L23, fev. 2009.

Schmidt, M.; Green, R. F. Quasar evolution derived from the Palomar bright quasar survey and other complete quasar surveys. *ApJ*, v. 269, p. 352–374, jun. 1983.

Schneider, P. *Extragalactic Astronomy and Cosmology: An Introduction*. [S.l.: s.n.], 2015.

Schönell, J. A. J. et al. Feeding Versus Feedback in AGNs from Near-Infrared IFU Observations: The Case of Mrk 766. *MNRAS*, v. 415, p. 200–220, jan. 2014.

Schönell, J. A. J. et al. Feeding versus feedback in active galactic nuclei from near-infrared integral field spectroscopy - XII. NGC 5548. *MNRAS*, v. 464, p. 1771–1782, jan. 2017.

Scoville, N. Z. et al. Velocity, reddening, and temperature structure of the H2 emission in Orion. *ApJ*, v. 253, p. 136–148, fev. 1982.

Silk, J.; Mamon, G. A. The current status of galaxy formation. *Research in Astronomy and Astrophysics*, v. 12, p. 917–946, ago. 2012.

Silverman, J. D. et al. The Evolution of AGN Host Galaxies: From Blue to Red and the Influence of Large-Scale Structures. *ApJ*, v. 675, p. 1025–1040, mar. 2008.

Simões Lopes, R. D. et al. A Strong Correlation between Circumnuclear Dust and Black Hole Accretion in Early-Type Galaxies. *ApJ*, v. 655, p. 718–734, fev. 2007.

Somerville, R. S. et al. A semi-analytic model for the co-evolution of galaxies, black holes and active galactic nuclei. *MNRAS*, v. 391, p. 481–506, dez. 2008.

Springel, V.; Di Matteo, T.; Hernquist, L. Modelling feedback from stars and black holes in galaxy mergers. *MNRAS*, v. 361, p. 776–794, ago. 2005.

Stasińska, G. et al. Can retired galaxies mimic active galaxies? Clues from the Sloan Digital Sky Survey. *MNRAS*, v. 391, p. L29–L33, nov. 2008.

Storchi-Bergmann, T. Resolved Outflows in Nearby AGN from Integral Field Spectroscopy. In: Chartas, G.; Hamann, F.; Leighly, K. M. (Ed.). *AGN Winds in Charleston*. [S.l.: s.n.], 2012. (Astronomical Society of the Pacific Conference Series, v. 460), p. 133.

Storchi-Bergmann, T. et al. Feeding versus feedback in NGC4151 probed with Gemini NIFS - II. Kinematics. *MNRAS*, v. 402, p. 819–835, fev. 2010.

Storchi-Bergmann, T. et al. Feeding versus feedback in NGC4151 probed with Gemini NIFS - I. Excitation. *MNRAS*, v. 394, p. 1148–1166, abr. 2009.

Storchi-Bergmann, T. et al. Two-dimensional Mapping of Young Stars in the Inner 180 pc of NGC 1068: Correlation with Molecular Gas Ring and Stellar Kinematics. *ApJ*, v. 755, p. 87, ago. 2012.

van der Marel, R. P.; Franx, M. A new method for the identification of non-Gaussian line profiles in elliptical galaxies. *ApJ*, v. 407, p. 525–539, abr. 1993.

Veilleux, S.; Cecil, G.; Bland-Hawthorn, J. Galactic Winds. *A&A*, v. 43, p. 769–826, set. 2005.

Veilleux, S. et al. Fast Molecular Outflows in Luminous Galaxy Mergers: Evidence for Quasar Feedback from Herschel. *ApJ*, v. 776, p. 27, out. 2013.

Westfall, K. B. et al. Asymmetric Drift and the Stellar Velocity Ellipsoid. *Astrophysics and Space Science Proceedings*, v. 3, p. 157, 2007.

Zschaechner, L. K. et al. The Molecular Wind in the Nearest Seyfert Galaxy Circinus Revealed by ALMA. *ApJ*, v. 832, p. 142, dez. 2016.

Zubovas, K.; King, A. R. AGN Winds and the Black-Hole - Galaxy Connection. In: Chartas, G.; Hamann, F.; Leighly, K. M. (Ed.). *AGN Winds in Charleston*. [S.l.: s.n.], 2012. (Astronomical Society of the Pacific Conference Series, v. 460), p. 235.

Apêndice I

Monthly Notices
of the
ROYAL ASTRONOMICAL SOCIETY

MNRAS **470,** 992–1016 (2017)
Advance Access publication 2017 May 29

doi:10.1093/mnras/stx1308

Gemini NIFS survey of feeding and feedback processes in nearby active galaxies – I. Stellar kinematics

Rogemar A. Riffel,[1]★ Thaisa Storchi-Bergmann,[2] Rogerio Riffel,[2]
Luis G. Dahmer-Hahn,[2] Marlon R. Diniz,[1] Astor J. Schönell[2]
and Natacha Z. Dametto[2]

[1]*Departamento de Física, Centro de Ciências Naturais e Exatas, Universidade Federal de Santa Maria, 97105-900 Santa Maria, RS, Brazil*
[2]*Departamento de Astronomia, Instituto de Física, Universidade Federal do Rio Grande do Sul, CP 15051, 91501-970 Porto Alegre, RS, Brazil*

Accepted 2017 May 24. Received 2017 May 18; in original form 2016 November 21

ABSTRACT

We use the Gemini Near-Infrared Integral Field Spectrograph (NIFS) to map the stellar kinematics of the inner few hundred parsecs of a sample of 16 nearby Seyfert galaxies, at a spatial resolution of tens of parsecs and spectral resolution of 40 km s^{-1}. We find that the line-of-sight (LOS) velocity fields for most galaxies are well reproduced by rotating disc models. The kinematic position angle (PA) derived for the LOS velocity field is consistent with the large-scale photometric PA. The residual velocities are correlated with the hard X-ray luminosity, suggesting that more luminous active galactic nuclei have a larger impact in the surrounding stellar dynamics. The central velocity dispersion values are usually higher than the rotation velocity amplitude, what we attribute to the strong contribution of bulge kinematics in these inner regions. For 50 per cent of the galaxies, we find an inverse correlation between the velocities and the h_3 Gauss–Hermitte moment, implying red wings in the blueshifted side and blue wings in the redshifted side of the velocity field, attributed to the movement of the bulge stars lagging the rotation. Two of the 16 galaxies (NGC 5899 and Mrk 1066) show an S-shape zero velocity line, attributed to the gravitational potential of a nuclear bar. Velocity dispersion (σ) maps show rings of low-σ values ($\sim$50–80 km s^{-1}) for four objects and 'patches' of low σ for six galaxies at 150–250 pc from the nucleus, attributed to young/ intermediate age stellar populations.

Key words: galaxies: active – galaxies: ISM – galaxies: kinematics and dynamics – infrared: galaxies.

1 INTRODUCTION

Active galactic nuclei (AGNs) characterize a critical phase in galaxy evolution in which its nuclear supermassive black hole (SMBH) is being fed due to gas accretion to the nuclear region. Once the accretion disc surrounding the SMBH is formed, feedback processes begin to occur, comprising jets of relativistic particles emitted from the inner rim of the accretion disc, winds emanating from outer regions of the disc and radiation emitted by the hot gas in the disc or by its corona (Elvis 2000; Frank, King & Raine 2002; Ciotti et al. 2010). The AGN feeding and feedback processes couple the growth of the SMBHs and their host galaxies, and are claimed to explain the correlation between the mass of the SMBH and the mass of the galaxy bulge (Ferrarese & Ford 2005; Somerville et al. 2008; Kormendy & Ho 2013). The feeding processes are a necessary condition to trigger the nuclear activity, while the feedback processes are now a fundamental ingredient in galaxy evolution models: without the AGN feedback, the models cannot reproduce the properties of the massive galaxies – these galaxies end up forming too many stars (Springel et al. 2005; Fabian 2012; Terrazas et al. 2016).

The study of feeding and feedback processes in AGNs requires a detailed mapping of the gas and stellar kinematics in the vicinity of the central engine. Usually these studies are based on high-spatial resolution integral field spectroscopy (IFS; e.g. Fathi et al. 2006; Storchi-Bergmann et al. 2007, 2009, 2010; Barbosa et al. 2009, 2014; Hicks et al. 2009, 2013; Sánchez et al. 2009; Riffel & Storchi-Bergmann 2011a; Riffel et al. 2013; Mazzalay et al. 2014; Riffel et al. 2014; Schönell et al. 2014; Diniz et al. 2015; Fischer et al. 2017). To isolate and quantify gas streaming motions towards the centre of galaxies or gas outflows from the nucleus through the gas kinematics, it is necessary to properly map the motions of the gas due to the gravitational potential of the galaxy. A way to map the gravitational potential of the galaxies is by two-dimensional

★ E-mail: rogemar@ufsm.br

Table 1. Sample: (1) galaxy's name; (2) redshift; (3) nuclear activity; (4) Hubble type as quoted in NED; (5) spectral resolution in Å; (6) angular resolution; (7) spectral band; (8) Gemini project code; (9) total exposure time; (10) hard X-ray luminosity (14–195 keV) from the *Swift*-BAT 60-month catalogue (Ajello et al. 2012); (11) reference for the stellar kinematics.

1 Galaxy	2 z	3 Act.	4 Hub. type	5 Sp. R.	6 An. R. (arcsec)	7 B	8 Project ID	9 Exp. T.	10 log L_X (erg s^{-1})	11 Ref.
NGC788	0.014	Sy2	SA0/a?(s)	3.5	0.13	*K*	GN-2015B-Q-29	4400	43.2	a
NGC1052[a]	0.005	Sy2	E4	3.4	0.14	*K*l	GN-2010B-Q-25	2400	41.9	a
NGC2110	0.008	Sy2	SAB0$^-$	3.4	0.15	*K*l	GN-2010B-Q-25	3600	43.3	b
NGC3227	0.004	Sy1.5	SAB(s)a pec	3.4	0.13	*K*l	GN-2016A-Q-6	2400	42.3	a
NGC3516	0.009	Sy1.5	(R)SB0^0?(s)	3.6	0.15	*K*	GN-2015A-Q-3	4500	42.7	a
NGC4051[a]	0.002	Sy1	SAB(rs)bc	3.2	0.17	*K*	GN-2006A-SV-123	4500	41.5	c
NGC4235	0.008	Sy1	SA(s)a edge-on	3.4	0.13	*K*l	GN-2016A-Q-6	4000	42.3	a
NGC4388	0.008	Sy2	SA(s)b? edge-on	3.5	0.14	*K*	GN-2015A-Q-3	800	43.3	a
NGC5506	0.006	Sy1.9	Sa pec edge-on	3.5	0.15	i	GN-2015A-Q-3	4000	43.1	a
NGC5548[a]	0.017	Sy1	(R')SA0/a(s)	3.5	0.20	*K*l	GN-2012A-Q-57	2700	43.4	a
NGC5899[a]	0.009	Sy2	SAB(rs)c	3.5	0.12	*K*l	GN-2013A-Q-48	4600	42.1	a
NGC5929[a]	0.008	Sy2	Sab? pec	3.2	0.12	*K*l	GN-2011A-Q-43	6000	–	d
Mrk607[a]	0.009	Sy2	Sa? edge-on	3.5	0.12	*K*l	GN-2012B-Q-45	6000	–	a
Mrk766	0.013	Sy1.5	(R')SB(s)a?	3.5	0.19	*K*l	GN-2010A-Q-42	3300	42.8	a
Mrk1066[a]	0.012	Sy2	(R)SB0$^+$(s)	3.3	0.15	*K*l	GN-2008B-Q-30	4800	–	e
Mrk1157[a]	0.015	Sy2	(R')SB0/a	3.5	0.12	*K*l	GN-2009B-Q-27	3300	–	f

[a]These galaxies do not follow all selection criteria and are part of the complementary sample.
a – This work; b – Diniz et al. (2015); c – Riffel et al. (2008); d – Riffel, Storchi-Bergmann & Riffel (2015c); e – Riffel & Storchi-Bergmann (2011a); f – Riffel & Storchi-Bergmann (2011b).

mapping of the stellar kinematics. So far, studies available for nearby galaxies show that the stellar kinematics usually present regular rotation within the inner kiloparsec (e.g. Barbosa et al. 2006; Ganda et al. 2006) and thus can be used to isolate possible non-circular motions from the gas kinematics (e.g. Riffel et al. 2008; Riffel & Storchi-Bergmann 2011a; Diniz et al. 2015).

Adaptive optics IFS at 10-m class telescopes provides an unprecedented possibility to map the stellar kinematics of nearby galaxies at spatial resolutions of a few tens of parsecs. So far, adaptive optics systems are available mainly in near-infrared (near-IR) wavelengths, where the dust extinction at the central regions of galaxies is less important than at optical bands. In addition, strong absorption CO bands are present in the spectra of galaxies, originated in giant and supergiant stars that dominate the continuum emission in the central regions (e.g. Maraston 2005; Riffel et al. 2015b). Thus, near-IR IFS at 10-m telescopes provides a unique tool to map the stellar kinematics at central region of active galaxies, at unprecedented spatial resolution, by fitting the CO absorption band-heads (e.g. Riffel et al. 2015a).

In this paper, we map the stellar kinematics of the inner 3 arcsec $\times$3 arcsec of a sample of 16 nearby Seyfert galaxies. This work is part of a larger project in which our group *AGN Integral Field Spectroscopy* (AGNIFS) aims to study the feeding and feedback processes of a sample of 30 nearby Seyfert galaxies, selected by their X-ray luminosity. The kinematic maps presented here will be used to isolate gas non-circular motions in future works by our group and to quantify gas inflows and outflows.

This paper is organized as follows: Section 2 presents the sample and a description of the observations and data reduction procedure, while the spectral fitting procedure is presented in Section 3. The resulting stellar kinematics maps are presented and discussed in Section 4 and the kinematic derived parameters are compared with those characterizing the large-scale discs of the host galaxies in Section 5.1. Finally, Section 6 presents the main conclusions of this work.

2 SAMPLE AND OBSERVATIONS

2.1 The sample

Our sample comprises 16 AGN host galaxies: 8 from a large Gemini proposal (PI Storchi-Bergmann) to obtain Near-Infrared Integral Field Spectrograph (NIFS) observations of 20 AGNs selected from the *Swift*-BAT 60-month catalogue (Ajello et al. 2012) to have 14–195 keV luminosities $L_X \geq 10^{41.5}$ erg s^{-1}, and 8 from previous similar NIFS observations by our group of nearby AGN hosts. Four of these eight galaxies have similar L_X luminosities and fout are not in the *Swift*-BAT catalogue. One additional source (Mrk 79) was observed in previous run with similar NIFS configuration, but the signal-to-noise ratio of the CO absorption band-heads was not high enough to allow stellar kinematics measurements. By the end of 2018, we should have additional observations of another 13 galaxies of the large proposal and thus will have in the end a total of 29 galaxies comprising 20 *Swift*-BAT selected galaxies plus the 8 galaxies included in this study (plus Mrk 79) that comprise what we call a 'complementary sample', and identified by the footnote *a* in Table 1.

Additional criteria for the sample is that the redshift is $z \leq 0.015$, and to be accessible for NIFS ($-30^\circ < \delta < 73^\circ$). The L_X criterion above defining the sample of the large proposal was adopted because the *Swift*-BAT 14–195 keV band measures direct emission from the AGN rather than scattered or re-processed emission, and is much less sensitive to obscuration in the line of sight (LOS) than soft X-ray or optical wavelengths, allowing a selection based only on the AGN properties. To assure that we would be able to probe the feeding and feedback processes via the gas kinematics, we further selected the galaxies having previously observed extended gas emission (e.g. Schmitt & Kinney 2000) and [O III]λ5007 luminosities. We have excluded from the sample a few galaxies that had guiding problems in the observations. A complete characterization of the sample will be presented in a forthcoming paper (Riffel et al., in preparation).

So far, we have already observed 20 galaxies with NIFS, but only for 16 of them we were able to measure the stellar kinematics by

fitting the *K*-band CO absorption bands at 2.3 μm. We were not able to obtain reliable fits of the remaining four objects (Mrk 3, Mrk 79, NGC 4151 and NGC 1068) due to the dilution of the *K*-band CO band-heads due to strong continuum emission. For the latter two, the stellar kinematics has already been studied using the *H*-band spectra (Storchi-Bergmann et al. 2012; Onken et al. 2014). The 16 galaxies selected for this study are listed in Table 1, together with relevant information.

2.2 Observations

We used the Gemini NIFS (McGregor et al. 2003) to observe the galaxies listed in Table 1. All observations were obtained using the Gemini North Adaptive Optics system ALTAIR from 2008 to 2016. The observations followed the standard Object–Sky–Sky–Object dither sequence, with off-source sky positions since all targets are extended, and individual exposure times that varied according to the target. The 'HK_G0603' filter and the 'Kl_G5607' and "K_G5605' gratings were used during the observations. Most of the observations were performed in the K_l band, with the spectra centred at 2.3 μm, while for five galaxies the spectra were obtained at the *K* band and centred at 2.2 μm. The spectral range for the K_l data is ∼2.080–2.500 μm and for the *K* band is ∼1.980–2.400 μm. Both ranges include the ^{12}CO and ^{13}CO absorption band-heads at ∼2.3 μm for all galaxies, used to measure the stellar kinematics.

The spectral resolution ranges between 3.2 and 3.6 Å, as obtained from the measurement of the full width at half-maximum (FWHM) of ArXe lamp lines, used to wavelength calibrate the spectra, close to the central wavelength. This translates to resolutions in the range of 42–47 km s^{-1} in the velocity space. The angular resolution is in the range of 0.12–0.20 arcsec, derived from the FWHM of flux distribution of the standard stars, corresponding to few tens of parsecs at the distance of most galaxies. More details about the observations are shown in Table 1.

2.3 Data reduction

The data reduction followed the standard procedure and was accomplished by using tasks specifically developed for NIFS data reduction, contained in the NIFS package, which is part of GEMINI IRAF package, as well as generic IRAF tasks and IDL scripts. The data reduction procedure included the trimming of the images, flat-fielding, sky subtraction, wavelength and s-distortion calibrations. The telluric absorptions have been removed using observations of telluric standard stars with A spectral type. These stars were used to flux calibrate the spectra of the galaxies by interpolating a blackbody function to their spectra. Finally, data cubes were created for each individual exposure at an angular sampling of 0.05 arcsec × 0.05 arcsec and combined in a final data cube for each galaxy. All data cubes cover the inner ∼3 arcsec × 3 arcsec, with exception of the data cube for NGC 4051 that covers the inner ∼3 arcsec × 4 arcsec, via spatial dithering during the observations (Riffel et al. 2008).

The median value of the signal-to-noise ratio (S/N) in the continuum of our sample ranges from 10 to 30, with the maximum value of up to S/N ∼ 100 observed for the nuclear spectrum of NGC 4051. The median value of the S/N for the ^{12}CO (2-0) band-head at 2.29 μm is larger than 3 for all galaxies of the sample.

Detailed descriptions of the observations and data reduction procedures for the galaxies already analysed are presented in Riffel, Storchi-Bergmann & Nagar (2010) for Mrk 1066, Riffel & Storchi-Bergmann (2011b) for Mrk 1157, Diniz et al. (2015) for NGC 2110 and Riffel et al. (2008) for NGC 4051. For the remaining objects, a more detailed discussion will be presented in a forthcoming paper (Riffel et al., in preparation).

3 SPECTRAL FITTING

The stellar line-of-sight velocity distribution (LOSVD) of each galaxy was obtained by fitting the spectra within the spectral range of ∼2.26–2.40 μm (rest wavelengths), which includes the CO absorption band-heads from ∼2.29 to ∼2.40 μm (Winge et al. 2009), usually amongst of the strongest absorption lines in the central region of galaxies (e.g. Riffel, Rodríguez-Ardila & Pastoriza 2006; Riffel et al. 2015b). The used spectral range also includes weaker absorption lines from Mg I and Ca I at 2.26–2.28 μm. The spectra were fitted by using the penalized pixel-fitting PPXF method (Cappellari & Emsellem 2004), which finds the best fit to a galaxy spectrum by convolving stellar spectra templates with a given LOSVD, under the assumption that it is reproduced by Gauss–Hermite series.

The PPXF code requires the use of spectral templates that are used to reproduce the galaxy's spectrum. We used the spectra of the Gemini library of late spectral type stars observed with the Gemini Near-Infrared Spectrograph (GNIRS) IFU and NIFS (Winge et al. 2009) as stellar templates. The spectral resolution of the stellar library is very similar to that of the spectra of the galaxies of our sample and the library includes stars with spectral types from F7 to M5, minimizing the template mismatch problem.

The spectral range used in the fit includes the [Ca VIII] λ2.321 μm emission line, which 'contaminates' the (3-1)^{12}CO band-head and affects the stellar kinematics measurements (Davies et al. 2006; Riffel et al. 2008). The [Ca VIII] is seen at the nucleus and close vicinity, being unresolved for most galaxies of our sample and we have excluded its spectral region from the fit when the line is present. In addition, we used the *clean* parameter of PPXF to reject all spectral pixels deviating more than 3σ from the best fit, to exclude possible remaining sky lines and spurious features.

In Fig. 1, we present examples of typical fits for the galaxies NGC 1052, NGC 788 and NGC 5899. The left-hand panels show the fits for the nuclear spectrum, while extra-nuclear spectra are shown at the right-hand panels, extracted at 0.5 arcsec south of the nucleus – chosen to represent typical extra-nuclear spectra. The observed spectra are shown as black dotted lines, the fits are shown in red and the regions masked during the fits, following the criteria explained above, are shown in green. As can be seen for NGC 788, the cleaning procedure properly excluded the region affected by the [Ca VIII] λ2.321 μm emission line, as well as spurious features. For all galaxies, the standard deviations of the residuals (observed – model) are similar to that of the galaxy spectra derived within a 200 Å spectral window, bluewards to the first CO absorption band-head, meaning that the spectra are well reproduced by the models.

The PPXF code returns as output, measurements for the radial velocity (V_{LOS}), stellar velocity dispersion (σ), and higher order Gauss–Hermite moments (h_3 and h_4) for each spatial position, as well as their associated uncertainties. Using the results of the fit, we have constructed two-dimensional maps for each fitted parameter (V_{LOS}, σ, h_3 and h_4), which are presented in the next section.

4 STELLAR KINEMATICS

Figs 2–12 show the resulting maps for the stellar kinematics of our sample. The stellar kinematics for NGC 4051, NGC 2110, NGC 5929, Mrk 1066 and Mrk 1157 was already discussed in previous works by our group (see references in Table 1). Thus, we present

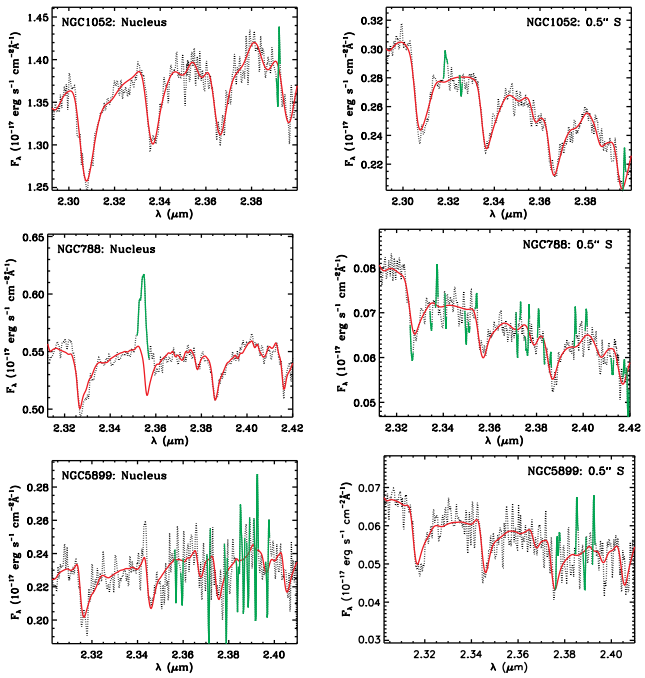

Figure 1. Examples of fits for the nuclear spectrum (left) and typical extra nuclear spectrum (right) for NGC 1052 (top panels), NGC 788 (centre panels) and NGC 5899 (bottom panels). The observed spectra are shown as black dotted lines, the best-fitting models as red continuous lines and the masked regions (following the criteria explained in the text) during the fits are shown in green.

the corresponding maps for these galaxies in Figs A1–A5 of the Appendix A, to be published online only.

To characterize the LOS velocity fields, we have symmetrized the stellar velocity field, using the *fit_kinematic_pa*[1] routine. This routine measures the global kinematic position angle (PA) and systemic velocity of the galaxy from integral field observations of the galaxy's kinematics. The method is described in Krajnović et al. (2006). Cappellari et al. (2007) and Krajnović et al. (2011) show examples of application of the method to study the large-scale stellar kinematics of large sample of galaxies of the SAURON and ATLAS^{3D} surveys.

In addition, we fitted the LOS velocity fields by a rotating disc model. The model was obtained using the DiskFit routine (Barnes & Sellwood 2003; Reese et al. 2007; Spekkens & Sellwood 2007; Sellwood & Sánchez 2010; Kuzio de Naray et al. 2012; Sellwood & Spekkens 2015) to fit the symmetrized velocity fields. This code fits non-parametric kinematic models to a given velocity field allowing the inclusion of circular and non-circular motions in a thin disc. Examples of application of this code for the gas and stellar kinematics of the inner region of active galaxies are shown in Fischer et al. (2015) and Riffel et al. (2015c), respectively. We fitted the symmetrized velocity field, instead of the observed one, as the rotating disc model is expected to be symmetric and small fluctuations in velocity due to higher uncertainties at some locations would result in a worse model for the stellar kinematics. During the fit, we have fixed the kinematical centre to the position of the peak of the continuum emission, and the systemic velocity and orientation of the line of nodes of the galaxy were fixed as the values obtained from the symmetrization of the velocity field to reduce the number of parameters to be fitted. The ellipticity and disc inclination were allowed to vary during the fit and the resulting fitted values for each galaxy are shown in Table 2.

Figs 2–12 are organized as follows:

(i) Top-left panel: the *K*-band image, obtained as the average flux between 2.20 and 2.30 μm. The continuous line shows the orientation of the kinematic major axis and the dotted line shows the orientation of the minor axis of the galaxy, obtained from the symmetrization of the stellar velocity field. The colour bar shows the flux scale in units of 10^{-17} erg s^{-1} cm^{-2} Å $^{-1}$.

(ii) Top-centre panel: measured LOS stellar velocity field obtained from the fit of the spectra using the PPXF routine (Cappellari & Emsellem 2004), following the procedure described in Section 3.

(iii) Top-right panel: symmetrized velocity field. The colour bar is shown in units of km s^{-1} and the systemic velocity of the galaxy was subtracted.

(iv) Middle-left panel: rotating disc model, obtained by fitting the symmetrized velocity field.

(v) Middle-centre panel: residual map obtained by subtracting the rotating disc model from the observed velocity field.

(vi) Middle-right panel: residual map obtained by subtracting the rotating disc model from the symmetrized velocity field, constructed to verify if the velocity field is well reproduced by the model.

(vii) Bottom-left panel: stellar velocity dispersion (σ) map. The colour bar shows the σ in km s^{-1} units.

(viii) Bottom-centre panel: map for the h_3 Gauss–Hermite moment. The h_3 moment measures asymmetric deviations of the LOSVD from a Gaussian velocity distribution (Gerhard 1993; van der Marel & Franx 1993; Riffel 2010). High (positive) h_3 values correspond to the presence of red wings in the LOSVD, while low (negative) h_3 values correspond to the presence of blue wings.

(ix) Bottom-right panel: map for the h_4 Gauss–Hermite moment that measures symmetric deviations of the LOSVD relative to a Gaussian velocity distribution. High (positive) h_4 values indicate LOSVD is more 'pointy' than a Gaussian, while low (negative) h_4 values indicate profiles more 'boxy' than a Gaussian.

In all figures, north is up and east is to the left and the grey regions represent masked locations. In these regions, it was not possible to obtain good fits due to low signal-to-noise ratio of the spectra or due to the non-detection of absorption lines (e.g. due to the dilution of the absorption lines by strong AGN continuum emission). The masked regions correspond to locations where the uncertainty in velocity or velocity dispersion is higher than 30 km s^{-1}, while for most other locations the uncertainties are smaller than 15 km s^{-1}.

A rotating disc pattern is recognized in the LOS velocity field for all galaxies, with a straight zero velocity line for most of them. For two galaxies – Mrk 1066 (Riffel & Storchi-Bergmann 2011a) and NGC 5899 (Fig. 10) – an S-shape zero velocity line is observed, which is a signature of the presence of a nuclear bar or spiral arms in these galaxies (e.g. Combes et al. 1995; Emsellem et al. 2006). For most galaxies, the maximum amplitude of the rotation curve is expected to be observed outside of the NIFS field of view (FoV). The rotation disc signature is clearly seen in the one-dimensional plots shown in Fig. B1, obtained by averaging the velocity and σ values within a pseudo-slit with width of 0.25 arcsec oriented along the major axis of the galaxy. The

[1] This routine was developed by M. Cappellari and is available at http://www-astro.physics.ox.ac.uk/mxc/software.

Table 2. Kinematic parameters obtained by symmetrize the stellar velocity. Col. 1: galaxy name; cols 2 and 3: systemic velocity (V_s) corrected for the heliocentric frame and orientation of the line of nodes (Ψ_0) derived from the symmetrization of the velocity fields; cols 4 and 5: disc ellipticity (e) and inclination (i) derived by modelling the velocity field using the DiskFit routine; cols 6 and 8: orientation of the major axis, ellipticity and inclination of the large-scale disc, as available at NED; col 9: the nuclear stellar velocity dispersion measured within a circular aperture with 150 pc diameter.

	FitKinematicPA		DiskFit		Large-scale disc			
Galaxy	V_s (km s^{-1})	Ψ_0 (°)	e	i(°)	Ψ_{0NED}(°)	e_{NED}	i_{NED} (°)	σ(km s^{-1})
NGC788	4034	120 ± 3	0.07 ± 0.01	20.8 ± 0.2	100	0.67	42.3	187 ± 4
NGC1052	1442	114 ± 3	0.32 ± 0.01	47.5 ± 0.2	120	0.71	45.6	245 ± 4
NGC2110	2335	156 ± 3	0.26 ± 0.01	42.5 ± 0.3	160	0.63	38.7	238 ± 5
NGC3227	1174	156 ± 3	0.30 ± 0.01	45.4 ± 0.2	152	0.88	62.0	130 ± 7
NGC3516	2631	54 ± 3	0.05 ± 0.01	18.2 ± 0.8	7	0.69	43.9	186 ± 3
NGC4051	717	130 ± 9	0.20 ± 0.01	37.3 ± 0.9	142	0.84	56.6	72 ± 3
NGC4235	2276	54 ± 3	0.25 ± 0.01	41.2 ± 0.5	50	0.94	70.1	183 ± 12
NGC4388	2537	96 ± 3	0.11 ± 0.01	27.7 ± 0.3	89	0.95	71.3	106 ± 6
NGC5506	1878	96 ± 3	0.48 ± 0.01	58.7 ± 0.3	90	0.97	76.1	–
NGC5548	5128	108 ± 3	0.51 ± 0.04	60.9 ± 6.8	60	0.34	19.9	276 ± 22
NGC5899	2616	24 ± 3	0.54 ± 0.01	62.7 ± 0.3	25	0.92	67.7	147 ± 9
NGC5929	2491	30 ± 9	0.51 ± 0.01	60.7 ± 0.5	38	0.69	43.9	134 ± 5
MRK607	2781	138 ± 3	0.47 ± 0.01	58.2 ± 0.1	135	0.94	70.1	132 ± 4
MRK766	3855	66 ± 3	0.05 ± 0.02	18.2 ± 3.7	110	0.77	50.2	78 ± 6
MRK1066	3583	120 ± 3	0.36 ± 0.01	50.2 ± 0.3	140	0.92	66.4	103 ± 4
MRK1157	4483	114 ± 3	0.29 ± 0.01	45.1 ± 0.9	95	0.88	61.3	92 ± 4

deprojected velocity amplitude within the NIFS FoV ranges from ∼50 to ∼300 km s^{-1}.

For five galaxies, the maximum σ value is smaller than 100 km s^{-1}, seven have maximum σ in the range of 100–150 km s^{-1} and four show the maximum $\sigma > 150$ km s^{-1}. In addition, distinct structures of low-σ values (∼50–80 km s^{-1}) are seen in the maps: low-σ rings or partial rings are seen for Mrk 1066, Mrk 1157, NGC 5929 and NGC 788. These rings have been identified by visual inspection and are marked in the corresponding σ maps as green ellipses. In all cases, the size of the structures is larger than the spatial resolution and the σ decrease is larger than the velocity resolution of the data. These structures have been attributed to intermediate-age stellar populations (ages in the range of 100–700 Myr; e.g. Riffel et al. 2010, 2011), with origin in kinematically colder regions that still preserve the kinematics of the gas from which they have been formed. Patches of low-σ are seen for Mrk 607, NGC 2110, NGC 3516, NGC 4051, NGC 4235 and NGC 5899, while three objects (NGC 1052, NGC 3227 and NGC 4388) show a centrally peaked σ distribution. These rings and partial rings are located at distances from the nucleus ranging between 150 and 250 pc. Nuclear σ values for each galaxy are presented in the last column of Table 2, obtained by fitting the nuclear spectrum integrated within a circular aperture with radius of 75 pc.

Most galaxies show low h_3 values ($-0.10 < h_3 < 0.10$), suggesting that their LOSVDs are well represented by a Gaussian velocity distribution. Exceptions are Mrk 607, Mrk1066 and NGC 4051 that show h_3 values larger than 0.15. For eight galaxies (NGC 1052, NGC 2110, NGC 3227, NGC 3516, NGC 4051, NGC 5506, Mrk 607 and Mrk 1066), the h_3 map is anticorrelated with the velocity field, with positive h_3 values seen at locations where rotation velocities are observed in blueshifts and negative h_3 values associated with regions where the rotation velocities are observed in redshifts. A similar trend (but not so clear) is observed for other four galaxies (NGC 4235, NGC 4388, NGC 5929 and Mrk 1157). In Fig. B2, we present plots of the LOS velocity versus h_3 for all galaxies, which show this anticorrelation clearly. The anticorrelation seen between h_3 and the LOS velocity can be interpreted as due do the contribution of stars rotating slower than those in the galaxy disc, probably due to motion in the galaxy bulge (e.g. Emsellem et al. 2006; Ricci, Steiner & Menezes 2016).

The h_4 moment maps show small values at most locations for all galaxies, with $-0.05 < h_4 < 0.05$. For some galaxies, which present strong low-σ structures (e.g. Mrk 1066, Mrk 607 and NGC 4051), higher positive h_4 values are observed co-spatial with the low-σ regions. This is also seen in the plots presented in Fig. B2, which show a trend of higher values of σ being observed in regions with negative h_4 values, while small σ values being associated with positive h_4 values. We interpret this correlation between low-σ and high h_4 values as an additional support to the presence of young/intermediate age stars at these locations, as more peaked velocity distributions are expected for young stars (as they are located in a thin disc structure).

The rotating disc models reproduce well the observed velocity fields for all galaxies, as seen in the residual velocity maps that show values smaller than 20 km s^{-1} at most locations. Table 2 shows the model parameters for each galaxy. The systemic velocities from the table are relative to the heliocentric frame. The deprojected velocity amplitude of the galaxies of our sample ranges from ∼60 km s^{-1} (for NGC 4051 – an Sc galaxy) to ∼340 km s^{-1} (for NGC 3516 – an S0 galaxy).

5 DISCUSSIONS

5.1 Comparison between kinematic and large-scale disc parameters

Table 2 shows the parameters derived from the symmetrization (using the FitKinematicPA routine) and from the fit of the rotation disc model (using the DiskFit code) of the velocity fields. These parameters can be compared to those obtained for the large-scale discs. The PA of the major axis from NED[2] (Ψ_{0NED}), shown in

[2] NASA/IPAC Extragalactic Database available at http://ned.ipac.caltech.edu/.

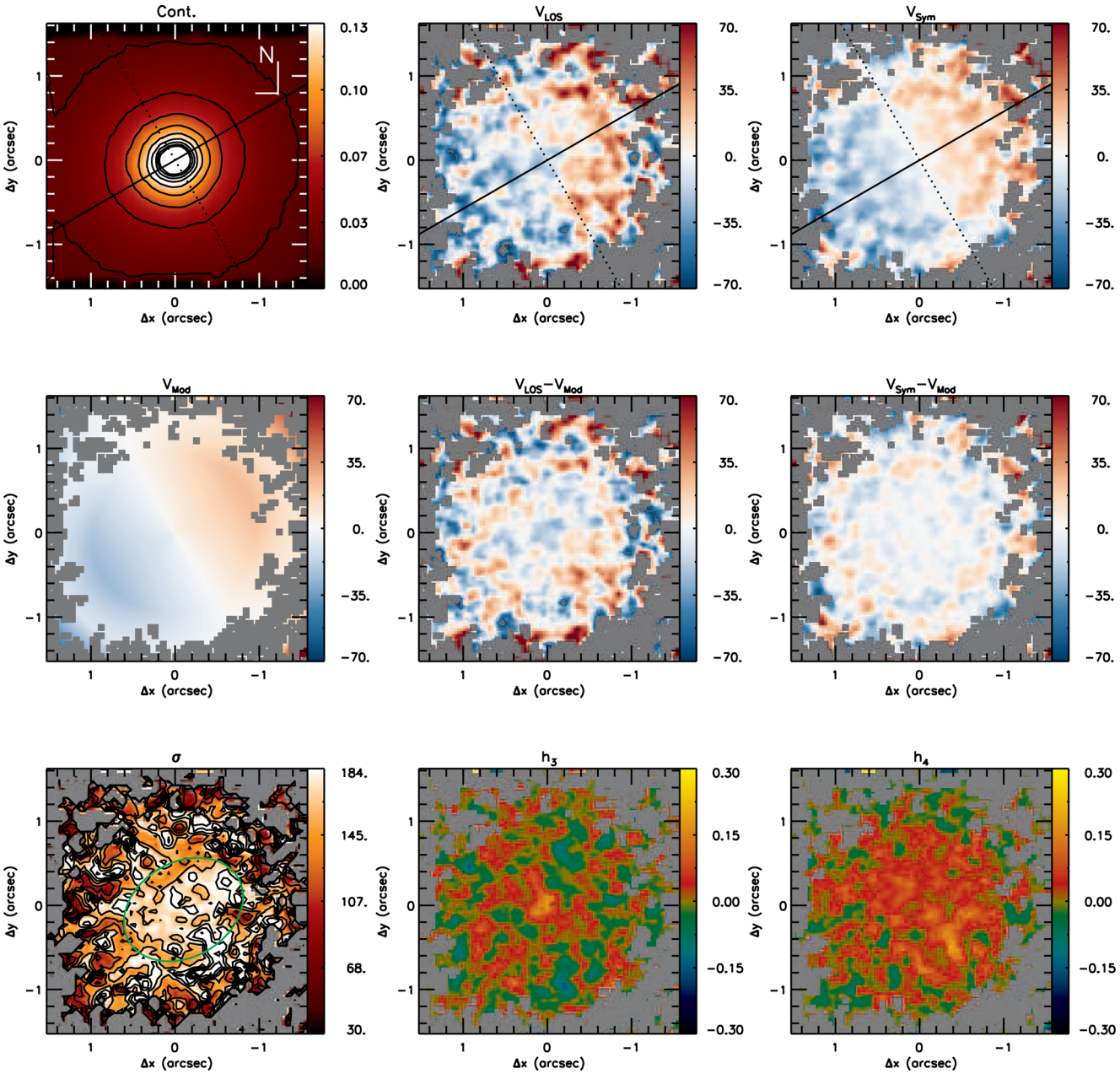

Figure 2. NGC 788: top-left: the *K*-band continuum image obtained by averaging the spectra, with the colour bar shown in units of 10^{-17} erg s^{-1} cm^{-2} Å^{-1}; top-middle: stellar velocity field; top-right: symmetrized velocity field; middle-left: rotating disc model; middle-middle: residual map for the symmetrized velocity field; middle-right: residual map for the observed velocity field; bottom-left: stellar velocity dispersion; bottom-middle: h_3 Gauss–Hermite moment and bottom-right: h_4 Gauss–Hermite moment. Grey regions are masked locations and correspond to regions where the signal to noise of the spectra was not high enough to get reliable fits. The continuous line identifies the orientation of the line of nodes and the dotted line marks the orientation of the minor axis of the galaxy. North is up and east left in all maps. The colour bar for velocity, model, residual maps and σ show the velocities in units of km s^{-1} and the systemic velocity of the galaxy was subtracted from the observed velocities.

Table 2 is derived from the K_S band photometry obtained from the Two Micron All Sky Survey (2MASS; Jarrett et al. 2003). The ellipticity ($e_{\rm NED}$) and inclination ($i_{\rm NED}$) of the disc are also obtained from the apparent major (a) and minor (b) axis available on NED data base from K_S images, as $e_{\rm NED} = 1 - \frac{b}{a}$ and $i_{\rm NED} = {\rm acos}(b/a)$, respectively.

In the left-hand panel of Fig. 13, we present a plot of the large-scale photometric PA of the major axis versus the kinematic PA derived from our NIFS velocity fields, constructed using the values of Ψ_0 shown in Table 2. This plot shows that the small-scale kinematic PA is in approximate agreement with the large-scale photometric one. The mean PA offset is $<\Psi_0 - \Psi_{0\rm NED}> = 3\overset{\circ}{.}9 \pm 5\overset{\circ}{.}7$. Only for three galaxies (NGC 5548, Mrk 766 and NGC 3516), there are significant discrepancies between small-scale kinematic and large-scale photometric major axes. NGC 5548 and Mrk 766 are almost face-on galaxies and thus it is hard to obtain a precise determination of Ψ_0, both from photometry and kinematics, justifying the discrepancy. For NGC 3516, the $\Psi_{0\rm NED}$ is distinct from that observed in optical images ($\Psi_0 = 56^\circ$; Schmitt & Kinney 2000) and from the stellar kinematics based on optical IFS

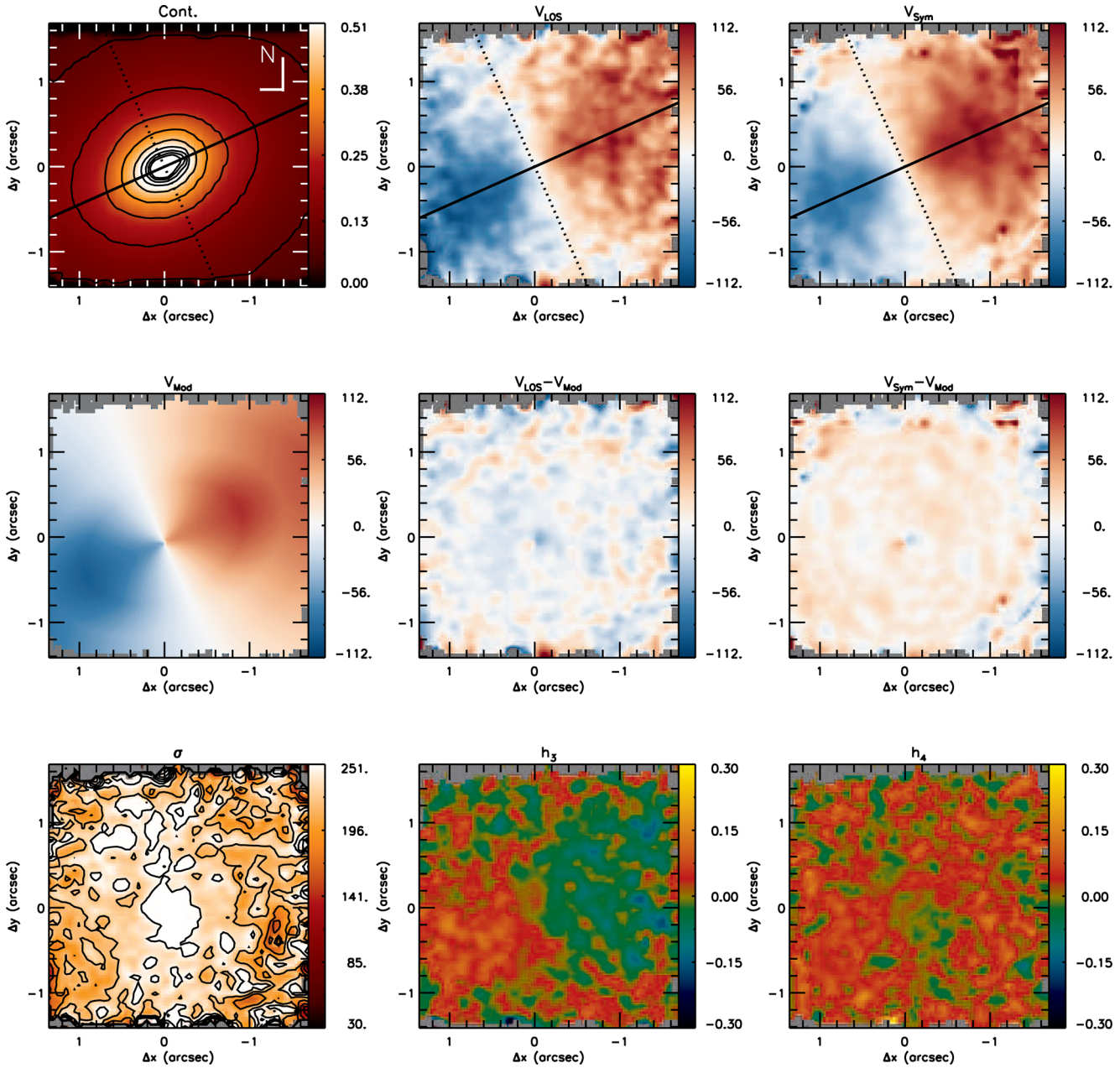

Figure 3. Same as Fig. 2 for NGC 1052.

($\Psi_0 = 53°$; Arribas et al. 1993). On the other hand, the Ψ_{0NED} for NGC 3516 is very similar to the orientation of the bar of the galaxy ($\Psi_0 = -10°$; Veilleux, Tully & Bland-Hawthorn 1993) and thus the value of Ψ_{0NED} may be biased due to the bar, which is stronger in near-IR bands.

Previous studies have found similar results. For example, the morphological study by Malkan, Gorjian & Tam (1998) of the inner kiloparsecs of nearby active galaxies showed that the resulting classification of the small-scale structure was very similar to the one given in the Third Reference Catalog (RC3; Corwin, Buta & de Vaucouleurs 1994), showing that not only the kinematic PA at small scale but also the photometric PA at small scale is similar to that at large scale.

Barbosa et al. (2006) used the Gemini Multi-Object Spectrograph (GMOS) IFU to map the stellar kinematics of the inner 200–900 pc of six nearby active galaxies by fitting the stellar absorption lines of the Calcium triplet around 8500 Å and also found that the kinematic PA at small scale is in good agreement with the large-scale photometric measurements. Dumas et al. (2007) used optical IFS to map the stellar and gas kinematics of the central kiloparsec of a matched sample of nearby Seyfert and inactive galaxies at angular resolutions ranging from 0.9 to 2.5 arcsec, using the SAURON IFU on the *William Herschel Telescope*. They found that the orientations of the kinematic line of nodes are very similar with those derived from large-scale photometry for both active and inactive galaxies. Falcón-Barroso et al. (2006) present the stellar kinematics of a sample of 24 spiral galaxies using the SAURON IFU. Their sample includes only five active nuclei and they found misaligned photometric and kinematic axes for nine objects in their sample (only one being an active galaxy), interpreted as being due to

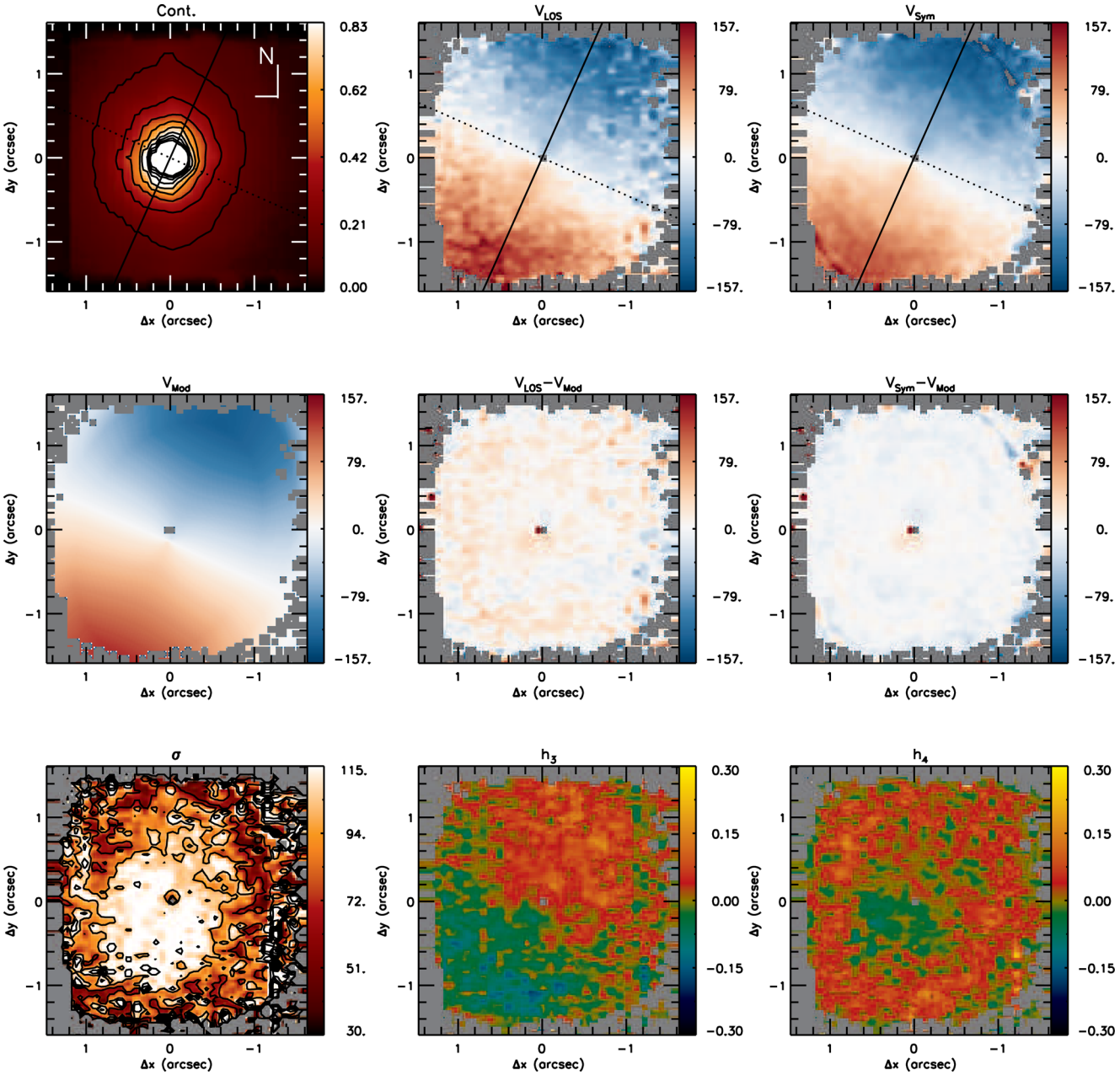

Figure 4. Same as Fig. 2 for NGC 3227.

non-axisymmetric structures (as bars) and more easily detected at low galaxy inclinations.

The middle and right-hand panels of Fig. 13 show the comparison between the large photometric (*y*-axis) and small kinematic (*x*-axis) scale disc inclination and ellipticity, respectively. In contrast to the orientation of the major axis of the galaxy, these parameters do not follow the same distribution at small and large scale. For most cases, both the inclination and the ellipticity of the disc at large scale are larger than that derived for the inner 3 arcsec $\times$3 arcsec. This result can be interpreted as being due to the fact that the large-scale measurements are dominated by the disc component as they are estimated from the apparent major and minor axis measurements obtained from large-scale K_S images, while at small scale, the near-IR emission is dominated by emission from evolved red stars at the bulge of the galaxy (e.g. Maraston 2005; Riffel et al. 2015b), which play an important role in the observed morphology and kinematics observed with NIFS.

5.2 Gravitational potentials and comparison with previous studies

The velocity residual maps for all galaxies of our sample show small values, indicating that the stellar velocity fields are well reproduced by the rotating disc model, with kinematic axes that follow the same orientation of large-scale measurements. In addition, the de-projected rotation velocity amplitude is always larger than the mean velocity dispersion, indicating the stellar kinematics of the galaxies of our sample are dominated by regular rotation. We can compare our results with previous studies of the stellar kinematics of active and inactive galaxies.

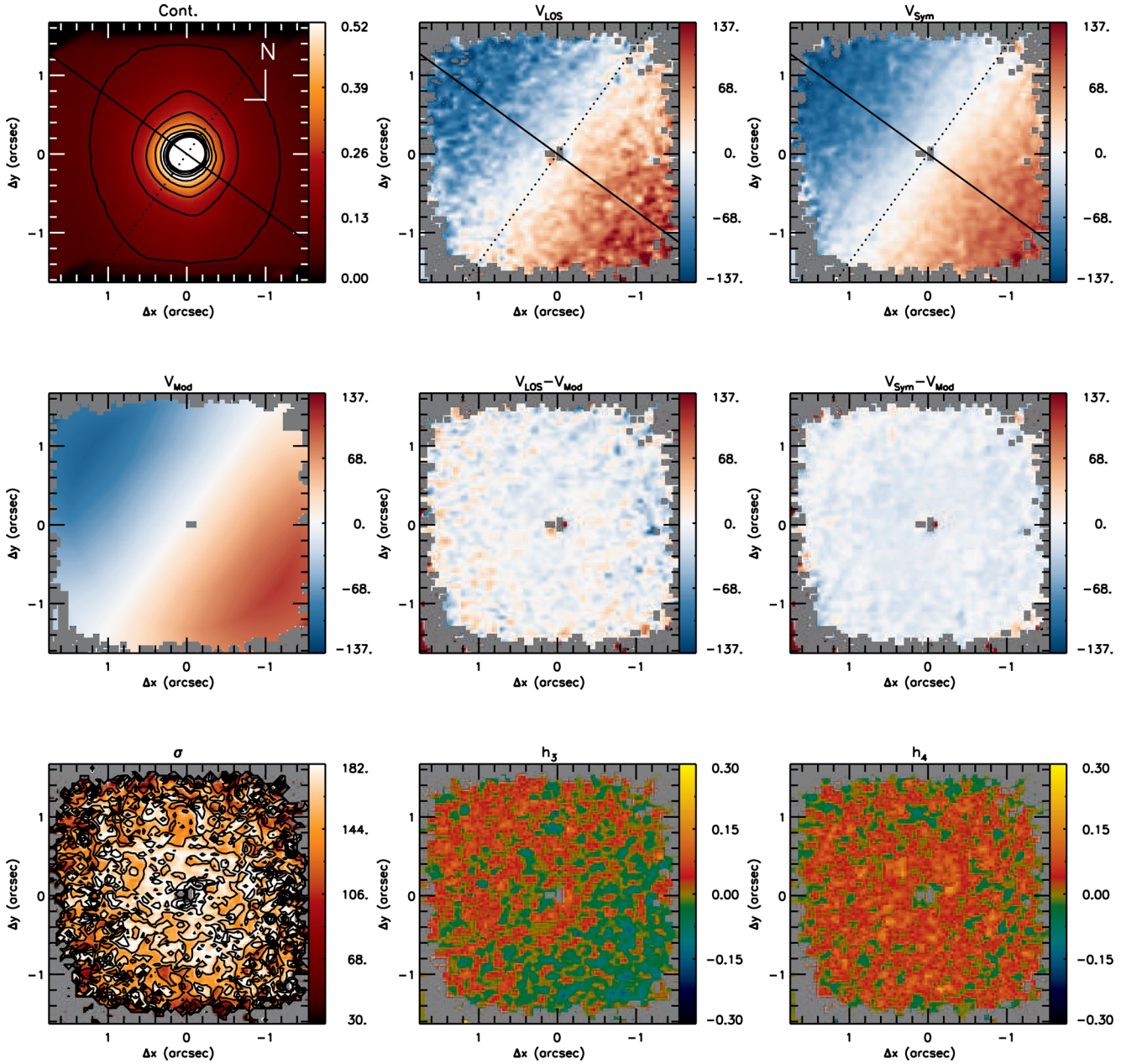

Figure 5. Same as Fig. 2 for NGC 3516.

Dumas et al. (2007) present the stellar kinematics of a sample of 39 active galaxies and a matched control sample, selected to have similar blue magnitudes, Hubble type and inclinations. They found that the stellar kinematics of both active and inactive galaxies show regular rotation patterns typical of disc-like systems. A similar result was found by Barbosa et al. (2006) using higher angular resolution (<1.0 arcsec) IFS with Gemini Telescopes of a sample of six nearby Seyfert galaxies. In addition, they found partial rings of low-σ values at 200–400 pc from the nucleus for three galaxies, interpreted as tracers of recently formed stars that partially keep the cold kinematics of the original gas from which they have formed. Falcón-Barroso et al. (2006) present kinematic maps for a sample of nearby spiral galaxies obtained with the SAURON IFU, which show regular stellar rotation for most galaxies. However, kinematic decoupled components are frequently seen in the inner region, as sudden changes in the velocity field, which are often associated with a drop in the σ and anticorrelated h_3 values with respect to the V_{LOS}. In addition, they found kinematic signatures of non-axisymmetric structures for 37 per cent of the galaxies of their sample (only one harbouring an AGN). For 20 per cent of their sample (five galaxies, none of them harbouring an AGN) they found kinematic signatures of bars as predicted in *N*-body simulations of barred potentials (e.g. Kuijken & Merrifield 1995; Bureau & Athanassoula 2005).

Hubble Space Telescope (*HST*) *H*-band images up to 10 arcsec radius and ground-based near-IR and optical images of a matched Seyfert versus non-Seyfert galaxy sample of 112 nearby galaxies show a statistically significant excess of bars amongst the Seyfert galaxies at practically all length-scales (Laine et al. 2002). In addition, they also found that Seyfert galaxies always show a preponderance of 'thick' bars compared to the bars in non-Seyfert

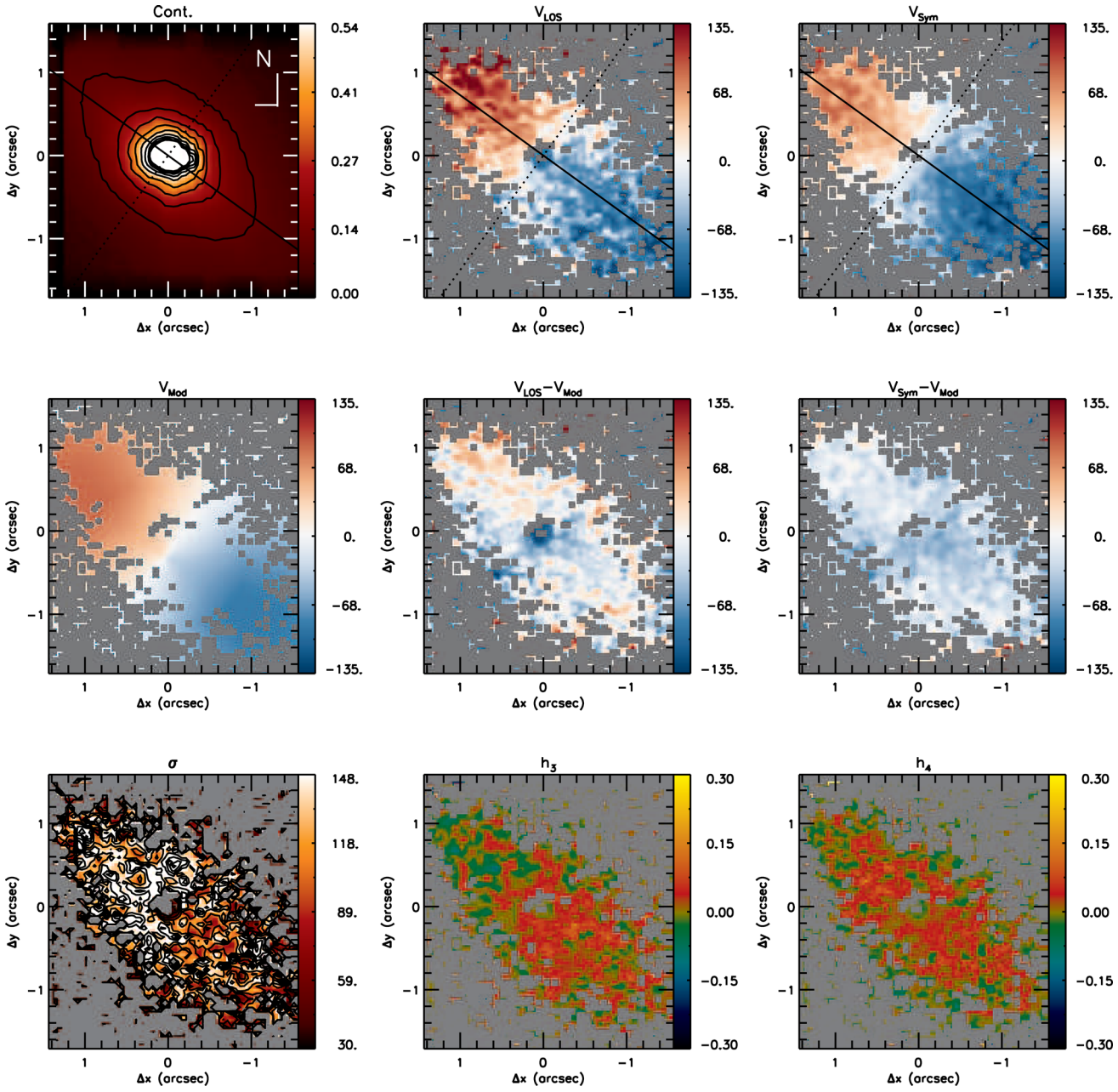

Figure 6. Same as Fig. 2 for NGC 4235.

galaxies. On the other hand, recent results show that AGN hosts at $0.2 < z < 1.0$ show no statistically significant enhancement in bar fraction compared to inactive galaxies (e.g Cheung et al. 2015). Large-scale bars are seen for 28.5 per cent of face-on spiral hosts of AGN, as obtained from the study of more the 6.000 AGN hosts of from the Sloan Digital Sky Survey (SDSS; Alonso, Coldwell & Lambas 2013).

Our kinematic maps suggest the presence of nuclear bars in only two galaxies: Mrk 1066 and NGC 5899, as revealed by the presence of an S-shape zero velocity line observed in the V_{LOS} maps (e.g. Combes et al. 1995; Emsellem et al. 2006). This corresponds to only 12.5 per cent of our sample, although the statistics is low so far and this result is preliminary. The rest of the galaxies are dominated by rotation. The difference in the proportion of barred galaxies or non-axisymmetric structures in our study relative to that of Falcón-Barroso et al. (2006) may be due to the small number of objects in both studies, and to the difference in the FoV of the two studies. Our FoV (3 arcsec × 3 arcsec) is smaller than those of previous studies, making it more difficult to identify kinematic signatures of bars as predicted in *N*-body simulations (e.g. Bureau & Athanassoula 2005), as double-hump rotation curves, broad σ profiles with a plateau at moderate radii and $h_3 - V_{LOS}$ correlation over the projected bar length. On the other hand, the photometric detection of bars mentioned above are mainly obtained using large-scale images. Thus, our results suggest that the motion of the stars is dominated by the gravitational potential of the bulge, as the FoV of our observations is smaller than the bulge length for all galaxies.

To further investigate how the galactic potentials and deviations from ordered rotation are related to the host galaxy and AGN, we plotted the mean value of the modulus of the residual velocities

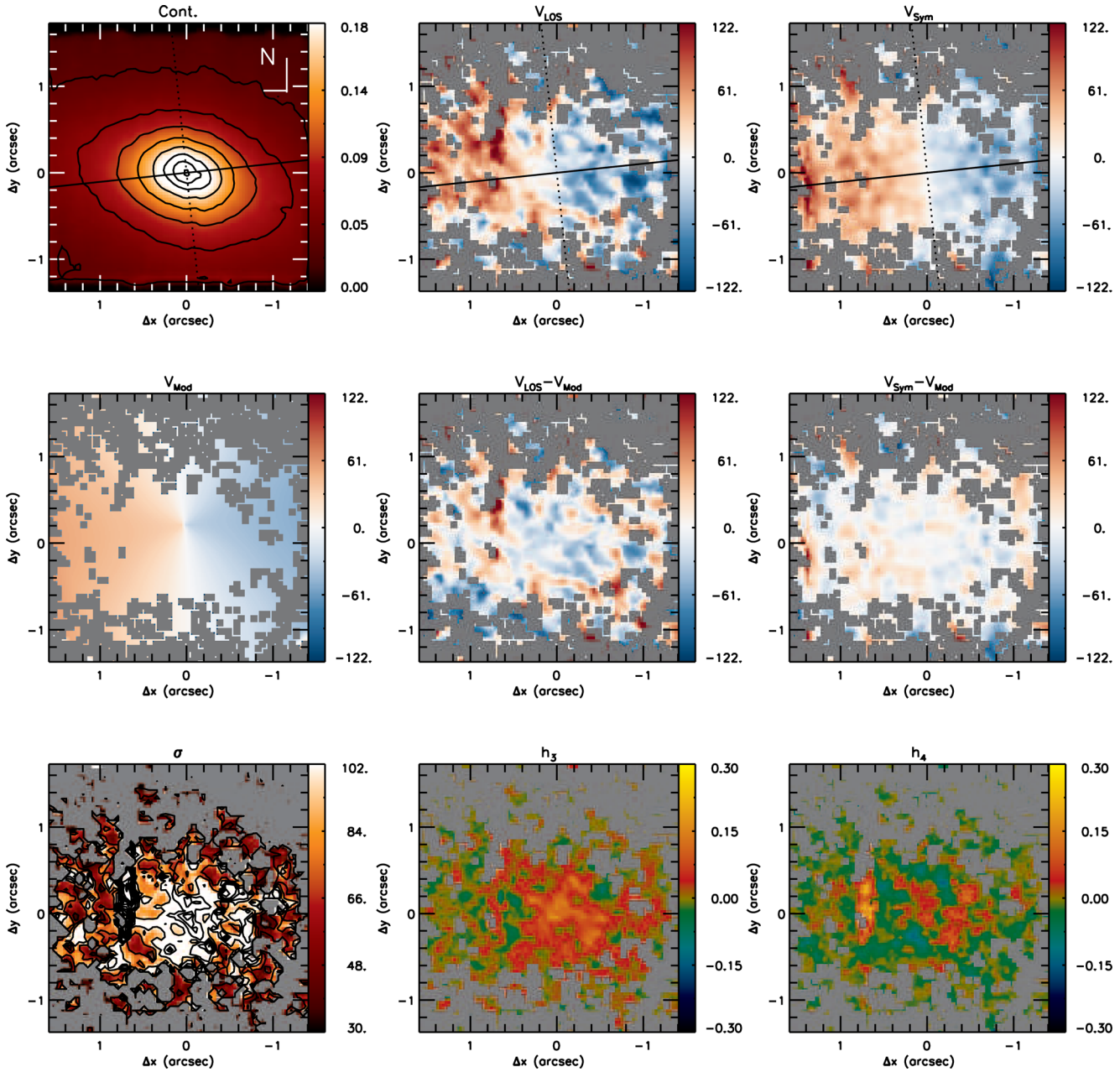

Figure 7. Same as Fig. 2 for NGC 4388.

($\langle|V_{res}|\rangle$), where $V_{res} = V_{LOS} - V_{mod}$, against the Hubble index and hard X-ray (14–195 keV) luminosity (L_X) from the *Swift*-BAT 60-month catalogue (Ajello et al. 2012), which measures direct emission from the AGN. These plots are shown in Fig. 14. For four galaxies of our sample (MRK1066, MRK1157, MRK607 and NGC5929), there are no X-ray luminosities available in the BAT catalogue and thus the $\langle|V_{res}|\rangle$ versus plot contains only 12 points. The $\langle|V_{res}|\rangle$ was estimated as the mean value of 10.000 bootstrap realizations in which for each interaction the $|V_{res}|$ is calculated for a sample selected randomly amongst the values observed in the residual map. The standard deviation in the simulated $|V_{res}|$ represents the intrinsic scatter of each residual map and is used as the uncertainty for $\langle|V_{res}|\rangle$.

The top panel of Fig. 14 shows that there is no correlation between $\langle|V_{res}|\rangle$ and Hubble index, with a Pearson correlation coefficient of only $R = 0.12$. This result shows that large-scale structures do not affect significantly the stellar kinematics of the inner kiloparsec of the galaxies of our sample.

On the other hand, the bottom panel of Fig. 14 suggests that $\langle|V_{res}|\rangle$ is correlated with L_X. We computed a Pearson correlation coefficient of $R = 0.74$, with less than 1 per cent of probability that this distribution of points can be generated by a random distribution. Although the number of points is small, this trend may mean that more luminous AGNs have a larger impact in the surrounding stellar dynamics. As a speculation, we propose that strong AGN may quench circum-nuclear star formation in the galaxy disc and thus the stellar motions have a more important component of bulge star kinematics. On the other hand, for lower luminosity AGNs, the active nuclei may not be powerful enough the quench the star formation and thus the stellar dynamics has a stronger

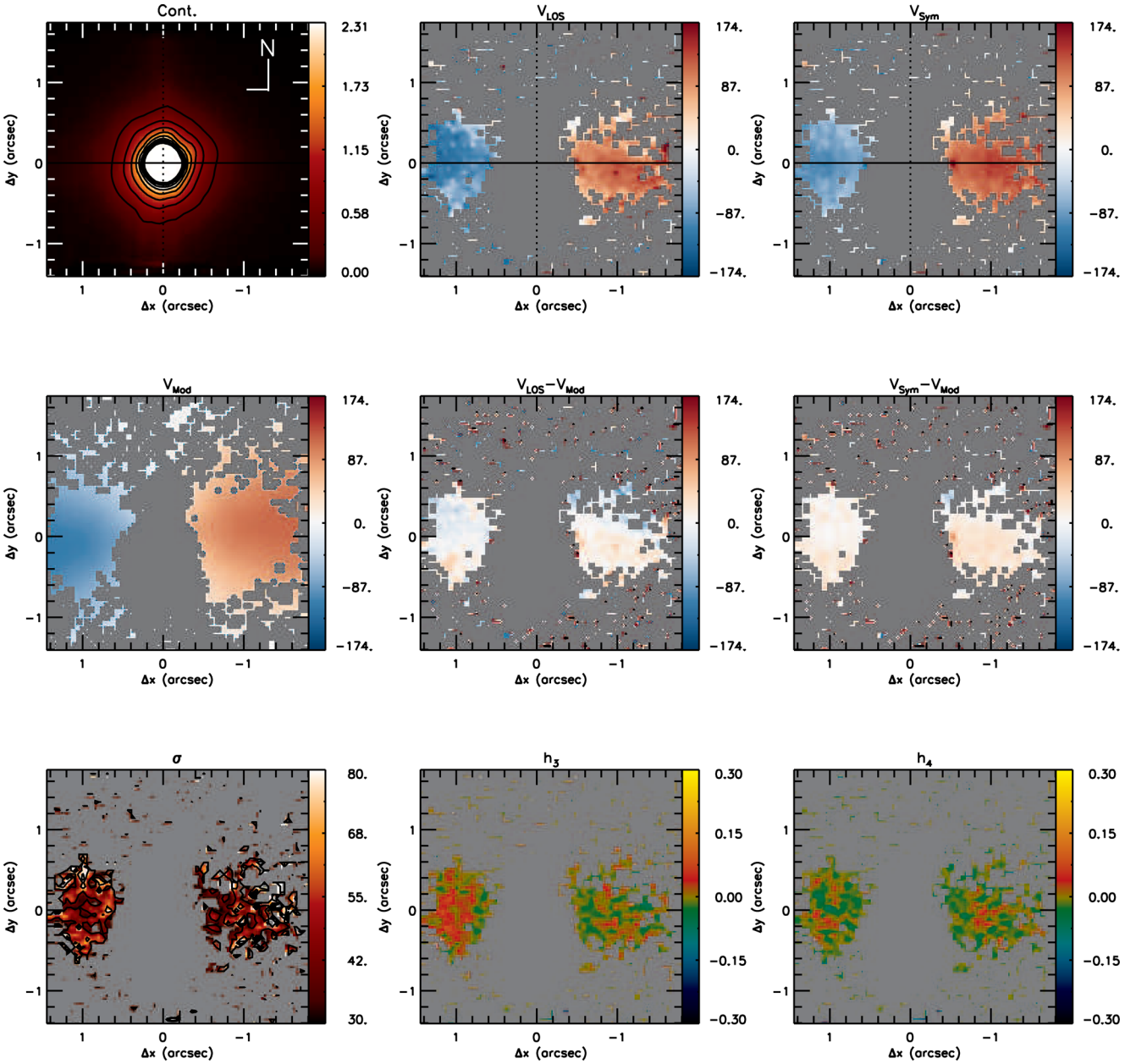

Figure 8. Same as Fig. 2 for NGC 5506.

contribution from stars more recently formed in the plane of the galaxy.

5.3 Implications to AGN feeding and star formation

The velocity dispersion maps show structures of lower σ than the surroundings ($\sim$50–80 km s^{-1}) for 10 galaxies (62 per cent) of our sample. Such velocity dispersion drops are commonly reported in the literature (e.g. Bottema 1989, 1993; Fisher 1997; García-Lorenzo, Mediavilla & Arribas 1999; Emsellem et al. 2001; Márquez et al. 2003; Barbosa et al. 2006; Falcón-Barroso et al. 2006) and have been interpreted as being tracers of relatively recent star formation as compared to the bulge stellar population (e.g. Emsellem et al. 2001, 2006; Márquez et al. 2003; Barbosa et al. 2006; Riffel et al. 2008). Indeed, stellar population synthesis using near-IR IFS with NIFS reveal that the low-σ rings seen in Mrk1066 and Mrk1157 are associated with an intermediate-age stellar population (<700 Myr; Riffel et al. 2010, 2011).

The low-σ structures may be related to accretion of gas to the inner kiloparsec of galaxies as a result of streaming motions towards the nucleus along nuclear bars or dust spirals, observed for several active galaxies by our group (e.g. Fathi et al. 2006; Riffel et al. 2008; Storchi-Bergmann et al. 2009; Riffel et al. 2013; Schnorr-Müller et al. 2014, 2016, 2017; Diniz et al. 2015; Lena et al. 2015) and other groups (e.g. Sánchez et al. 2009; van de Ven & Fathi 2010; Smajić et al. 2015). Several works have been aimed to investigate the presence of nuclear bars and dust spirals in active and inactive galaxies using high-resolution *HST* images (Laine et al. 2002; Pogge & Martini 2002; Simões Lopes et al. 2007; Martini, Dicken & Storchi-Bergmann 2013). These studies reveal an excess of bars in Seyfert galaxies, when compared to a matched sample of inactive galaxies (Laine et al. 2002) and dust structures seem to be present in

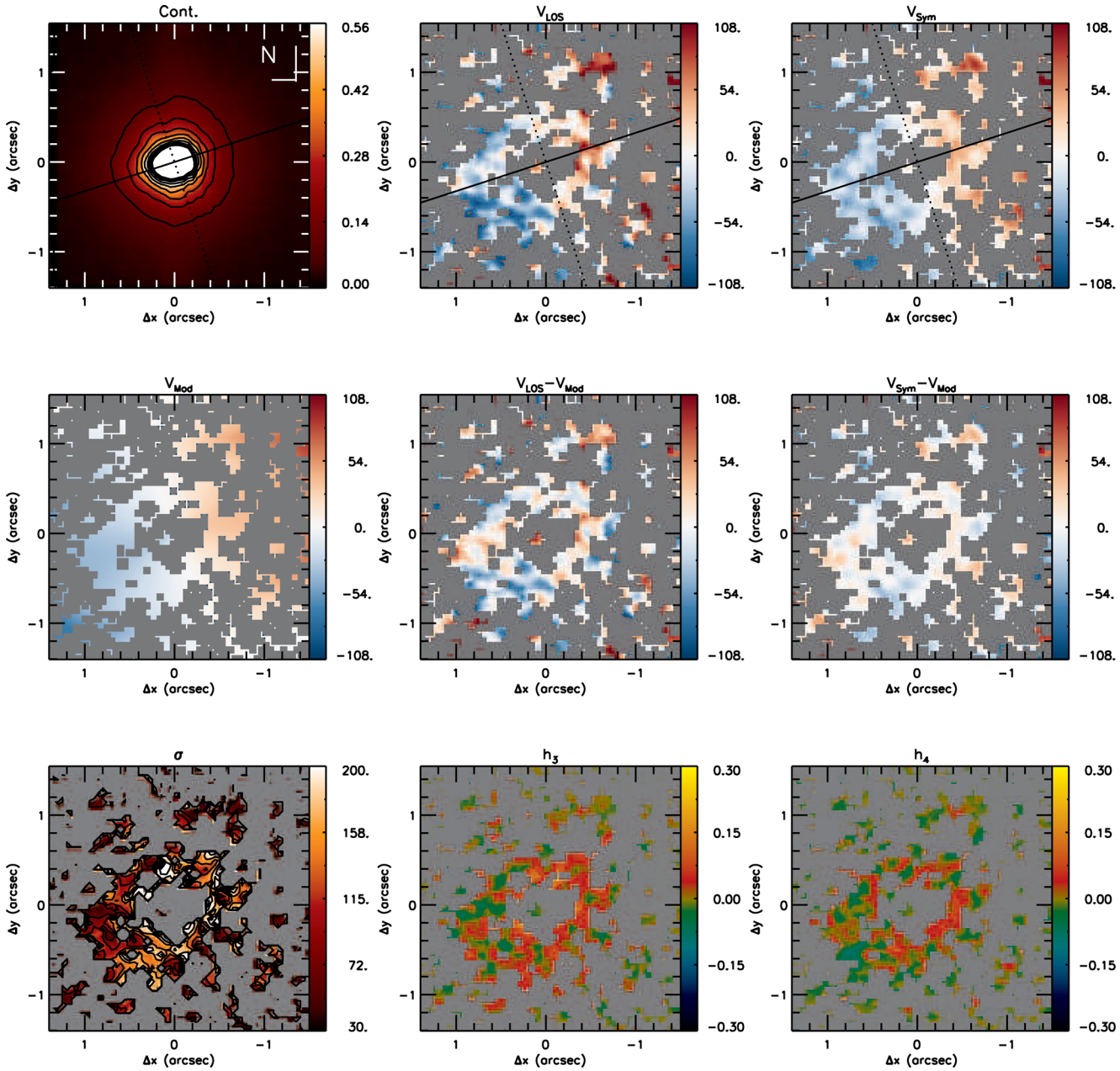

Figure 9. Same as Fig. 2 for NGC 5548.

all early-type AGN hosts, while only 26 per cent of inactive early-type show significant dust in the nuclear region (Simões Lopes et al. 2007). For late-type galaxies, large amount of dust is observed for both active and inactive galaxies (Simões Lopes et al. 2007).

The observed gas inflows mentioned above can lead to the accumulation of large reservoirs of gas that can feed both star formation and the AGN. In such scenario, it would be expected that low-σ structures should be more frequent in active than in inactive galaxies. However, several studies report the presence of low-σ structures in inactive galaxies. For example, Falcón-Barroso et al. (2006) found that at least 46 per cent of their sample of spiral galaxies show σ-drops, most of them being inactive. A similar result is reported by Ganda et al. (2006), who found central σ drops for many objects of their sample of 18 spiral galaxies. On the other hand, these drops are not commonly observed in elliptical galaxies (Emsellem et al. 2004). Thus, the presence of low-σ may be related to recent star formation in the inner kiloparsec of the galaxies of our sample, but possibly unrelated to the nuclear activity.

5.4 The stellar kinematics and AGN feeding and feedback processes

This paper is the first of a series in which we will investigate the AGN feeding and feedback processes using *J* and *K* band NIFS observations of a sample of nearby active galaxies selected using the hard X-ray luminosity as main criterion. The results presented here will be used to compare gas and stellar kinematics to isolate non-circular motions, by constructing residual maps between the observed velocity fields for the ionized (traced by [Fe II] and H recombination lines) and molecular (traced by H_2 emission lines)

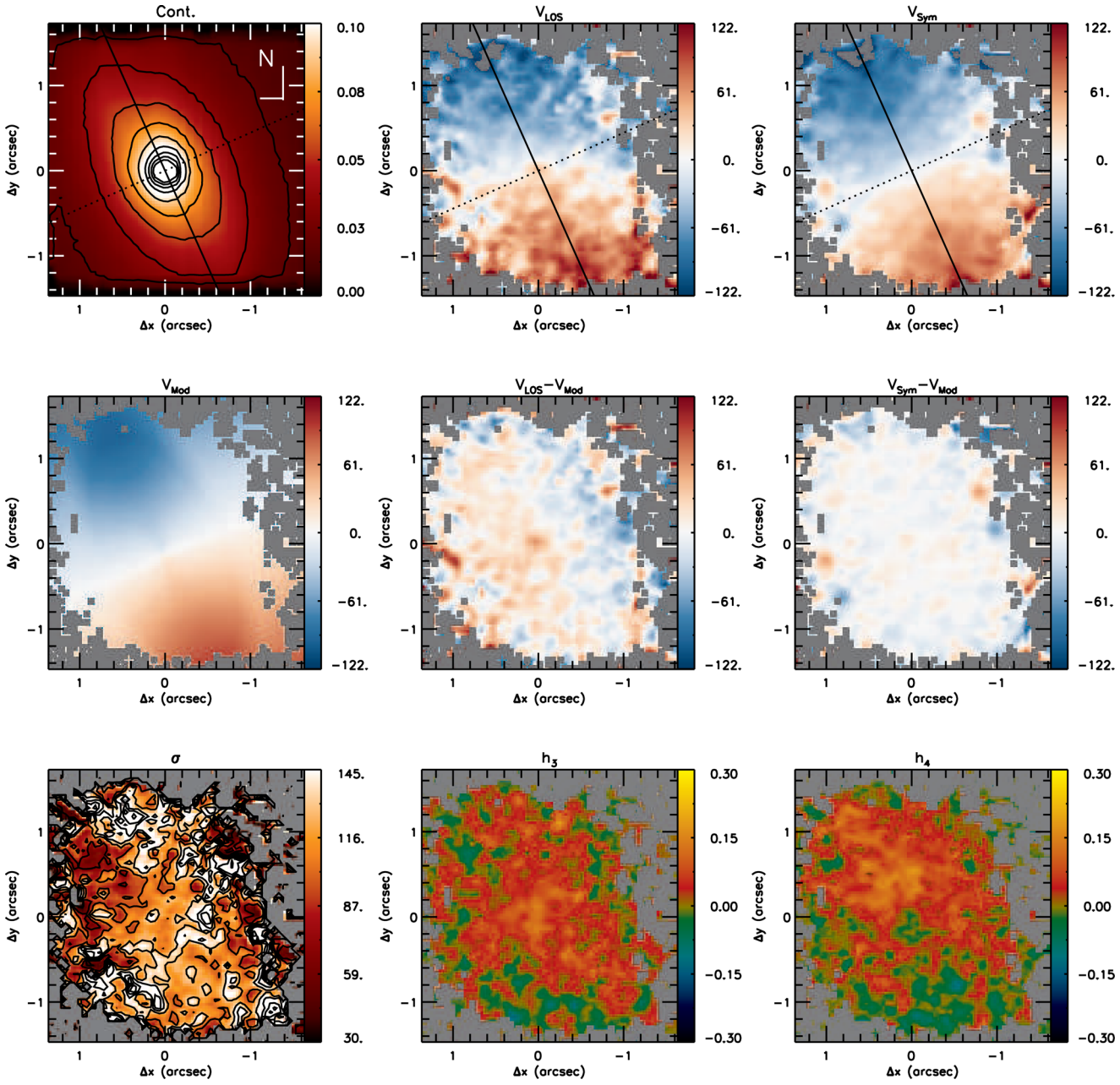

Figure 10. Same as Fig. 2 for NGC 5899.

gas and the rotating disc models presented here. The analysis of the residual maps, together with velocity channel maps along the emission-line profiles, will allow us to identify possible gas inflows and outflows. Similar methodology has already been successfully used by our AGNIFS group (e.g. Riffel et al. 2008; Riffel & Storchi-Bergmann 2011a; Riffel et al. 2013; Riffel & Storchi-Bergmann 2011b; Diniz et al. 2015). The gas inflow and outflow rates can be compared with AGN properties (e.g. bolometric luminosity and accretion rate) to draw a picture of the feeding and feedback processes in AGNs.

6 CONCLUSIONS

We used near-IR IFS to map the stellar kinematics of the inner 3 arcsec × 3 arcsec of a sample of 16 nearby Seyfert galaxies. We present maps for the radial velocity, velocity dispersion and higher order Gauss–Hermite moments, obtained by fitting the CO stellar absorptions in the *K* band. The observed velocity fields were symmetrized and modelled by a thin rotating disc to derive kinematical parameters. The main results of this work are as following:

(i) The observed velocity fields for all galaxies show regular rotation. In addition, for two galaxies (Mrk 1066 and NGC 5899) the velocity field shows an S-shape zero velocity line that is interpreted as a signature of nuclear bars.

(ii) The residuals of the modelling of the stellar velocity field are correlated with the hard X-ray luminosity, suggesting that the nuclear source plays a role on the observed stellar dynamics of the inner kiloparsec of the galaxies, with stronger AGNs showing less-ordered stellar orbits than weak AGNs.

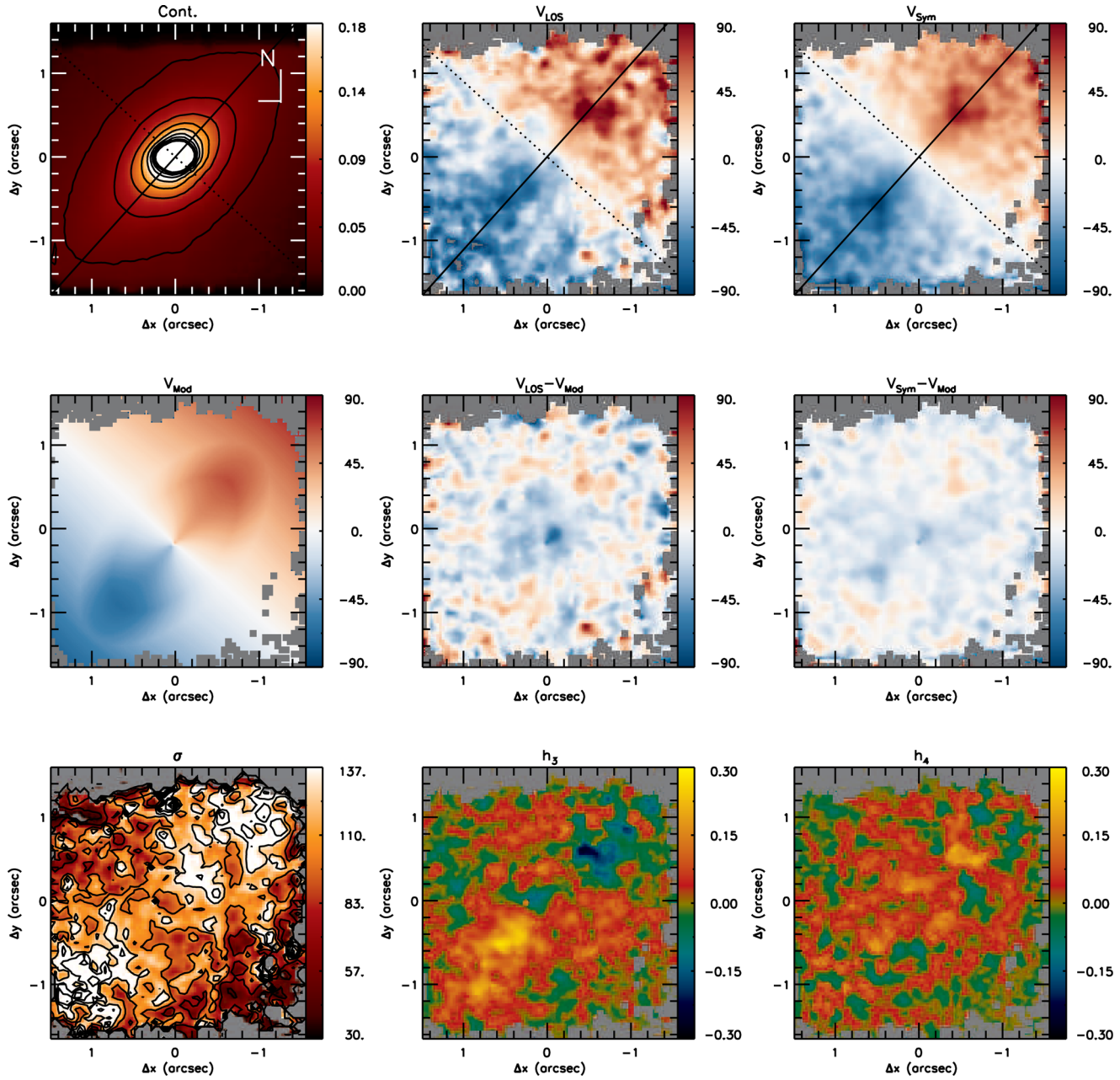

Figure 11. Same as Fig. 2 for Mrk 607.

(iii) The velocity dispersion maps show low-σ ($\sim$50–80 km s^{-1}) rings for four galaxies (Mrk 1066, Mrk 1157, NGC 5929 and NGC 788) or 'patches' of low-σ structures (for Mrk 607, NGC 2110, NGC 3516, NGC 4051, NGC 4235 and NGC 5899) at typical distances of 200 pc, interpreted as being originated in young/intermediate age stellar populations. Centrally peaked σ maps are observed for three galaxies (NGC 1052, NGC 3227 and NGC 4388).

(iv) The h_3 moment is anticorrelated with the velocity field for eight galaxies (NGC 1052, NGC 2110, NGC 3227, NGC 3516, NGC 4051, NGC 5506, Mrk 607 and Mrk 1066) – positive h_3 values seen at locations where the velocity field shows blueshifts and $h_3 < 0$ for locations where the velocity field shows redshifts. The presence of these wings are attributed to the contribution of stars from the galaxy bulge that present lower rotation velocities.

(v) The h_4 maps show small values at most locations for all galaxies. For the galaxies with low-σ rings, higher h_4 values are observed co-spatially with the ring, being interpreted as an additional signature of young/intermediate age stars at these locations.

(vi) The observed velocity fields are well reproduced by a rotating disc model, with deprojected velocity amplitudes in the range of $\sim$60–340 km s^{-1}.

(vii) The orientations of the line of nodes derived from the small-scale velocity fields are similar to the photometric major axis orientations of the large-scale discs, while the disc ellipticity and inclination are smaller at small scale, as compared to those at large scale.

The stellar kinematics and rotating disc models derived in this work will be compared to the gas kinematics and flux distributions

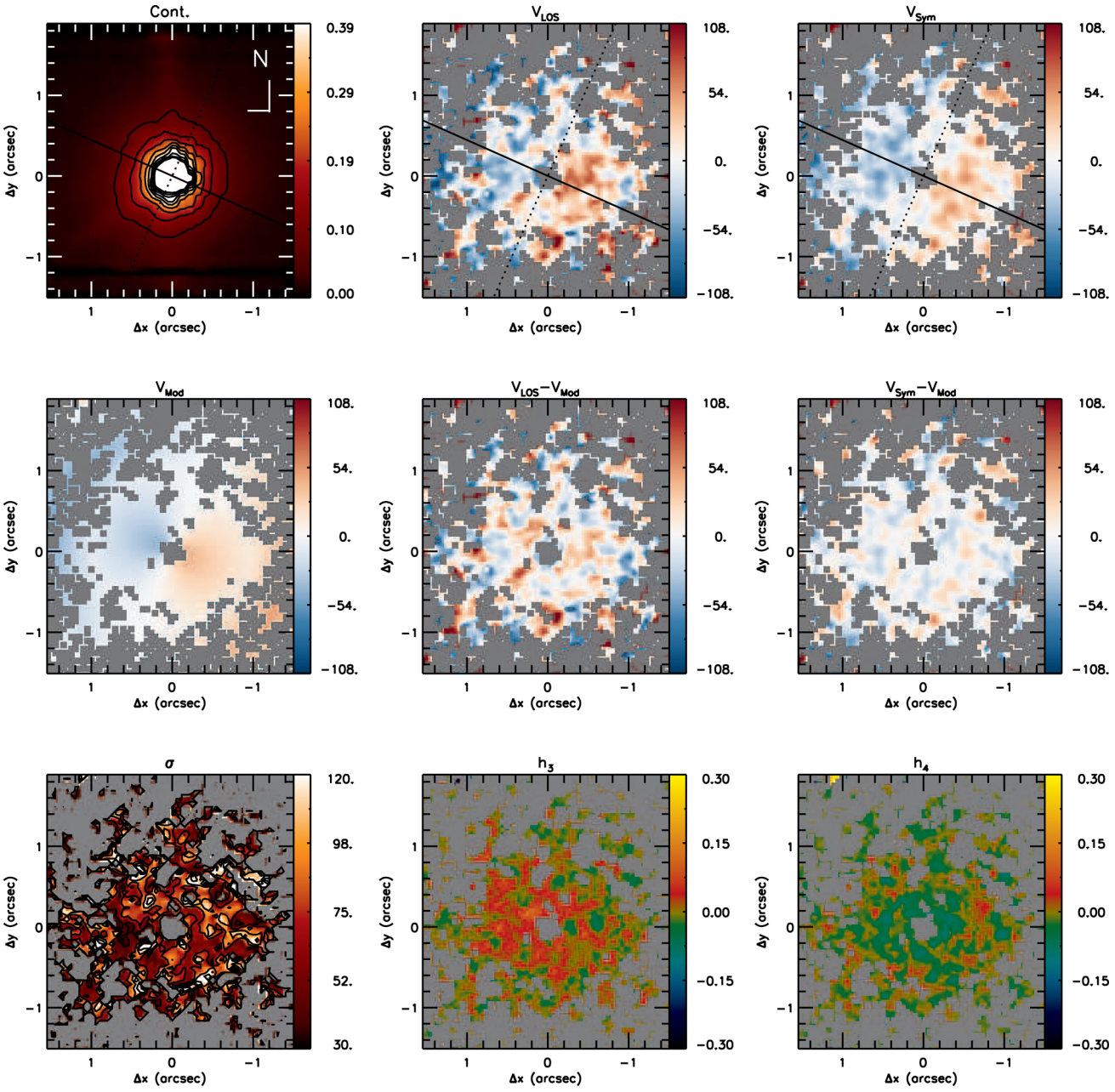

Figure 12. Same as Fig. 2 for Mrk 766.

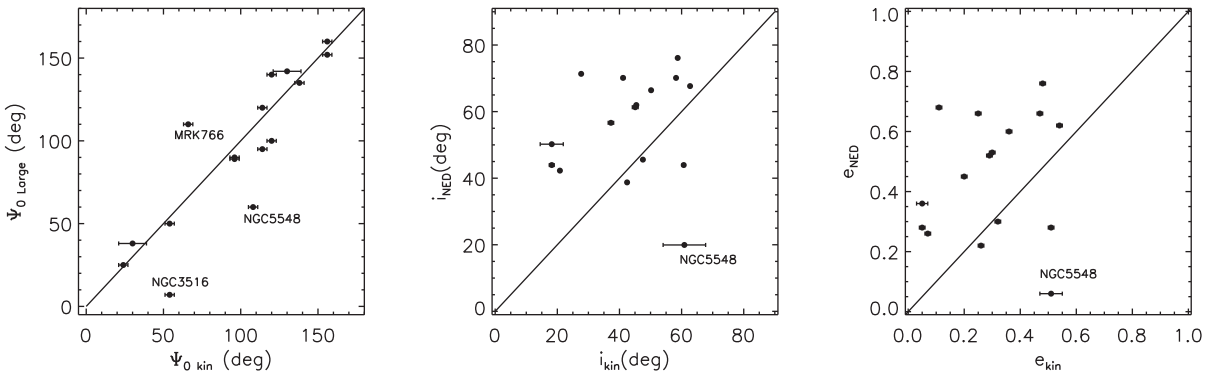

Figure 13. Comparison of large-scale photometric (*y*-axis) and small-scale kinematic (*x*-axis) PAs (left), inclination (middle) and ellipticity (right). Continuous lines show one-to-one relations.

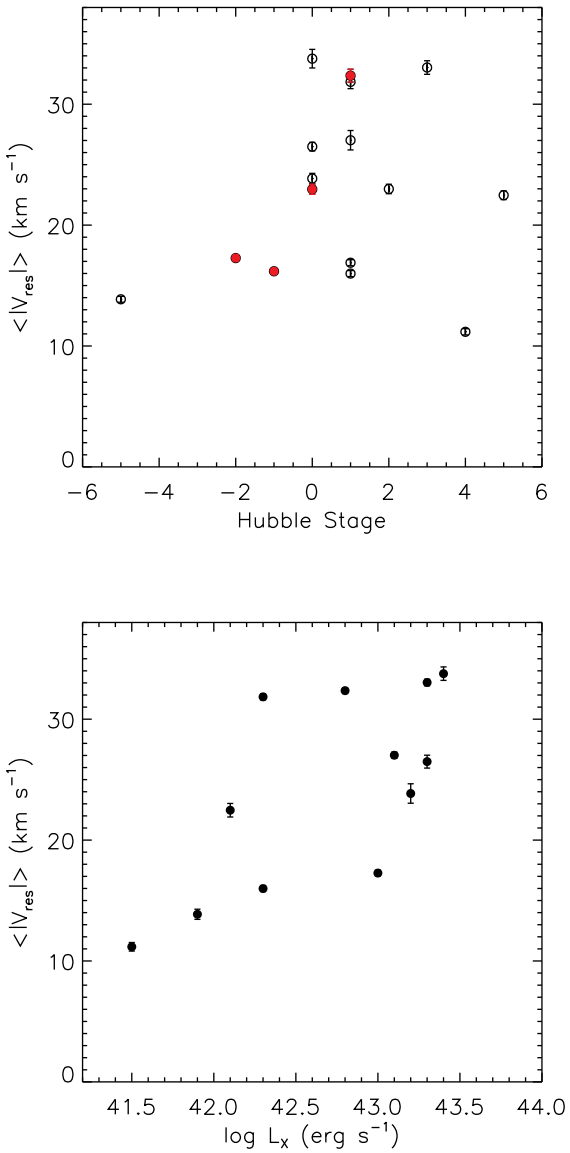

Figure 14. Plots of the standard deviation of the residual maps ($\langle|V_{res}|\rangle$) versus Hubble index (top) and X-ray luminosity (L_X, bottom). In the top panel, filled circles correspond to barred galaxies.

in future studies with the aim of isolating and quantifying non-circular motions in the gas of the galaxies of our sample to map and quantify feeding and feedback processes in our AGN sample.

ACKNOWLEDGEMENTS

We thank an anonymous referee for useful suggestions that helped to improve the paper. This study is based on observations obtained at the Gemini Observatory, which is operated by the Association of Universities for Research in Astronomy, Inc., under a cooperative agreement with the NSF on behalf of the Gemini partnership: the National Science Foundation (United States), the Science and Technology Facilities Council (United Kingdom), the National Research Council (Canada), CONICYT (Chile), the Australian Research Council (Australia), Ministério da Ciência e Tecnologia (Brazil) and south-east CYT (Argentina).

This research has made use of the NASA/IPAC Extragalactic Database (NED) that is operated by the Jet Propulsion Laboratory, California Institute of Technology, under contract with the National Aeronautics and Space Administration. We acknowledge the usage of the HyperLeda data base (http://leda.univ-lyon1.fr). RAR and RR thank CNPq and FAPERGS for financial support.

REFERENCES

Ajello M., Alexander D. M., Greiner J., Madejski G. M., Gehrels N., Burlon D., 2012, ApJ, 749, 21
Alonso M. S., Coldwell G., Lambas D. G., 2013, A&A, 549, A141
Arribas S., Mediavilla E., García-Lorenzo B., Del Burgo C., 1997, ApJ, 490, 227
Barbosa F. K. B., Storchi-Bergmann T., Cid Fernandes R., Winge C., Schmitt H., 2006, MNRAS, 371, 170
Barbosa F. K. B., Storchi-Bergmann T., Cid Fernandes R., Winge C., Schmitt H., 2009, MNRAS, 396, 2
Barbosa F. K., Storchi-Bergmann T., McGregor P., Vale T. B., Riffel R. A., 2014, MNRAS, 455, 2353
Barnes E. I., Sellwood J. A., 2003, AJ, 125, 1164
Bottema R., 1989, A&A, 221, 236
Bottema R., 1993, A&A, 275, 16
Bureau M., Athanassoula E., 2005, ApJ, 626, 159
Cappellari M., Emsellem E., 2004, PASP, 116, 138
Cappellari M. et al., 2007, MNRAS, 379, 418
Cheung E. et al., 2015, MNRAS, 447, 506
Ciotti L. et al., 2010, ApJ, 717, 707
Combes F., Boissé P., Mazure A., Blanchard A., 1995, Galaxies and Cosmology. Springer, Berlin
Corwin H. G., Buta R. J., de Vaucouleurs G., 1994, AJ, 108, 2128
Davies R. I. et al., 2006, AJ, 646, 754
Diniz M. R., Riffel R. A., Storchi-Bergmann T., Winge C., 2015, MNRAS, 453, 1727
Dumas G., Mundell C. G., Emsellem E., Nagar N. M., 2007, MNRAS, 379, 1249
Elvis M., 2000, ApJ, 545, 63
Emsellem E., Greusard D., Combes F., Friedli D., Leon S., Pécontal E., Wozniak H., 2001, A&A, 368, 52
Emsellem E. et al., 2004, MNRAS, 352, 721
Emsellem E., Fathi K., Wozniak H., Ferruit P., Mundell C. G., Schinnerer E., 2006, MNRAS, 365, 367
Fabian A., 2012, ARA&A, 50, 455
Falcón-Barroso J. et al., 2006, MNRAS, 369, 529
Fathi K., Storchi-Bergmann T., Riffel R. A., Winge C., Axon D. J., Robinson A., Capetti A., Marconi A., 2006, ApJ, 641, L25
Ferrarese L., Ford H., 2005, Space Sci. Rev., 116, 523
Fischer T. C. et al., 2017, ApJ, 834, 30
Fischer T. C., Crenshaw D. M., Kraemer S. B., Schmitt H. R., Storchi-Bergmann T., Riffel R. A., 2015, ApJ, 799, 234
Fisher D., 1997, AJ, 113, 950
Frank J., King A., Raine D. J., 2002, Accretion Power in Astrophysics. Cambridge Univ. Press, Cambridge
Ganda K., Falcón-Barroso J., Peletier R. F., Cappellari M., Emsellem E., McDermid R. M., de Zeeuw P. T., Carollo C. M., 2006, MNRAS, 367, 46
García-Lorenzo B., Mediavilla E., Arribas S., 1999, ApJ, 518, 190
Gerhard O. E., 1993, MNRAS, 265, 213
Hicks E. K. S., Davies R. I., Malkan M. A., Genzel R., Tacconi L. J., Sánchez F. M., Sternberg A., 2009, ApJ, 696, 448
Hicks E. et al., 2013, ApJ, 768, 107
Jarrett T. H., Chester T., Cutri R., Schneider S. E., Huchra J. P., 2003, AJ, 125, 525
Kormendy J., Ho L. C., 2013, ARA&A, 51, 511
Krajnović D., Cappellari M., de Zeeuw P. T., Copin Y., 2006, MNRAS, 366, 787
Krajnović D. et al., 2011, MNRAS, 414, 2993
Kuijken K., Merrifield M. R., 1995, ApJ, 443, L13

Kuzio de Naray R., Arsenault C. A., Spekkens K., Sellwood J. A., McDonald M., Simon J. D., Teuben P., 2012, MNRAS, 427, 2523
Laine S., Shlosman I., Knapen J. H., Peletier R. F., 2002, ApJ, 567, 97
Lena D. et al., 2015, ApJ, 806, 84
McGregor P. J. et al., 2003, Proc. SPIE, 4841, 1581
Malkan M. A., Gorjian V., Tam R., 1998, ApJS, 117, 25
Maraston C., 2005, MNRAS, 362, 799
Márquez I., Masegosa J., Durret F., González Delgado R. M., Moles M., Maza J., Pérez E., Roth M., 2003, A&A, 409, 459
Martini P., Dicken D., Storchi-Bergmann T., 2013, MNRAS, 420, 2249
Mazzalay X. et al., 2014, MNRAS, 438, 2036
Onken C. et al., 2014, ApJ, 791, 37
Pogge R. W., Martini P., 2002, ApJ, 569, 624
Reese A. S., Williams T. B., Sellwood J. A., Barnes E. I., Powell B. A., 2007, AJ, 133, 2846
Ricci T. V., Steiner J. E., Menezes R. B., 2016, MNRAS, 463, 3860
Riffel R. A., 2010, Ap&SS, 327, 239
Riffel R. A., Storchi-Bergmann T., 2011a, MNRAS, 411, 469
Riffel R. A., Storchi-Bergmann T., 2011b, MNRAS, 417, 2752
Riffel R., Rodríguez-Ardila A., Pastoriza M. G., 2006, A&A, 457, 61
Riffel R. A., Storchi-Bergmann T., Winge C., McGregor P. J., Beck T., Schmitt H., 2008, MNRAS, 385, 1129
Riffel R. A., Storchi-Bergmann T., Riffel R., Pastoriza M. G., 2010, ApJ, 713, 469
Riffel R. A., Storchi-Bergmann T., Nagar N. M., 2010, MNRAS, 404, 166
Riffel R., Riffel R. A., Ferrari F., Storchi-Bergmann T., 2011, MNRAS, 416, 493
Riffel et al., 2013, MNRAS, 430, 2249
Riffel R. A., Storchi-Bergmann T., Riffel R., 2014, ApJ, 780, 24
Riffel R. A. et al., 2015a, MNRAS, 446, 2823
Riffel R. et al., 2015b, MNRAS, 450, 3069
Riffel R. A., Storchi-Bergmann T., Riffel R., 2015c, MNRAS, 451, 358
Sánchez F. M., Davies R. I., Genzel R., Tacconi L. J., Eisenhauer F., Hicks E. K. S., Friedrich S., Sternberg A., 2009, ApJ, 691, 749
Schmitt H. R., Kinney A. L., 2000, ApJS, 128, 479
Schnorr-Müller A., Storchi-Bergmann T., Nagar N. M., Robinson A., Lena D., Riffel R. A., Couto G. S., 2014, MNRAS, 437, 1708
Schnorr-Müller A., Storchi-Bergmann T., Robinson A., Lena D., Nagar N. M., 2016, MNRAS, 457, 972
Schnorr-Müller A., Storchi-Bergmann T., Ferrari F., Nagar N. M., 2017, MNRAS, 466, 4370
Schönell A. J., Riffel R. A., Storchi-Bergmann T., Winge C., 2014, MNRAS, 445, 414
Sellwood J. A., Sánchez R. Z., 2010, MNRAS, 404, 1733
Sellwood J. A., Spekkens K., 2015, preprint (arXiv:1509.07120)
Simoes Lopes R. et al., 2007, ApJ, 655, 718
Smajić S., Moser L., Eckart A., Busch G., Combes F., García-Burillo S., Valencia-S. M., Horrobin M., 2015, A&A, 583, A104
Somerville et al., 2008, MNRAS, 391, 481
Spekkens K., Sellwood J. A., 2007, ApJ, 664, 204
Springel et al., 2005, MNRAS, 361, 776
Storchi-Bergmann T., Dors O., Jr, Riffel R. A., Fathi K., Axon D. J., Robinson A., 2007, ApJ, 670, 959
Storchi-Bergmann T., McGregor P., Riffel R. A., Simões Lopes R., Beck T., Dopita M., 2009, MNRAS, 394, 1148
Storchi-Bergmann T., Simões Lopes R., McGregor P., Riffel R. A., Beck T., Martini P., 2010, MNRAS, 402, 819
Storchi-Bergmann T., Riffel R. A., Riffel R., Diniz M., Borges Vale T., McGregor P., 2012, ApJ, 755, 87
Terrazas B. A., Bell E. F., Henriques B. M. B., White S. D. M., Cattaneo A., Woo J., 2016, ApJ, 830, L12
van de Ven G., Fathi K., 2010, ApJ, 723, 767
van der Marel R. P., Franx M., 1993, ApJ, 407, 525
Veilleux S., Tully R. B., Bland-Hawthorn J., 1993, AJ, 105, 1318
Winge C., Riffel R. A., Storchi-Bergmann T., 2009, ApJS, 185, 186

APPENDIX A: STELLAR KINEMATICS BASED ON ALREADY PUBLISHED DATA

Figs A1–A5 show maps for the stellar kinematics of galaxies with previous measurements already published by our group.

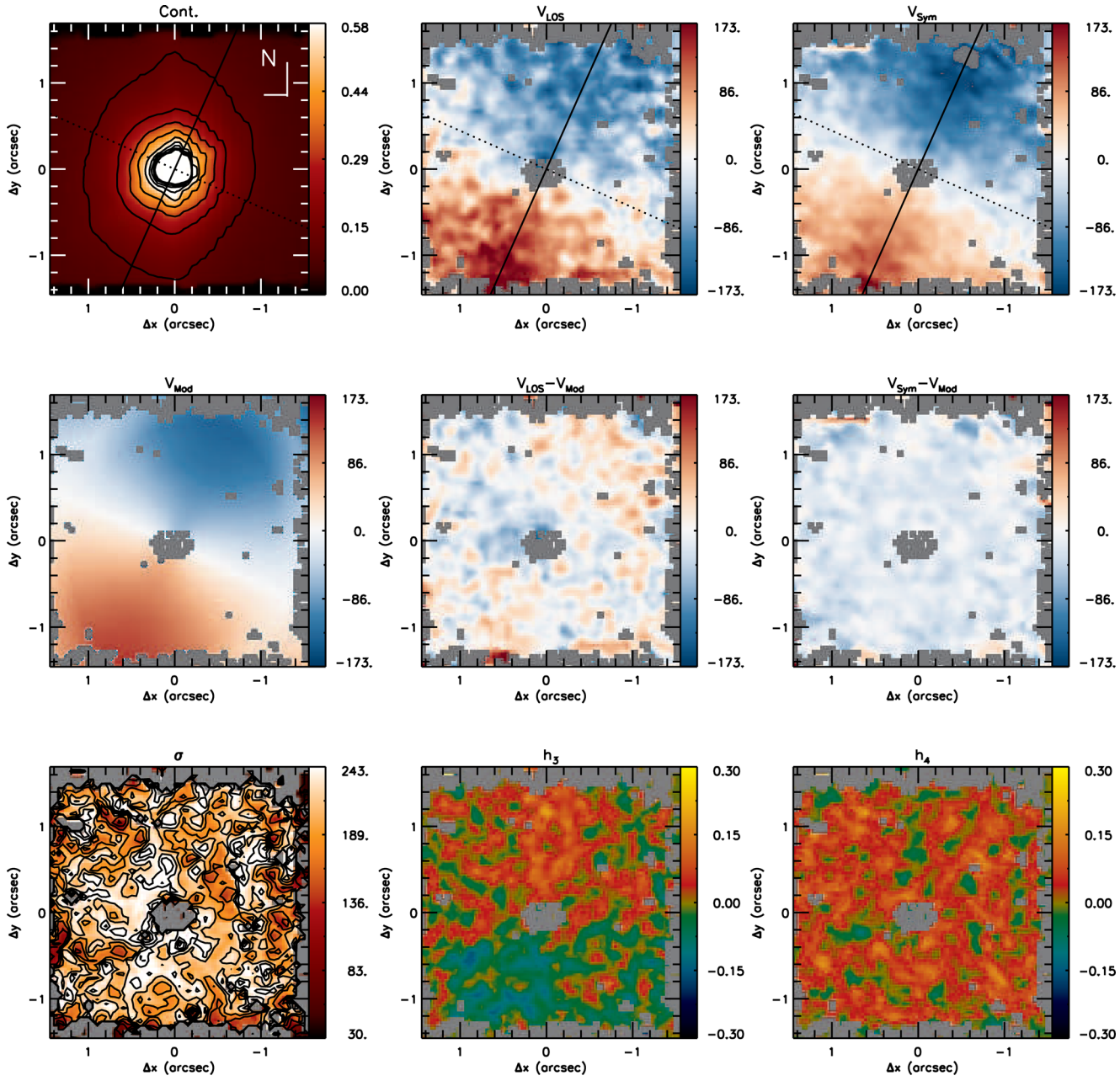

Figure A1. Same as Fig. 2 for NGC 2110. The original stellar kinematics measurements are presented in Diniz et al. (2015).

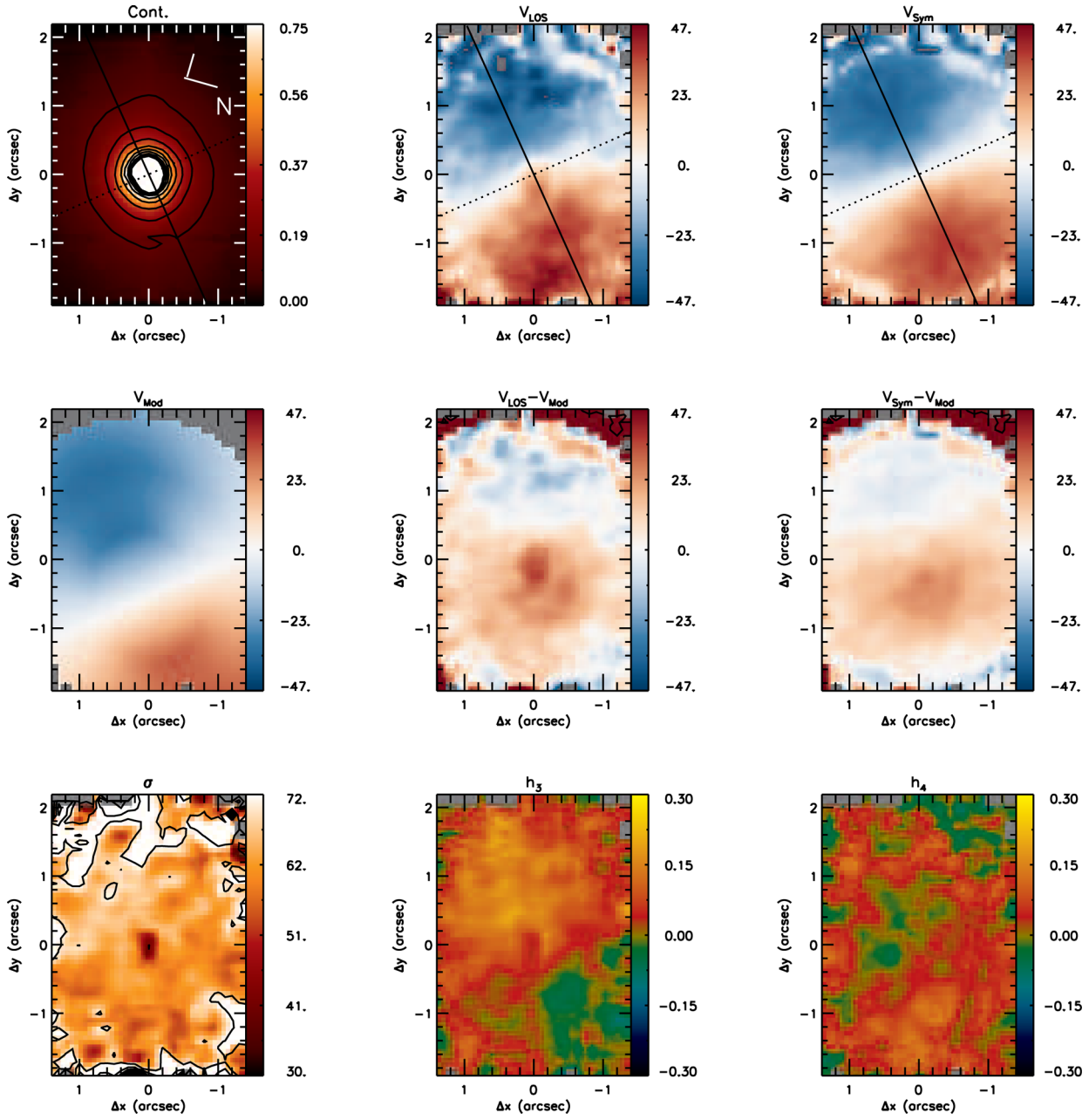

Figure A2. Same as Fig. 2 for NGC 4051. The original stellar kinematics measurements are presented in Riffel et al. (2008).

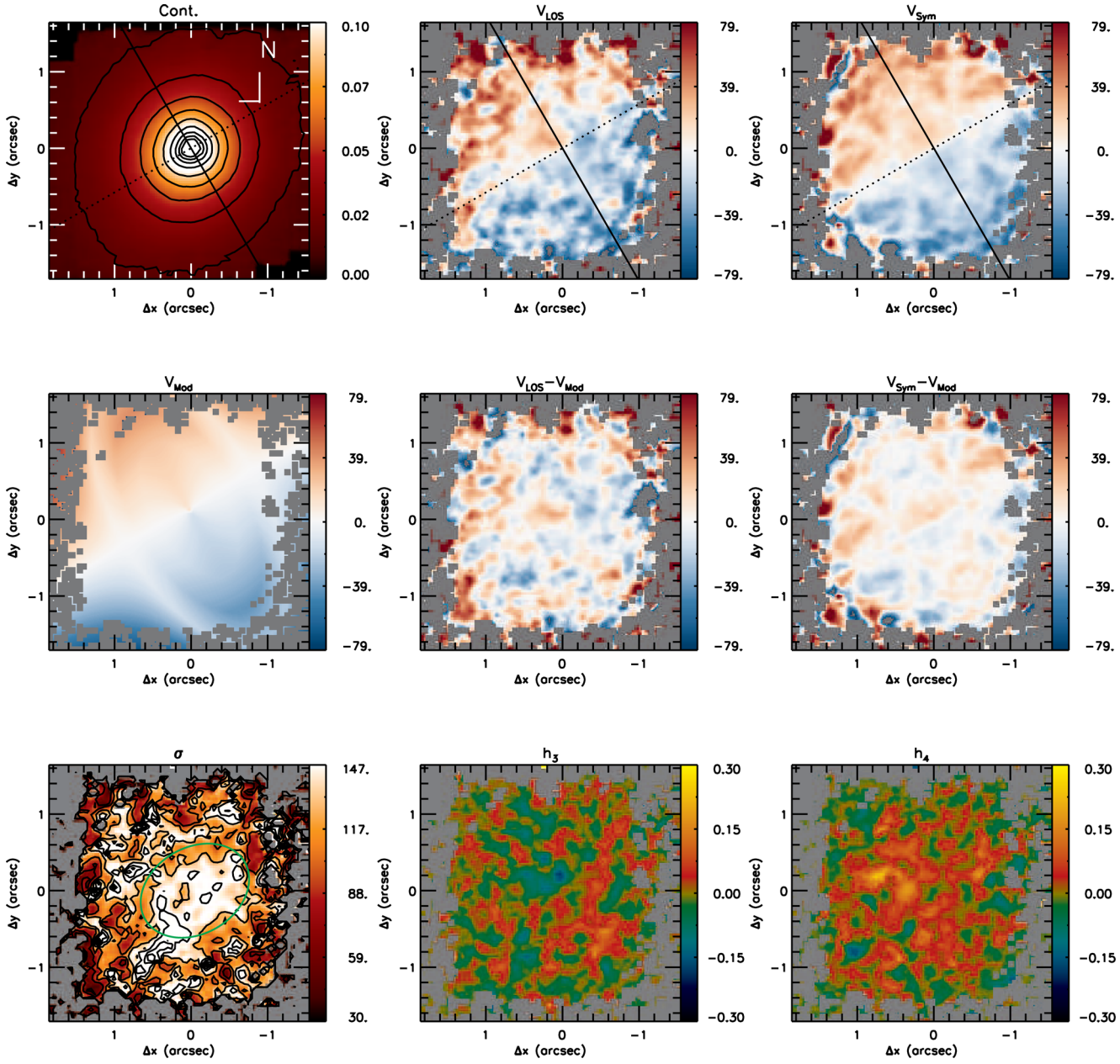

Figure A3. Same as Fig. 2 for NGC 5929. The original stellar kinematics measurements are presented in Riffel et al. (2015c).

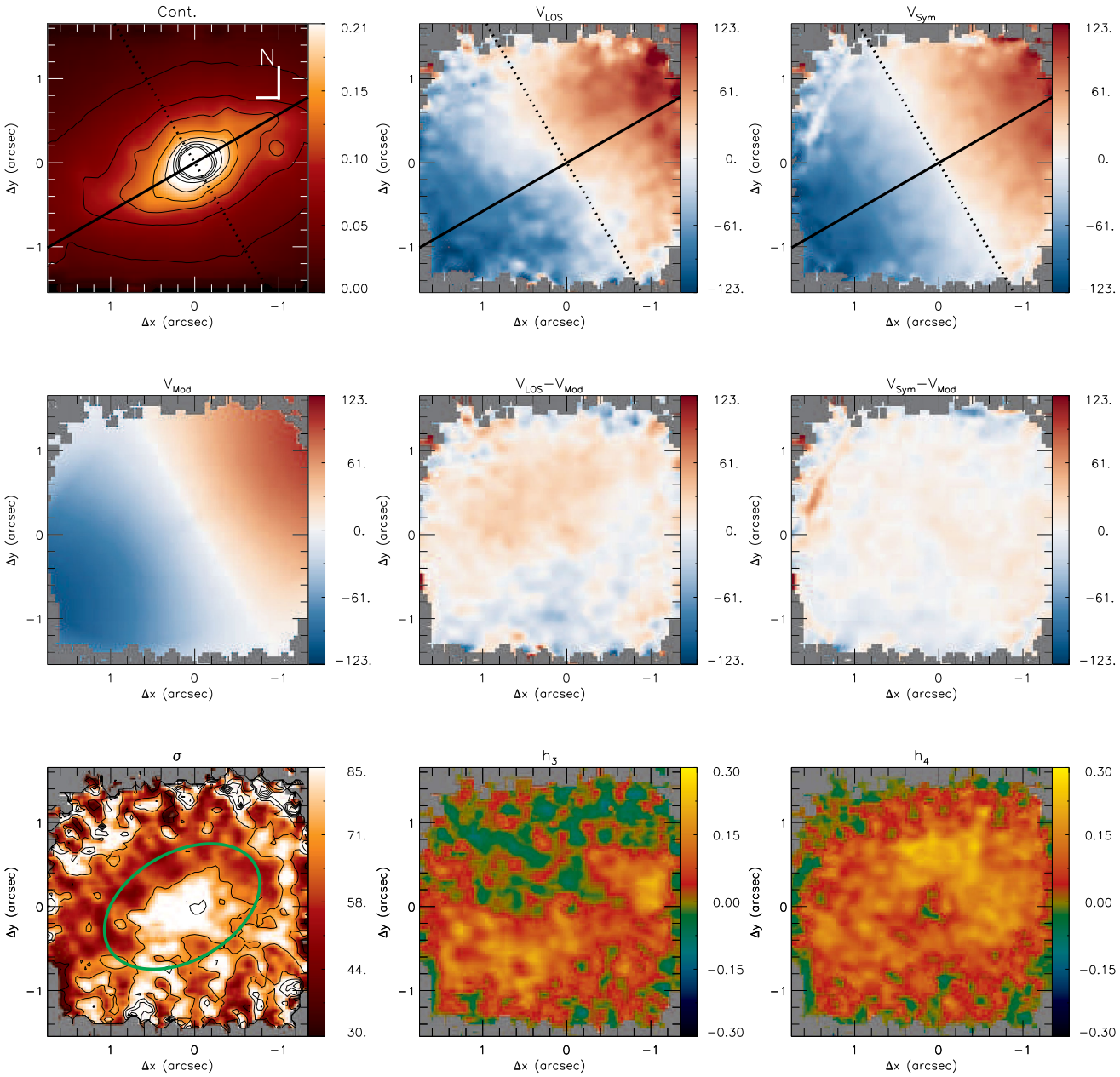

Figure A4. Same as Fig. 2 for Mrk 1066. The original stellar kinematic measurements are presented in Riffel & Storchi-Bergmann (2011a).

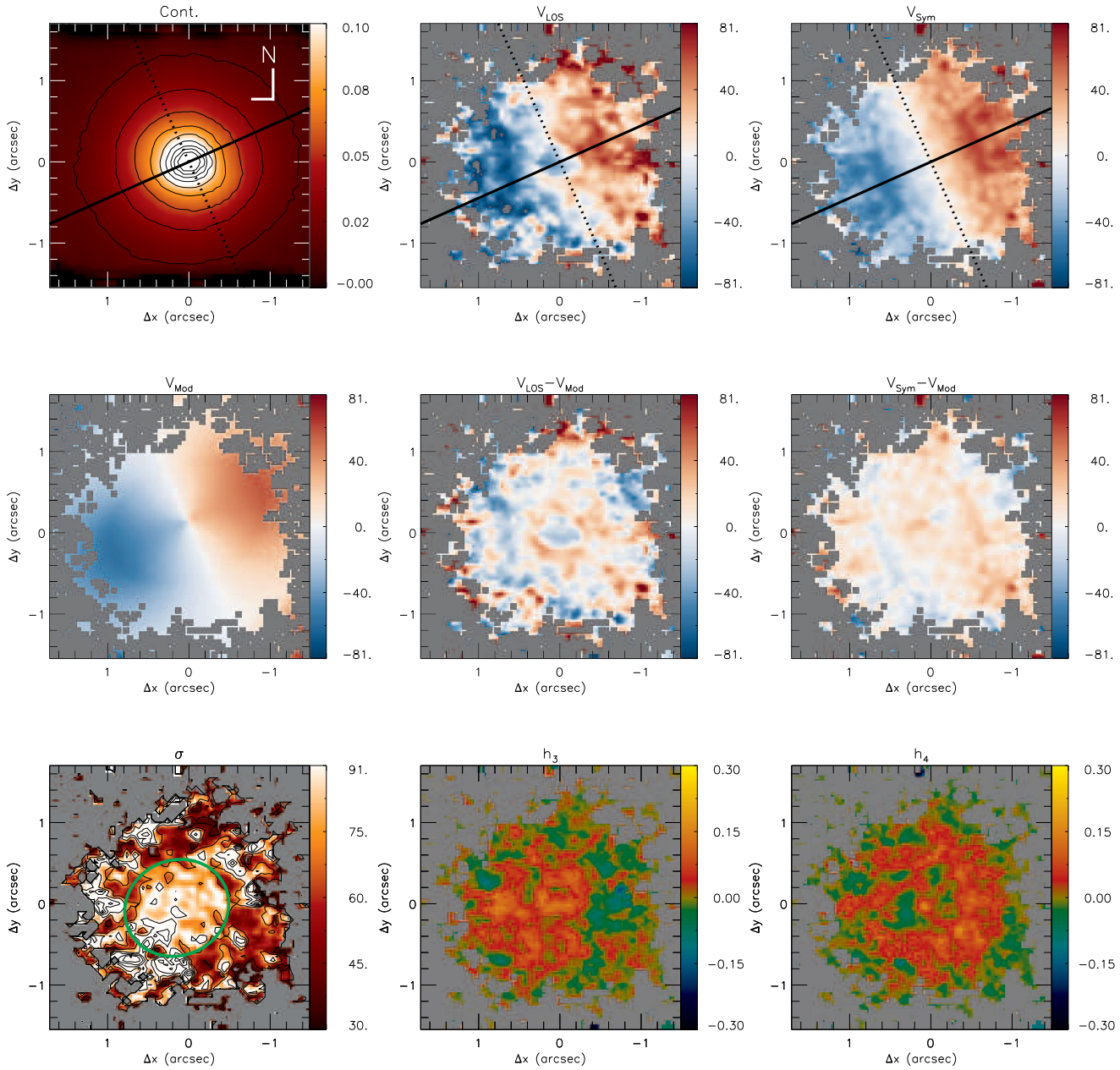

Figure A5. Same as Fig. 2 for Mrk 1157. The original stellar kinematic measurements are presented in Riffel & Storchi-Bergmann (2011b).

APPENDIX B: ONE-DIMENSIONAL CUTS FOR THE STELLAR KINEMATICS

Fig. B1 shows one-dimensional cuts along the major axis of the galaxies for the LOS velocity (left) and σ (right). Plots of the LOS velocity ($V_{\rm LOS}$) versus h_3 and σ versus h_4 using all spaxels are shown in Fig. B2.

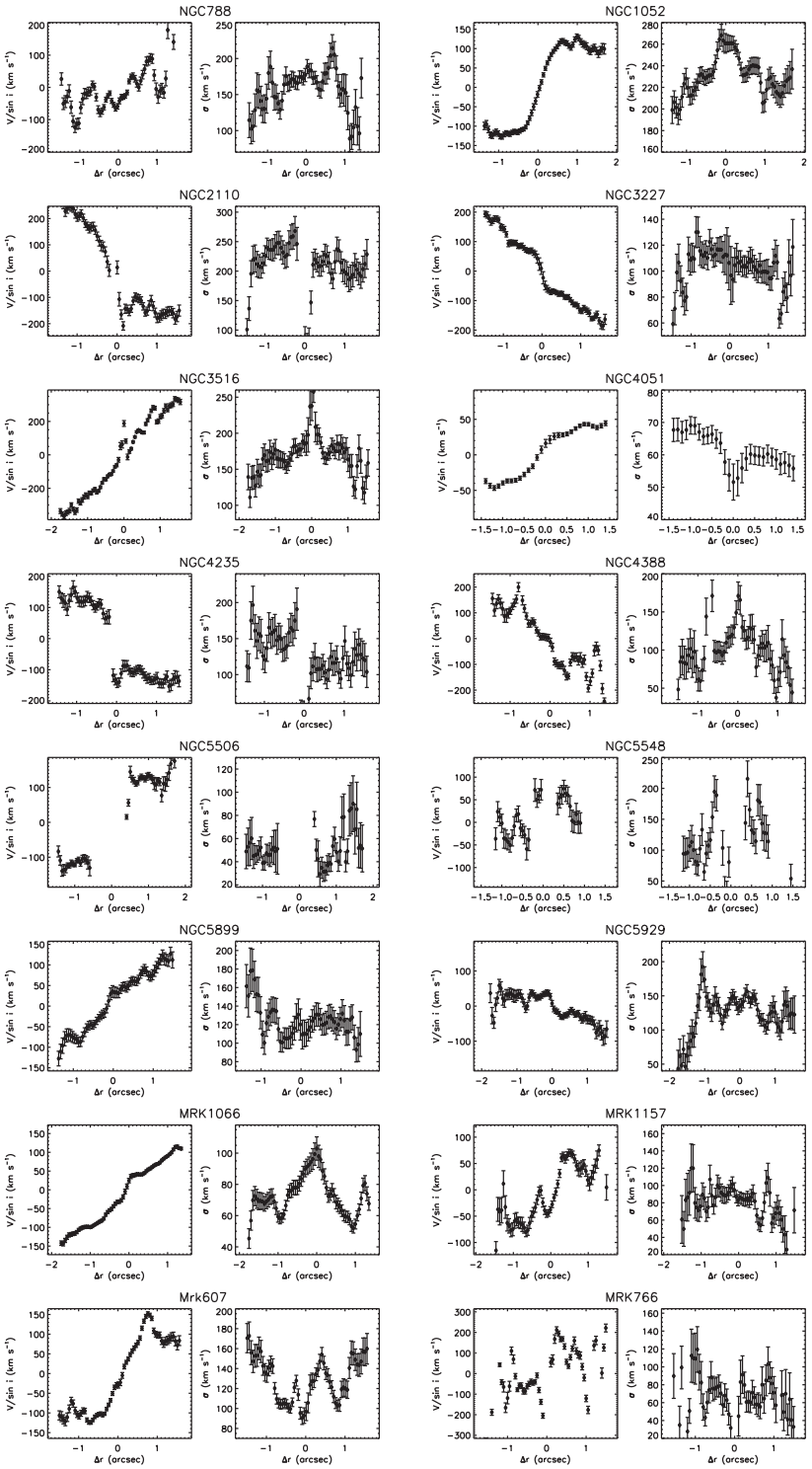

Figure B1. One-dimensional cuts along the major axis of the galaxies obtained by averaging the observed velocities within a pseudo-slit with 0.25 arcsec width. The orientation of the major axis and the inclination of the disc used in these plots are from Table 2.

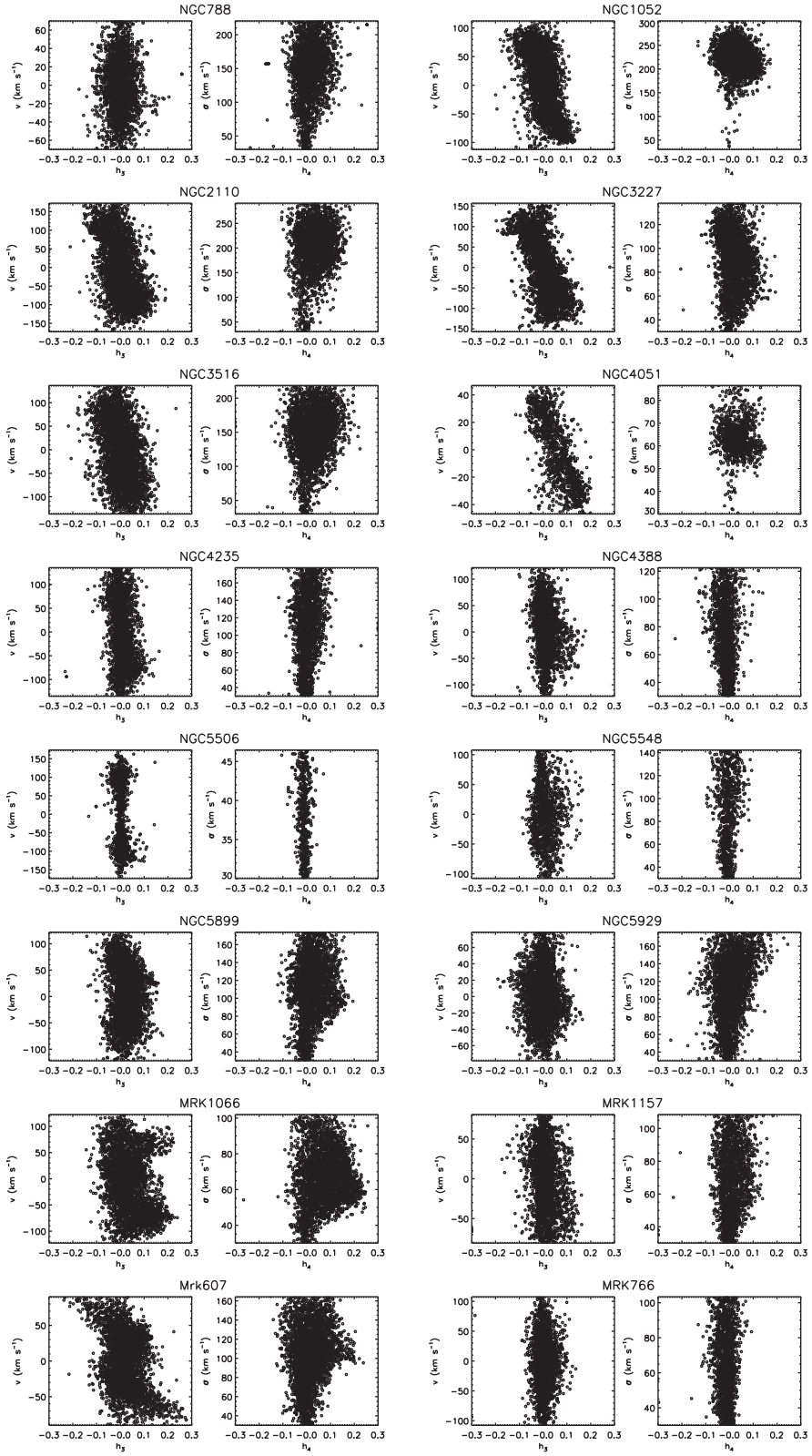

Figure B2. Plots of the LOS velocity ($V_{\rm LOS}$) versus h_3 and σ versus h_4 for the galaxies of our sample. For most galaxies, $V_{\rm LOS}$ and h_3 are anticorrelated and a trend of higher values of σ being observed at locations with negative h_4 values and smaller σ values associated with positive h_4 values.

This paper has been typeset from a TEX/LATEX file prepared by the author.